The Numerical Study of Heat Transfer and Multiphase Flows in Sub-Atmospheric Industrial Evaporators

Jujar Singh Panesar

Submitted in accordance with the requirements for the degree of
Doctor of Philosophy

The University of Leeds
School of Chemical and Process Engineering

September 2016

This thesis is dedicated to my mother Balwant Kaur Panesar,
and to my father Narinder Singh Panesar.

Acknowledgements

I would like to express my sincere gratitude equally to Professor Peter Heggs and Dr Alan Burns for their support of my PhD. I am indebted to them for their supervision, contributions and patience in guiding me to produce this work. They brought laughter, experience and wisdom to our many supervisor meetings which was invaluable for progress. I shall never forget “the heat transfer coefficient is the figment of the imagination of the heat transfer engineer”.

In addition to my academic advisors I would like to thank Mr Waqas Ahmad, Dr Steve Graham, Dr Steve Baker, Dr Julian Spencer, Dr Bob Geddes and Dr Richard Jarvis of the National Nuclear Laboratory (NNL), for their assistance in providing key information on the operations of the unscaled test rigs; the scaled test rig; and the Sellafield evaporators.

I am thoroughly appreciative to the organising committee of The John Fox Award in selecting me as their first research student to win the award. The award funds contributed towards an overseas research placement at the *Institut für Fluiddynamik* at *Helmholtz-Zentum Dresden-Rossendorf* (HZDR), Germany. The funds allowed me the opportunity to learn about novel models developed at HZDR for Eulerian-Eulerian multiphase flow, which helped me in completing the research outcomes in this thesis. With this, I would also like to express my gratitude to Dr Eckhard Krepper, Dr Thomas Höhne and Dr Dirk Lucas at HZDR who helped to facilitate my placement, and provided advice in my research.

The journey I shared with the friends I worked alongside in the research office was invaluable to the success of my work. They provided humour in the face of adversity which helped during the long days in the research office.

It would not have been possible to have undertaken this PhD without the encouragement of my family who pushed me to succeed since our humble beginnings before my PhD had begun, and will no doubt continue to do so long into the future. Therefore I am eternally appreciative to my older brothers Ranveer and Taranjit Singh Panesar, and their families for being a part of my journey. Lastly words will never be adequate enough to describe the importance the love and support my mother had provided to me. Her affection never failed to reach me wherever I was.

Finally I am eternally indebted to my beloved wife Mahsa Shahi Avadi. Her steadfast and unconditional love and support was a foundation on which I was able to rely on and thereby produce this work. Her enduring patience during my countless late nights of “just checking simulations” will never be forgotten. Thank you Mahsa.

Abstract

The Sellafield site in Cumbria, UK maintains three steam heated evaporators which operate at sub-atmospheric pressure. They are used to evaporate and thus concentrate nitric acid based highly active liquor, which is a by-product arising from reprocessing spent nuclear fuels. Corrosion occurs on the internal surfaces of the evaporators in contact with the liquors. The rates of corrosion are a function of the local surface temperatures and heat transfer rates. Therefore accurate heat transfer predictions inside the evaporators is highly desirable as it enables good predictions to the rates of corrosion.

The aim of this study was to use engineering calculations and computational fluid dynamics (CFD) to provide predictions of the continuity, momentum and energy transfer occurring inside evaporators operating at sub-atmospheric pressure. Three evaporator scales were chosen for this study: (i) two small unscaled cylindrical test rigs which were 0.1 m diameter, and had liquid fill depths of 0.1 m and 2.215 m respectively; (ii) a test rig representing a quarter scale slice of an industrial evaporator, and had a liquid fill depth of 0.8m; (iii) and lastly Sellafield Evaporator C, which represented a full scale industrial evaporator design, and had a fill depth of 2.35 m.

Thermal resistance investigations were performed on the unscaled cylindrical test rigs which proved conduction heat transfer through the walls removed all sensitivity to the specified boundary conditions. Single phase CFD simulations were also performed on the test rigs which showed a symmetrical geometry assumption could not be used to simplify the modelling approach.

Two phase Eulerian-Eulerian CFD simulations were performed on the one quarter scaled test rig. A custom length scale for use in the interfacial area density was developed and used. The length was a function of a user prescribed rate constant. In the simulations evaporation at the free surface was modelled. Published experimental data was used to validate the simulations, and showed that the length scale required a rate constant of 1 Hz to simulate evaporating flows at sub-atmospheric pressure.

The CFD models which were developed were applied to the simulations of the full scale industrial evaporator design, Sellafield Evaporator C. The results shows the evaporator behaved similar to an unconstrained thermosyphon reboiler with distinct counter rotating convection cells. Indications of nucleate boiling was not present on all heat transfer surfaces as previously thought, which meant surface corrosion rates may be lower than anticipated.

Table of Contents

List of Tables

List of Figures

List of Symbols

Roman Letters

Symbol	**Meaning**	**Units**
$\tilde{A}$	Grouped thermophysical properties	-
C_P	Isobaric heat capacity	J/kgK
C_{SF}	Surface finish	-
D	Diameter	m
e	Error estimate in the GCI procedure	-
f	Frequency	Hz
F	Gorenflo and Kenning multiplication factor	-
g	Acceleration due to gravity	m/s^2
h	Heat transfer coefficient	W/m^{2}K
h	Mesh size in the GCI procedure	-
$\Delta H'_{lg}$	Augmented enthalpy of vaporisation	J/kg
ΔH_{lg}	Enthalpy of vaporisation	J/kg
k	Turbulent kinetic energy	J/kg
k	Thermal diffusivity	m^2/s
L	Characteristic length scale	m
M	Molar mass	g/mol
p	Apparent order in the GCI procedure	-
P	Pressure	bar
P'	Modified pressure term	Pa
$\dot{q}$	Heat flux	W/m^2
$q(p)$	Function in the GCI procedure	-
$\dot{Q}$	Heat transfer rate	W
r	Radius	m
R	Specific thermal resistance	m^{2}K/W
$\bar{R}$	Universal gas constant	J/Kmol
S	Source term in the conservation equations	Various
t	Time	s
T	Temperature	°C
T^*	Dimensionless temperature	-
$U_{i,j,k}$ or u	Velocity	m/s
V	Volume	m^3

Greek Letters

Symbol	**Meaning**	**Units**
δ	Condensate film thickness	m
ρ	Density	kg/m^3

μ	Dynamic viscosity	kg/ms
λ	Thermal conductivity	W/mK
σ	Surface tension coefficient	N/m
v	Kinematic viscosity	m^2/s
ϕ	Variable	Various
β	Coefficient of expansion	K^{-1}
β	Length scale model rate constant	Hz
ω	Turbulence frequency	Hz
ε	Turbulence dissipation rate	J/kg.s
ε	Difference in variable value in the GCI procedure	Various
Γ	Interphase mass transfer	kg/m^2s
θ	Contact angle	°

Subscripts

Symbol	**Meaning**
sat	Saturation
$inner$	Inner
α	Liquid phase
β	Gaseous phase
s	Surface or interface
l	Liquid
g	Gas
w	Wall surface
O	Out
k	Knuckle
∞	Far field
1	Initial state
2	Secondary state
$crit$	Critical
max	Maximum
R	Reduced value
P	Denotes a pressure correction factor
q	Reduced heat flux
$a0$	Reference roughness
ext	Extrapolated value
$Short$	Short test rig
$Tall$	Tall test rig
stm	Steam
csn	Condensation
eff	Effective viscosity
t	Turbulent viscosity

Acronyms

Symbol	Meaning
HALES	Highly active liquor evaporation and storage
THORP	Thermal oxide reprocessing plant
NDA	Nuclear Decommissioning Authority
CFD	Computational fluid dynamics
NNL	National Nuclear Laboratory
ONR	Office for Nuclear Regulation
MC	Average mean condensation model
LC	Local condensation model
RPI	Rensselaer Polytechnic Institute
MuSiG	Multiple size group
SIMPLE	Semi implicit method for pressure linked equations
GCI	Grid convergence index
AMG	Algebraic multigrid method
EVM	Eddy viscosity models
EDH	Eddy diffusion hypothesis

Mathematical Notation

Symbol	Meaning
Δ	Change in property
∂	Partial derivative
∇	Del operator
sgn	Signum function

Dimensionless Numbers

Symbol	Meaning
Pr	Prandtl number
Gr	Grashof number
Ra	Rayleigh number
Nu	Nusselt number

Chapter 1

Introduction to the Work

The highly active liquor (HAL) evaporators are steam heated vessels at the Sellafield site in the UK. The vessels form part of the highly active liquor evaporation and storage (HALES) operating unit. The purpose of the evaporators is to concentrate highly active raffinates up to 100-fold by evaporation (Wilson, 1996 chap. 9) into concentrate. These concentrates are termed highly active liquor (HAL), which after concentration is vitrified into a solid glass resin for eventual long term storage (Upson, 1984; Plumb and Mackay, 1988). Figure 1.1 (a) is the general arrangement of the HAL evaporators with superimposed dimensions (Upson, 1984), and Figure 1.1 (b) is a general schematic of the evaporators (Perry and Geddes, 2011).

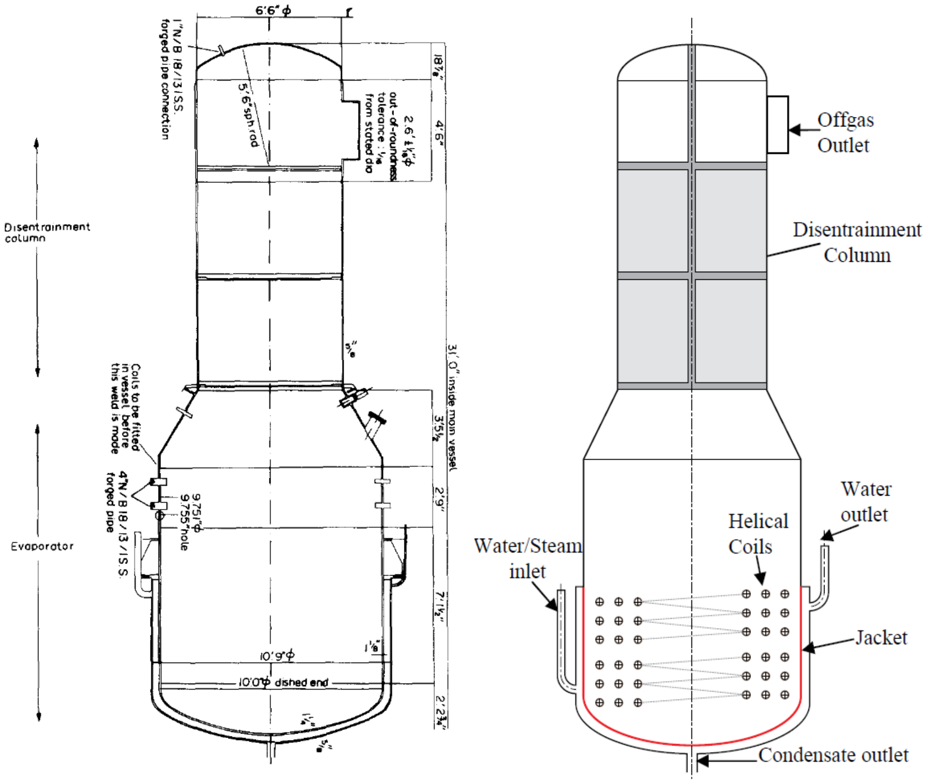

(a) (Upson, 1984) (b) (Perry and Geddes, 2011)

Figure 1.1: (a) General arrangement the evaporators (Upson, 1984); (b) general schematic of the evaporators (Perry and Geddes, 2011).

The HAL evaporators comprise two main sections, a lower evaporating section and an upper disentrainment column. In the Sellafield evaporators the HAL has a depth of almost 2.3

m (Geddes et al., 2009). This corresponds to a free surface position at just above the helical coils in Figure 1.1 (b). The pressure above the free surface is termed the ullage pressure.

The HAL evaporators are steam heated. A steam supply is routed through an external heating jacket and internal helical coils, which are both in contact with the liquor. As the steam condenses inside the jacket and coils, heat is transferred into the liquor causing it to evaporate and become concentrated. The jacket and coils are shown in Figure 1.1 (b).

The evaporators are batch operated. During the evaporation of a liquor stock, a continuous feed of liquor from the stock tanks is supplied to the evaporator vessel at the same rate of evaporation (Perry and Geddes, 2011). This ensures that the free surface level is maintained during operation. There are two types of liquor streams: those from the thermal oxide reprocessing plant (THORP) and those from the Magnox reprocessing plant, both of which are at Sellafield. The THORP facility reprocesses spent fuel from advanced gas cooled reactors and light water reactors. The Magnox facility reprocesses fuel from legacy Magnox reactors. Liquor streams from the THORP facility take around 12 days to concentrate inside the evaporator, compared to 40 days for Magnox (Wakem et al., 2009).

There are three HAL evaporators currently in operation at the Sellafield site. Evaporators A, B and C became operational in 1970, 1983 and 1990 respectively. The Nuclear Decommissioning Authority (NDA) are currently funding the construction of Evaporator D at the Sellafield site (Robson and Candy, 2009). Additionally there is an evaporator of a similar design in operation at the Rokkasho Mura nuclear reprocessing site in Japan (Plumb and Mackay, 1988).

The continued operation of the Sellafield HAL evaporators is highly desirable for the remaining reprocessing operations. Without the availability of the evaporators, reprocessing of spent nuclear fuel would be under threat (Robson and Candy, 2009).

1.1 Evaporator Issues

The HAL concentrated in the evaporators are nitric acid based and consequently very corrosive. The rates of corrosion occurring on the evaporator surfaces in contact with the liquor, and by extension the thickness of the vessel walls are one of the factors which dictate the operational life of the evaporators (Upson, 1984; Plumb and Mackay, 1988; Perry and Geddes, 2011). The corrosion rates of the metal surfaces in contact with the HAL are a function of the temperatures of those surfaces, where an increase in temperature leads to an increase in corrosion rates (Perry and Geddes, 2011; Geddes et al., 2009).

To mitigate against excessive corrosion, the evaporators operate at sub-atmospheric pressure, where the pressure in the ullage space is operationally recorded at 50 - 70 mm Hg (Upson, 1984) (equivalent to 67 – 93 mbar). Operating at sub-atmospheric pressures reduces the temperatures required evaporation to occur, and thus minimises the operating temperature envelope. Since the vessels evaporate and concentrate liquors at a much lower temperature compared to operating at atmospheric pressures and above, the temperatures of the surfaces in contact with the liquor remain relatively low and hence reduces the rates of corrosion (Perry and Geddes, 2011; Geddes et al., 2009).

During the evaporation process crystalline salt solids become precipitated (Wakem et al., 2009). The liquor must remain acidic in order to minimise excessive precipitation of crystalline salt solids during evaporation (Upson, 1984). One of the many crystalline salt solids which are in suspension inside the liquor is zirconium hydrogen phosphate (ZHP) (Geddes et al., 2009). Solids within the liquor also have the potential to inhibit effective heat transfer into the liquor (Wakem et al., 2009). However in addition to this the solids may themselves also be heat emitting due to decay heat. All of these factors contribute to the risk of corrosion. There is also the potential risk that crystalline salt solids settle on the base of the evaporator and act as a thermal blanket. This would result in increased surface temperatures of the base of the evaporator under the solids, and consequently will increase the rates of corrosion. The movement of the solids and its collisions with the internal structure of the evaporators may also lead to erosion, further contributing to the wear of the evaporator.

The equivalent concentration, or normality of HAL changes with concentration factor. Higher acidic normalities result in higher rates of corrosion. Figure 1.2 is a plot of normality of nitric acid and HAL against concentration factor for an inlet feed acidity of 2.50 N (Upson, 1984). During the early stages of HAL concentration the normality rapidly increases to 9 N within a concentration factor of 20, before reducing to a steady state at a concentration factor of 120 and above. This is in contrast to the behaviour of pure nitric acid which remains steady after a concentration factor of 40. Excessive precipitation of the crystalline salt solids does not occur in the HAL when the normality is at its highest due to the high acidic concentration. However this does have excessive corrosion potential.

All three evaporators currently in operation at Sellafield are showing signs of internal surface corrosion on all heat transfer surfaces in contact with the liquor. Since surface corrosion rates are a function of surface temperature, the temperature distributions on those surfaces must be deduced as accurately as possible during evaporator operation. To accomplish this, the modes of heat transfer on each surface must be predicted. Thermal radiation heat transfer may also play a factor in the overall heat transfer system.

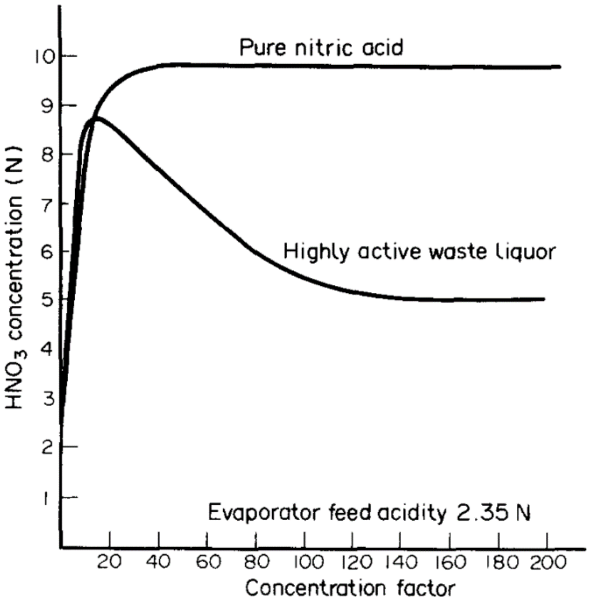

Figure 1.2: Acid concentration profiles during evaporation. The nitric acid concentration in the HAL increases rapidly to 9 N in early stages of evaporation, until concentration factor of 20 and then reduces to a steady concentration (Upson, 1984). Image reproduced with permission from Elsevier.

1.2 Aims of this Study

The aims of this study was to use engineering calculations and CFD to provide predictions of the continuity, momentum and energy transfer occurring inside evaporators operating at sub-atmospheric pressure. Specifically the aims were to:

1. Determine the mechanisms driving heat transfer, evaporation and fluid flow within sub-atmospheric evaporators, and identify the modes of heat transfer occurring within the liquid.
2. Establish the resistances to heat and fluid flow within the evaporator systems and determine how these resistances can affect normal operations of evaporators operating at sub-atmospheric pressure.
3. Highlight existing and novel methods of using numerical models and methods to provide useful information on evaporating flows at sub-atmospheric pressure.
4. With the previous points all taken into consideration, provide information on the distribution of heat transmission and corresponding temperature distributions on the internal surfaces of the evaporators.

1.3 Scope of the Current Work

This study followed a methodological approach. In CHAPTER 1 the work was introduced and the aims clearly defined. In CHAPTER 2, a critical review of the available literature is conducted, identifying information that led to accomplishing the aims, also ensuring that the work in this thesis was novel. In CHAPTER 3 the methods which were used to ensure accurate solutions in the CFD simulations were discussed, which was critical for numerical accuracy.

In CHAPTER 4 two unscaled test rigs commissioned by the National Nuclear Laboratory were introduced. These test rigs were commissioned to try and provide flow conditions similar to those found in the industrial evaporator, Sellafield Evaporator C. A combination of one dimensional heat transfer network approaches, and two and three dimensional single phase CFD approaches were used to try and replicate the types of behaviour occurring in the test rigs. The two methods were compared against each other to ascertain their validity.

In CHAPTER 5 the scaled test rig is introduced, which is one quarter scale experimental test rig depicting a thin slice through Evaporator C. This test rig was far more representative of the evaporators operating at Sellafield. Multiphase CFD boiling simulations were performed on the scaled test rig, and experimental data was used to validate the CFD models. The methods used to simulate the scaled test rig were developed from the foundations established in CHAPTER 4.

In CHAPTER 6 the physical dimensions of Sellafield Evaporator C are introduced. This draws special attention to the complexity of vessel. In addition to this the complex boundary conditions that were used in the CFD simulations for Evaporator C were discussed.

In CHAPTER 7 multiphase CFD simulations using the validated CFD methods established in CHAPTER 5 were used to predict heat transfer and multiphase flows in Evaporator C. Finally in CHAPTER 8 the overall conclusions and recommendations for further work were discussed.

Figure 1.3 illustrates a block diagram summarising the chapters and how they are interlinked to form the thesis.

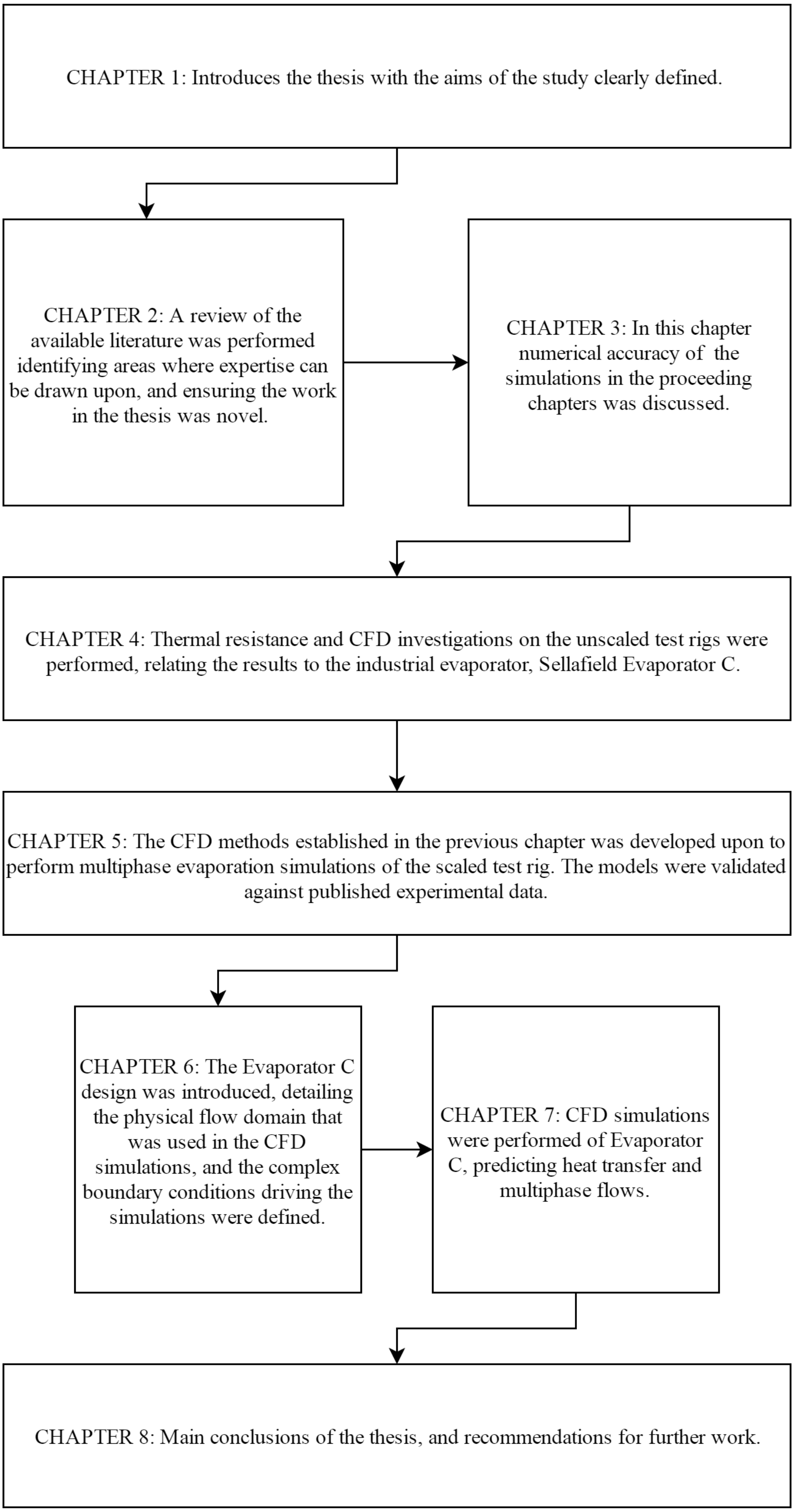

CHAPTER 1: Introduces the thesis with the aims of the study clearly defined.

CHAPTER 2: A review of the available literature was performed identifying areas where expertise can be drawn upon, and ensuring the work in the thesis was novel.

CHAPTER 3: In this chapter numerical accuracy of the simulations in the proceeding chapters was discussed.

CHAPTER 4: Thermal resistance and CFD investigations on the unscaled test rigs were performed, relating the results to the industrial evaporator, Sellafield Evaporator C.

CHAPTER 5: The CFD methods established in the previous chapter was developed upon to perform multiphase evaporation simulations of the scaled test rig. The models were validated against published experimental data.

CHAPTER 6: The Evaporator C design was introduced, detailing the physical flow domain that was used in the CFD simulations, and the complex boundary conditions driving the simulations were defined.

CHAPTER 7: CFD simulations were performed of Evaporator C, predicting heat transfer and multiphase flows.

CHAPTER 8: Main conclusions of the thesis, and recommendations for further work.

Figure 1.3: Block diagram illustrating the structure of the thesis and the way the chapters are interlinked.

Chapter 2

Literature Review

2.1 Introduction

The Sellafield site in Cumbria, UK is the country's principal nuclear reprocessing site. Currently the site has no generating capacity as the previous four power reactors are being decommissioned. Future generating capacity close to the site is currently being considered. Principally the site is used to support the nuclear fuel cycle by reprocessing spent nuclear fuel. An outline of the nuclear fuel cycle is shown in Figure 2.1.

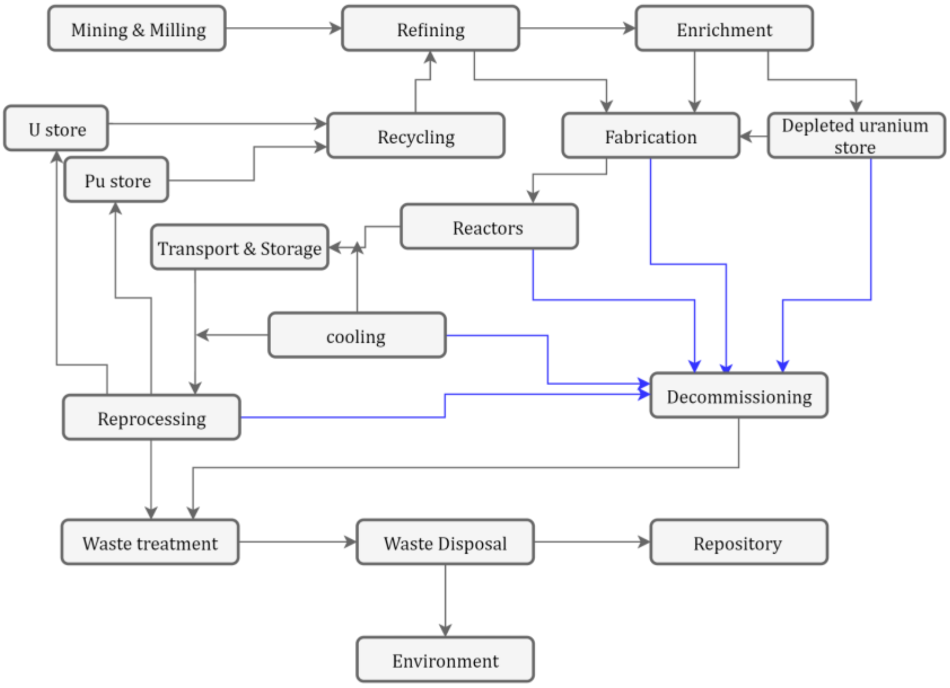

Figure 2.1: Outline of the nuclear fuel cycle (adapted from Wilson (1996)).

In the outline of the fuel cycle in Figure 2.1 the process termed *Waste Treatment* is critical to the cycle. Without it highly active waste arisings from the *Reprocessing* and *Decommissioning* steps cannot be processed, its amount reduced and managed. To do without the *Waste Treatment* step is not permissible as the Office for Nuclear Regulation have capped highly active waste arisings to be no greater than 6524 teU (Office for Nuclear Regulation, 2015b). Hence in order to allow the fuel cycle to operate effectively, the *Waste Treatment* process must be available at all times, or risk halting the reprocessing operations. Waste arisings from the *Reprocessing* and *Decommissioning* steps of the fuel cycle in Figure 2.1 are predominantly HAL.

2.2 Origins of Highly Active Liquor (HAL)

In the UK the main nuclear reactor types are the Magnox reactor and the advanced gas cooled reactor. Typically fuel within the reactors are replaced with newer ones when its ability to maintain criticality is only just achievable when the reactor is at full power (Wilson, 1996 p. 89).

On removal from the reactors, the fuel, now termed spent fuel, is placed in temperature controlled onsite spent fuel ponds where they are allowed to cool. Fuel elements are stored in the fuel ponds for around 1 year (Upson, 1984), but in some instances it may spend over twenty years in the fuel ponds (Wilson, 1996 p. 111).

After sufficient cooling in the onsite ponds, the spent fuel is placed in transport flasks and transported to the Sellafield site for reprocessing (Upson, 1984). Although Magnox reactors are no longer in operation, any spent fuel from legacy operations are sent to the Magnox reprocessing plant. Spent fuel from advanced gas cooled reactors and pressurised (or boiling) water reactors are sent to the THORP reprocessing plant. Upon arrival at either the Magnox or THORP reprocessing plants in Sellafield, the spent fuel is removed from the transport casks and placed in fuel ponds at the Sellafield site where it is allowed to cool even further (Upson, 1984).

After sufficient cooling at the Sellafield ponds, the fuel cladding is stripped from the fuel, and the fuel is then dissolved in nitric acid solution. Chemical separation processes recovers the unused uranium and plutonium from the solution. After chemical separation, the remaining product is a waste liquid, termed raffinate. Up to 99% of the fission product activity is contained in the liquid (Upson, 1984) which gives it its radioactive properties. The raffinate is also nitric acid based which causes it to be corrosive. Once the raffinate is ready to be processed, it is sent to the HALES plant for volume reduction and concentration prior to solidification by vitrification into a glass solid.

2.3 Volume Reduction and Concentration

Figure 2.2 is a flow diagram of the HALES plant at Sellafield (Upson, 1984) which houses Evaporator A, B or C (dashed red border). The image shows the processes raffinate undergoes prior to evaporation and post evaporation.

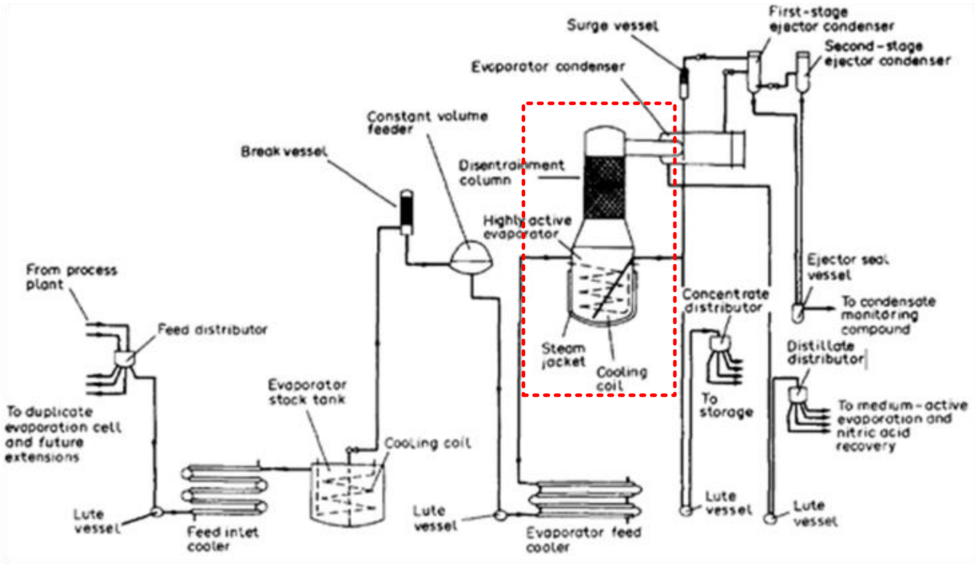

Figure 2.2: Flow diagram of the HALES plant at Sellafield (Upson, 1984).

Volume reduction and concentration of the HAL is achieved in the following steps (Upson, 1984):

1. The raffinate is pre-cooled via the feed inlet cooler and then directed to the evaporator stock tank where it is allowed to cool further before being pumped to Evaporator A, B or C via an ejector system.
2. The raffinate enters the evaporators. When sufficient liquor level has been achieved, steam feed supplied heat to the evaporator via an external heating jacket and internal helical coils, which allowed the liquor to evaporate under vacuum. To maintain a constant liquor level the rate of feed from the stock tank is approximately the rate of evaporation. This allows the evaporator to maintain steady state conditions.
3. The generated vapour from the evaporation process is condensed in the overhead evaporator condenser to form distillate. Its activity is constantly monitored. In the event of high activity, the distillate can be re-routed to the evaporator stock tank; otherwise it is transferred to the medium active evaporation plant.
4. This process continues until the required evaporation factor has been achieved at the end of the batch. The remaining contents within the evaporator is termed HAL concentrate.
5. At the end of the batch evaporation the steam feed is deactivated and cooling water is pumped inside the external jacket and internal coils to ensure the concentrate temperature does not exceed 60°C before being vacuum ejected to a storage tank.
6. Eventually there are two products that arise from evaporating the raffinate. These are the medium activity distillate (the condensed liquid form of the vapour), and the HAL concentrate (the remaining product after evaporation). The distillate and concentrate

are separately denitrated and following further processes are eventually made immobile by vitrification into a glass solid.

2.4 Evaporators A and B

Evaporators A and B came online in 1970 and 1983 respectively. Evaporator B is the principle evaporator out of the two, whilst A is the reserve in case B is out of commission. They are used to evaporate liquors arising from the Magnox plants only (Office for Nuclear Regulation, 2015a). Both evaporators contain an external heating jacket and four internal helical coils.

Both evaporators are coming to the end of their operational life. Their operability is undermined by defects such as pinhole failures due to excessive corrosion of the evaporators walls by the liquor (Office for Nuclear Regulation, 2015a). Operational experience and best practices have helped to design and commission Evaporator C.

2.5 Evaporator C

Evaporator C can evaporate liquors arising from both Magnox and THORP facilities. Evaporator C comprises an external heating jacket and six internal helical coils (as opposed to four in Evaporators A and B). The evaporator is constructed from corrosion resistant 18/13/1 stainless steel (Robson and Candy, 2009). Unlike Evaporators A and B, Evaporator C has not suffered a pinhole failure. To safeguard against failure a minimum wall thickness limit is set for the evaporator safety case. There is a safe operating thickness for the evaporator shell walls and the coil walls. Currently three of the six coils are removed from service due to reaching their end of life safety case limits (Office for Nuclear Regulation, 2015a).

Recently there has been a drive to better understand the heat and flow transmission occurring in Evaporator C, in order to provide accurate temperature distributions and to better predict corrosion. Robson and Candy (2009) state in their work that “the remnant life [of the evaporators] is limited by the remaining corrosion allowance in the evaporator base”. The rates of corrosion are a function of the temperatures occurring on those surfaces (Plumb and Mackay, 1988), therefore accurate predictions of surface temperatures of the evaporators is highly desirable. Determining accurately the surface temperatures would give some indication to the operators of such vessels on the corrosion rates which may substantiate life time extensions of the vessels. Additionally accurate predictions of the heat and flow in the existing evaporators would provide help to engineers to design better vessels in the future.

It is widely accepted in the limited literature that internal metal surface corrosion of the Sellafield evaporators is a major issue (Upson, 1984; Plumb and Mackay, 1988; Perry and Geddes, 2011), where the lifetime of the evaporators are limited by the rates of corrosion occurring on the inside metal surfaces. To mitigate against this the Sellafield evaporators are operated under a vacuum or reduced pressure. This has the advantage that the saturation temperatures of the liquor are far lower at vacuum compared to above vacuum pressures. Since the rate of corrosion is a function of temperature (Perry and Geddes, 2011), operating at vacuum has the benefit of reducing internal surface corrosion on the internal surfaces, since the operating envelope for temperature is low. According to Plumb and Mackay (1988) other benefits of operating the evaporators at a vacuum are:

1. The potential for improving the evaporation capacity by increasing the temperature driving force.
2. Adherence to design codes, some which state safe operation must be achieved within temperature safety limits.

As well as the issue of corrosion occurring inside of the evaporators, operating at vacuum pressure presents a number of other operational issues which is the motivation for this work.

2.6 Past Work Related to the Sellafield Evaporators

Geddes et al. (2009) performed an iterative calculation procedure based on the precedence ordering technique (Heggs and Walton, 1998) to estimate the heat flux and temperature distribution over the length of the internal coils of the Sellafield evaporators. The authors assumed boiling occurred on all heated surfaces. Within the precedence ordering technique they used six different correlations for the boiling heat transfer coefficient, and then compared the respective surface temperatures evaluated from using the six boiling heat transfer coefficients. From the six boiling correlations that were used, the largest disagreement for the coil surface temperature was 9°C, and the process liquor was assumed to be water.

Geddes et al. (2009) also performed iterative precedence ordering calculations based on single phase free convection occurring from the coil surface of Evaporator C. They also performed calculations of boiling and free convection from a corroded surface. Their results showed that very large heat fluxes of 300 kW/m^2 were achieved when the coil surface was not corroded and its surface temperature was around 88°C when using the Cooper (1984) boiling correlation. This contrasts a free convection simulation which was performed, which at the same surface temperature of that of the boiling correlation, a heat flux of only 15 kW/m^2 was achieved. Comparatively the heat flux for boiling from the equivalent corroded surface yields a heat flux of around 150 kW/m^2, and no data is presented for free convection occurring from a corroded surface. Unfortunately no mention was made as to which correlation was used for the equivalent free convection calculations, which means significant conservatism must be taken when using their convection results for a comparative study. In addition to this Geddes et al. used fixed values for the thermophysical properties of water. This does bring into question the reliability of the results that they achieved from the precedence ordering technique, since the thermophysical properties of water will be dependent on the surface temperature of the coils which was evaluated. Curve fitted correlations of the thermophysical properties of water are available (Alane, 2007) which are functions of temperature and pressure.

In their work Geddes et al. (2009) also presented boiling saturation temperature curves with respect to depth for various corrosive liquors found in the industrial Sellafield evaporators. Most of the curves had an almost linear relationship for the boiling saturation temperature corresponding to liquor depth.

Wakem et al., (2009) presented an overview of the heat transfer modelling work that was undertaken between National Nuclear Laboratory (NNL) and Sellafield Ltd to remove conservative predictions on the condition of the Sellafield evaporators. Wakem et al. used the precedence ordering technique in a similar manner to the work presented by Geddes *et al.*, (2009) to predict the wall superheat of the HALES evaporators when using the Cooper (1984) boiling correlation. Although no numerical results are presented for this investigation, the authors claim that the calculated wall superheat was more than the minimum superheat required at the onset of nucleate boiling when using a well-known correlation for the onset of nucleate boiling.

Wakem et al. (2009) also presented a brief CFD investigation, modelling one of their experimental test rigs as a 2D rectangular slice through the centre, and used water as the liquor in a single phase convection simulation. Although no information was provided as to if the simulation was laminar or turbulent, or if good CFD practices where adhered to (such as high resolution discretisation schemes, mesh analysis and solution independence), some noteworthy conclusions was drawn from their work. Firstly when the walls of the vessel were hot or cold, the circulatory behaviour of the fluid changed drastically. The extremity of this observation was seen since when the walls were “cold” there were many circulation cells, and no observable pattern could be defined. When the walls were “hot” the liquor behaved as two large circulation cells, where the liquor was driven up the centreline and walls. Furthermore, a definitive conclusion from both simulations of “cold” and “hot” walls is that the flow was strongly asymmetric and anisotropic, putting the authors assumption of a 2D rectangular slice through the centre into question. Results from a preliminary CFD investigation of heat and fluid flow localised to the base of the Sellafield HALES evaporators was conducted, however no description is provided as to the nature of the investigation, nor were any definitive findings presented.

Perry and Geddes (2011) developed an analytical correlation for the condensation heat transfer coefficient for condensing steam on the outer surface of the toroidal section of the external heating jacket in the Sellafield evaporators. The need for a bespoke condensation correlation for the toroidal section occurs since “corrosion levels [of the heat transfer surface] double with every 8°C rise in metal [surface] temperature” (Perry and Geddes, 2011). This quickly becomes a problem since the current model to predict the condensing heat transfer coefficient in the Sellafield evaporators uses an area average mean condensation (MC) heat transfer coefficient, which does not take the varying thickness of condensate into consideration. Hence the uniform film thickness assumption may incorrectly over or underestimate the surface metal surface temperature. Using the same assumptions as those used by Nusselt (1916), Perry and Geddes alleviated the uniform film thickness problem by developing a local condensation (LC) model, where the value of the condensation heat transfer coefficient is a function of the geometry profile of the Sellafield evaporators, and takes the form shown in Eq. 2.1. The value $\tilde{A}$ contains the terms for the thermophysical properties of the condensate film, and is expressed in Eq. 2.2.

$$h = \lambda_l \left[\frac{\delta_l^4 (r_0 + r_k)^{4/3} + 4\tilde{A} r_k \int_0^{\theta} (r_0 + r_k \cos\theta)^{4/3} (\cos\theta)^{1/3} d\theta}{(\cos\theta (r_0 + r_k \cos\theta))^{4/3}} \right]^{-1/4} \tag{2.1}$$

The value $\tilde{A}$ contains the terms for the thermophysical properties of the condensate film, and is expressed as

$$\tilde{A} = \frac{\mu_l \lambda_l (T_{sat} - T_w)}{\rho_l (\rho_g - \rho_l) g \Delta H'_{lg}} \tag{2.2}$$

Perry and Geddes arrived at this model by applying a mass, momentum and energy balance on a fluid element within a condensate layer attached to the toroidal section, in the same manner as the original Nusselt (1916) formulation. The Perry and Geddes formulation is slightly more involving as it accounts for the curvature of the knuckle, which is accommodated by integrating with respect to a polar coordinate system. The older MC model was compared to the newer LC model. The results of the surface temperatures and heat fluxes corresponding to the liquor depth for the MC and LC models were in agreement. However the newer LC model gave more accurate temperature and heat flux values at the bottom of the evaporator. Furthermore, the LC model was able to predict a thickening condensate layer at the underside of the evaporator, suggesting the newer LC correlation had been operating as designed. However the LC model should be compared with empirical data to reinforce the models’ strengths. As the Perry and Geddes LC models are based on the original assumptions as those presented by Nusselt (1916), it also inherently shares its weaknesses as both models assume laminar condensation, and that only conduction heat transfer occurs within the film.

Kwong and Graham (2011) presented CFD simulations of flow with solids present at the base of a Sellafield Evaporator C. The aim of the work was to determine the conditions in the liquor that would lead to an increase in internal surface temperatures, and hence increase in the rate of corrosion. The CFD simulations were single phase, and a porosity function was used to model a central blockage region and the heating coils. Despite the simulations being single phase, source terms were added to the momentum equations to represent the effect of boiling. Furthermore a layer of solids at the base of the evaporator was modelled as a non-Newtonian power law viscous fluid, characterised by the Herschel–Bulkley non-Newtonian model. Furthermore a 2D axisymmetric approach was taken.

Using the Herschel–Bulkley assumption, a parametric study was undertaken changing one of four parameters whilst keeping three fixed, where the parameters were the yield stress, viscosity of the non-Newtonian fluid (which represented the solids), consistency factor and power law index. From the parametric study, reducing the yield stress of the non-Newtonian fluid had the greatest contribution to erosion at the base of the simulated evaporator. Additionally, increasing the yield viscosity had a similar effect as decreasing the yield stress in that it contributed greatly to the erosion of the evaporator base. The consistency factor and power law index of the non-Newtonian fluid had little to no effect on the erosion of the base.

Using the Herschel–Bulkley assumption to model solid movement at the base of the Sellafield evaporators was shown to be a computationally inexpensive method that provided physically realistic characteristics. However the approach of the Herschel–Bulkley assumption is limited. The works by Kwong and Graham do not show any indication of solid fluid interactions and particulate settling and this is very likely to occur within the free convection cells of the evaporator. Furthermore there is little to no evidence to suggest that adding source terms to the momentum equation to represent the effect of boiling at the base has any significant contribution to the results. In addition to this, the coils of the evaporator, and the central blockage region of the evaporator was modelled using a porous medium. This may lead to unphysical solutions as a porous medium would allow fluid to pass through it. However the benefit of this model is that Kwong and Graham have demonstrated a computationally inexpensive way to model the Sellafield evaporators using porous mediums to model flow resistances (such as the coils), and a non-Newtonian fluid to model solids close to the base acting as a viscous fluid. Although the works of Kwong and Graham may not be entirely accurate, it could be an appropriate starting point to multiphase simulations.

One of the main engineering problems in the Sellafield evaporators and NNL test rigs is that the magnitude of boiling and condensation phase change in the heat transfer system is not known for certain. This is also one of the primary reasons why it is difficult to predict metal surface temperatures in the Sellafield evaporators, and relate it to estimating the life of the various heating components. Hence CFD may be able to yield a solution to this engineering problem.

2.7 Phase Change and Multiphase Flow

The operation of the Sellafield evaporators is driven by heat transfer. There are three modes of heat transfer: conduction, convection and radiation (Incropera and Dewitt, 2002). These modes are well understood in terms of how they transfer heat from the heat source to the heat sink. Of the three modes, radiation is the fastest at transmitting heat. Thermal radiation is not dependent on the thermophysical properties of the medium through which the heat is transported. However it is dependent on the surface properties which radiation heat transfer is emitted from, and absorbed into. Rates of conduction and convection heat transfer are strongly dependent on the thermophysical properties of the medium through which heat transfer occurs. Heat transfer rates in convection are faster than conduction due to the eddy transport modes found in convection, which are much faster than molecular transport modes found in conduction.

Boiling and condensing flows are types of convection processes. Convection heat transfer can be characterised by the heat transfer coefficient, which describes the heat flux transmitted from a surface per degree. The heat transfer coefficient is sensitive to the of the thermophysical properties of the liquid, the temperature difference $(T_w - T_\infty)$ and the surface properties (Kreith et al., 2010 chap. 1).

The magnitude of the convective heat transfer coefficient varies depending on the mode of heat transfer. Kreith et al. (2010 chap. 1) suggests the heat transfer coefficients take the values in Table 2.1.

Fluid	Heat transfer coefficient [W/m^{2}K]
Air, free convection	1 – 5
Superheated steam or air, forced convection	5 – 50
Oil, forced convection	10 – 300
Water, forced convection	50 – 3000
Water, boiling	500 – 10000
Steam, condensing	1000 – 20000

Table 2.1: Range of heat transfer coefficients reported by Kreith et al. (2010 chap. 1).

Bergman et al. (2011 chap. 1) also suggested a range of heat transfer coefficients in Table 2.2.

Fluid	Heat transfer coefficient [W/m^{2}K]
Gases, free convection	2 – 25
Liquids, free convection	50 – 1000
Gases, forced convection	25 – 250
Liquids, forced convection	100 – 20000
Boiling or condensation	2500 – 100000

Table 2.2: Range of heat transfer coefficients reported by Bergman et al. (2011 chap. 1).

Although the orders of magnitude are in agreement between the values presented in Table 2.1 and Table 2.2, the maximum and minimum range of values are in disagreement. This suggests considerable errors should be expected when determining the heat transfer coefficient under varied conditions such as free convection, or boiling.

In free convection systems circulations occurs due to the local density differences inside the liquid corresponding to the local temperature gradients. The effects of liquid circulations due to local density differences are prevalent in free convection systems and less so in forced convection systems. This is because liquid movement in the latter case relies on an external force to induce movement, such as a pump or an ejector system.

In Figure 2.3 (Bergman et al., 2011 chap. 9) unstable fluid recirculation occurs because the density variations acts against the gravitational body force. The unstable regime occurs when $T_2 > T_1$. Liquid movement only occurs when the temperature gradients exceed a critical value leading to convection currents. When this happens the density of the fluid decreases against the direction of gravity, and the buoyancy forces are large enough to overcome viscous drag forces leading to unstable liquid circulations. In the unstable case in Figure 2.3 the density at position 1, ρ_1 is greater than the density at position 2, ρ_2. This enables a displacement effect, where dense packets of fluid at position T_1 sink, and less dense packets of fluid at position T_2 rise. For the stable case in Figure 2.3 fluid circulations do not occur when $T_1 > T_2$. This is because the fluid density at position T_2 is greater than the density at T_1. The net density difference occurs in the direction of the gravitational body forces and no bulk motion of the fluid occurs. In this configuration heat transfer occurs primarily due to conduction in the liquid.

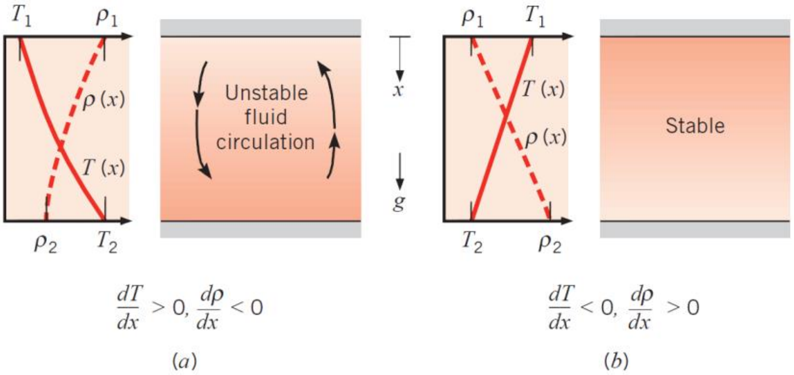

Figure 2.3: (a) Convection regime involving unstable fluid circulations, where the density variation acts against gravitational forces; (b) a stable regime involving no fluid circulations. Image from Bergman et al. (2011).

Engineers working in the field of thermal phase change have debated the definition of boiling for many years. In their early work Rohsenow and co-authors (Rohsenow and Hartnett, 1973; Rohsenow et al., 1985) originally defined boiling as "the process of evaporation associated with vapour bubbles in a liquid”. However liquid to vapour transition during thermal phase change is not confined to bubbles in a liquid. For example, vapour may be generated at the free surface of a liquid. To accommodate all types of boiling the most commonly accepted definition is that of Collier and Thome (1994) who state “boiling is defined as being the process of addition of heat to a liquid in such a way that generation of vapour occurs”. This definition is also accepted by the wider heat transfer community including the updated works of Rohsenow et al. (1998).

There is no evidence to suggest that the definition of condensation has followed the same existential crisis as boiling. It is simply accepted as the process where a vapour is converted to its liquid state (Bejan and Kraus, 2003). Research into condensation achieved considerable attention after the German mechanical engineer, Wilhelm Nusselt laid the foundation and pioneered his analytical solution for the steady state condensation of vapours on vertical flat plates (Nusselt, 1916).

Multiphase flows involve interactions between more than one material, for example fluid-fluid and fluid-solid interactions. Boiling and condensation fall under the category of multiphase flows. It is very difficult for engineers to predict the behaviour of multiphase flows. The difficulty arises from trying to predict the interactions between the different materials. These interactions are often transient in nature. Predicting those interactions are extremely difficult in simple domains such as vertical or horizontal pipes and ducts (see CHAPTER 6 for a discussion on in tube condensation and multiphase flows). Unfortunately, applications in reality are rarely this simple, and often involve complex geometries. Some engineering examples of where multiphase flows are used in complex geometries are thermosiphon reboilers, stirred tank reactors and internal combustion engines. Just like phase change, multiphase flows are ubiquitous.

There are three established methods to predict the behaviour of multiphase flows, and all methods complement each other. These are engineering calculations, experimental investigations and numerical investigations. We can use engineering calculations to derive relations from first principles. For example in the book by Tritton (1988, chap.9) a comparison of the analytical solution for the drag coefficient of a falling sphere in a viscous fluid in the Stokes regime is compared to experimental observations. There is good agreement between the analytical solution and experimental observations. Beyond the Stokes regime, analytical solutions to the viscous flow equations do not exist, due to the complex nature of the problem. In their book, Clift et al. (1978, chap.5) provided a comprehensive review of different empirical and semi empirical drag formulations. The formulations are determined from detailed experimental analysis, where the flow equations do not otherwise have a simple analytical solution for the drag coefficient as found in the Stokes regime. One of the most widely used correlations for the drag coefficient (which is also included in the review by Clift et al.,) is that of Schiller and Naumann (1935). Numerical investigations can take the experimental analysis further. For example instead of analysing a single spherical particle falling in a fluid, investigators can investigate a population of falling particles to reveal complex solutions otherwise difficult to observe under experiment such as particle – particle interactions. On their own, engineering calculations, experimental investigations and numerical investigations are rarely sufficient to unravel the mysteries of multiphase flows. When combined they provide a powerful tool for engineers to use.

2.8 Boiling

The Sellafield evaporators boil highly active liquors (HAL) to achieve the required evaporation factors. Boiling inside pressure vessels has received considerable attention over many years. Due to its importance, and coupled with the fascination of the complex phenomena involved, vast literature is available on the subject (Rohsenow et al., 1998). Most of the available literature on boiling refers to atmospheric pressures and above. There are fewer equivalent studies for boiling at sub-atmospheric pressures. However the fundamental mechanisms which drive boiling are the same under all pressures.

Boiling heat transfer is more complex than single phase convection. All of the variables associated with convection including those associated with the phase change are also relevant

(Kreith et al., 2010). Boiling can be classified as pool boiling or forced convective boiling. In pool boiling liquid convection and bubble detachment from a surface is self-induced without external influence such as a fan. In forced convective boiling, pool boiling mechanisms still exist with the added contribution from external means. Heat transfer coefficients from forced convective boiling are generally higher than in pool boiling.

2.9 The Boiling Curve

Nukiyama (1966) conducted a well-known boiling experiment which involved heating a nichrome wire immersed in water at atmospheric pressure. As power to the nichrome wire was increased, bubbles began to form at the wire-water interface which was attributed to boiling. The result of the investigation is the Nukiyama boiling curve for saturated water at atmospheric pressure, as shown in Figure 2.4 (Bergman et al., 2011).

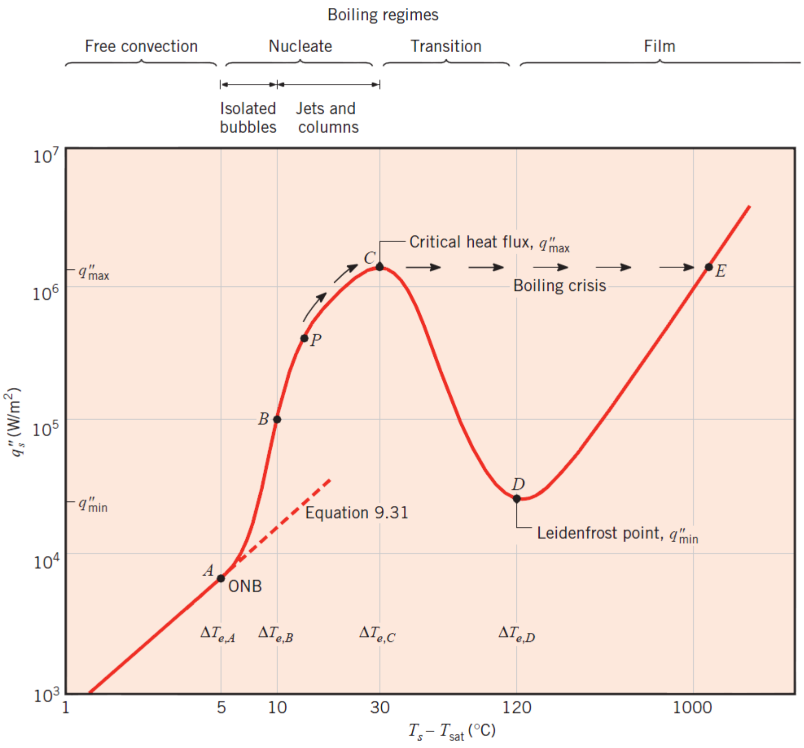

Figure 2.4: Nukiyama's boiling curve for water at atmospheric pressure. Image from Bergman et al. (2011).

In Figure 2.4 region A, free convection occurs until the onset of nucleate boiling is achieved at point B. In region AB, isolated bubbles form at nucleation sites and separate from the surface. Point A is identified as the beginning of nucleate boiling. In region BP the contribution from surface heat flux begins to reduce, and in region PC the contribution from surface heat flux reduces until the critical heat flux is reached at point C. At this point considerable vapour is being formed, which makes it difficult for the liquid to continuously wet the surface. At point CD the curve enters the transition zone where the formation of vapour bubbles is now so rapid that a vapour film begins to form on the surface. Finally at point DE film boiling dominates where the surface is completely covered by a vapour blanket. In this instance heat transfer from the surface to the liquid occurs by a combination of conduction and radiation through the vapour.

2.9.1 Onset of Boiling

At heated walls, the nucleation of vapour occurs with some degree of superheat above the saturation temperature. This is called the onset temperature of nucleate boiling. This is represented by point A in Figure 2.4. Table 2.3 summarises some of the most well-known correlations to predict the onset temperature of nucleate boiling.

Expression	Notes	Source	Equation
$\Delta T_{sat} = \left(\frac{8\sigma T_{sat} v_g \dot{q}}{\Delta H_{lg} \lambda_l}\right)^{1/2}$	Pool boiling correlation based on equating the temperature gradients in the thermal boundary layer.	Davis & Anderson (1966)	(2.3)
$\Delta T_{sat} = \left(\frac{8\sigma T_{sat} v_g \dot{q}}{\Delta H_{lg} \lambda_l}\right)^{1/2} \mathrm{Pr}_l$	Study of the boundary layer distortion due to the presence of the bubble.	Frost and Dzakowic, (1967)	(2.4)
$\Delta T_{sat} = \frac{2\sigma T_{sat} v_g}{r_{max} \Delta H_{lg}} + \frac{\dot{q} r_{max}}{\lambda_l}$	Applicable for well wetting fluids such as refrigerants.	Spindler, (1994)	(2.5)

Table 2.3: Well-known correlations to predict the onset of nucleate boiling in pool boiling situations.

The Davis & Anderson (1966) correlation given by Eq. 2.3 is based on fitting temperature profiles. Figure 2.5 is an image showing the nucleation of three bubbles of different radii. Line XY is the critical temperature a bubble must achieve to allow it to grow. This activity occurs within the laminar sub-layer where heat transfer from the wall to the fluid is due to molecular conduction. Thus if the wall is at temperature T_{w1} then the temperature profile never exceeds T_{crit}. If the wall is at temperature T_{w2} the temperature profile does exceed critical temperature profile at bubble radii at A and C. Any bubbles within this size range at temperature T_{w2} will be able to grow. If the wall temperature is at $T_{w,crit}$ then the temperature profile just touches the critical temperature line XY tangentially which corresponds to bubble B. Davis & Anderson (1966) came to Eq. 2.3 by equating the slopes of the temperature profile and critical temperature line XY.

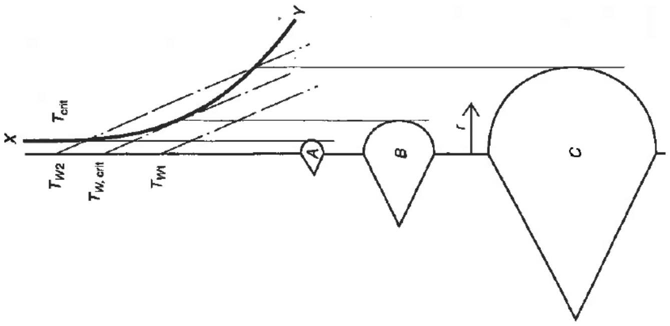

Figure 2.5: Bubble nucleation from a heated wall (Rohsenow et al., 1998).

The fundamental assumption by Davis & Anderson (1966) is the linear temperature profile due to pure conduction through the laminar sub-layer in the boundary layer. However in the presence of bubbles this layer is distorted and the linear temperature profile is no longer valid.

Rohsenow et al. (1998) report that despite Eq. 2.3 giving “reasonably good results in many cases” some deviations may occur. Namely due to the absence of accounting for the presence of bubbles and its effect on the required temperature difference, and the critical radius required to initiate bubble nucleation may be larger than the maximum radius allowed for bubble nucleation.

A further observation which may significantly lead to errors is that the expression in Eq. 2.3 does not account for surface properties such as nucleation site density, and it does not account for bubble departure diameter and bubble departure frequency. It may be argued that these factors may not be required at the ONB, since the ONB is the precise moment just before boiling takes place, i.e. single phase convection is still the dominating mechanism for heat transfer. However those factors will be important when estimating boiling heat transfer rates using empirical correlations or modelling boiling using CFD.

2.10 Wall Boiling

A critical radius exists for a vapour bubble that is in equilibrium with the surrounding liquid as shown in Eq. 2.6. If the bubble radius is less than r^* then the bubble will condense back into its liquid state. If the bubble radius is more than r^* then the bubble has the potential to grow.

$$r^* = \frac{2\sigma T_{sat} v_g}{\Delta H_{lg} \Delta T_{sat}} \tag{2.6}$$

The derivation of the critical radius can be found in a number of well-known published works such as Hewitt et al. (1994) or Rohsenow et al. (1998).

Bubble nucleation occurs in one of two ways, homogeneous or heterogeneous nucleation. Under homogeneous, nucleation occurs in the bulk liquid due to statistical molecular fluctuations in the liquid phase, causing microscopic nucleation sites in the liquid itself (Rohsenow et al., 1998). Walls in contact with the liquid, and the properties of the walls such as conductivity and roughness have little to no effect on homogeneous boiling. The temperatures required to initiate homogeneous nucleation are extremely high. Hewitt et al., (1994) reports that for water at atmospheric pressure, even though the saturation temperature is around 100°C, the homogeneous nucleation temperature would be 320°C, that is, 220°C of superheat is required to change phase from liquid to vapour from within the liquid.

Homogeneous nucleation occurs under very special circumstances where large superheats are required for phase change. Under these circumstances special conditions are usually met, such as using ultra smooth surfaces to prevent heterogeneous nucleation, and/or carefully removing dissolved gases which can aid heterogeneous nucleation (Rohsenow et al., 1998). Given that the conditions required for homogeneous nucleation are difficult to achieve under controlled laboratory conditions, there is no evidence to suggest homogeneous nucleation is practical under large industrial conditions. However curiosity on the subject has driven investigators to study the phenomenon. Rohsenow et al., (1998) provides a brief introduction to homogeneous nucleation, and also recommends literature for further reading into the subject.

Heterogeneous nucleation occurs far more commonly than homogeneous nucleation. Heterogeneous nucleation occurs at the interface between a solid surface and liquid. The superheat required to achieve boiling at the surface are orders of magnitude less than homogeneous. The surface properties in contact with the liquid play a more crucial role in heterogeneous boiling. Under heterogeneous conditions, bubbles are nucleated from microscopic cavities on the heat transfer surface in contact with the liquid. Trapped gasses grow from these nucleation sites under superheated conditions. Figure 2.6 is an illustration of nucleation cavities of various sizes.

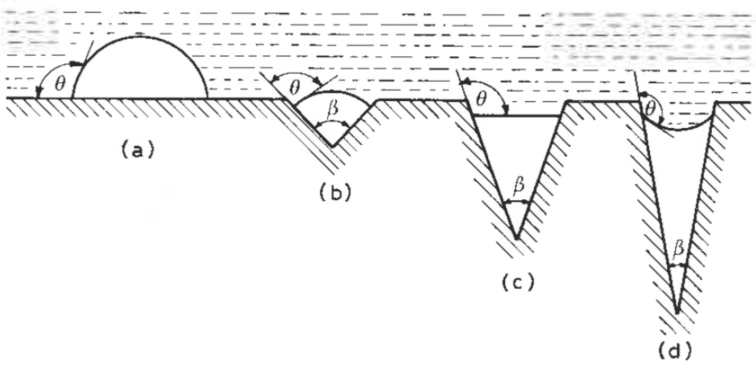

Figure 2.6: Cavities at the solid liquid interface (Collier and Thome, 1994).

The degree of superheat is a function of the contact angle contact angle θ as shown in Figure 2.6 (Collier and Thome, 1994; Rohsenow et al., 1998). In Figure 2.6 (a), there is an absence of a nucleation site, and the bubble formed on the planar surface is formed via homogeneous nucleation and its associated large superheats as previously described. In Figure 2.6 (b), (c) and (d) the nucleation sites are active sources of vapour generation. Small superheats, in the order of 10 – 15°C is required for bubble growth.

Figure 2.7 shows bubble growth from an idealised cavity. As the bubble grows from the cavity, there is a minimum critical value which the bubble radius takes, which corresponds to the maximum superheat required to support bubble growth. Very small cavities have very small minimum critical values of bubble radius, which means high superheats are required to initiate nucleate boiling. In fact Rohsenow et al. (1998) suggests with increasing heat flux, and consequently increasing superheats, smaller cavities become more active.

From what has been established so far, there is a clear distinction that nucleation size, nucleation site density, and the minimum critical radius for growth is a function of the surface heat flux, and consequently the degree of superheat. Other factors also arise when considering bubble departure from a heated surface. These are the bubble departure diameter from a nucleation site, and the bubble departure frequency.

The bubble departure diameter is the theoretical size the diameter of the vapour bubble must have to detach from a heated surface. This should not be confused with the critical minimum radius of growth described earlier. Hence bubble growth from a surface does not guarantee bubble departure from that surface as vapour bubbles can collapse back into the bulk liquid if the conditions allow.

Vapour bubbles released from a heated surface follow a cyclic profile, which according to Collier & Thome (1994) is inversely proportional to the sum of the bubble growth time and the bubble waiting time. This is the bubble departure frequency.

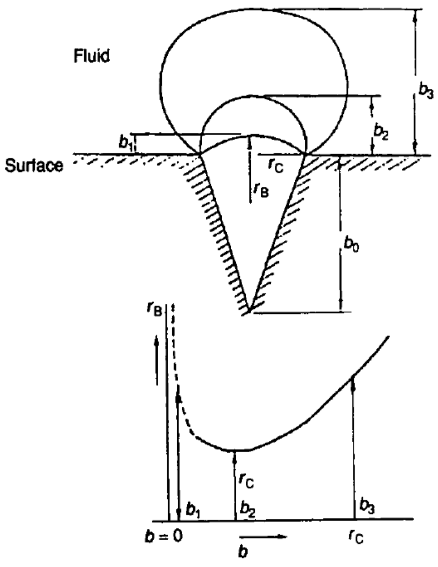

Figure 2.7: Bubble growth from an idealised cavity (Hewitt et al., 1994).

2.11 Wall Boiling Correlations

There are many correlations for the nucleate boiling heat transfer coefficient. The value they provide varies considerably (Hewitt et al., 1994) due to their formulation. For example some correlations do not take the boiling surface properties into consideration (such as the Forster and Zuber (1955) correlation) and others do (such as the Cooper (1984) correlation). Some of the most widely used and documented correlations are as follows (Hewitt et al., 1994):

- Forster and Zuber (1955)
- Mostinski (1963)
- Bier et al., (1982)
- Cooper (1984)
- Rohsenow (1951)
- Gorenflo and Kenning (2010)

The Forster and Zuber (1955) boiling model is one of the earliest correlations which was developed to predict the nucleate boiling heat transfer coefficient. It takes the form as shown in Eq. 2.7.

$$h = \frac{0.00122 \Delta T_{sat}^{0.24} \Delta P_{sat}^{0.75} c_{p,l}^{0.45} \rho_l^{0.45} \lambda_l^{0.75}}{\sigma^{0.5} \Delta H_{lg}^{0.24} \rho_g^{0.24}} \tag{2.7}$$

Hewitt et al., (1994) recommends using the Clausius-Clapeyron relation to evaluate the pressure drop in the Forster and Zuber boiling model as shown in Eq. 2.8.

$$\Delta P_{sat} = \exp\left[\frac{\Delta H_{lg}}{\bar{R}}\left(\frac{1}{T} - \frac{1}{T_{sat}}\right)\right] \tag{2.8}$$

Surface effects are not taken into consideration in the Forster and Zuber correlation, which puts the models reliability into question.

The Mostinskii (1963) correlation in Eq. 2.9 differs substantially from the Forster and Zuber correlation. It includes much fewer terms, and the boiling coefficient is a function of the heat flux. However in similar fashion to the Forster and Zuber model, no terms are taken into consideration to include surface effects.

$$h = 0.00417 P_{crit}^{0.69} \dot{q}^{0.7} F_P \tag{2.9}$$

The pressure correction factor for the Mostinskii correlation is given as

$$F_P = 1.8 P_R^{0.17} + 4 P_R^{1.2} + 10 P_R^{10} \tag{2.10}$$

The pressure correction factor in itself includes a reduced pressure term given as

$$P_R = \frac{P_{sat}}{P_{crit}} \tag{2.11}$$

Bier et al. (1982) uses an alternative correlation for the pressure correction factor in Eq. 2.10. The alternative pressure correction factor by Bier et al. is recommended for design purposes as shown in Eq. 2.12 and the boiling model in Eq. 2.9 remains unchanged.

$$F_P = 2.1 P_R^{0.27} + [9 + (1 - P_R^2)^{-1}] P_R^2 \tag{2.12}$$

The Cooper (1984) correlation in equation Eq. 2.13 is analogous to the Mostinskii and Bier et al. correlations in that a heat flux term is included in the evaluation of the heat transfer coefficient. However it deviates from the Forster and Zuber, Mostinskii and Bier et al. correlations as it contains a term to account for the surface properties, in this case known as the roughness parameter of the boiling surface. If the roughness parameter is not known it is recommended to assign it a value of unity.

$$h = 55 \dot{q}^{0.67} P_R^{0.12 - 0.2 \log R_P} (-\log P_R)^{-0.55} M^{-0.5} \tag{2.13}$$

The pressure correction factor in the Cooper (1984) correlation is the same as that given in Eq. 2.10.

In a similar fashion to the Cooper correlation, the Rohsenow (1951) correlation includes a term to account for the surface properties, denoted as a liquid-surface constant. However the Rohsenow correlation is slightly more involved and does not directly involve a term for the heat transfer coefficient as shown in Eq. 2.14. The heat flux must be solved for which can then output the heat transfer coefficient since $\dot{q} = h(T_s - T_{sat})$.

$$\frac{C_{p,l}(T_s - T_{sat})}{\Delta H_{lg}} = C_{SF}\left\{\frac{\dot{q}}{\mu_l \Delta H_{lg}}\sqrt{\frac{\sigma}{g(\rho_l - \rho_l)}}\right\}^{0.33}\left[\frac{C_{p,l}\mu_l}{\lambda_l}\right]^n \qquad (2.14)$$

The exponent *n* has a value of unity for water, and 1.7 for other fluids (Hewitt et al., 1994). The value of the surface finish C_{SF} is dimensionless, and values can be obtained from Collier and Thome (1996). For convenience some of the most common liquid surface combinations are presented in Table 2.4.

Liquid surface combination	**C_{SF}**
Water on polished copper	0.0128
Water on lapped copper	0.0147
Water on scored copper	0.0068
Water on ground and polished stainless steel	0.0080
Water on Teflon-pitted stainless steel	0.0058
Water on chemically etched stainless steel	0.0133
Water on mechanically polished stainless steel	0.0132

Table 2.4: Commonly occurring liquid-surface combinations for use in the Rohsenow correlation (Collier and Thome, 1996).

Hewitt et al. (1994) and Serth (2007) both demonstrated the accuracy and agreement of the five boiling correlations mentioned. They provided solutions for a sample boiling heat transfer problem which was solved five times, each using one of the five heat transfer coefficients. A wide and significant variation was found between each solution. The solutions from Hewitt et al., (1994) are displayed in Table 2.5. The five solutions differ very significantly, with a difference in the orders of magnitude. The wide variation in the solution, and the lack of agreement can be explained due to how boiling heat transfer is very sensitive to the precise conditions at the boiling surface (Serth, 2007).

Boiling correlation	**Heat transfer coefficient (W/m^2K)**
Forster and Zuber	5,512
Mostinski	2,528
Bier et al.	5,134
Cooper	23,212
Rohsenow	1,182

Table 2.5: Solutions to the sample boiling problem presented in Hewitt et al., (1994).

It is not practical to include detailed surface characteristics in a boiling correlation, as the boundary conditions will likely be based on ideal surface conditions. In practice ideal surface conditions are never met due to fouling of the surfaces (which include corrosion and erosion) over time. Additionally due to the often complicated design of process heat transfer equipment it may be difficult or impossible to observe directly the conditions at the heat transfer surface. This has implications on boiling models which require the user to input surface properties. It means that surface conditions which cannot be directly obtained from process plant would need to be estimated, and then inserted into a boiling model. This in itself will introduce a significant error if surface properties are factored when estimating boiling heat transfer coefficients. For this reason it is ideal to design boiling heat transfer models which are largely independent of surface properties.

The Gorenflo and Kenning (2010) nucleate boiling correlation is a recent addition to the literature when compared to the earlier Forster and Zuber (1955) nucleate boiling heat transfer coefficient. The Gorenflo and Kenning correlation differs substantially from all other nucleate boiling correlations previously discussed. It is presented in a dimensionless form of a reduced heat transfer coefficient as shown in Eq. 2.15.

$$\frac{h}{h_0} = F_q F_P F_W \tag{2.15}$$

As Eq. 2.15 shows, the reduced heat transfer coefficient is a function of a reduced heat flux term (F_q), a pressure correction factor (F_{p^*}) and a term to describe the influences of the boiling surface (F_W). For boiling water, the reduced heat flux term is evaluated using

$$F_q = \left(\frac{q}{q_0}\right)^n \tag{2.16}$$

The exponent n is evaluated using

$$n = 0.9 - 0.3P_R \tag{2.17}$$

where P_R denotes the reduced pressure which can be determined used Eq. 2.11. The pressure correction factor F_P is evaluated using

$$F_P = 1.73P_R^{0.27} + 6.1P_R^2 + \frac{0.68P_R^2}{1-P_R^2} \tag{2.18}$$

To determine the influences of the boiling surface the following correlation should be used.

$$F_W = \left(\frac{R_a}{R_{a0}}\right)^{2/5} \tag{2.19}$$

The values for the reference heat transfer coefficient and reference heat flux should be read from graphs of experimental data as shown in Figure 2.8 The reference roughness (R_{a0}) should be taken as 0.4 µm. In Figure 2.8 the reference heat transfer coefficient is denoted by α_0 and deviates from the nomenclature used in this work.

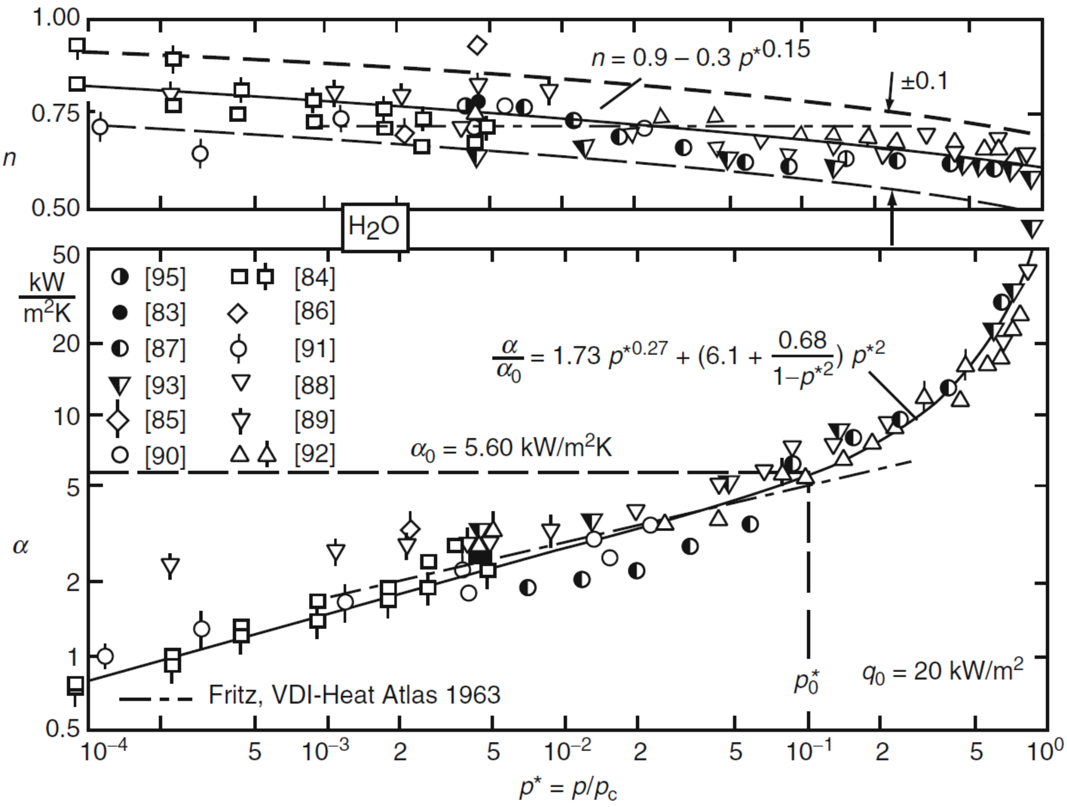

Figure 2.8: Heat transfer coefficient and exponent n as a function of reduced pressure for boiling water (Gorenflo and Kenning, 2010).

2.12 Boiling at Sub-Atmospheric Pressures

Boiling can be classified as to whether it is sub-cooled boiling or saturated boiling (Bergman et al., 2011). In sub-cooled boiling the vast majority of the liquid is below the saturation temperature. Any vapour formation at heated walls in sub-cooled boiling condenses back into the bulk pool. In saturated boiling the local temperature is usually greater than the local saturation temperature which allows vapour bubbles to grow and detach from heated surfaces.

Boiling at sub-atmospheric pressures occurs in many engineering processes such as thermosiphon reboilers, refrigeration systems, and heat exchangers (Tu, 1999). Despite this there are few equivalent studies of boiling fluids at these pressures compared to boiling at atmospheric pressures and above (Tu and Yeoh, 2002). There is a demand to better understand boiling at low pressures, especially sub-atmospheric pressures for industrial use, such as the evaporators used at the Sellafield site (D. a. McNeil et al., 2015).

2.13 Thermosiphon Systems

It has been speculated in previous works that evaporators operating at sub-atmospheric pressure may behave similar to a thermosiphon reboiler. A thermosiphon is a passive pumpless heat exchange system, which is used to circulate a fluid for use in a number of industrial applications. A thermosiphon can be considered a pumpless system since fluid circulation occurs within the system due to the density difference corresponding to the difference in temperature within the process fluid. There are different types of thermosiphon systems which may or may not include boiling of the process fluid.

Thermosiphons are used in a many engineering applications such as gas turbine blade cooling (Ogale, 1968). Ogale studied the thermal performance of gas turbine blades when they are filled with liquid metals. Heat from the hot gasses pass over the tips of the rotor blades and transferred to the blade root. The blade root is cooled by use of a secondary coolant (distilled water). The relative temperature difference between the tips of the blades and roots of the blades cause capillary action in the liquid metals, acting as an efficient and pumpless heat transmission mechanism.

Vertical thermosiphon reboilers are used in separation processes, and are used as a reliable means of heat input into distillation, stripping and absorption towers (Alane and Heggs, 2011). Alane and Heggs also report they are also applied in the nuclear and desalination industries for concentration purposes.

2.14 Other Relevant Works

Milnes et al. (2012) successfully conducted a CFD investigation of the HyperVapotron fusion device, with validation against experimental data. A majority of the computational models chosen were within the RANS framework, where limited computationally intense large eddy simulations were conducted to improve the accuracy of the RANS approach. Milnes et al. used the RPI wall boiling model developed by Podowski et al. (1997) to model nucleate boiling at the wall. When compared to experimental data, it was found that the RPI model was able to accurately predict the onset of nucleate boiling and the increase of average void fraction. However the RPI model did under predict the peak void fraction by more than 60% suggesting improvements in this area were essential. Improvements were made by using Ünal’s (1976) correlations for bubble departure diameter, and the inter phase heat transfer was fixed by fixing the inter phase Nusselt number to 2 (this value was determined when comparing experimental data with numerical results). Using the modified boiling model the results from the simulations were promising. Compared to the standard boiling model, the modified boiling model reduced the error from 24% to 13% at a wall heat flux of around 10 MW/m^2. The modified RPI boiling model was also tested against three validation cases where the modified model was in some cases able to better predict the characteristics of those validation cases. The work by Milnes et al. gives an indication as to the sensitivity on boundary conditions of boiling and near wall turbulent flow, which the Sellafield evaporators share similar characteristics.

Yeoh et al. (2008) studied low pressure subcooled boiling flows with the consideration of bubble departure frequency from a heated surface. The domain that was used resembled a vertical annular channel where forced convective subcooled boiling flow was modelled.

Forced convective subcooled boiling flow through an upward channel will cause vapour bubbles to “slide” along the heated wall before they are detached. If the original hypothesis is true with regards to the existence of a subcooled nucleate boiling region in the Sellafield evaporators, then bubble slippage before departure from the wall may be significant. The study by Yeoh et al. involved advancing existing mechanistic models to include the sliding bubble phenomena and its effects, and incorporating it in a modified MuSiG model to simultaneously calculate bubble coalescence, breakage and condensation back into liquid. It is known as the improved wall heat partition model.

It is argued by Yeoh et al. that Cole’s (1960) empirical correlation for bubble release frequency as shown in Eq. 2.20 may not be valid for low pressure sub-cooled boiling flows and hence a mechanistic approach to bubble release frequency should be adopted.

$$f = \sqrt{\frac{4g(\rho_l - \rho_g)}{3D_b\rho_1}} \tag{2.20}$$

The improved wall heat partition model incorporated into the MuSiG algorithm does produce promising results compared to the experimental data presented by Zeitoun and Shouskri (1997). The Sauter mean bubble diameter profiles were in good agreement with experimental data. The void fractions at the heated sections were also in agreement, however the CFD simulations contradicted experimental data for the void fractions near the channel exit for some boundary conditions. The mechanistic model also adequately predicted the bubble departure and lift off diameters. There was acceptable agreement between the CFD simulations and experimental data for the growth and waiting times of bubble frequency at local superheated and sub-cooled wall temperatures.

Talebi et al. (2009) studied sub-cooled boiling flow in a vertical channel at low pressures. It has been suggested by Talebi et al. that empirical models developed for high-pressure boiling applications are not valid at low pressures (1-2 bar). There may be further implications when considering pressures approaching close to vacuum conditions (0.05 – 0.9

bar). The investigation by Talebi et al. involved applying a two-fluid mathematical model to numerically solve the governing equations for sub-cooled boiling flow in a vertical channel by use of the commercial CFD package, Ansys CFX. The investigation was simplified to a two-dimensional rectangular channel where the SIMPLE scheme was used to solve the discretised equations.

Talebi et al. simplified the investigation further by treating the liquid as a continuous phase, and the vapour bubbles as a dispersed phase. As a benchmark to validate the CFD investigation Talebi et al. used the boundary conditions and subsequent available experimental data published by Zeitoun and Shoukri (1997). There was good agreement between the numerical CFD results and the experimental data by Zeitoun and Shoukri. At high flow rates bubble coalescence played a significant role indicating the possible requirement of a turbulence model to capture the flow physics beyond laminar bubbly flows. Although there was good agreement between CFD and experiment it is difficult to ascertain how turbulence and bubble coalescence will affect the predictability of heat transfer.

Convection and circulation of the process liquor will occur within the Sellafield evaporators. The circulation of fluid within these two can be considered as free convection circulation inside a cavity, which is known as Rayleigh–Bénard convection where the heated fluid may develop a regular pattern of convection cells inside differentially heated cavities as shown in Figure 2.9.

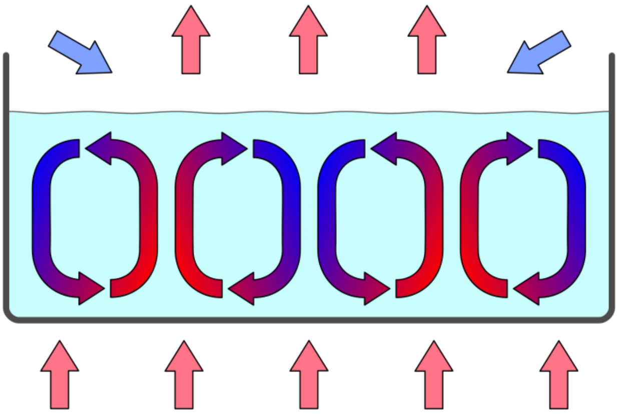

Figure 2.9: Rayleigh–Bénard convection cells in a cavity heated from the bottom (permission is granted to copy, distribute and/or modify under the terms of the GNU Free Documentation License).

Rossby (1969) conducted an experimental study of a thin uniformly heated rotating layer of fluid. It was reported by Rossby that the stability of the fluid depended greatly on the non-dimensional Rayleigh, Taylor and Prandtl numbers. Similarly Bergé and Dubois (1984) presented a physicist’s approach to Rayleigh-Bénard convection. They report that a critical Rayleigh number equal to 1707 exists which is a universal value independent of the fluid. At this critical number bulk fluid motion occurs due to convection, which presides over the stationary pure conduction heat transfer in the fluid. This value is also valid for large aspect ratio geometries where the horizontal length is much greater than the vertical length. It is reported that when the horizontal length of the domain is larger than the vertical depth a stationary roll pattern is generally observed where the axes of the rolls are usually perpendicular to the lateral walls, and the rolls are usually equidistant and parallel. In the work presented by Bergé and Dubois the aspect ratio is an important dimensionless quantity for Rayleigh-Bénard convection. For rectangular shaped domains it is the ratio of the horizontal to vertical dimensions. For a cylindrical domain it is the ratio of the radial to the vertical dimensions, which may be representative of the geometry of the Sellafield evaporators.

Conjugate heat transfer may be significant if large temperature differences occur at the boundaries. Heggs et al. (1990) investigated the effect of wall thermal conductivity and thickness of a vertical cylindrical duct, and how it affected flow and temperature distributions of fluid travelling vertically upwards against gravity. In the investigation the Prandtl, Reynolds and Grashof numbers were kept constant at 7, 50 and 10000 respectively. The Grashof number was deliberately chosen to be large to encourage flow reversals in most situations studied. The finite difference method was employed to solve the governing equations. The ratio of pipe wall to fluid thermal conductivities had values of 50, 5 and 0.5. Considering typical values of the thermal conductivity of water which was the test fluid that was used, the ratios covered tubes of wall materials with thermal conductivities in the range of 0.275 – 35.0 W/mK which covered pipe materials such as stainless steel and many plastics. The ratio of the radii of the outside to inside walls had values of 1.1, 1.25 and 1.4. Hence the variables of the investigations were pipe wall thermal conductivities and the pipe wall thicknesses.

Heggs et al. discovered that large values of the ratio of the wall to fluid thermal conductivity had significant upstream effects on the flow and temperature distributions inside the cylindrical pipe. Small values of the ratio of the wall to fluid thermal conductivity had significant downstream effects on the flow and temperature distributions. It was concluded that it may be invalid to completely omit wall domain boundary conditions in combined convection where flow reversals are present. It was found the pipe wall thermal conductivities and the pipe wall thicknesses are an influencing factor on the flow and temperature distributions inside the cylindrical pipe, especially where the Reynolds number of flow is low. This is a significant factor to consider when modelling the Sellafield evaporators. If conjugate effects are important they may need to be included within the numerical models.

2.15 Summary

The selection of the papers reviewed have yielded important details regarding the heat transfer and multiphase flow conditions that are expected inside the Sellafield evaporators. The literature states that boiling at sub-atmospheric pressures may be difficult to model, and that further tweaks may be needed to enhance boiling and turbulence models specific to the application. In addition to this, modelling free convection using numerical techniques may present a challenge when considering if it is laminar or turbulent. Furthermore, convection (and implicitly boiling and condensation) may directly be effected within numerical simulations if wall conjugate heat transfer is not modelled.

Chapter 3

Statement on Numerical Accuracy and Procedure

3.1 Introduction

Numerical accuracy is paramount to the results presented in this thesis. Numerical error can occur due to a multitude of reasons. These are, but are not limited to, using a poor quality mesh, using the wrong models (or lack thereof), and obtaining poor or no convergence. The purpose of this chapter is to discuss how numerical accuracy was obtained in the CFD simulations. This comprised of meeting stringent quality controls for the mesh; performing mesh sensitivity studies; ensuring full residual convergence for all governing equations; ensuring global flux imbalances were no more than 1% of the total flow entering and leaving the domain; and applying appropriate monitor points to monitor key flow variables to ensure the solution being solved was physically realistic.

3.2 Mesh Considerations

Without a good quality mesh to resolve flow features in pertinent regions, numerical round off error and numerical diffusion may be introduced into the simulation which will influence the end results. To remove these errors, a user would typically undertake more than two simulations on increasing mesh densities in pertinent regions, in order to ascertain a mesh independent solution for a particular variable of interest. For example one may be interested in near wall velocity at some locations in the solution domain. This value of the near wall velocity may change with mesh density. In order to remove this uncertainty a mesh sensitivity study should be performed to isolate the best mesh for that variable. An example of how the mesh density may change the results is shown by Figure 3.1.

In this example mesh 3 would be chosen as the ideal mesh to proceed with for further simulations. This is because further mesh refinement does not yield a significant increase in accuracy for the near wall velocity, but will unnecessarily consume more computational resources and likely increase simulation compute times.

The formal grid convergence index (GCI) procedure developed by Celik et al. (2008) was used to perform the mesh sensitivity studies in this study. It is a method that is used to determine the uncertainty due to mesh discretisation in CFD simulations. It uses the Richardson extrapolation method, in addition to a custom method developed by Celik et al., to provide discretization error estimation. This is a rigorous procedure that has been used with success in many works which use CFD in a wide range of diverse applications. For example, Harrison et al. (2010) used the method in their works to report the discretization error and select an appropriate mesh for their CFD simulations, which predicted wakes in horizontal axis tidal turbines, and compared their results to experimental data. Aydin (2012) used the method in his work to arrive to a final mesh independent simulation, which modelled free surface flow in a triangular labyrinth side weir, which is a common problem within hydraulic engineering. Further diverse examples of the use of GCI as the mesh sensitivity procedure of choice can be found in the works by Westra et al. (2010), Promvonge et al. (2010) and Trivedi et al. (2013). The GCI method is also the preferred method of some peer reviewed journals to report the uncertainty due to discretization in CFD applications.

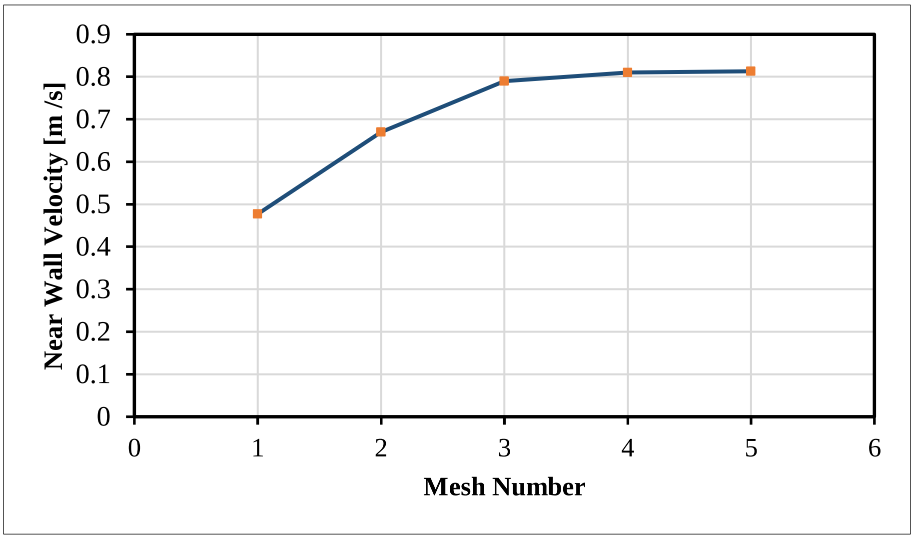

Figure 3.1: The effect of near wall velocity as a function of increasing mesh density.

3.2.1 Steps for the Mesh Sensitivity Study

For the CFD results reported in this thesis a mesh sensitivity study was performed using the GCI procedure. The mesh sensitivity studies were performed in simplified situations. It is well known that evaporation simulations require far smaller time steps to simulate accurately due to the small time scales involved in the calculations. They also require more computational resources since they are far more elaborate models which produce large computational matrices during the compute process. Performing repetitive evaporation simulations on more than two meshes is not prudent as it is very time consuming. Rather than perform a mesh sensitivity study on a difficult evaporation problem, a simpler yet related problem of free convection prior to free surface evaporation was chosen as the flow problem which was required to be independent of the mesh resolution. Free convection simulations require less elaborate numerical models, and do not require as small a time step for convergence as boiling simulations do. This reduces the requirements both from the constraint of time and computational resources.

The GCI procedure comprises generating at least three significantly different meshes for the desired problem, differing by their mesh density. Increased mesh density between the meshes was applied in regions of importance to the simulations, for example at heated walls and at free surface positions. Figure 3.2 is an example of increasing mesh density for four different meshes at the surfaces of the physical flow domain (part of the work presented in CHAPTER 5).

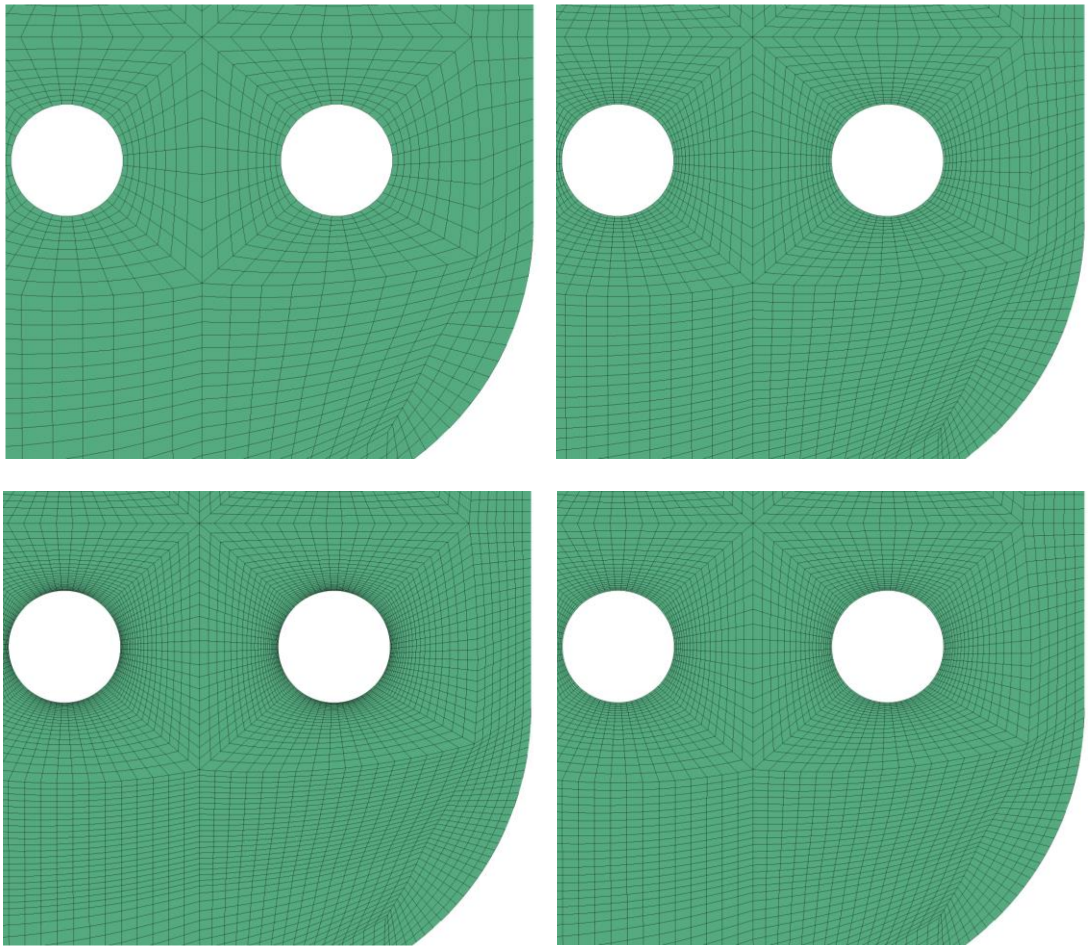

Figure 3.2: Starting from top left, clockwise: meshes 1 to 4 used in the GCI study to ascertain the uncertainty due to discretization and to enable the selection of a suitable mesh. The meshes form part of the work presented in CHAPTER 5.

When at least three significantly meshes were generated, mesh size of each mesh was represented mathematically as defined by Eq. 3.1.

$$h = \left[\frac{1}{N}\sum_{i=1}^{n}(\Delta V_i)\right]^{\frac{1}{3}} \tag{3.1}$$

Meshes were refined globally, but more so in positions where variables needed to be independent of the mesh resolution, such as wall temperatures. The refinement factor between the meshes (between mesh 1 and 2; mesh 2 and 3, and so on) is defined as shown in Eq. 3.2.

$$r = \frac{h_{coarse}}{h_{fine}} \tag{3.2}$$

From experience Celik et al. (2008) reported that the refinement factor between the meshes must be greater than 1.3. In this work, if it was found that it was not greater than 1.3, then meshes would be refined to meet this condition. Allowing for the identities in Eq. 3.1 and 3.2 being satisfied, identical simulations were performed on all meshes, for each physical flow domain, for each chapter where CFD results are presented.

In all of the works presented in this study the GCI sensitivity study was based on the results from the simulations of transient free convection. Convergence details of these simulations such as the residual target are discussed in the next section. Transient free convection was chosen as it is the condition prior to evaporative flows at the free surface. Steady state pure conduction heat transfer in the system (no momentum transfer), and steady state free convection was not chosen as the benchmark test cases for the mesh sensitivity study. This is because a steady state pure conduction solution is unphysical inside the liquid, and solution convergence for steady state free convection is not guaranteed.

$$h_1 < h_2 < h_3 < h_4 \tag{3.3}$$

$$r_{21} = \frac{h_2}{h_1} \quad r_{32} = \frac{h_3}{h_2} \quad r_{43} = \frac{h_4}{h_3} \tag{3.4}$$

Once identical simulations on the relevant meshes were complete, pertinent variables important to the investigation were outputted. These were the variables which were required to be independent of the mesh resolution. Examples included wall temperatures, interfacial area densities and velocity monitor points. The relative difference between the variables due to the change in mesh density is denoted as shown in Eq. 3.5.

$$\varepsilon_{21} = \phi_2 - \phi_1 \quad \varepsilon_{32} = \phi_3 - \phi_2 \quad \varepsilon_{43} = \phi_4 - \phi_3 \tag{3.5}$$

In the GCI method the apparent order between subsequent meshes (mesh 1, 2 and 3; mesh 2, 3 and 4, and so on) was determined using the expression in Eq. 3.6. The expression for the apparent order $p_{1,2,3}$ is provided. The expression for apparent order $p_{2,3,4}$ follows a similar naming convention, but is not shown here.

$$p_{1,2,3} = \frac{1}{\ln(r_{2,1})} \left| \ln \left| \frac{\varepsilon_{32}}{\varepsilon_{21}} \right| + q(p) \right| \tag{3.6}$$

The function $q(p)$ is defined by Eq. 3.7.

$$q(p) = \ln\left(\frac{r_{21}^p - s}{r_{21}^p - s} \right) \tag{3.7}$$

The function s is defined as

$$s = \mathrm{sgn}\left(\frac{\varepsilon_{32}}{\varepsilon_{21}} \right) \tag{3.8}$$

In order to solve for the apparent order in Eq. 3.6, an iterative approach was taken since the solution is a function of itself, as shown by Eq. 3.7, where r is raised to the power of the apparent order. This was solved for in the computing program MATLAB using the Newton Raphson iterative technique, converging to a tolerance of 1 x 10^{-6}.

Once the apparent order for the meshes were computed, extrapolated values of the variables were deduced. This was achieved by using the expression in Eq. 3.9.

$$\phi_{ext}^{21} = \frac{r_{21}^{p}\phi_1 - \phi_2}{r_{21}^{p} - 1} \tag{3.9}$$

In a similar fashion extrapolated values between mesh 2 and 3, and so on, were calculated, denoted by ϕ_{ext}^{32} et cetera. With this, error estimates of the variables were determined. The approximate relative error was determined by the expression in Eq. 3.10.

$$e_a^{21} = \left|\frac{\phi_1 - \phi_2}{\phi_1}\right| \tag{3.10}$$

A similar procedure was followed for e_a^{23} and if required, e_a^{34}. The extrapolated relative error was determined using the expression in Eq. 3.11.

$$e_{ext}^{21} = \left|\frac{\phi_{ext}^{12} - \phi_1}{\phi_{ext}^{12}}\right| \tag{3.11}$$

Again, e_{ext}^{32} and if required, e_{ext}^{43} were deduced using a similar convention. Finally the fine grid convergence index was determined using the expression in Eq. 3.12. In a similar fashion GCI_{fine}^{32} and if necessary GCI_{fine}^{43} were deduced.

$$\mathrm{GCI}_{fine}^{21} = \frac{1.25 e_a^{21}}{r_{21}^{p} - 1} \tag{3.12}$$

The approximate relative error in Eq. 3.10 provides a comparison in the variables between two meshes. The flaw in this method is that there is no indication to determine which value is the correct value. To alleviate this issue, the extrapolated relative error described by Eq. 3.10 benchmarks the calculated value of a variable for each mesh against the extrapolated variable. The extrapolated variable arises from the Richardson extrapolation. Although Richardson extrapolation has it shortcomings, the authors of the GCI mesh sensitivity method, Celik et al. (2008) mention that it is the most reliable method available to predict numerical uncertainty. The fine grid convergence index assesses the overall performance between the meshes for the variables of interest. Large values of GCI for each variable relate to large discretization errors due to the mesh. Small values of GCI relate to small errors. No guidelines are provided by Celik et al. (2008) as to the value which GCI should take. In this work it is taken close to 1%, and lower if possible. Celik et al. (2008) also mention GCI values can be seen as a numerical version of experimental error bars for particular variables of interest. The mesh which produced the lowest errors based on the GCI method was chosen as the mesh on which to perform further complex simulations.

3.3 Mesh Quality Controls

In the framework of CFD, physical flow domains are discretised into a mesh, and the conservation equations governing the physical problem are solved for in control volumes. Ansys CFX is a vertex centred finite volume CFD solver. This means that control volumes are created around cell vertices. Cell centred finite volume CFD solvers also exist, where mesh cells physically represent the control volume. Commercial examples of cell centred finite volume CFD codes are Ansys Fluent and CD Adapco Star CCM+. Figure 3.3 (Kroll et al., 2010 chap. 4) illustrates the differences between vertex centred and cell centred schemes. The computational node (represented by the white circle) is surrounded by the control volume (shaded area labelled K_m). The example illustration shows a tetrahedron mesh. If a hexahedral mesh was used a similar convention would follow. The minor difference would be the control volume shapes, where both vertex centred and cell centred would yield hexahedral control volumes.

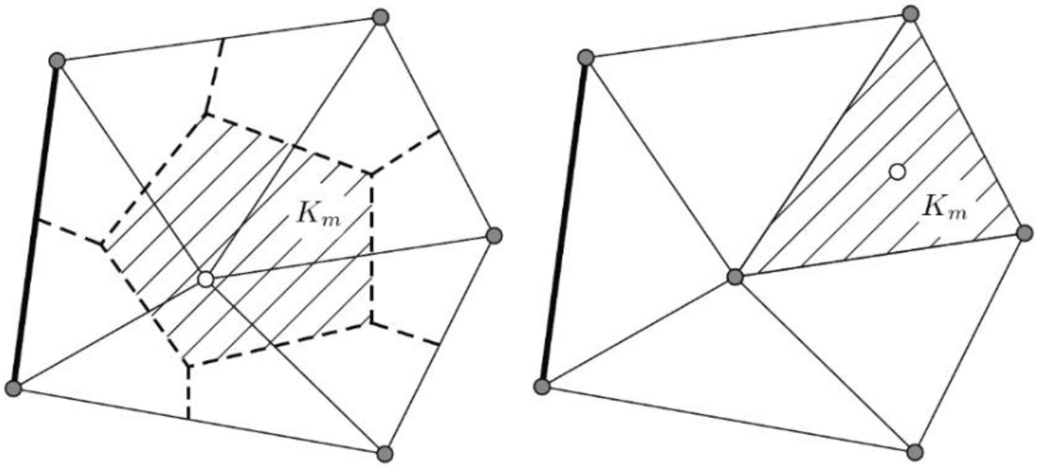

Figure 3.3: (Left) A vertex cantered CFD scheme; (right) a cell centred CFD scheme (right). Image adapted from Kroll et al., (2010 chap. 4).

Kroll et al. (2010) mention vertex centred schemes are popular. This is because they provide more fluxes per variable that is solved for, and offer half the memory footprint compared to cell centred schemes. Aside from the lower memory usage, the vertex centred scheme as found in Ansys CFX is desirable for the types of flows considered in this study. Buoyancy driven flows rarely follow an ordered pattern and usually contain adverse pressure gradients. These gradients give rise to velocity gradients which are not ordered. Having a vertex centred control volume with many control volume faces helps to capture those velocity gradients since more fluxes are captured. This means the interpolation of velocity between control volume vertices are less exaggerated.

Vertex centred and cell centred CFD codes can both read the same mesh. How those codes store information on those meshes is the underlying fundamental difference (vertex centred or cell centred schemes dictate how information such as pressure and velocity arrays are stored on control volume faces and vertices). Due to this difference, each code has a special set of mesh requirements. This means if a single mesh was created, it may satisfy the requirements for a good mesh in Ansys CFX (vertex centred), yet not satisfy the requirements for a good mesh for Ansys Fluent (cell centred), since both codes have mesh requirements tailored to their schemes (vertex centred or cell centred).

All of the meshes used in this thesis were stringently designed so that they satisfied the mesh requirements of the chosen CFD solver, Ansys CFX. The meshes were created in the highly customisable and documented meshing code, ICEM CFD, which is a versatile tool in creating high quality meshes for CFD applications. ICEM CFD has its own internal requirements for a good quality mesh which were also satisfied (the requirements by Ansys CFX and ICEM CFD do not contradict each other, so it was possible to satisfy the requirements of both algorithms). These mesh requirements were satisfied for all cell types in the mesh. These are hexahedrons, tetrahedrons, pyramids, and prisms and their 2D counterparts (quads and triangles), as shown in Figure 3.4 (Paul et al., 2004 chap. 5). More information on discretizing physical flow domains into a mesh for CFD with particular emphasis on industrial applications can be found by the works of Paul et al. (2004).

Ansys CFX has three principal mesh requirements. These are mesh orthogonality, mesh expansion and mesh aspect ratio and all three requirements were satisfied at all times. Satisfying these requirements is important as not doing so will increase discretisation error and encourage divergence, which cannot be afforded in difficult to converge numerical CFD simulations such as evaporation.

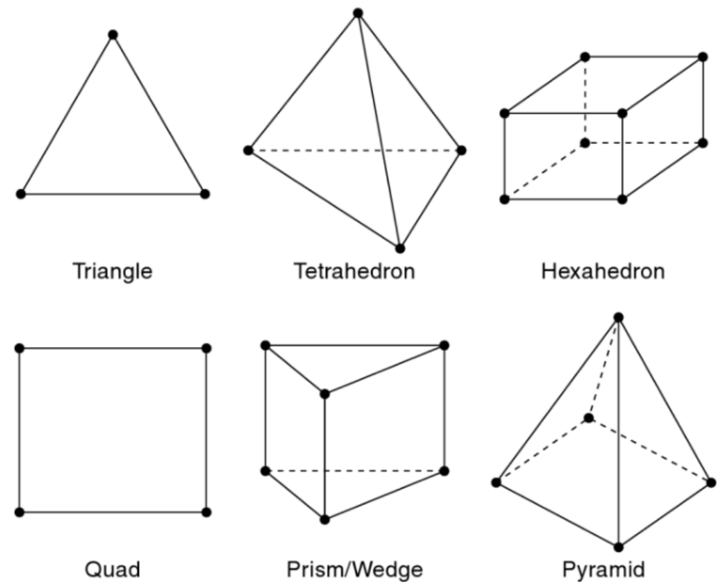

Figure 3.4: The different types of cells that can be used in the meshes (Paul et al., 2004 chap. 5).

3.3.1 Mesh Orthogonality

The mesh orthogonality is defined as the deviation from optimum angles in a cell. A perfectly orthogonal hexahedral or quad cell has 90° angles. Likewise a perfect equilateral pyramid, prism or triangle cell has angles of 60°. Figure 3.5 (Ansys Inc, 2010a) is an example of mesh orthogonality in two cells, where each cell has two vectors denoting cell direction.

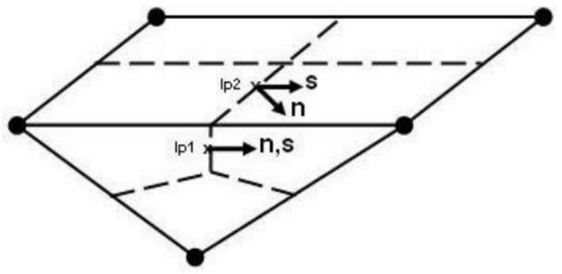

Figure 3.5: Mesh orthogonality in a triangle and quad cell (Ansys Inc, 2010a).

Meshes were checked so that the minimum and maximum permissible orthogonality face angles were no less than 10° and no more than 170°.

3.3.2 Mesh Expansion Ratio

Mesh expansion ratio is the rate of change of one cell relative to the next adjacent cell. It is measured by the ratio of the maximum to minimum distances inside the control volume. The mesh expansion for two cells is shown in Figure 3.6 (Ansys Inc, 2010a). The acceptable range for the mesh expansion ratio is no greater than 20, with lower expansion ratios offering greater accuracy in the results. For the meshes designed in this thesis, a maximum limit of 18 was set to limit the effect of numerical diffusion in pertinent areas of the physical flow domain.

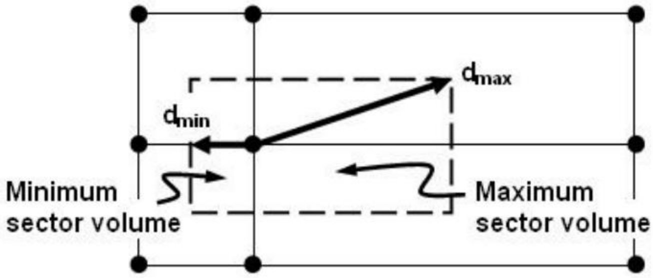

Figure 3.6: Mesh expansion ratio between two cells (Ansys Inc, 2010a).

3.3.3 Mesh Aspect Ratio

The mesh aspect ratio is the last mesh metric which Ansys CFX uses to benchmark meshes against. It is the ratio of maximum edge length to minimum edge length for a control volume. Figure 3.7 (Ansys Inc, 2010a) illustrates this between two cells in more detail.

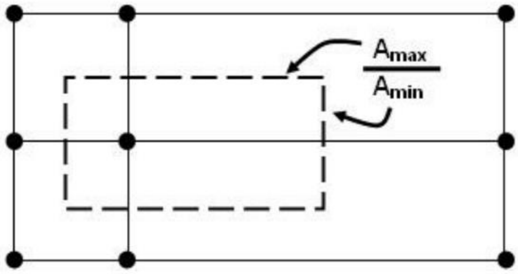

Figure 3.7: Mesh aspect ratio between two cells (Ansys Inc, 2010a).

All of the simulations performed in this study were done so in double precision. For double precision numerics, the mesh aspect ratio must not exceed 1000. For all meshes generated checks were made to ensure this was the case. For reference, if using a single precision solver, a mesh aspect ratio must be no more than 100.

3.4 Mesh Types

There are three types of mesh, structured, unstructured, and hybrid. Hybrid is a combination of structured and unstructured types. Structured and unstructured meshes differ in the way the cells are aligned in the physical flow domain. Structured meshes typically contain ordered hexahedral cells that are aligned with the direction of the flow. Unstructured meshes typically contain random cells of tetrahedron, prism and pyramid cells which are not aligned with the direction of flow. Please note, unstructured hexahedral meshes are possible.

In the early days of CFD, mesh data in structured meshes was written in logical arrays. The first row in the first column in the first matrix of the array contained information on the position of first node in the mesh (and so on for the subsequent mesh nodes). This had memory saving advantages, where structured CFD solvers could take advantage of this mesh file storage format (Mazumder, 2015). This convention has since been dropped, and mesh data is stored and passed to the CFD solver in other (unordered) formats which are more efficient for today's computer hardware standards. Hence nowadays most, if not all CFD solvers are unstructured solvers, in that they do not expect to read in structured mesh data. Despite this it is desirable to CFD engineers to design meshes to structured standards (cells aligned to flow direction). This is because they reduce numerical diffusion in the solution since the cells are aligned with the flow direction, and they contain fewer cells for the like-for-like unstructured counterpart.

Figure 3.8 is a comparison between structured (top) and unstructured (bottom) meshes for a simple pipe, with a radius of 2 cm and a length of 10 cm. For the purposes of the example, and to provide a fair comparison, the mesh controls for both meshes were kept the same, with a minimum cell size of 5.7 x 10^{-3} cm, and maximum cell size of 0.5 cm. The inflation at the walls had 10 layers with a total thickness of 0.5 cm, and each layer growing by a factor of 1.2. For the structured mesh the cell count was 13120, and in the unstructured mesh the cell count was 27947.

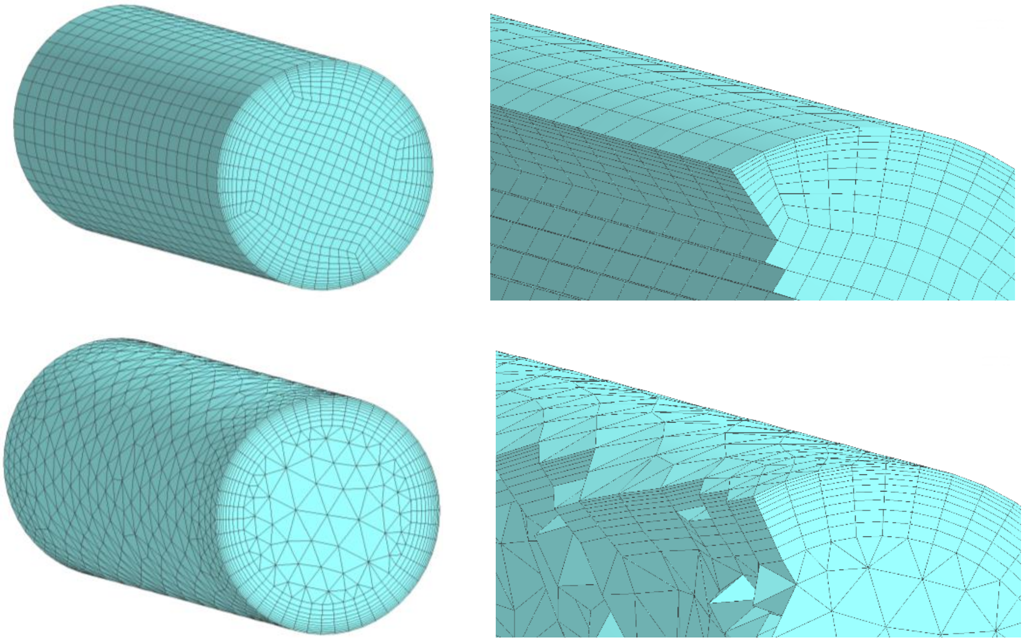

Figure 3.8: (Top) Structured mesh with cells aligned in the direction of flow for a simple pipe problem; (bottom) unstructured mesh with the cells not aligned in the direction of flow.

In the structured mesh example the cells are arranged logically flowing longitudinally along the length of the pipe, and increasing radially in size due to inflation from the walls.

The entire mesh in the structured example is made up of hexahedral cells, including the inflation layers, as shown in the top right image in Figure 3.8. If the flow direction was from an inlet to an outlet in the pipe the structured mesh would be aligned to the direction of the flow.

In the unstructured example the inflation layers on the wall, which comprises prism cells follows the length of the pipe. However the prism cells on the surface of the walls are not ordered. Furthermore the tetrahedron cells flood fills the remaining volume in complete random order. As a consequence of the greater node connectivity in the unstructured example, the unstructured mesh has 72% more cells than the structured mesh (13120 cells compared to 27947 cells). Furthermore the cells in the unstructured mesh have no general alignment, where cells are positioned against the general expected flow direction, which would increase false numerical diffusion. If solutions on both meshes were required to be solved for within the same wall clock time, the unstructured mesh would require greater computational resources compared to the structured mesh.

3.5 Structured Meshes

Structured meshes rely on blocking topologies. Blocking topologies are hexahedron “blocks” which decompose the physical flow domain and allow for local mesh controls to be applied to each block. The blocking topology for the pipe example is shown in Figure 3.9. This is one type of blocking topology called an O-Grid. Other topologies such as, but not limited to C-Grid and H-Grid exist. Further details on blocking and structured meshes can be found in Ansys ICEM guide. Generally, structured meshes require time and careful planning to create good blocking topologies in order to generate a successful mesh. However this comes with a time penalty, where the first attempts at creating blocking topologies for a structured mesh may not be successful, and a lot of time may be spent planning on the topology layout. The time penalty diminishes with increased experience to structured meshing. Furthermore, there is a trade-off where significant time is saved during the compute process when solving a CFD solution on the mesh, and significant solution accuracy compared to unstructured meshes are achieved due to the ordered nature and reduced number of cells.

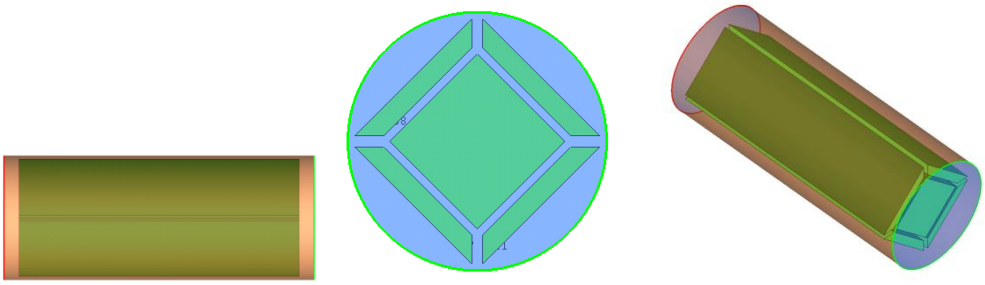

Figure 3.9: O-Grid blocking topology for the structured mesh of a pipe example.

Structured meshes are relatively straight forward to generate on simple physical flow domains such as the pipe example. However they require more thought and consideration for applications which are not as straight forward. The CFD simulations on the unscaled test rigs in CHAPTER 4, and simulations on the one quarter scaled test rig in CHAPTER 5 utilises structured meshing. Although meshing these geometries using a structured approach was not as straight forward as the pipe example, they were able to be blocked and meshed in a structured manner.

3.6 Unstructured Meshes

Unstructured meshes are suited to complex geometries. The generation of unstructured meshes does not require the planning of intricate blocking topologies. However unstructured mesh generation introduces challenges in their own right. Some of these challenges include, but are not limited to, ensuring a good quality surface shell mesh, and ensuring inflation layer collision does not occur. Perhaps one of the most challenging aspects of unstructured mesh generation is to manage the transition between different cell types, and ensuring that the transition produces satisfactory cells. For example the cells which make up the inflation layers are prism cells. The bulk volume of the physical flow domain is made up of tetrahedron cells. In addition to this it is not unusual to have inflation layers to end abruptly due to a multitude of reasons. This means pyramid cells will have to be introduced which act as the transfer medium between a five sided prism cell, and a four sided tetrahedron cell. Figure 3.4 and Figure 3.8 has illustrated some of these concepts.

There are many methods and algorithms to generate an unstructured mesh. Some of the more popular methods are documented in the works by Shewchuk (1997), Owen (1998), and more recently by Blazek (2015). The CFD simulations for Evaporator C used an unstructured approach. The CFD setup is described in CHAPTER 6 and the CFD results are presented in CHAPTER 7. The geometry for Evaporator C is complex, containing internal sweeping structures inside the vessel, to which it was very difficult to apply a structured blocking topology. Therefore an unstructured approach for meshing was deemed the most suitable.

The method used to generate the unstructured mesh was built from best practices, and trial and error suited to the geometry of Evaporator C. The method comprised 8 steps.

1. Apply pre-mesh clean-up of the geometry. This involved deleting duplicate and overlapping geometry curves, checking for holes in the geometry, and ensuring geometry good practices were met.
2. Set the global mesh sizing controls. For example the maximum and minimum cell sizes; the minimum size proximity; the number of cells in gaps that met the minimum size proximity, and inflation settings. Set the local sizing controls on parts that are different to the global settings.
3. Generate a uniform octree mesh using a suitable edge criterion and a suitable number of post mesh smoothing iterations.
4. Delete the octree volume mesh, but retain the octree surface shell mesh.
5. Smooth the surface mesh according to good mesh orthogonality metrics, and then smooth the surface mesh further with the Laplace smoothing algorithm.
6. Generate the volume mesh from the smoothed Octree surface mesh, by harnessing the Delaunay algorithm coupled with the TGrid advancing front method.
7. Apply inflation at the boundaries of interest using the post prism boundary method. Ensure inflation at boundaries do not collide in regions where physical space is very small.
8. Perform post mesh generation checks including checking for poor quality cells, ensuring all cells met the maximum and minimum mesh metric requirements and export the mesh into a readable format for the CFD solver.

3.7 Convergence Control

Successful solution convergence of CFD simulations is paramount in order to present results based on those simulations. Without solution convergence, the results from the simulations may be unphysical and erroneous. In all of the final CFD solutions presented in this study, full solution convergence was achieved. There are three factors which define solution convergence. These are (i) ensuring that the root mean square of the residual level for all governing transport equations has reduced sufficiently; (ii) the global imbalance for each governing equation should be less than 1% of the total fluxes in and out of the physical flow domain; (iii) and ensuring monitor points of variables in pertinent locations do not exhibit sporadic behaviour. The achievement of these factors are dictated not only by the mesh quality as previously discussed, but also the type of analysis (steady state or transient), the numerical scheme (high resolution schemes) and the suitability of the chosen time step to describe the flow.

Ansys CFX uses a coupled algebraic multigrid method to solve the system of governing equations. Once discretised, all governing equations are non-linear, but may be expressed in quasi-linear form, as follows

$$[A(\varphi)][\varphi] = [b(\varphi)] \tag{3.13}$$

where $A(\varphi)$ is a matrix which depends on the solution (φ), and $b(\varphi)$ is a source vector, which also depends on the solution (φ). Eq. 3.13 is solved iteratively by the process of linearization. Given an approximate solution to the variable φ^n, the matrix and source vector are evaluated at φ^n, and these are then used to construct a linear equation for the next solution φ^{n+1}, as follows:

$$[A(\varphi^n)][\varphi^{n+1}] = [b(\varphi^n)] \tag{3.14}$$

The linearised equations may be solved using an iterative linear equation solver, thus yielding the improved solution φ^{n+1}. The Algebraic Multigrid Method (AMG) is usually selected, because of its superior scalability properties for large meshes.

The above linearization procedure is repeated iteratively, until the exact solution to the non-linear equation in Eq. 3.13 is approached. Such iterations are called outer iterations, or coefficient loops, in order to distinguish them from the inner iterations employed to solve the linear system Eq. 3.14.

The convergence of the non-linear iterative procedure is monitored by computing the local residual error at the start of each coefficient loop. This is a measure of how well the solution obeys Eq. 3.13 at each grid point, and is given by

$$r^n = b - A\varphi^n \tag{3.15}$$

where $A = A(\varphi^n)$ and $b = b(\varphi^n)$. The magnitude of the residual vector is called the residual norm, and is usually defined by the root mean square of the residual vector values summed over all grid nodes, or by the maximum absolute value of the residual vector values. The iterative procedure is assumed to be converged when the magnitude of residual error has fallen below a user-specified convergence criterion.

In practice, the convergence criterion is in fact applied to a normalized residual vector, in order to make it non-dimensional, and hence applicable universally to all equations in the system. The normalized residuals take the form

$$\left[\tilde{r}_\varphi\right] = \frac{[r_\varphi]}{a_P \Delta\varphi} \tag{3.16}$$

where a_P is a measure of the diagonal component of the matrix A, and $\Delta\varphi$ is a measure of the solution change. The precise details of how the normalization factors are computed are rather complex, and are not given in the user documentation, as they are regarded as proprietary.

Root mean square residual errors are not enough on their own to determine if a solution is converged. Global solution imbalances are used with the root mean square residuals to determine convergence. The global solution imbalance is the ratio of the equation imbalance to the maximum flow inside the domain. A negative value indicates total flow lost out of the physical flow domain, and a positive imbalance indicates total flow gained into the physical flow domain. Ideally this should be zero. However due to numerical round off error, this cannot be entirely possible. A global solution imbalance of less than 1% of the total flow is acceptable, with lower values being more desirable. For all simulations reported in this thesis the global solution imbalances were checked to ensure they were less than 1%.

The final check for convergence is monitoring of key variables in pertinent locations in the solution domain. For a steady state simulation, when a solution is fully converged the monitored variables should not change with accumulated iteration. If it does then it could indicate either that the steady state solution is not fully converged, or a pseudo steady state solution has been found. In either case a transient approach should be taken as such behaviour of the monitored variables is an indication of transient behaviour.

The suitability of the time step was determined individually for each respective case (simulations of the unscaled test rigs, scaled test rigs, and Evaporator C). This is described in their respective chapters. A universal time step does not exist which describes all types of flows, which would aid successful convergence of the linearized solution.

3.8 Summary

This chapter serves as the statement of numerical accuracy for this study. In this chapter many different possible sources for numerical error was introduced, and the steps taken to alleviate numerical error was discussed. To treat discretization error, and subsequently the steps taken to perform a mesh sensitivity study the GCI method developed by Celik et al. (2008) was used. The meshes were designed stringent quality controls ensuring adherence to good values of cell orthogonality, expansion ratio and aspect ratio. In addition to this, structured meshes were used for the unscaled and scaled test rigs, and unstructured meshes used in the more complex industrial Evaporator C case. The simulations were computed against stringent convergence criteria, harnessing good best practices to ensure successful convergence. This included solving all simulations to residual standards of 1×10^{-5}, ensuring global imbalances were less than 1% of the total flow for each conservation equation, and monitoring solution variables to ensure a physically realistic solution had been achieved.

Chapter 4

Computational Analysis on the Unscaled Test Rigs

4.1 Introduction

The National Nuclear Laboratory have commissioned two small-scale test rigs, which are cylindrical, non-radioactive and steam heated, in order to characterise the transport phenomena occurring within the industrial evaporator design, Sellafield Evaporator C. These two test rigs are termed the short and a tall test rig respectively. The main difference between the two is the volume and depth of liquid they can accommodate. The test rigs boil liquids under conditions similar to those found in Evaporator C, and hence, provide insight into the flow phenomena occurring within Evaporator C.

It would have been very difficult to perform a heat transfer analysis on the industrial evaporator design, Sellafield Evaporator C without first performing an analysis on a simpler, smaller system first to establish a foundation to build upon. The behaviour in the unscaled short and tall test rigs were analysed to establish this foundation. Firstly, a one-dimensional thermal resistance investigation on the test rigs yielded heat flux and temperature distributions. Secondly, single-phase CFD simulations provided a greater information on the behaviour of the test rigs, and set a foundation for the proceeding CFD simulations on the one-quarter scale test rig and the industrial evaporator. Figure 4.1 is a schematic of the short and tall test rigs. In Figure 4.1 the cylindrical glass walls are not drawn.

The two test rigs are cylindrical glass vessels, and have an internal diameter of 0.1 m. The base of the test rigs is stainless steel and has a thickness of 0.02 m. In both test rigs, dry saturated steam condenses underneath the stainless steel base plate. This heats the liquid column above it. The steam pressure is 2.46 bar, which has a saturation temperature corresponding to 126.9 °C. The ullage pressure above the free surface for both test rigs is set to 0.1 bar. As vapour evaporates from the free surface, it condenses in an overhead condenser and returns as sub-cooled condensate. This is supplied back into the rigs above the free surface. This maintains a constant volume at all times, as is found in Evaporator C.

The short test rig depicted by Figure 4.1 (left) has a fill depth of 0.1 m. This gives a 1:1 ratio for the diameter to fill depth. The short test rig provides insight into the transport phenomena when the vessel width and fill depth are equal, or almost equal, which is true in Evaporator C. The internal diameter of Evaporator C is 3.05 m and the fill depth is 2.35 m. Hence, the ratio of diameter to fill depth for Evaporator C is 1:1.3, which is slightly more than the short test rig. The only mode of heating into the short test rig is the steam heating occurring underneath the base plate.

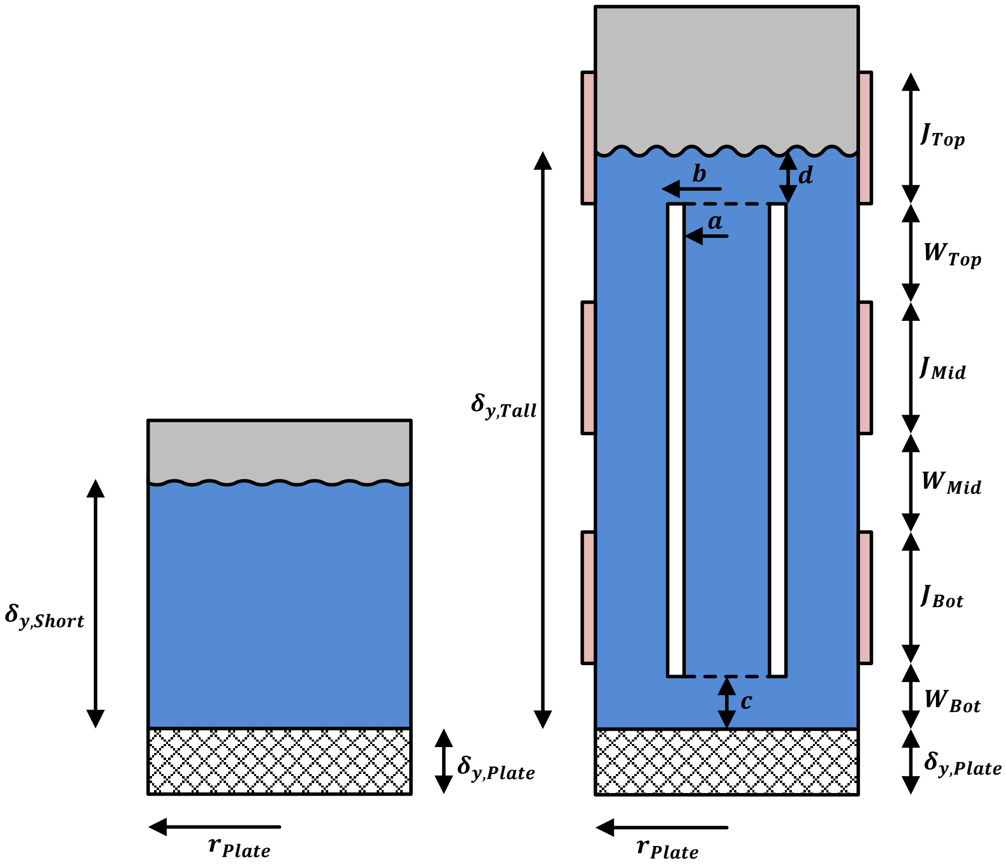

Figure 4.1: Schematic of the short test rig (left) and tall test rig (right), not drawn to scale.

The tall test rig has a fill depth of 2.215 m. The ratio of diameter to fill depth is 1:22.15. This is considerably more than the ratio for the short test rig, and more than the ratio for Evaporator C. The large ratio found in the tall test rig is due to the large fill depth. Principally the tall test rig provides insight into the flow phenomena in the liquor, when there is a large head effect, which occurs in Evaporator C. The fill height of Evaporator C is 2.35 m, which is slightly more than the fill height in the tall test rig.

Three water jackets at intermittent heights around the tall test rig provide additional heating and the rig contains a draught tube as shown in Figure 4.1 (right). The inclusion of the three heating jackets is an attempt at replicating steam condensation on the outer walls of the jacket in Evaporator C. The purpose of the draught tube is to replicate the effect of the physical presence of the internal helical coils and other associated equipment found in Evaporator C. The ratio of the annulus to core area of the draught tube is the same as the annulus to core area of the internal helical coils of Evaporator C. The annulus area is the inside cross sectional area of the outer shell of Evaporator C; and the core area is the inside cross sectional area of the helical core of the inner evaporator coils. The draught tube has the same scaling factor as Evaporator C, as shown in Eq. 4.1.

$$SF = \frac{\text{Annulus Area}}{\text{Core Area}} = \frac{\pi/_{4}\left(D_{shell}^{2} - D_{inner\ coils}^{2}\right)}{\pi/_{4} D_{inner\ coils}^{2}} = \left(\frac{D_{shell}}{D_{inner\ coils}}\right)^{2} - 1 \tag{4.1}$$

The dimensions of the short and tall test rigs and the thermosphysical properties of the associated materials found in the test rigs are summarised in Table 4.1. The configuration of the tall test rig is shown in Figure 4.2 (NNL Private Communication, 2013). The short test rig has an identical configuration with the test section replaced by the short test rig.

Property	**Symbol**	**Value**
Short test rig liquid fill height	$\delta_{y,Short}$	0.1 m
Tall test rig liquid fill height	$\delta_{y,Tall}$	2.215 m
Draught tube inner diameter	a	0.023 m
Draught tube outer diameter	b	0.025 m
Draught tube stand-off clearance	c	0.02 m
Draught tube top clearance	d	0.15 m
Bottom wall height for the tall test rig	W_{Bot}	0.25 m
Middle wall height for the tall test rig	W_{Mid}	0.185 m
Top wall height for the tall test rig	W_{Top}	0.18 m
Bottom jacket height for the tall test rig	J_{Bot}	0.49 m
Middle jacket height for the tall test rig	J_{Mid}	0.78 m
Top jacket height for the tall test rig	J_{Top}	0.33 m
Wall thickness of the outer glass of both test rigs	Not denoted	0.002 m
Glass thermal conductivity (Pyrex)	λ_{Glass}	1.4 W/mK
Base plate thickness	$\delta_{y,Plate}$	0.02 m
Base plate radius	r_{Plate}	0.05 m
Thermal conductivity (AISI 302 stainless steel)	λ_{Plate}	15.1 W/mK
Density (AISI 302 stainless steel)	ρ_{Plate}	8055 kg/m^3
Specific heat capacity (AISI 302 stainless steel)	$C_{P,Plate}$	480 J/kgK

Table 4.1: Test rig dimensions and thermophysical properties of the liquid.

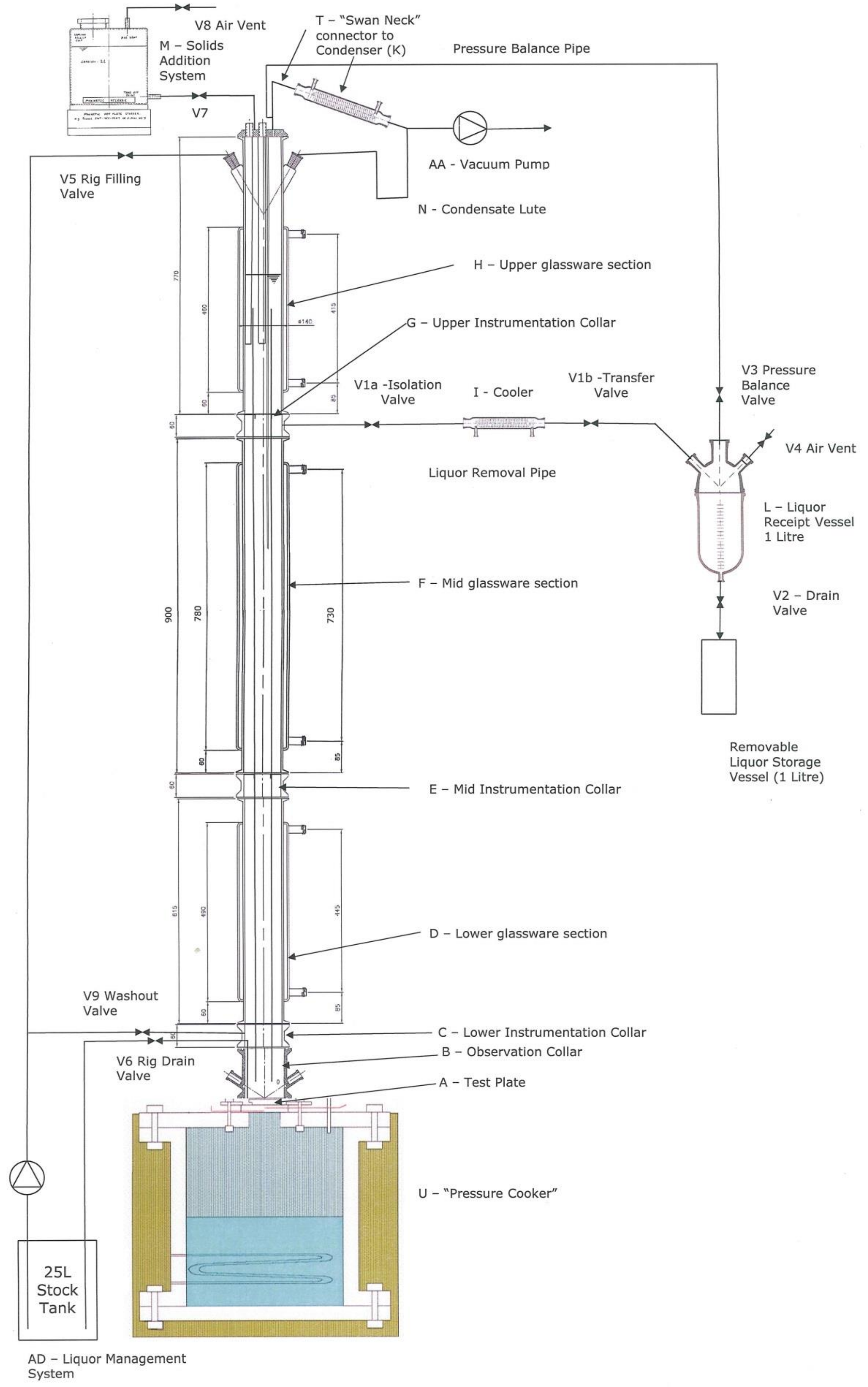

Figure 4.2: Tall test rig configuration. The short test rig has a similar configuration (NNL Private Communication, 2013).

4.2 Previous Work Undertaken

Previously the National Nuclear Laboratory performed experimental and computational studies on the two test rigs. A program of experimental work on the short test rig ended more than five years ago, but unfortunately, the results from the studies were not made formally available by NNL. However, the investigators did informally describe the behaviour in a personal communication, which stated nucleate boiling occurred on all heated surfaces in the test rig. The geometry and operating conditions of the short test rig were described in the previous subsection.

The National Nuclear Laboratory also performed past experimental and numerical studies on the tall test rig. The studies comprised an experimental programme consisting of two phases, and one simulation study, which used symmetric CFD domains to model the test rigs.

The experimental program for the tall test rig comprised two phases. In phase one of the programme (NNL Private Communication, 2011), the thermal hydraulics of the water in the column with and without the draught tube present was investigated by increasing the steam pressure. The ullage pressure was kept at sub-atmospheric conditions at 0.1 bar, and the steam saturation pressure and hence temperature was increased from 2.61 to 6.57 bar. This corresponded to saturated steam temperatures of 128.8 and 162.4 °C respectively. The approximate range of heat fluxes through the base plate was 30 to 57.8 kW/m^2. The water inside the heating jackets did not exceed 127°C and total heat input into the jackets did not exceed 3 kW.

The main finding of phase one was that without the draught tube, temperature of the water close to the top surface of the base plate rose with increasing steam pressure and temperature. The pattern of the liquid circulations in the liquid column seemed random and disordered. In contrast to this, with the inclusion of the draught tube the water temperature close to the top surface of the base plate remained steady with increasing steam pressure and temperature. The water temperature remained close to the local saturation temperature at the positions where measurements were made. The draught tube caused the water to recirculate in an ordered pattern, upwards between the draught tube and vessel walls, and downward in the core of the draught tube which impinged on the upper plate surface.

In phase two (NNL Private Communication, 2013) a more comprehensive program of experimental work was performed and the recommendations of the pilot study in phase one were implemented. The main recommendations were mainly geometrical ones concerning the test rig, and improvements on the standard operating procedure. Some improvements included increasing the size of some of the glassware, and replacing the existing under sized condenser with a more suitable one. The experimental work in phase two comprised a myriad of experimental tests, which tested each variable in the configuration of the tall test rig. This included variations of the height of the stand-off of the draught tube (denoted by c in Figure 4.1), changing the steam pressure and temperature inside the pressure cooker, changing the jacket temperatures, changing the water depths, and changing the ullage pressure. The emphasis of the study was to observe how each configuration and operating conditions affected the thermohydraulic behaviour under sub-atmospheric pressures, even though the ullage pressure varied.

The main findings of phase two reinforced the main findings in phase one. At sub-atmospheric ullage pressure, water at the free surface travels down the centre of the draught tube and displaces warmer water close to the upper surface of the plate. This forced a convective cooling effect on the upper plate, which resulted in steady temperatures. The flow with the tube in place resembled a thermosyphon reboiler system.

The CFD simulation study performed by the National Nuclear Laboratory (NNL Private Communication, 2013) used the commercial code Ansys Fluent to model the flows inside the tall test rig, at atmospheric pressure. The CFD simulations were single phase, simulating sub-cooled buoyancy driven flow inside the liquid column, at three draught tube standoff distances (denoted by c in Figure 4.1) of 20, 40 and 60 mm. A summary of the boundary conditions that were used for the simulations are tabulated in Table 4.2, and represents one of the configurations which was tested in phase two of the experimental program. The temperatures of the lower, middle and upper jackets were set to boundary conditions of 70, 60 and 50 °C respectively. The non-heated walls and free surface had mixed boundary conditions applied to it, using a heat transfer coefficient of 3 W/m^{2}K, and outside ambient temperature 20 °C for the non-heated walls, and outside ullage temperature 45 °C for the free surface. The free surface was treated as a free slip zero shear wall.

Investigations of two physical flow domains were reported: firstly axisymmetric conditions represented the physical geometry for all three draught tube standoff distances. Secondly, one partial 3D flow domain, swept 180° about the central axis represented the physical geometry for the 40 mm standoff case only. The meshes used a structured hexahedral approach, and the flow numerics for advection and diffusion were second order transient. Lastly the $k - \omega$ SST turbulence model was used to capture turbulence effects.

The axisymmetric simulations computed total transient time of 100 minutes. The results yielded satisfactory behaviour for momentum, where the bulk circulation rates followed the general pattern produced in the experimental test rigs. However, the values of the velocities were slightly higher than expected in the CFD simulations compared to experiment. The energy fields did not agree, with predictions of temperatures 13 °C hotter than expected at the vicinity of the upper plate. Despite the minor errors in the momentum and energy fields, the CFD investigation was commendable as it yielded important information on the potential heat and flow distributions inside the test rig.

The partial 180° 3D simulations computed a total transient time of 35 minutes. The partial 3D simulations suffered the same drawbacks as the axisymmetric simulations where the direction of the momentum of the bulk flow appeared to be accurate. However, the magnitude of those circulations and the corresponding temperatures were greater than expected.

Property	**Value**
Ullage pressure	1 bar
Initial temperature	20 °C
Steam temperature	110 °C
Ambient "outside" temperature	20 °C
Ullage temperature	45 °C
Lower jacket temperature	70 °C
Middle jacket temperature	60 °C
Upper jacket temperature	50 °C
Non-heated walls heat transfer coefficient	3 W/m^{2}K
Free surface heat transfer coefficient	3 W/m^{2}K

Table 4.2: Boundary conditions of the CFD investigation performed by the National Nuclear Laboratory.

4.3 Review of the Unscaled Test Rigs

The short and tall test rigs are not scaled geometries of Evaporator C. Hence, they are not physically representative of Evaporator C. Furthermore, the test rigs do not accommodate like for like boundary conditions. For example, the test rigs do not allow for condensation on all heated surfaces, only underneath the stainless steel base plate. In addition to this, there is no heat generation inside the water to represent heating from the internal helical coils in Evaporator C.

In the short test rig although the aspect ratio (vessel diameter to fill height) is similar to Evaporator C, the short test rig does not account for the head effect. Furthermore heating to the water is via steam condensation underneath the base plate. Additional external heating to the liquid column was not implemented which would have represented the external heating jacket in Evaporator C. Lastly, the short test rig does not contain any apparatus inside it to disturb the natural buoyancy driven flow patterns, as found in Evaporator C such as the internal heating coils.

In the tall test rig, the draught tube forced the flow to behave in an unnatural way, which yielded circulation patterns that may not be representative of those found inside the industrial evaporator, Sellafield Evaporator C. The draught tube was justified since Evaporator C has a core to annulus ratio between the vessel shell and the inner coils. Other geometrical factors within Evaporator C were not present inside the tall test rig. For example the spaces between the three internal helical coils. In order to accommodate this in the tall test rig two additional concentric draught tubes would need to be present inside the test rig. This would certainly disrupt the flow behaviour in the tall test rig compared to the single draught tube configuration.

Despite the shortcomings of the two test rigs, the investigations performed on them provided relatively important insights into the possible flow phenomena occurring inside Evaporator C.

4.4 Thermal Resistance Investigation on the Unscaled Test Rigs

The thermal resistance investigation involved generating systems of algebraic equations that described the one dimensional heat flux and temperature distributions inside the two unscaled test rigs. The equations emanated from the solution of heat fluxes through thermal resistance networks, as shown by the single thermal resistance representation in Eq. 4.2,

$$\frac{\dot{Q}}{A} = \dot{q} = \frac{T_2 - T_1}{R} \tag{4.2}$$

where $\dot{q}$ is the heat flux (heat transfer rate per unit area) between temperatures T_1 and T_2 and R denotes the specific thermal resistance (the reciprocal of the heat transfer coefficient), which has units of m^2K/W, and not the absolute thermal resistance, which has units of K/W.

Figure 4.3 illustrates the thermal resistance networks for the short and tall test rigs under three theoretical heat transfer modes in the water: pure conduction, free convection and nucleate boiling on the upper plate surface. The thermal resistance networks assumed that heat transfer occurred vertically through the test rigs, and ignored heat transfer in other directions.

Each resistance denoted by R in Figure 4.3 describes a mode of heat transfer. Resistances R_1 and R_2 are steam condensation underneath the base plate and conduction through the base plate respectively. These were common for all three cases that were under consideration. The remaining resistances in Figure 4.3 (a), (b) and (c) were particular for each case, and their descriptions are in their respective sub-sections. Each resistance was governed by two temperatures and a common heat flux.

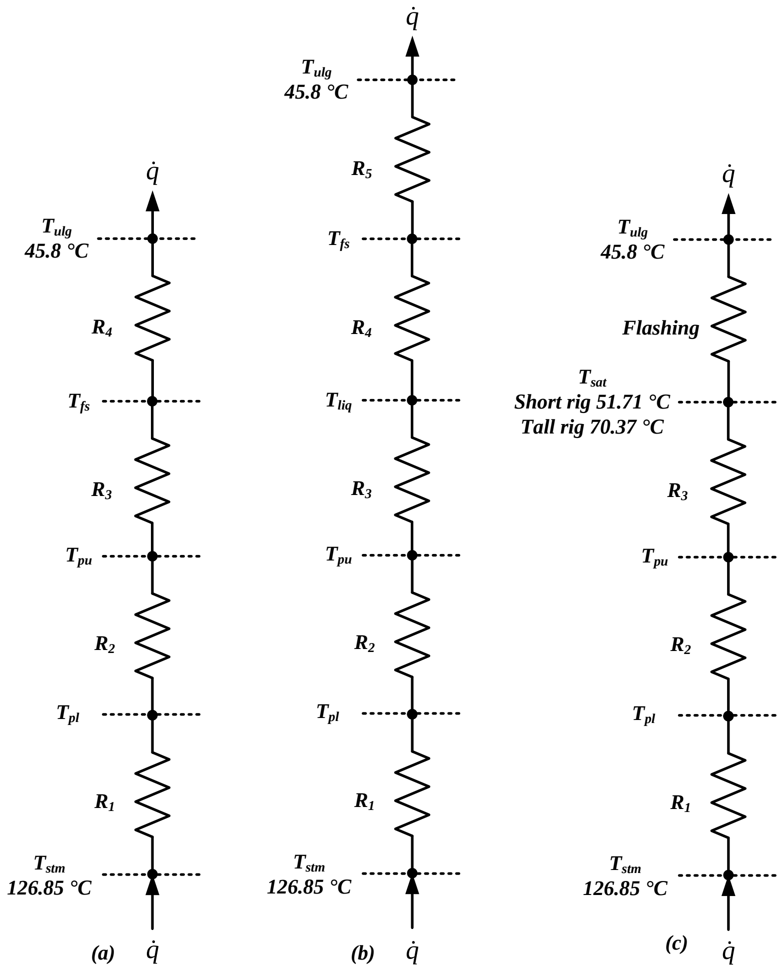

Figure 4.3: Thermal resistance networks for case (a) pure conduction through the liquid column, case (b) free convection in the liquid column, and case (c) nucleate boiling in the liquid column.

The temperatures in the thermal resistance networks in Figure 4.3 corresponded to a particular position in the test rigs. For all three cases T_{stm}, T_{pl} and T_{pu} corresponded to the temperatures at the positions of the condensing steam, lower plate and upper plate respectively. For the pure conduction case in Figure 4.3 (a), T_{fs} and T_{ulg} corresponded to the temperatures at the free surface and ullage headspace respectively. For the free convection case in Figure 4.3 (b), T_{liq} was the liquid temperature halfway between the upper plate surface and the free surface, and T_{fs} and T_{ulg} had the same definition as described for the pure conduction case in Figure 4.3 (a). Lastly, for the nucleate boiling case in Figure 4.3 (c), T_{sat} was the local saturation temperature corresponding to the local pressure at the upper plate surface, and T_{ulg} had the same definition as before. In each case, there was a common heat flux.

In each test case in Figure 4.3, a number of equations similar to that in Eq. 4.2 were generated which described heat transfer through each thermal resistance. Each investigation had two known temperatures at the extremes of the system. The remaining variables were unknown, which were the heat flux, and intermediary temperatures. Since the number of equations was the same as there were unknowns, it is possible to solve for the variables in the system using the computer program detailed in APPENDIX 1, which harnessed the Newton Raphson iterative method to provide a solution to the network.

4.4.1 Assumptions

The assumptions used in the thermal resistance investigation was as follows:

1. The heat transfer analysis was one dimensional in the vertical y direction.
2. Two temperatures in the system were known (Dirichlet boundary conditions) which were the steam and ullage temperatures for the pure conduction and free convection cases (a) and (b) respectively; or the steam and liquid saturation temperatures for nucleate boiling case (c).
3. The ullage pressure was set to 0.1 bar.
4. For all three cases, the common steam saturation temperature was set to 126.9 °C.
5. For the pure conduction and free convection cases the ullage temperature was set to 45.8°C corresponding to the ullage saturation pressure of 0.1 bar. For the nucleate boiling cases the saturation temperatures of the liquid at the upper plate surface were 51.7 °C and 70.4 °C for the short and tall test rigs respectively.
6. The liquid column contained water and fouling was not considered.
7. In the pure conduction case, the thermal conductivity of water was constant throughout the liquid column.
8. In the free convection case the liquid was divided by two rotating convection cells between the upper plate and free surface.
9. In the boiling case, nucleate boiling occurred on the upper plate surface.
10. Radiation heat transfer was ignored and the sidewalls were adiabatic.
11. A program written in the computer language MATLAB computed solutions to the governing equations. This used the Newton Raphson iterative approach as the main solver. Details of this program are described in APPENDIX 1.
12. Curve fitted correlations as a function of temperature were used for the thermophysical properties of water (Alane, 2007).

4.4.2 Test Case A: Pure Conduction through the Liquid Column

Figure 4.3 (a) represents the thermal resistance network diagram for the pure conduction case through the liquid column. There were four resistances in sequence described by Eq. 4.3 to 4.6. Eq. 4.3 describes the condensation resistance underneath the base plate, Eq. 4.4 and 4.5 describes the conduction resistances through the base plate and liquid column respectively, and Eq. 4.6 describes the free convection resistance in the ullage headspace. The four unknown values that were determined were the heat flux, lower plate, upper plate and free surface temperatures.

$$\dot{q} = \frac{T_{stm} - T_{pl}}{R_{csn}} = h_{csn}\left(T_{stm} - T_{pl}\right) \tag{4.3}$$

$$\dot{q} = \frac{T_{pl} - T_{pu}}{R_{Plate}} = \left(\frac{\lambda}{\delta y}\right)_{Plate}\left(T_{pl} - T_{pu}\right) \tag{4.4}$$

$$\dot{q} = \frac{T_{pu} - T_{fs}}{R_{Liquid}} = \left(\frac{\lambda}{\delta y}\right)_{Liquid}\left(T_{pu} - T_{fs}\right) \tag{4.5}$$

$$\dot{q} = \frac{T_{fs} - T_{ulg}}{R_{cvn}} = h_{cvn}\left(T_{fs} - T_{ulg}\right) \tag{4.6}$$

Two correlations for the condensing heat transfer coefficient were used independently of each other in Eq. 4.3. These were the analytical Nusselt (1916) heat transfer coefficient for condensing vapours on vertical surfaces; and the empirical Gerstmann and Griffith (1967) correlation for condensing vapours underneath downward facing surfaces.

The analytical Nusselt heat transfer coefficient took the form shown in Eq. 4.7.

$$\mathrm{Nu} = \frac{h_{csn}L}{\lambda_l} = 0.943\left[\frac{\rho_l(\rho_l - \rho_g)g\Delta H'_{lg}L^3}{\mu_l\lambda_l(T_{stm} - T_{pl})}\right]^{1/4} \tag{4.7}$$

The enthalpy of vaporisation in Nusselt's correlation was replaced with an augmented enthalpy of vaporisation (Rohsenow, 1956), which took into effect the condensate sub-cooling as shown in Eq. 4.8.

$$\Delta H'_{lg} = \Delta H_{lg} + 0.68C_{p,l}\left(T_{stm} - T_{pl}\right) \tag{4.8}$$

Although the Nusselt formulation was designed for vertical surfaces, it was useful to use it here, as it was arguably the most widely used condensing heat transfer coefficient used in the open literature. In addition to this, the small accuracy of phase change heat transfer coefficients nullifies most of the conditions under which they must be used.

The second correlation used for condensing heat transfer coefficient was that of Gerstmann and Griffith (1967). The coefficient is a function of the vapour phase Rayleigh number. Its formulation was different to the traditional formulation (the product of Prandtl and Grashof numbers) as shown in Eq. 4.9.

$$\mathrm{Ra} = \frac{g\rho_l(\rho_l - \rho_g)\Delta H_{l,g}}{\mu_l(T_{stm} - T_{pl})\lambda_l}\left(\frac{\sigma}{g(\rho_l - \rho_g)}\right)^{3/2} \tag{4.9}$$

The Nusselt number in the Gerstmann and Griffith correlation was found to be dependent on the Rayleigh number regime as shown in Eq. 4.10, where $10^6 < \mathrm{Ra} < 10^8$ denoted laminar flow, and $10^8 < \mathrm{Ra} < 10^{10}$ denoted turbulent flow.

$$\mathrm{Nu} = \begin{cases} 0.69\mathrm{Ra}^{0.20} & 10^6 < \mathrm{Ra} < 10^8 \\ 0.81\mathrm{Ra}^{0.193} & 10^8 < \mathrm{Ra} < 10^{10} \end{cases} \tag{4.10}$$

The relation in Eq. 4.11 determined the Nusselt number, and consequently allowed the heat transfer coefficient to be determined.

$$\mathrm{Nu} = \frac{h_{csn}}{\lambda_l}\left(\frac{\sigma}{g(\rho_l - \rho_g)}\right)^{0.5} \tag{4.11}$$

The free convection heat transfer coefficient in the ullage region in Eq. 4.6 was treated as a hot surface facing upward from the free surface (or a cold surface facing downward) (McAdams, 1954) as shown in Eq. 4.12.

$$\mathrm{Nu} = \frac{h_{cvn}L}{\lambda_l} = \begin{array}{lll} 0.54\mathrm{Ra}^{1/4} & 10^4 \le \mathrm{Ra} \le 10^7 & \mathrm{Pr} \ge 0.7 \\ 0.15\mathrm{Ra}^{1/3} & 10^7 \le \mathrm{Ra} \le 10^{11} & all\ \mathrm{Pr} \end{array} \tag{4.12}$$

In this instance the Rayleigh number for Eq. 4.12 took the traditional definition (as opposed to the custom definition in Eq. 4.9) as shown in Eq. 4.13.

$$\mathrm{Ra} = \mathrm{GrPr} = \frac{g\beta\Delta T L^3}{\nu k} \tag{4.13}$$

4.4.3 Test Case B: Free Convection in the Liquid Column

The network for free convection in Figure 4.3 (b) had five sequential thermal resistances. The first two resistances were identical to Test Case A, which were condensation on the lower plate surface, and conduction through the base plate. These were described by Eq. 4.3 and 4.4 respectively.

The following two resistances in Figure 4.3 (b) represented free convection in the liquid column. It was assumed there were two convection cells inside the liquid column which were treated as a hot surface facing upward from the upper plate as shown in Eq. 4.14, and a cold surface facing downward from the free surface as shown in Eq. 4.15 (McAdams, 1954), and hence the heat transfer coefficients were treated by Eq. 4.12. This assumed there was a temperature, T_{liq} at the midpoint of the liquid column.

The free convection resistance in the ullage head space was also identical to the previous case, which is described by Eq. 4.6. Hence the governing equations for Test Case B: Free Convection in the Liquid Column were (in order of thermal resistances) Eq. 4.3, 4.4, 4.14, 4.15 and 4.6. The five unknown values that were determined were the heat flux, lower plate temperature, upper plate temperature, mid liquor temperature and free surface temperature.

$$\dot{q} = \frac{T_{pu}-T_{liq}}{R_{cvn}} = h_{cvn}\left(T_{pu} - T_{liq}\right) \tag{4.14}$$

$$\dot{q} = \frac{T_{liq}-T_{fs}}{R_{cvn}} = h_{cvn}\left(T_{liq} - T_{fs}\right) \tag{4.15}$$

4.4.4 Test Case C: Nucleate Boiling in the Liquid Column

The network diagram for nucleate boiling in Figure 4.3 (c) had three resistances. In order of their resistance to heat transfer, these were condensation underneath the stainless steel base plate, conduction heat transfer through the base plate, and nucleate boiling on the top surface of the base plate. The condition of vapour once it was generated was not considered. For example, it was not considered if vapour collapses back into the liquid column, or rises through the liquid column and thereby escaping at the free surface.

The thermal resistances described by Eq. 4.3 and 4.4 in Test Case A remained applicable for the nucleate boiling case. Eq. 4.16 described nucleate boiling occurring at the upper plate surface. Hence the governing equations for Test Case C: Nucleate Boiling in the Liquid Column were (in order of thermal resistances) Eq. 4.3, 4.4 and 4.16. The five unknown values that were determined were the heat flux, lower plate temperature and upper plate temperature.

$$\dot{q} = \frac{T_{pl}-T_{sat}}{R_{boil}} = h_{boil}\left(T_{pl} - T_{sat}\right) \tag{4.16}$$

It was assumed that nucleate boiling occurred at the upper plate surface, where the local saturation temperature corresponded to the local saturation pressure, which depended on the liquor depth and the ullage pressure in the headspace. The saturation temperature was determined using Antoine's vapour pressure correlation as shown in Eq. 4.17, which used the constants suggested by Linstrom and Mallard (Linstrom and Mallard, 2001), which for A, B and C were 5.20389 bar, 1733.926°C and -39.485°C respectively.

$$\log_{10} P_{sat} = A - \frac{B}{C+T_{sat}} \tag{4.17}$$

The saturation pressure was evaluated as shown in Eq. 4.18.

$$P_{sat} = P_{ulg} + \rho g \delta y_{Liquid} \tag{4.18}$$

From Eq. 4.18 the two saturation pressures at the upper surface of the plate for the short and tall test rigs were computed as 0.11 bar and 0.31 bar respectively. These figures were computed when the ullage pressure is set to 0.1 bar, the density of water as 998 kg/m^3, and the liquid depth at either 0.1 m or 2.215 m (depending on the test rig). Hence, from Eq. 4.17, the saturation temperatures were 51.7°C and 70.4°C for the short and tall test rigs respectively. For the boiling case, at the free surface it was assumed the liquor flashes to vapour.

Six individual correlations were used for the nucleate boiling heat transfer coefficient in Eq. 4.16. The first was the Forster and Zuber (1955) correlation defined in Eq. 4.19.

$$h_{boil} = \frac{0.00122 \Delta T_{sat}^{0.24} \Delta P_{sat}^{0.75} C_{pl}^{0.45} \rho_l^{0.45} \lambda_l^{0.75}}{\sigma^{0.5} \Delta H_{lg}^{0.24} \rho_g^{0.24}} \tag{4.19}$$

The second and third were the Mostinski (1963) and Bier et al. (1983) correlations, which shared the same expression for heat transfer coefficient shown in Eq. 4.20, however differed by their definition for the pressure correction factor as shown by Eq. 4.21 and 4.22 respectively.

$$h_{boil} = 0.00417 P_C^{0.69} \dot{q}^{0.7} F_P \tag{4.20}$$

$$F_P = 1.8 P_R^{0.17} + 4 P_R^{1.2} + 10 P_R^{10} \tag{4.21}$$

$$F_P = 2.1 P_R^{0.27} + [9 + (1 - P_R^2)^{-1}] P_R^2 \tag{4.22}$$

The fourth and fifth correlations were the Cooper (1984) and Rohsenow (1951) correlations, shown by Eq. 4.23 and 4.24 respectively.

$$h_{boil} = 55 \dot{q}^{0.67} P_R^{0.12 - 0.2 \log R_P} (-\log P_R)^{-0.55} M^{-0.5} \tag{4.23}$$

$$h_{boil} = C^{1/0.33} \tag{4.24}$$

In the Rohsenow correlation the constant C was defined by Eq. 4.25.

$$C = \frac{C_P (T_{pl} - T_{sat})}{C_{SF} \Delta H_{lg}} \left(\frac{C_p \mu_l}{\lambda_l} \right)^{-n} \left(\frac{h_{boil} \Delta T_{sat}}{\mu_l \Delta H_{lg}} \sqrt{\frac{\sigma}{g(\rho_l - \rho_g)}} \right)^{-0.33} \tag{4.25}$$

The exponent n was taken as unity, which is valid for boiling water (and 1.7 for other fluids) (Hewitt et al., 1994). The value of the surface finish was dimensionless, and values were obtained from Collier and Thome (1996). In this investigation, its value was 0.0080.

The sixth and final correlation used for the boiling coefficient in Eq. 4.16 was that by Gorenflo and Kenning (2010), as shown in Eq. 4.26.

$$h_{boil} = h_0 F_P \left(\frac{\dot{q}}{\dot{q}_0} \right)^n \left(\frac{R_p}{R_{p,0}} \right)^{0.133} \tag{4.26}$$

The correlation was a function of a pressure correction factor, which for boiling water is determined using Eq. 4.27.

$$F_p = 1.73 P_R^{0.27} + \left(6.1 + \frac{0.68}{1 - P_R} \right) P_R^2 \tag{4.27}$$

The exponent, n in Eq. 4.26 was determined using the correlation in Eq. 4.28.

$$n = 0.9 - 0.3P_R^{0.15} \tag{4.28}$$

The values for the reference heat transfer coefficient, surface roughness and heat flux were 5600 W/m^{2}K, 0.4 µm, and 20,000 W/m^2 respectively.

Hewitt et al. (1994) reported that there are large deviations between the boiling heat transfer coefficients, and no general guidelines could be provided on the boiling correlation that should be used. Hence, in this study, six widely different correlations were used.

The wall superheat required to initiate nucleate boiling for each test case was calculated using the Davis and Anderson (1966) correlation, as shown in Eq. 4.29.

$$\Delta T_{ONB} = T_{pu} - T_{sat} = \left(\frac{8\sigma T_{sat}\nu\dot{q}}{H_{lg}\lambda_l}\right)^{0.5} \tag{4.29}$$

4.4.5 Results of the Investigations of the Thermal Resistance Networks

The results from the thermal resistance investigation for the three cases: conduction, free convection and boiling are shown in Table 4.3, Table 4.4 and Table 4.5 respectively. The overall heat transfer coefficients were orders of magnitude lower in case A and B than in case C. This is because the values of the free convection heat transfer coefficients in the ullage region were small, which reduced the overall heat transfer coefficient, since they corresponded to higher thermal resistances. In cases A and B, convection heat transfer in the ullage region was the dominating thermal resistance. Comparatively the results show condensation heat transfer offered little resistance to heat transfer in both cases.

In case C, the dominating thermal resistance was conduction heat transfer through the base plate. The overall heat transfer coefficients for case C were far greater than for cases A and B. All three cases shared the same conduction thermal resistance through the base plate, and in all three cases, their resistance values were the same. To reduce the conduction thermal resistance, and consequently increase the heat flux through the system, the thickness of the base plate would need to be reduced; or alternatively a base plate material with a higher thermal conductivity than stainless steel would need to be used.

In case C with the exception of the Cooper correlation, all boiling heat transfer coefficients were in the same order of magnitude, despite their very diverse formulations. Rohsenow et al. (1998) reported that the square root of the molecular weight in the Cooper correlation was an oversimplification which could yield significant errors in the value of the boiling heat transfer coefficient. This may explain why the Cooper correlation produced such high heat transfer coefficients compared to the other boiling models.

There is very little variation in the solutions when using either the Nusselt or Gerstmann and Griffith condensing correlations on both test rigs. This is because the thermal resistance due to conduction in the plate removed any sensitivity of the solution to using different condensation or boiling heat transfer coefficients. For all boiling heat transfer coefficients, the temperature difference between the upper plate surface and liquor saturation exceeded the calculated wall superheat required to initiate nucleate boiling when calculated using Eq. 4.29.

Condensing Correlation	T_{pl} (°C)	T_{pu} (°C)	T_{fs} (°C)	$\dot{q}$ (W/m^2)	h_{csn} (W/m^{2}K)	$(\lambda/\delta y)_{Plate}$ (W/m^{2}K)	$(\lambda/\delta y)_{Liquid}$ (W/m^{2}K)	h_{ulg} (W/m^{2}K)	U (W/m^{2}K)	ΔT_{ONB} (°C)
	<u>Results for the Short Test Rig</u>									
Nusselt	126.8	126.7	102.5	148	181905	755	6.13	2.62	1.83	0.5
Ger. & Grif.	126.8	126.7	102.5	148	41767	755	6.13	2.62	1.83	0.5
	<u>Results for the Tall Test Rig</u>									
Nusselt	126.8	126.8	56.9	19	358626	755	0.28	1.74	0.24	0.1
Ger. & Grif.	126.8	126.8	56.9	19	67973	755	0.28	1.74	0.24	0.1

Table 4.3: Results from test case A: pure conduction through the liquid column. The boundary conditions are steam and ullage temperatures, which have values of 126.9 °C for steam, and 45.8 °C for the ullage respectively.

Condensing Correlation	T_{pl} (°C)	T_{pu} (°C)	T_{liq} (°C)	T_{fs} (°C)	$\dot{q}$ (W/m^2)	h_{csn} (W/m^{2}K)	$(\lambda/\delta y)_{plat}$ (W/m^{2}K)	h_{pu} (W/m^{2}K)	h_{pd} (W/m^{2}K)	α_{fs} (W/m^{2}K)	U (W/m^{2}K)	ΔT_{ONB} (°C)
	<u>Results for the Short Test Rig</u>											
Nusselt	126.8	126.5	126.1	125.7	228	157666	755	520	520	2.85	2.81	0.6
Ger. & Grif.	126.8	126.5	126.1	125.7	228	37694	755	520	520	2.85	2.81	0.6
	<u>Results for the Tall Test Rig</u>											
Nusselt	126.8	126.5	126.1	125.7	228	157666	755	520	520	2.85	2.81	0.4
Ger. & Grif.	126.8	126.5	126.1	125.7	228	37694	755	520	520	2.85	2.81	0.4

Table 4.4: Results from test case B: free convection in the liquid column. The boundary conditions are steam and ullage temperatures, which have values of 126.9 °C for steam, and 45.8 °C for the ullage respectively.

Boiling Correlation	Condensing Correlation	T_{pu} (°C)	T_{pl} (°C)	$\dot{q}$ (W/m^2)	α_{csn} (W/m^{2}K)	$(\lambda/\delta y)_{plate}$ (W/m^{2}K)	α_{boil} (W/m^{2}K)	U (W/m^{2}K)	ΔT_{ONB} (°C)
Results for the Short Test Rig									
Forster and Zuber	Nusselt	125.0	61.0	48364	26446	755	3637	611	8.7
	Ger. & Grif.	122.4	60.7	46583	10559	755	3563	588	8.5
Mostinskii	Nusselt	125.0	60.0	49095	26315	755	3994	620	8.7
	Ger. and Gr.	122.4	59.8	47224	10524	755	3887	596	8.5
Bier et al.	Nusselt	124.9	56.4	51670	25872	755	5904	653	8.9
	Ger. and Gr.	122.1	56.3	49651	10399	755	5742	627	8.8
Cooper	Nusselt	124.5	48.1	57708	24939	755	132000	729	9.4
	Ger. and Gr.	121.4	48.1	55336	10133	755	128340	699	9.3
Rohsenow	Nusselt	124.8	55.7	52225	25780	755	6538	660	9.0
	Ger. and Gr.	122.0	55.5	50181	10372	755	6366	634	8.8
Gorenflo and Kenning	Nusselt	125.1	64.4	45838	26922	755	2733	579	8.4
	Ger. and Gr.	122.7	64.3	44106	10697	755	2650	557	8.3
Results for the Tall Test Rig									
Forster and Zuber	Nusselt	125.7	79.2	35084	29425	755	3979	621	4.5
	Ger. and Gr.	123.9	79.0	33853	11396	755	3905	599	4.4
Mostinskii	Nusselt	125.7	79.6	34775	29512	755	3763	616	4.4
	Ger. and Gr.	123.9	79.5	33525	11423	755	3668	594	4.4
Bier et al.	Nusselt	125.6	78.1	35870	29209	755	4634	635	4.5
	Ger. and Gr.	123.8	78.0	34561	11340	755	4515	612	4.4
Cooper	Nusselt	125.4	70.7	41284	27875	755	130070	731	4.8
	Ger. and Gr.	123.2	70.7	39675	10972	755	126660	702	4.7
Rohsenow	Nusselt	125.5	75.7	37638	28745	755	7077	666	4.6
	Ger. and Gr.	123.6	75.6	36236	11212	755	6900	642	4.5
Gorenflo and Kenning	Nusselt	125.8	82.3	32835	30080	755	2760	581	4.3
	Ger. and Gr.	124.1	82.2	31664	11580	755	2682	561	4.2

Table 4.5: Results from test case C: nucleate boiling in the liquid column. The boundary conditions are steam and liquid saturation temperatures, which have values of 126.9 °C for steam, and 47.7 °C and 70.4 °C for liquid saturation for the short and tall test rigs respectively.

4.4.6 Thermal Resistance Results: Discussion and Summary

The thermal resistance investigation was shown to be a rapid technique in predicting the temperature and heat flux distributions inside a heat transfer system. The limitations to the thermal resistance investigation was that it is one-dimensional. Information in other dimensions was not taken into account. However the one dimensional assumption allowed the rapid computation of a solution, even with non-linear heat transfer correlations.

The investigation had shown that using different condensation and boiling coefficients did not yield a significant change in solution. This is because conduction through the base plate was the limiting thermal resistance. It effectively removed sensitivity of the system to the types of condensing and boiling correlations used.

4.5 CFD Investigation of the Unscaled Test Rigs

A limitation of the thermal resistance investigation was that it did not provide information regarding the mass and momentum transfer inside the liquid columns, such as velocities and pressures. Instead, assumptions had to be made, such as the number of convection cells occurring within the liquid column (in the free convection cases), or the position of boiling inside the system (in the nucleate boiling cases). Furthermore, the thermal resistance investigation was only one-dimensional; hence, further information was required of the heat transfer and circulations inside the test rigs.

CFD simulations were performed of the two test rigs and their results compared to the results from the thermal resistance investigation. For the short test rig, simulations for 2D axisymmetric and full 3D geometries were performed, in order to ascertain if axisymmetric conditions were a viable alternative to a full 3D simulation. Furthermore, a full 3D simulation was performed on the tall test rig. The commercial code Ansys CFX v14.0 was used to perform the CFD simulationsin this chapter.

Upon start-up, the thermal behaviour of the liquor in the test rigs is dominated by pure conduction for a finite time, until a critical Rayleigh number is achieved wherein free convection dominates until phase change takes place. The primary time of interest for the CFD cases is when phase change occurs in the bulk liquor. During this time a pseudo steady state condition exists, where flow features repeat periodically.

4.5.1 Governing Equations

In a later section of this chapter it is shown that the momentum and heat transfer inside the system was turbulent, based on calculations of the Rayleigh number. Due to this reasoning, provisions were made for the modelling of turbulence inside the system by use of the eddy viscosity hypothesis.

The CFD code Ansys CFX solves a set of conservation equations for each fluid phase. Single phase flow in the simulations was considered. Multiphase boiling flow was not simulated. However a mathematical indicator was developed to show where boiling may take place in the system. The conservation equations that were solved were the Unsteady Reynolds Averaged Navier Stokes (URANS) equations. In addition to the momentum equations, turbulence transport equations were solved for in order to predict turbulent viscosity within the framework of the eddy viscosity hypothesis. The single phase continuity equation is shown in Eq. 4.30.

$$\frac{\partial \rho}{\partial t} + \frac{\partial}{\partial x_j}\left(\rho U_j\right) = 0 \tag{4.30}$$

The single phase unsteady momentum equation for eddy viscosity based turbulence models is described by Eq. 4.31.

$$\frac{\partial \rho u_i}{\partial t} + \frac{\partial}{\partial x_j}\left(\rho u_i u_j\right) = -\frac{\partial P'}{\partial x_i} + \frac{\partial}{\partial x_j}\left[\mu_{eff}\left(\frac{\partial u_i}{\partial x_j} + \frac{\partial u_j}{\partial x_i}\right)\right] + S_M \tag{4.31}$$

The modified pressure term P' contains contributions from the static pressure P and normal turbulent stresses, as defined in Eq. 4.32. The second term on the left hand side is the contribution from turbulent kinetic energy, k. The third term accounts for dilatational stresses, and is only significant for compressible flow

$$P' = P + \frac{2}{3}\rho k + \frac{2}{3}\mu_{eff}\frac{\partial u_k}{\partial x_k} \tag{4.32}$$

The effective viscosity μ_{eff} contains contributions from the molecular viscosity μ and the turbulent viscosity μ_t, as defined in Eq. 4.33.

$$\mu_{eff} = \mu + \mu_t \tag{4.33}$$

The turbulent viscosity is sometimes known as the eddy viscosity, and is computed by the classes of RANS turbulence models known as eddy viscosity models (EVMs). These models employ the eddy viscosity hypothesis, which assumes that turbulent mixing can be modelled in a manner similar to molecular mixing. In such models, the eddy viscosity is given by

$$\mu_t = C_\mu \rho \frac{k^2}{\varepsilon} \tag{4.32}$$

where k is the turbulent kinetic energy, ε is the rate of turbulence energy dissipation, and C_μ is an empirical constant, usually assumed to be equal to 0.09. The class of EVMs referred to as $k - \varepsilon$ models solve modelled transport equations for k and ε. The class of EVMs referred to as $k - \omega$ models solve modelled transport equations for k and the turbulence frequency $\omega = C_\mu^{-1}\,\varepsilon/k$, in which case the eddy viscosity is expressed as in Eq. 4.34.

$$\mu_t = \rho \frac{k}{\omega} \tag{4.33}$$

Wilcox (2006) provided further details on the most common turbulence models and their transport equations.

The $k - \varepsilon$ class of turbulence models are distinguished by their requirement of supplementary logarithmic wall functions at the walls. This is because the ε transport equation is singular, so cannot be integrated all the way up to the wall. On the other hand, the $k - \omega$ class of turbulence models can be integrated all the way up to the wall. Hence they are reputed to provide more reliable predictions of wall boundary layers. On the other hand, they prove to be unphysically sensitive to free stream turbulence far from walls.

A class of hybrid models has been developed, which blend the $k - \varepsilon$ and $k - \omega$ models in such a way to combine the advantages of each (Menter, 1994). The baseline (BSL) $k - \omega$ model blends the ω and ε transport equations in a way which is equivalent to the Wilcox $k - \omega$ model near walls, and equivalent to the standard $k - \varepsilon$ model far from walls.

The Shear Stress Transport (SST) $k - \omega$ model is based on the BSL $k - \omega$ model, with additional terms included to account for near wall shear stress transport. The model generally provides good predictions for flows, which involve strong streamline curvature, adverse pressure gradients, wall bounded flows and flow separations. For completeness, the governing equations for k and ω are provided below.

$$\frac{\partial(\rho k)}{\partial t} + \frac{\partial}{\partial x_j}\left(\rho u_j k\right) = \frac{\partial}{\partial x_j}\left[\left(\mu + \frac{\mu_t}{\sigma_{k3}}\right)\frac{\partial k}{\partial x_j}\right] + P_{ks} + P_{kb} - \beta' \rho k \omega \tag{4.35}$$

$$\frac{\partial(\rho \omega)}{\partial t} + \frac{\partial}{\partial x_j}\left(\rho u_j \omega\right) = \frac{\partial}{\partial x_j}\left[\left(\mu + \frac{\mu_t}{\sigma_{\omega 3}}\right)\frac{\partial \omega}{\partial x_j}\right]$$

$$+(1 - F_1) 2\rho \frac{1}{\sigma_{\omega 2}\omega} \frac{\partial k}{\partial x_j} \frac{\partial \omega}{\partial x_j} + \alpha_3 \frac{\omega}{k} P_{ks} + +P_{\omega b} - \beta_3 \rho \omega^2 \tag{4.36}$$

P_{ks} and P_{kb} denote shear production and buoyancy production terms. F_1 is the blending factor between the ω and ε transport equations, and is a complex function of wall distance and turbulence quantities. The $k - \omega$ SST model has been used extensively in modelling flows in industry and academia (Menter et al., 2003). It is a well-validated turbulence model, having been used with success in a variety of diverse applications. Consequently, the CFD simulations presented here were based on single phase, transient turbulent flow using the k - ω SST turbulence model (Menter, 1994).

The thermal energy equation for solids, that is for conjugate problems is shown in Eq. 4.37. The velocity term refers to solid motion if it is modelled. In the absence of solid motion, and for constant material properties, Eq. 4.37 reduces to the ubiquitous parabolic Laplace heat equation.

$$\frac{\partial(\rho h)}{\partial t} + \nabla \cdot (\rho \boldsymbol{u} h) = \nabla \cdot (\lambda \nabla T) + \boldsymbol{S}_E \tag{4.37}$$

The single phase thermal energy equation for fluids is almost identical to that of solids. For fluids, using eddy viscosity based RANS models, the relation is shown in Eq. 4.38. In this case, the velocity term refers to fluid motion. Turbulent mixing is modelled using the eddy diffusion hypothesis (EDH), which assumes that turbulent heat fluxes are proportional to mean enthalpy gradients, with a constant of proportionality equal to Γ_t, known as the eddy diffusivity.

$$\frac{\partial(\rho h)}{\partial t} + \nabla \cdot (\rho \boldsymbol{u} h) = \nabla \cdot (\lambda \nabla T + \Gamma_{\mathrm{t}} \nabla H) + \tau : \nabla \boldsymbol{u} + \boldsymbol{S}_E \tag{4.38}$$

Γ_{t} is assumed to be proportional to the eddy viscosity, as indicated in Eq. 4.39. σ_t is an empirical constant known as the turbulent Prandtl number.

$$\Gamma_{\mathrm{t}} = \frac{\mu_t}{\sigma_t} \tag{4.39}$$

The source term for fluids includes the fluid shear stress terms and the velocity gradients. The term $\tau : \nabla u$ represents viscous dissipation and is always positive.

4.5.2 Assumptions in the CFD Models

A number of assumptions were made in the CFD modelling. It was assumed the liquid in the test rigs was water, and that the flow was turbulent. Buoyancy turbulent production and dissipation source terms were treated within the turbulence model. Condensation heat transfer underneath the base plate was modelled by a condensation heat transfer coefficient on the bottom surface of the base plate, coupled with an outside temperature equal to the steam saturation temperature. Similarly the wall thickness of the glass walls was not taken into consideration in the physical flow domains. To account for these, they are absorbed in the prescription of the wall boundary conditions in terms of an overall external heat transfer coefficient. No fouling or contact resistance was assumed on any of the heat transfer surfaces.

The simulations were single phase and did not consider two phase boiling flows. Furthermore radiation heat transfer was not considered to have an effect contributing to the system. The flows inside the test rig were assumed to be turbulent in nature. This was determined by computing the Rayleigh number for the flow, which was defined by Eq. 4.13. The temperature difference in the Rayleigh number was taken to be the overall driving temperature for the system, which was the difference between steam and ullage temperatures. This had the effect of inflating the calculated Rayleigh number, but also represented its upper limit. The thermophysical properties were computed on the saturation line and at a mean temperature between these two temperatures. Traditionally the properties are evaluated at a mean film temperature, however this is not known. The length scale was taken to be the height of the liquid column for each respective test rig. Table 4.6 lists the properties which were used to compute the Rayleigh number for the short and tall test rigs.

Property	**Value**
Steam temperature T_{stm} [°C]	126.9
Ullage temperature T_{ulg} [°C]	45.8
Driving temperature ΔT [°C]	81.1
Mean temperature T_{mean} [°C]	86.35
Kinematic viscosity ν [m^2/s]	3.39 x 10^{-7}
Thermal diffusivity α [m^2 /s]	1.65 x 10^{-7}
Thermal expansivity β [K^{-1}]	6.82 x 10^{-4}
Length scale for the short test rig L [m]	0.1
Length scale for tall test rig L [m]	2.215
Acceleration due to gravity g [m/s^2]	9.81
Rayleigh number for the short test rig	9.71 x 10^9
Rayleigh number for the tall test rig	1.05 x 10^{14}

Table 4.6: Rayleigh number properties for the short and tall test rigs.

The short test rig was computed to have a Rayleigh number of 9.71x10^9 and the tall test rig is computed to have a Rayleigh number of 1.05x10^{14}. Bergman et al. (2011) mention that values less than 10^8 are laminar, and more than 10^8 are turbulent. Therefore based on the Rayleigh number computations the flows inside the short and tall test rigs were deemed both turbulent in nature. The short test rig Rayleigh number was close to the transition between laminar and turbulent regimes. The system was assumed to be turbulent for the task of performing the simulations since using a turbulence model in CFD can aid solution convergence.

4.5.3 Boundary Conditions

Three test cases were simulated, which were 2D axisymmetric and 3D geometries for the short test rig, and a 3D geometry for the tall test rig. The 2D axisymmetric and 3D cases for the short test rig had identical boundary conditions, barring some minor differences to account for the difference in geometry. The 3D case for the tall test rig also shared identical boundary conditions as the short test rig, with additional conditions to account for the heating jackets as show in Figure 4.1.

In all three cases the free surface was modelled as an opening boundary condition. An opening condition allowed fluid to leave or re-enter, or to do a combination of both at different positions on the boundary where it was applied. This does not imply a multiphase simulation was performed, where the free surface was explicitly tracked. Rather, fluid was allowed to leave or re-enter the domain based on the velocity components at that surface.

As part of the prescription of the opening boundary condition, the opening pressure and temperature was defined. The opening pressure was set to the ambient pressure outside of the opening. This was the ullage pressure. The opening temperature was set to the temperature at which liquid was allowed to return back inside the domain. This was set to the ullage temperature corresponding to the ullage pressure. Hence the opening pressure and temperatures were set to 0.1 bar and 45.8 °C respectively. It must be noted setting the ullage temperature to 45.8 °C had the effect of forcing the liquid to re-enter the domain at a temperature not necessarily at the same as the temperature it left with.

In the short and tall test rigs, ambient heat loss from the non-jacketed side walls and from the non-insulated sides of the base plate were taken into consideration. At the vertical sides of the baseplate, the correlation recommended by Churchill and Chu (1975) as shown in equation Eq. 4.34 was used. This is a well-known correlation which is valid for heat transfer from vertical surfaces. This was applied with an ambient outside temperature taken as 26.9 °C. The thermophysical properties were evaluated at the ambient air temperature.

$$\mathrm{Nu} = \frac{h_{cvn}L}{\lambda_l} = \left(0.825 + \frac{0.387\mathrm{Ra}^{1/6}}{\left[1+(0.492/\mathrm{Pr})^{9/16}\right]^{8/27}}\right) \tag{4.34}$$

At the non-jacketed walls of the liquid column an average heat transfer coefficient was applied. This took into consideration the wall glass thickness, δx as shown in equation Eq. 4.35.

$$h_{wall} = \frac{1}{\left(\frac{\delta x}{\lambda}\right)_{glass} + \frac{1}{h_{cvn}}} \tag{4.35}$$

Although the test rigs were cylindrical, the use of a planar relation for the conduction resistance was not considered detrimental. In later simulations similar conditions were treated as radial systems.

The tall test rig had an internal draught tube completely submerged within the liquid. These walls were treated as adiabatic no slip walls. Furthermore, the tall test rig had three heating jackets. Physically these jackets are water jackets. Unfortunately further information was not supplied by the National Nuclear Laboratory regarding their operating conditions. However it was advised the temperatures inside the jackets were approximately 50, 60 and 70 °C for the top, middle and lower jackets respectively. Hence, in the CFD modelling, the temperatures of the liquid in the jackets were set to fixed temperatures of 50, 60 and 70 °C for the top, middle and lower jackets respectively.

In both test rigs, condensation underneath the base plate was treated with a heat transfer coefficient applied to the lower plate surface with an outside temperature. The correlation applied was the Nusselt (1916) heat transfer coefficient described by Eq. 4.7. The outside temperature was the steam temperature which was 126.9 °C. The justification was that the results from the thermal resistance investigation showed the problem was insensitive to the type of condensing correlation that is used.

4.5.4 Boiling Indicator

An implicit method of detecting phase change was used by defining a new variable called T^* as defined by equation 4.36. Using this definition, if T^* is greater than zero, then boiling may occur, and if T^* is less than zero, boiling will not occur. The saturation temperature was not provided directly by the CFD solver. This was defined by using the Antoine's vapour pressure equation as shown in equation (4.17), and it was inserted into Eq. 4.36 as a user defined expression.

$$T^* = \frac{T_{local} - T_{sat}}{T_{sat}} \tag{4.36}$$

4.5.5 Convergence Strategy

During experimental operation, the test rigs operated at a pseudo steady state condition. The transient averaged temperatures and velocities fluctuated around mean values. In order to replicate this within the framework of the CFD investigation, the simulations were initially advanced in time to overcome the initial transient effects. This was achieved by initially using a steady state solver with large false time steps. Proceeding this a transient simulation using smaller transient time steps were used to for the final reportable simulation results.

The convergence strategy used was to first solve a pure conduction simulation (no flow, no turbulence modelling) with large false time steps employed for the fluid and solid domains shown in Eq. 4.37. The thermal diffusivity term in Eq. 4.37 was calculated independently for the solid (baseplate) and fluid (liquor) domains.

$$\delta t \approx \frac{L^2}{k} \tag{4.37}$$

The result for the pure conduction case was then used as the initial state for a free convection steady state simulation using first order upwind schemes for the advection numerics. The first order upwind scheme induces additional numerical dissipation, so increases the likelihood of achieving a steady solution. This in turn was used as the initial state for a more accurate simulation using high resolution schemes for the advection numerics.

The false time step for the steady state simulations in the fluid domain was determined by using the relationship shown in Eq. 4.38 This time step was chosen to resolve the frequency of internal gravity waves in the buoyant flows. Time steps larger than this were avoided, as they lead to lack of convergence (Ansys Inc, 2010a).

$$\delta t \approx \sqrt{\frac{D}{\beta g \Delta T}} \tag{4.38}$$

All of the measures up to this point were to ensure a suitable initial guess for the final transient simulations which were computed for 30 s for the short and tall test rigs. A simulation time of 30 s was arbitrarily chosen to ascertain if periodic flow features occured within this window.

In the transient simulations, high resolution numerics for the advection scheme and a second order backward Euler method for the transient scheme were used. An adaptive time stepping approach was taken which allowed the solver to select a suitable time step for convergence. In this approach, the solver computed a suitable time step within a user specified minimum and maximum range of time steps and minimum and maximum number of coefficient loops per time step. The solver attempts to increase or decrease the time steps, based on achieving successful convergence of each equation within the specified range of coefficient loops.

For the adaptive time stepping configuration, the minimum and maximum time steps chosen were 0.01 and 29 s respectively. The minimum and maximum number of coefficient loops were 1 and 6 respectively. Lastly the time step decrease and increase factors were 0.75 and 1.1 respectively. Convergence of each simulation was ensured by letting the root mean square and maximum non-dimensionalised residuals of the momentum, mass, energy and turbulence equations fall to at least 10^{-4}. Additionally to ensure conservation of the solved equations domain imbalances were monitored at the end of every simulation to ensure that they were less than 0.01 % of the maximum imbalance over the entire domain. Lastly, the values of temperature and velocity at selected monitor points inside the domain were recorded during the simulation to monitor for pseudo steady state periodic flow features.

4.5.6 Computer Hardware Used for the Simulations

The simulations were performed on the high performance computing facilities at the University of Leeds facility ARC2 (Advanced Research Computing 2). The simulations were performed on 3 nodes of 16 CPUs (48 CPUs) with 32GB of error correcting code memory per node available to the CFD solver. The transient free convection simulations took around 10 wall clock hours to complete.

4.5.7 Physical Flow Domain

The physical flow domains for the two test rigs comprised a solid base plate, and a liquid column above the baseplate. Heat transfer through the base plate was treated as a conjugate heat transfer problem. The flow domains did not include the head space above the liquid free surface. Hence the test rigs were modelled as single phase. Furthermore the physical flow domains neglected the thickness of the glass walls surrounding the liquid column.

Two flow domains were tested for the short test rig. These were a 2D axisymmetric domain, and a full 3D domain. The purpose of this was to ascertain if buoyancy driven flows, such as those found in the unscaled test rigs and in Evaporator C, could be modelled by using symmetric conditions. If so, this would reduce model complexity and reduce simulation compute times. Figure 4.4 (left) shows the 2D axisymmetric domain superimposed on the 3D domain which shows their relative differences. Figure 4.4 (centre) and (right) are the 2D axisymmetric and 3D flow domains respectively.

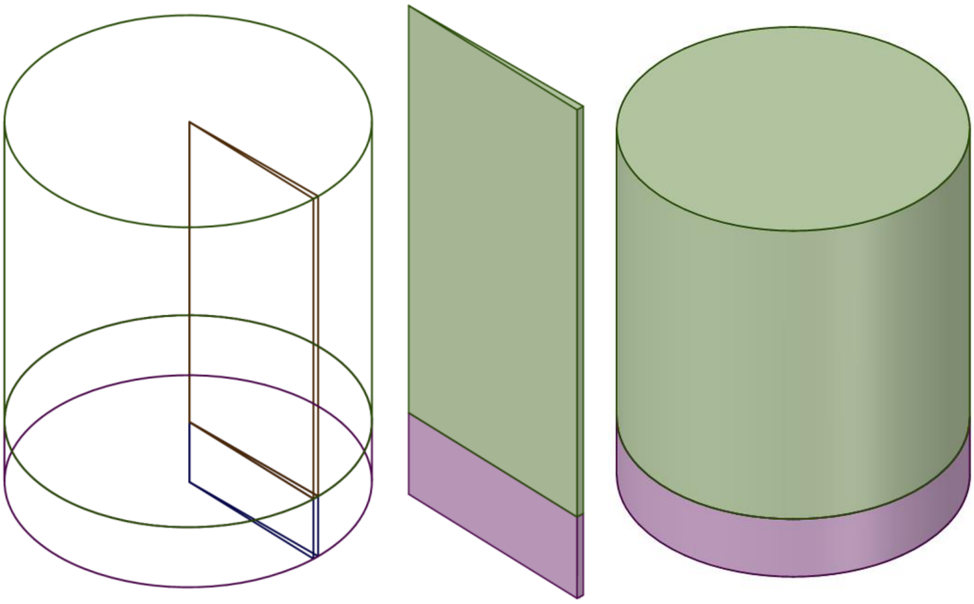

Figure 4.4: (Left) 2D axisymmetric and 3D physical flow domains, (centre) 2D axisymmetric flow domain, (right) 3D flow domain.

The 2D axisymmetric geometry was rotated 2 degrees about the central y axis. To prevent poorly shaped elements from being formed at the axis, and to facilitate hexahedral cells inside the domain, the geometry tapered to a finite radius, rather than tapering directly to the axis. This is known as nipping the tip as shown in Figure 4.5. To the authors knowledge, this procedure is not formally documented, but is recommended within circles of the CFD community. The radius of the nip tip r_{np} should be sufficiently small that such that removal material will not cause detriment to the results. In the 2D axisymmetric geometry, this value was taken as 1e-6 m. The base plate radius was 5 cm. So the nip tip radius represented less than 1% of the base plate radius. Nipping the tip had the advantage of producing high quality hexahedral elements close to the axis. This is desirable to prevent spurious results in those areas due to poorly formed elements.

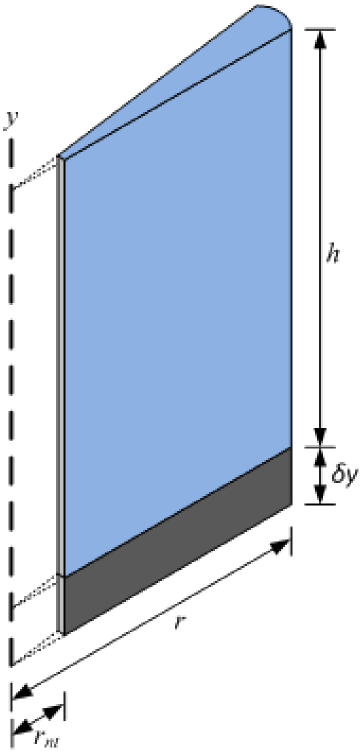

Figure 4.5: The 2D axismymmetric geometry is tip is nipped in order to facilitate hexahedral cells during the meshing procedure.

For the tall test rig, only a 3D physical flow domain was used. This is shown by Figure 3.1. The image on the left in Figure 3.1 shows the wireframe of the geometry, exposing the internal draught tube. The image in the centre shows the bottom portion of the tall test rig, and the image on the right shows the top portion of the tall test rig.

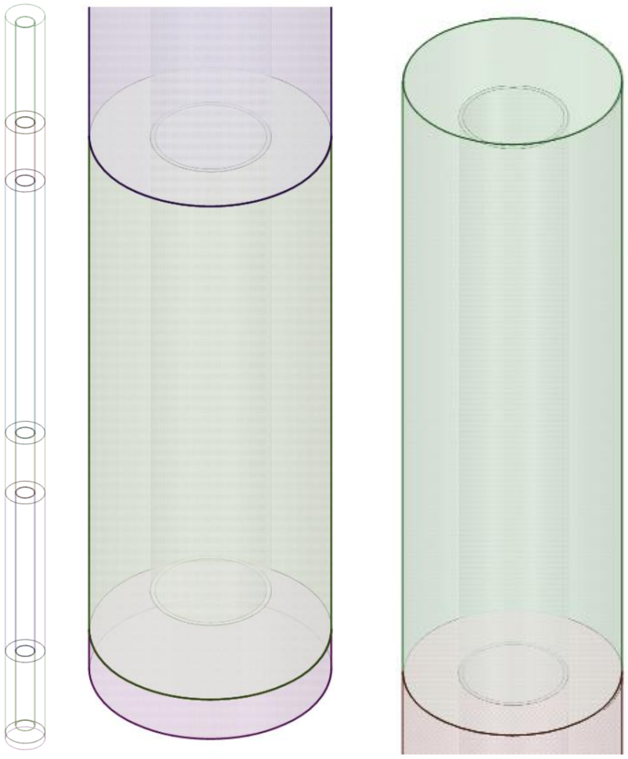

Figure 4.6: The 3D physical flow domain for the tall test rig. (Left) wireframe view showing the internal draught tube, (centre) bottom section of the test rig, (right) top section of the test rig.

4.5.8 Mesh Sensitivity Study

A mesh sensitivity study was performed for all three physical flow domains. These were the 2D axisymmetric case and 3D case for the short test rig, and the 3D case for the tall test rig. The meshes were of the structured type, comprising hexahedral cells. Three meshes were generated for each simulation case, and the formal grid convergence index (GCI) procedure developed by Celik et al. (2008) was used to perform the mesh sensitivity studies. The meshes generated adhered to the stringent quality criteria set out in CHAPTER 3. Structured meshes and their benefits, along with the GCI mesh sensitivity study procedure were also discussed in CHAPTER 3.

For all three studies, 2D axisymmetric and 3D for the short test rig, and 3D for the tall test rig two variables were chosen as the parameters to ensure a mesh independent solution. These were the area averaged transient average heat transfer coefficient and Y^+ values at the upper plate surface. The mesh density at the remaining walls had the same density as that of the wall at the upper plate surface. Therefore using variable values at the upper plate surface to gauge global mesh performance was prudent without exhausting effort.

Three meshes were tested in each mesh sensitivity study. The mesh statistics for the three meshes used in the 2D axisymmetric mesh independence study are listed in Table 4.7.

The wall clock time taken to produce a simulation time of 30 s for each mesh is also included in Table 4.7. As expected, the computational time increased with mesh density.

	Mesh Statistics				**Mesh Size**		
Mesh	**Max. Face Angle [°]**	**Min. Face Angle [°]**	**Max. Edge Length Ratio**	**Max. Cell Vol. Ratio**	**No. of Nodes**	**No. of Elements**	**Compute time [min]**
1	91.1	88.9	180.9	1.44	25740	12551	121.8
2	95.6	84.4	304.6	1.44	39480	19344	150.2
3	93.3	85.6	480.7	1.42	61115	29800	187.3

Table 4.7: Mesh statistics for the three meshes used in the 2D axisymmetric mesh independence study on the short test rig.

The generated parameters for the mesh sensitivity study on the 2D axisymmetric case and the final grid convergence index are shown in Table 4.8. For the heat transfer coefficient on the upper plate surface the grid convergence index (GCI) is 0.4% between meshes 3 and 2, compared to 2.6% between meshes 2 and 1. The extrapolated errors are comparatively very large. This is because the extrapolated values of the heat transfer coefficient are orders of magnitude less than the true values, which is an artefact of using the Richardson extrapolation method. This large variation is due to the Richardson extrapolation step, and illustrates why it should not be used in isolation to determine mesh independence. The GCI for the area averaged Y^+ are 20.9% between meshes 2 and 1, and 16.6% between meshes 3 and 2. At face value, these seem very high. However since all three Y^+ values fall within the required limits (less than 1), the low near wall Re number formulation near wall is utilised, which was the aim of the ultra fine mesh refinement at the walls in order to take full advantage of the $k - \omega$ SST turbulence formulation. Based on this information the mesh that is used for the CFD analysis is mesh 2.

The blocking strategy and final mesh used for the 2D axisymmetric simulations are shown in Figure 4.7. The hexahedral cells at the radial axis of the geometry (and the remaining cells) met all the quality requirements which were outlined in CHAPTER 4. This meant the nip tipping of the geometry worked as intended, and removed the possible generation of poorly shaped elements in that region. Out of the three meshes, which were tested, mesh 2 was chosen.

	ϕ = Area averaged heat transfer coefficient on the upper plate surface	**ϕ = Area averaged Y^+ on the upper plate surface**
$\boldsymbol{\phi_1}$	770 [W/m^{2}K]	0.27
$\boldsymbol{\phi_2}$	848 [W/m^{2}K]	0.06
$\boldsymbol{\phi_3}$	861 [W/m^{2}K]	0.02
$\boldsymbol{r_{21}}$	1.16	1.16
$\boldsymbol{r_{32}}$	1.16	1.16
$\boldsymbol{P}$	12.15	11.99
$\boldsymbol{\phi_{ext,21}}$	-94 [W/m^{2}K]	0.25
$\boldsymbol{\phi_{ext,32}}$	-16 [W/m^{2}K]	0.04
$\boldsymbol{e_{apx,21}}$	10.1%	77.6%
$\boldsymbol{e_{apx,32}}$	1.6%	61.4%
$\boldsymbol{e_{ext,21}}$	919.4%	6.0%
$\boldsymbol{e_{ext,32}}$	5309.2%	33.9%
$\boldsymbol{GCI_{21}}$	2.6%	20.9%
$\boldsymbol{GCI_{32}}$	0.4%	16.6%

Table 4.8: Mesh statistics for the three meshes used in the 2D axisymmetric short test rig mesh independence study.

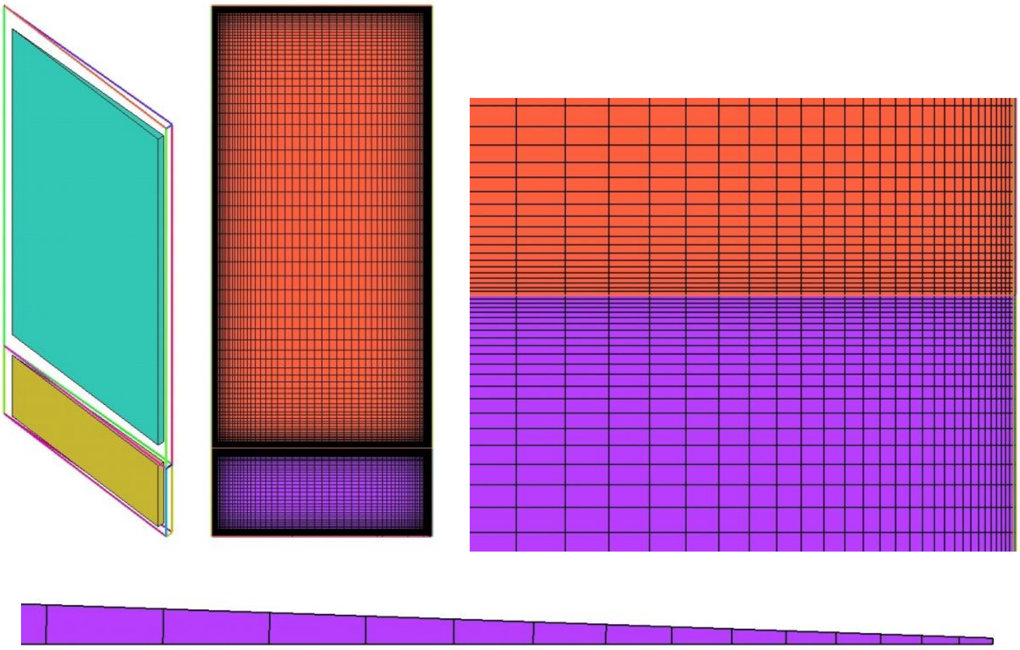

Figure 4.7: (Starting top left and going clockwise) hexahedral blocking strategy; planar view of the global mesh resolution; zoomed in view of the near wall inflation at the interface of the water column (orange) and baseplate (purple); and zoomed in plan view of the hexahedral cells accommodating the nipped tip.

The mesh statistics for the 3D geometry for the simulations on the short test rig are listed in Table 4.9. All of the mesh statistics met the requirements set out on CHAPTER 3.

	Mesh Statistics				Mesh Size		
Mesh	**Max. Face Angle [°]**	**Min. Face Angle [°]**	**Max. Edge Length Ratio**	**Max. Cell Vol. Ratio**	**No. of Nodes**	**No. of Elements**	**Compute time [min]**
1	128.5	63.4	98.4	1.39	185520	181154	274.7
2	131.2	54.8	112.1	1.41	416014	406224	824.7
3	102.0	83.2	411.4	1.40	942299	920124	1098.7

Table 4.9: Mesh statistics for the three meshes used in the 3D short test rig mesh independence study.

Furthermore, the results from the mesh independence study on the three meshes of the 3D short test rig investigation are listed in Table 4.10. The results followed a similar pattern to the independence study for the 2D axisymmetric short test rig case. The extrapolated error for the heat transfer coefficients were very large, due to the very small-extrapolated values based on the Richardson extrapolation. However the grid convergence index error falls to within acceptable limits. Based on this information mesh 2 was used.

	ϕ = Area averaged heat transfer coefficient on the upper plate surface	**ϕ = Area averaged Y^+ on the upper plate surface**
ϕ_1	910 [W/m^{2}K]	1.40
ϕ_2	1035 [W/m^{2}K]	0.41
ϕ_3	1050 [W/m^{2}K]	0.10
r_{21}	1.309	1.309
r_{32}	1.313	1.313
P	8.04	4.36
$\phi_{ext,21}$	-141 [W/m^{2}K]	1.43
$\phi_{ext,32}$	-17 [W/m^{2}K]	0.45
$e_{apx,21}$	13.8%	70.6%
$e_{apx,32}$	1.4%	75.7%
$e_{ext,21}$	743.5%	2.1%
$e_{ext,32}$	6304.1%	8.2%
GCI_{21}	2.2%	39.5%
GCI_{32}	0.2%	41.5%

Table 4.10: Mesh statistics for the three meshes used in the 3D short test rig mesh independence study.

The blocking strategy and final mesh used for the 3D short test are shown in Figure 4.8. The blocking strategy is such that the final mesh was in the format of an O-Grid in order to capture the curvature of the edges of the test rig. An O-Grid is one type of topology for the structured meshing approach, which was explained briefly in CHAPTER 3.

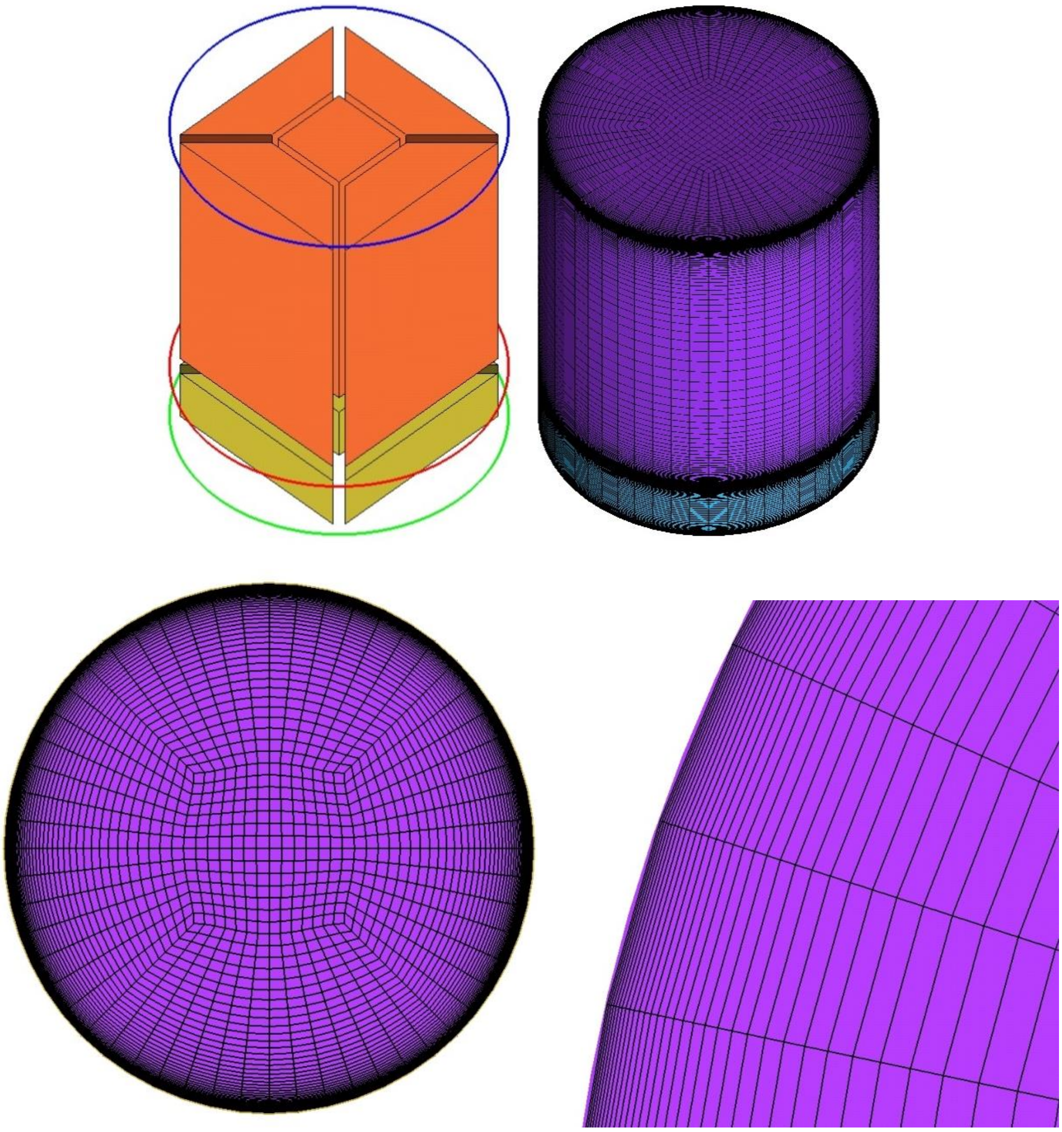

Figure 4.8: (Starting top left and going clockwise) hexahedral O-Grid blocking strategy; isometric view of the global mesh resolution; zoomed in view of the near wall inflation at the walls of the test rig; and plan view of the hexahedral cells in an O-Grid configuration.

The mesh statistics of the final case, the 3D tall test rig simulations are listed in Table 4.11. The simulations for the tall test rig took noticeably longer to compute since they require more cells in the physical flow domain.

The results from the last mesh independence study are listed in Table 4.12. The grid convergence indices for the heat transfer coefficient increase between meshes 2 and 3, compared to meshes 1 and 2, suggesting slightly greater error is associated with mesh 3. Mesh 1 failed to meet the required Y^+ of less than 1, where meshes 2 and 3 did. However the GCI errors are large for the Y^+ variable. This is due to the large spread in the data, and that only three meshes were tested. Therefore the data sample was limited. Despite this, a 23% GCI relative error for mesh 2 is acceptable as the Y^+ values still fall within the requirements, which was required to be less than 1. Based on this information mesh 2 was used for the CFD simulations on the tall test rig.

	Mesh Statistics				**Mesh Size**		
Mesh	**Max. Face Angle [°]**	**Min. Face Angle [°]**	**Max. Edge Length Ratio**	**Max. Cell Vol. Ratio**	**No. of Nodes**	**No. of Elements**	**Compute time [min]**
1	134.6	56.5	65.4	1.56	602877	581664	1350
2	169.8	10.2	2308.5	1.56	1183596	1158528	4200
3	171.5	42.0	2351.0	1.56	1712804	1676528	8100

Table 4.11: Mesh statistics for the three meshes used in the 3D tall test rig mesh independence study.

	ϕ = Area averaged heat transfer coefficient on the upper plate surface	**ϕ = Area averaged Y^+ on the upper plate surface**
$\boldsymbol{\phi_1}$	1071 [W/m^{2}K]	1.37
$\boldsymbol{\phi_2}$	1055 [W/m^{2}K]	0.18
$\boldsymbol{\phi_3}$	1012 [W/m^{2}K]	0.11
$\boldsymbol{r_{21}}$	1.258	1.258
$\boldsymbol{r_{32}}$	1.131	1.131
$\boldsymbol{P}$	10.21	7.61
$\boldsymbol{\phi_{ext,21}}$	17 [W/m^{2}K]	1.44
$\boldsymbol{\phi_{ext,32}}$	61 [W/m^{2}K]	0.11
$\boldsymbol{e_{apx,21}}$	1.5 [W/m^{2}K]	87.0
$\boldsymbol{e_{apx,32}}$	4.1%	38.2%
$\boldsymbol{e_{ext,21}}$	6122%	5.1%
$\boldsymbol{e_{ext,32}}$	1644%	59%
$\boldsymbol{GCI_{21}}$	0.2%	23%
$\boldsymbol{GCI_{32}}$	2.0%	31%

Table 4.12: Mesh statistics for the three meshes used in the 3D tall test rig mesh independence study.

The blocking strategy for the tall test rig required more thought and planning than for the 2D axisymmetric and 3D cases for the short test rig. This is because the tall test rig contained the draught tube, which complicates the geometry with regards to the blocking topology. The final blocking topology was an o-grid contained within an o-grid. This is better illustrated by the topology in Figure 4.9, which shows the blocking strategy in the absence of the draught tube (where the standoff appears, as denoted by c in Figure 4.1), and in the presence of the draught tube. A planar view of the mesh resolution is also detailed in Figure 4.9, again without and with the draught tube; and an isometric view of the mesh at the horizontal midpoint of the test rig is shown, along with the internal mesh layout close to the draught tube.

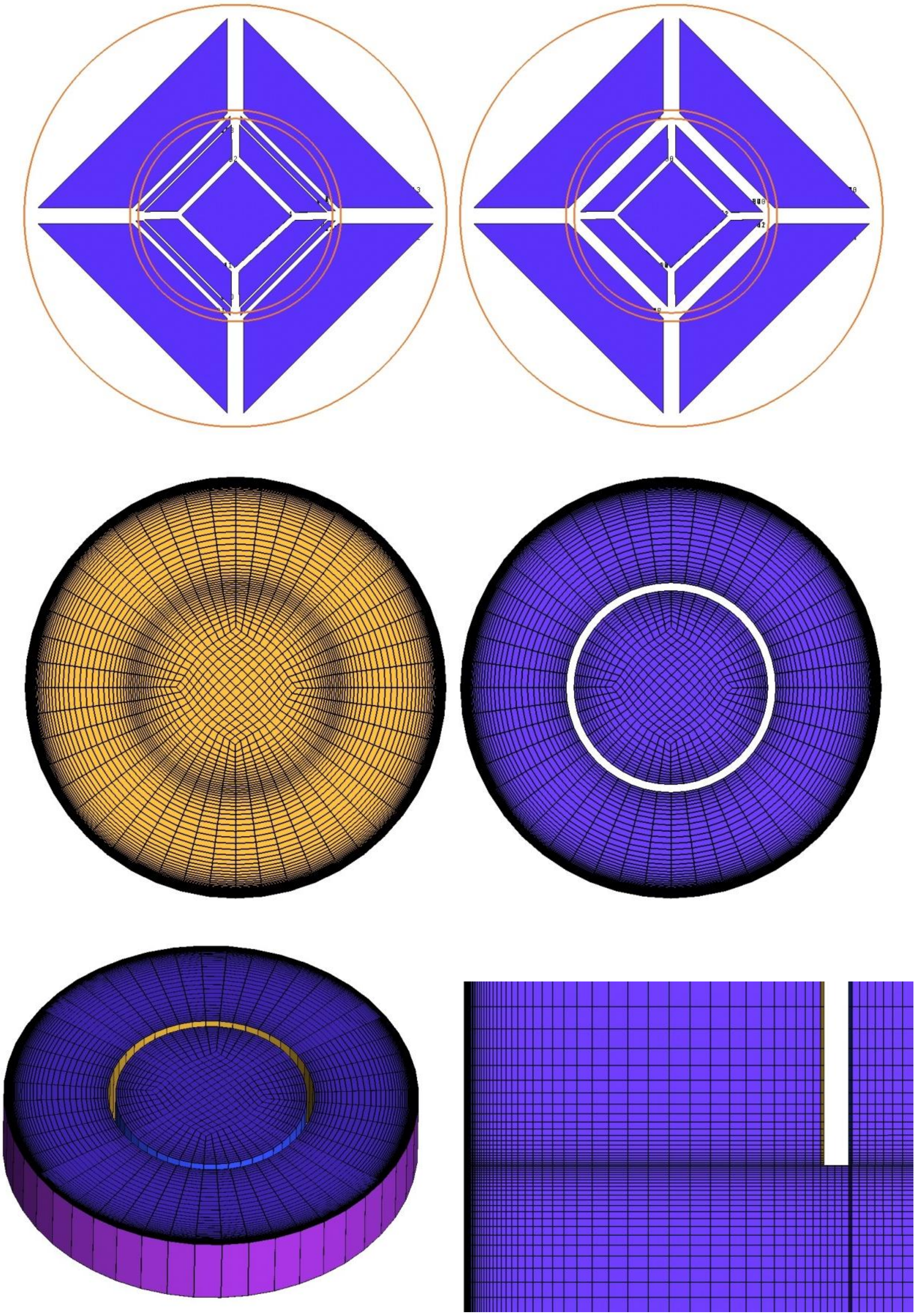

Figure 4.9: (Starting top left and going left to right) hexahedral O-Grid blocking strategy in the absence of the draught tube; O-Grid blocking strategy with the draught tube; plan view of the mesh in the absence of the draught tube; plan view of the mesh around the draught tube; one cell thick isometric illustration of the mesh around the draught tube; and planar view of the internal mesh close to the draught tube.

4.5.9 Simulation Results and Comparison to Thermal Resistances

In this section the results from the final 30 s simulation times are discussed. The simulations performed prior to this are not discussed because they were not fully converged solutions, and they existed purely to accelerate the flow fields for the conservation equations and thus provide an initial guess for the final transient runs. Furthermore only time averaged results are presented for all three cases. The steady state simulations prior to the transient simulations advanced the solution sufficiently in time. This removed any evolution of the solution with respect to time. Hence the results were pseudo steady state, where the variables were fluctuating around a mean value.

Proof of convergence is presented for the 2D axisymmetric short test rig. The 3D short test rig and the 3D tall test rig followed similar convergence behaviour. The root mean square residuals for the 2D axisymmetric case are shown in Figure 4.10, and the temperature and velocity monitor points are displayed in Figure 4.11 and Figure 4.12. The residuals are plotted in log base 10, and indicate all conservation equations to not exceed 1.0x10^{-5}. The global imbalances during the simulation compute time are less than 1% of the total fluxes into and out of the domain. The temperature plots in Figure 4.11 remain constant with respect to time indicating the steady state solution prior to the transient simulation had advanced the simulation as intended. The velocity plots in Figure 4.12 show more chaotic behaviour. This is to be expected since the top of the test rigs are modelled as an opening, allowing water to leave and re-enter the domain as required, significantly disturbing the flow patterns.

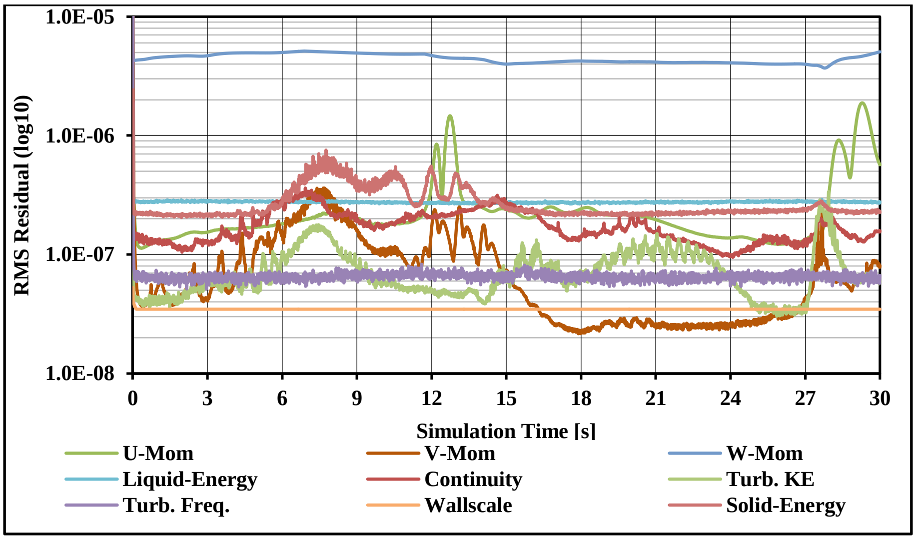

Figure 4.10: Root mean square residuals (log10) for the 2D axisymmetric case.

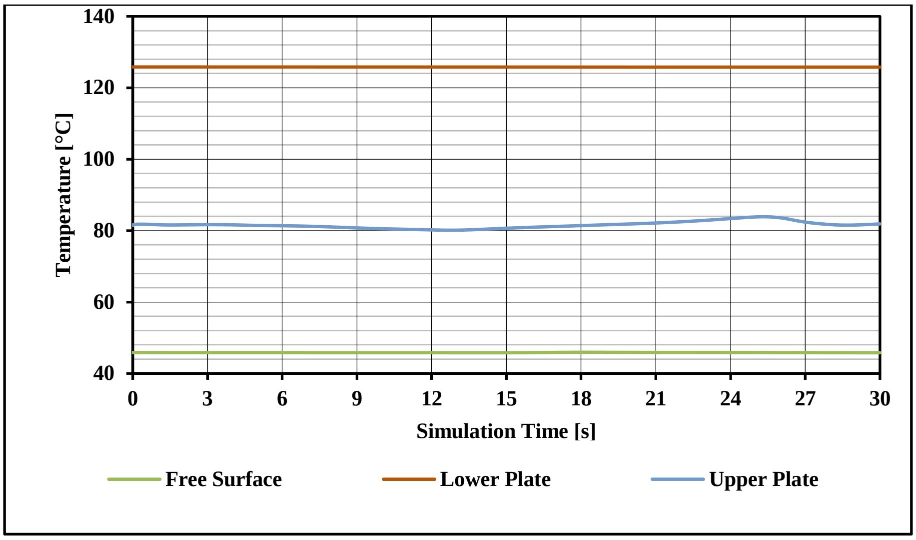

Figure 4.11: Monitor points of temperature at three pertinent locations during the simulation compute process.

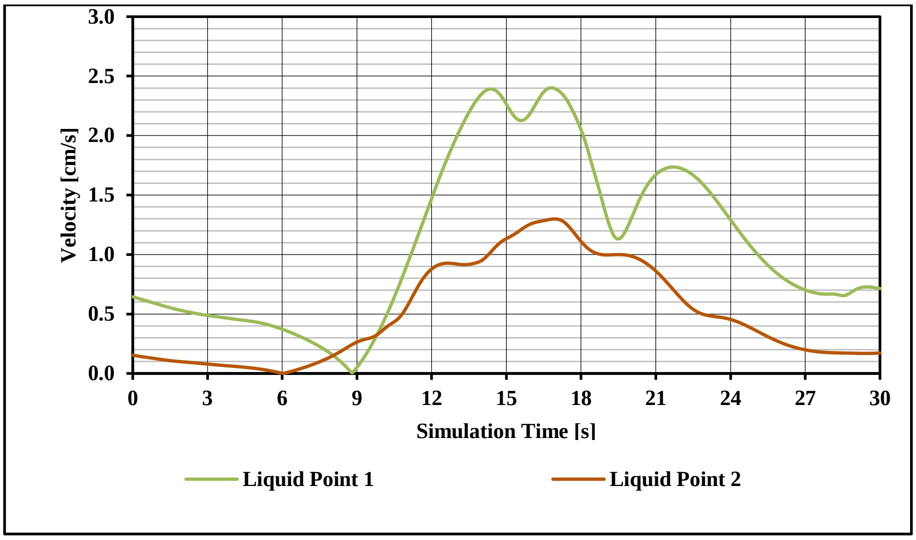

Figure 4.12: Monitor points of velocity at two pertinent locations during the simulation compute process.

Figure 4.13 illustrates four key variables in the 2D axisymmetric case, which are transient averaged over the simulation time (30 s). These variables are the temperatures, dimensionless T^* (defined in Eq. 4.36), velocity magnitudes and direction, and eddy viscosity ratios. The largest temperature variation occurs through the base plate. There is little temperature variation in the liquid, and remains close to 45°C, which is also very close to the saturation temperature of 45.8°C, which corresponds to the ullage pressure of 0.1 bar. This implies the system is well-mixed, allowing relatively colder fluid from the free surface to displace warmer currents in the water. The contours of T^* reveal values greater than 0 occur at the upper plate surface, which indicates potential regions of boiling. It is a potential and not a certainty, because nucleate wall boiling requires some degree of superheat to achieve the onset of boiling. The streamlines indicate two core counter rotating convection cells, constrained within the radial centre line (left wall) and the outer glass wall (right). There are two smaller counter rotating convection cells at the upper plate surface, which have relatively low velocities of 0.8 to 1.0 cm/s. The contours of eddy viscosity ratio are an indication of the turbulence intensity. The eddy viscosity ratio is the ratio of turbulence viscosity and dynamic molecular viscosity. As a guide, values greater than 10 transitions into turbulent flows, and lower than 10 tending to 0 indicates laminar flow. The flow is laminar at the upper plate surface and the outer glass wall, and is turbulent in the bulk liquid, including at the line of symmetry (this is the radial axis, which is the left hand side wall). Laminar flow is featured at the upper plate surface and outer glass wall, because zero slip conditions are applied which evaluated wall shear stresses on those surfaces, as shown in Eq. 4.39. On the other hand symmetry boundary conditions apply zero shear conditions on their respective surfaces, which results in greater velocities at the symmetry surfaces, which consequently increases the eddy viscosity ratio at those surfaces, as shown in the contours of eddy viscosity.

$$\tau_w = -\mu \frac{du_i}{dn} \tag{4.39}$$

Figure 4.14 shows the equivalent contours of temperature, dimensionless T^*, streamlines and eddy viscosity ratio for the 3D short test rig case. The contours of temperature and dimensionless T^* are in agreement with the 2D axisymmetric short test rig case. Most of temperature variation occurs across the base plate. Furthermore, the values of dimensionless T^* are greater than zero at the upper plate surface, agreeing with the 2D axisymmetric case. The behaviour of the streamlines and the contours of the eddy viscosity ratio are in disagreement with the 2D axisymmetric case. The 3D short test rig shows two large counter rotating convection cells for the entire domain, compared to two large, and two small counter rotating convection cells for the 2D axisymmetric half domain. Furthermore, the values of the eddy viscosity ratio in the centre of the 3D short test rig are lower than those at the line of symmetry in the 2D axisymmetric case.

The simulations using a 2D axisymmetric geometry produce an unphysical solution because the imposition of axisymmetry enforces an unstable solution which is broken in the simulations using a full 3D geometry. In the 2D axisymmetric case, the instantaneous time-dependent solution is forced to be axisymmetric, constrained by the physical free slip wall which represents the symmetry line. In the full 3D case the instantaneous time-dependent fields are not restricted to be axisymmetric. The time-averaged 3D solution is axisymmetric; however this axisymmetric solution cannot be predicted using 2D axisymmetric conditions. Therefore symmetric conditions may not be permitted to model buoyancy driven flows found in the unscaled test rigs; the scaled test rig; and Evaporator C.

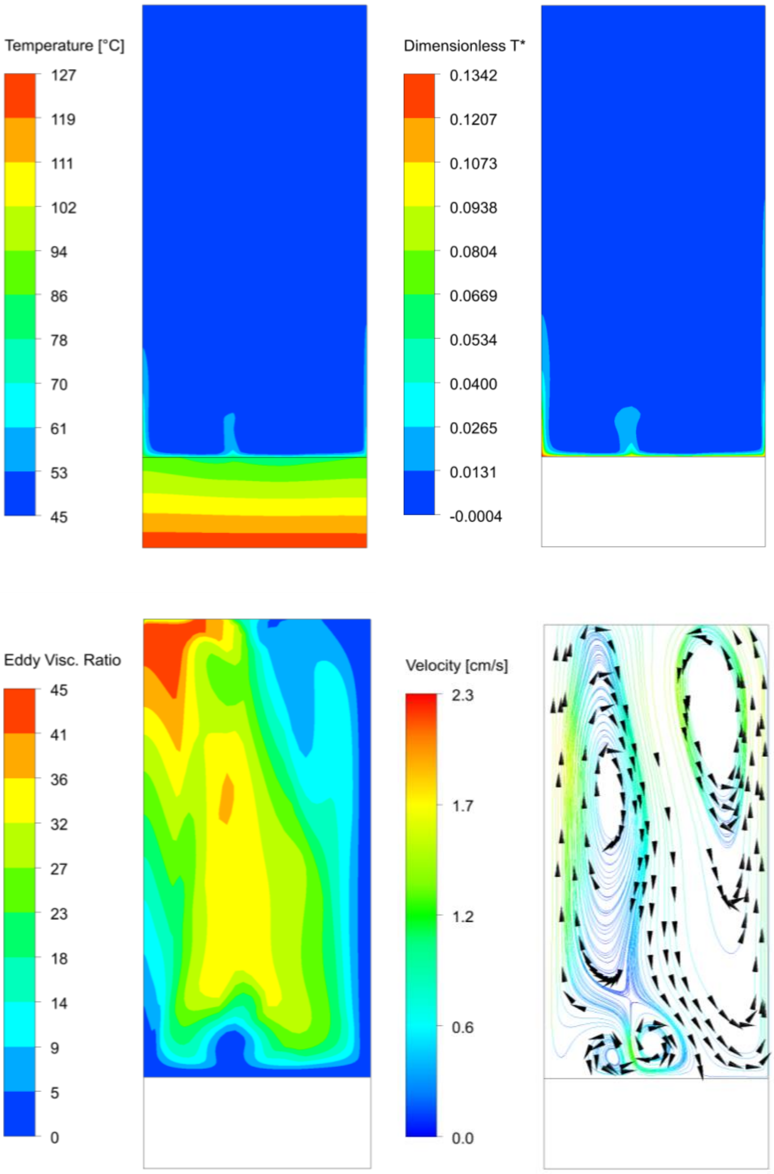

Figure 4.13: (Starting top left and going clockwise, transient averaged values over 30 s) temperature in the baseplate and liquid column; dimensionless T^* in the water indicating boiling regions; streamlines in the water with superimposed arrow heads indicating flow direction; and eddy viscosity ratio indicating turbulence intensity.

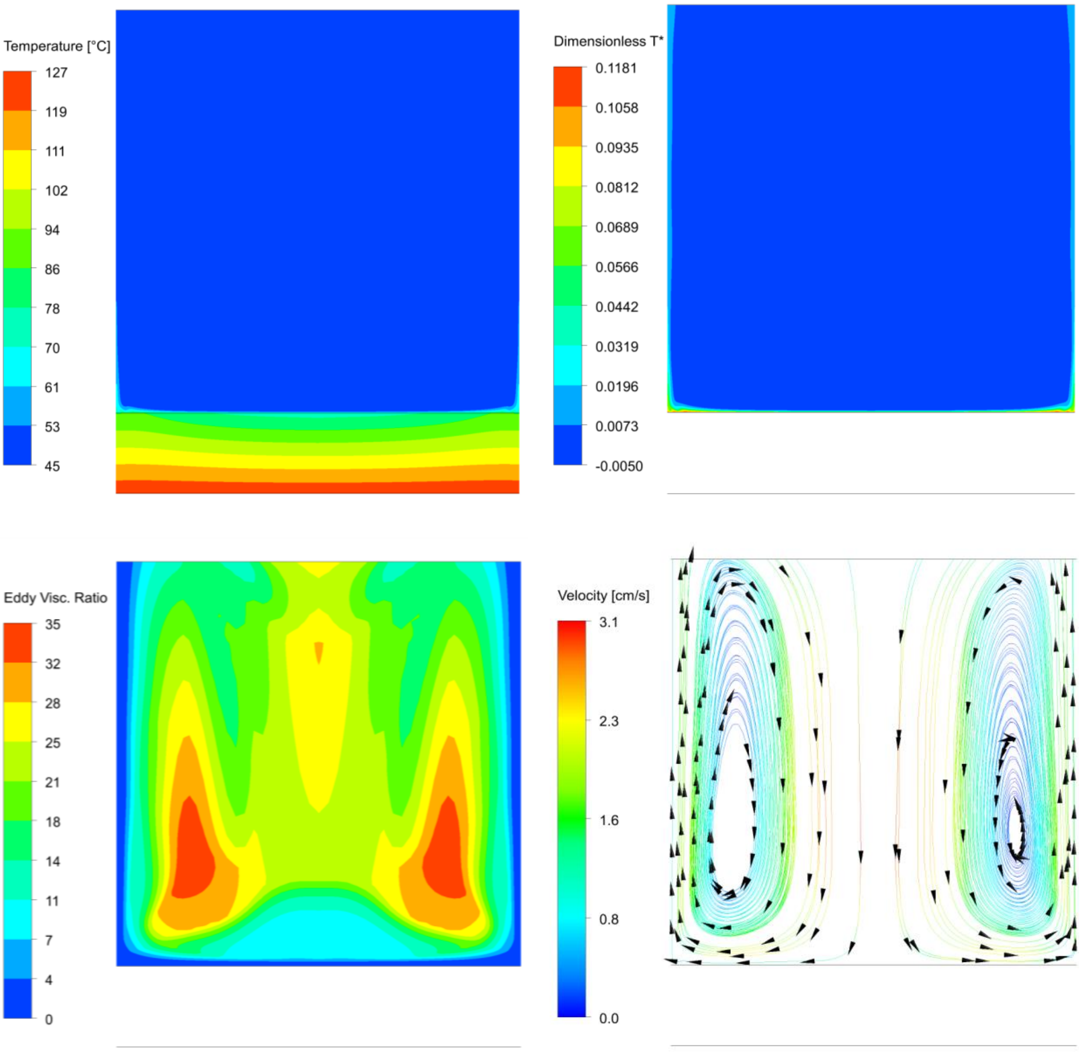

Figure 4.14: (Starting top left and going clockwise, transient averaged values over 30 s) temperature in the baseplate and liquid column; dimensionless T^* in the water indicating boiling regions; streamlines in the water with superimposed arrow heads indicating flow direction; and eddy viscosity ratio indicating turbulence intensity.

Figure 4.15 and Figure 4.16 are time averaged contours of temperature, dimensionless T^*, water streamlines and eddy viscosity ratio inside the tall test rig, with Figure 4.15 displaying an area close to the upper plate surface, and Figure 4.16 showing an area at the top opening, where the free surface would be. A complete visual illustration of these variables in their entirety inside the tall test rig is displayed in Figure 4.17. In all three figures, the contours of temperature exhibit the same behaviour as the short test rig where the largest temperature difference occurs across the baseplate. The entire liquid column remains close to 45 °C, despite additional heating into the water via three external heating jackets.

The contours of T^* indicate behaviour far different to that in the short test rig. The bottom half of the water column is sub-cooled, as shown in T^* contours in Figure 4.15. This is in contrast to the values of T^* at the top of the test rig where the free surface is, which clearly reveals a superheated region where the local saturation temperature is exceeded. This is better illustrated by the contours of T^* in Figure 4.16. Figure 4.17 shows how the water column switches behaviour from sub-cooled to superheated approximately half way up the test rig. This is attributed to the absolute pressure inside the system, which more than doubles from the free surface (0.1 bar) to the upper plate surface (0.31 bar), which directly effects the local saturation temperature (45.8 °C at the free surface, and 70.2 °C at the upper plate surface). This immediately suggests boiling is highly sensitive to large hydrostatic heads in systems under a vacuum, which is the type of system found in Evaporator C.

The streamlines for the system are counter intuitive. The flow direction travels downward between the draught tube and vessel walls, and upward through the draught tube. This is counter intuitive because additional heating is supplied to the water via the three external heating jackets. Therefore the local water density and temperature at the outer walls should be less than the local density and temperature inside the unheated core, which would suggest downward travel inside the draught tube, and upward travel at the outer walls. The draught tube forces circulations of the water counter to its natural flow direction. The standoff value for the draught tube was taken as 2 cm, and in the experimental campaigns this is a variable. In the experimental campaigns discussed in Section 4.2, the stand-off values were 2 cm and greater, and for values greater than 2 cm the water travelled down the draught tube, counter to that simulated here. Therefore the momentum behaviour is clearly sensitive to the stand-off distance. Small clearances similar to the stand-off are found in Evaporator C. One example is the distance between the steam sparger and the vessel shell, and the geometries of are described in CHAPTER 6. Therefore the bifurcation phenomena found in the tall test rig may be present inside Evaporator C.

The contours of eddy viscosity ratio in Figure 4.15, Figure 4.16 and Figure 4.17 imply largely laminar flow, where its value tends to a value of 10, and lower. The contours suggest the greatest region of turbulence is at the free surface. This does not have any significant connotations in single phase flow in the absence of evaporation at the free surface. However when a more detailed analysis is undertaken in the next section, where the free surface and boiling is physically modelled, the transfer of turbulence across the free surface may be significant.

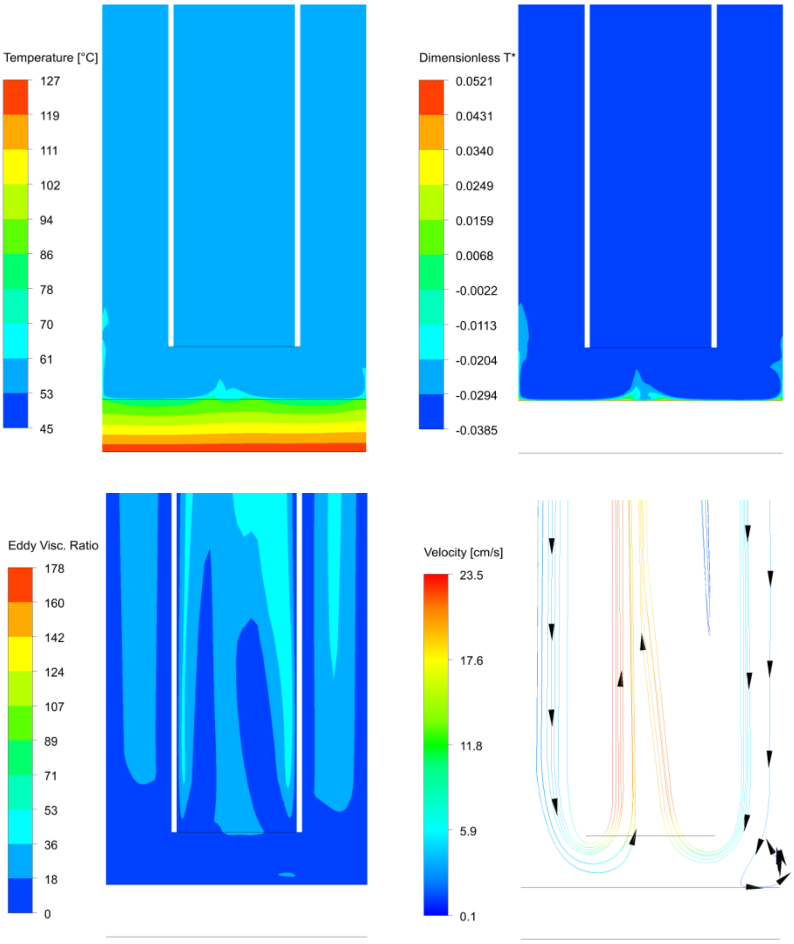

Figure 4.15: (Starting top left and going clockwise, transient averaged values over 30 s, displaying the bottom portion of the test rig) temperature in the baseplate and liquid column; dimensionless T^* in the water indicating boiling regions; streamlines in the water with superimposed arrow heads indicating flow direction; and eddy viscosity ratio indicating turbulence intensity.

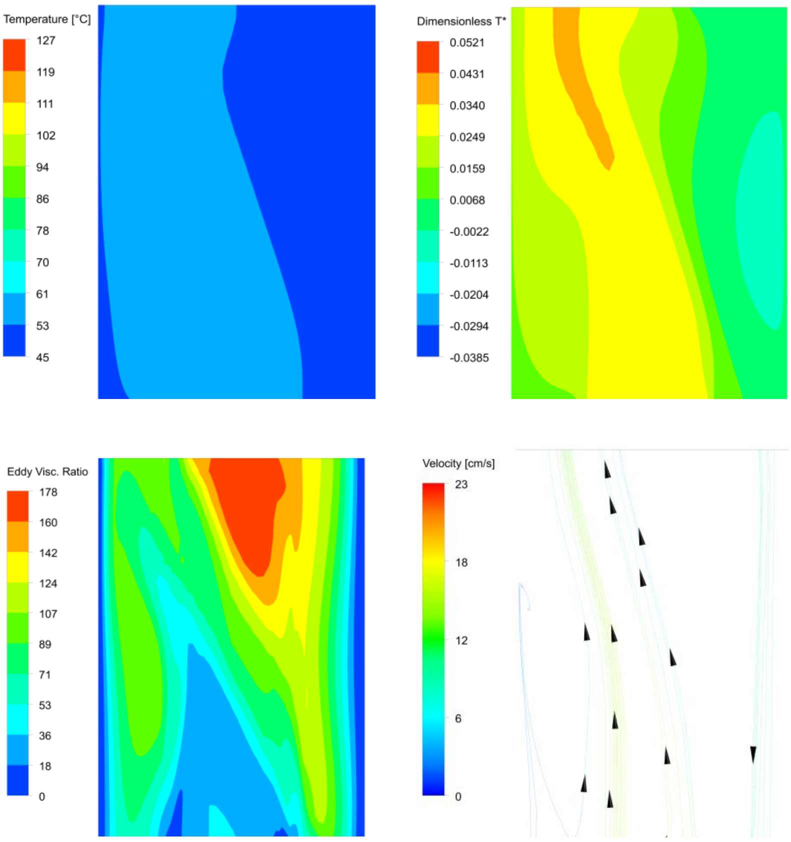

Figure 4.16: (Starting top left and going clockwise, transient averaged values over 30 s, displaying the top portion of the test rig) temperature in the baseplate and liquid column; dimensionless T^* in the water indicating boiling regions; streamlines in the water with superimposed arrow heads indicating flow direction; and eddy viscosity ratio indicating turbulence intensity.

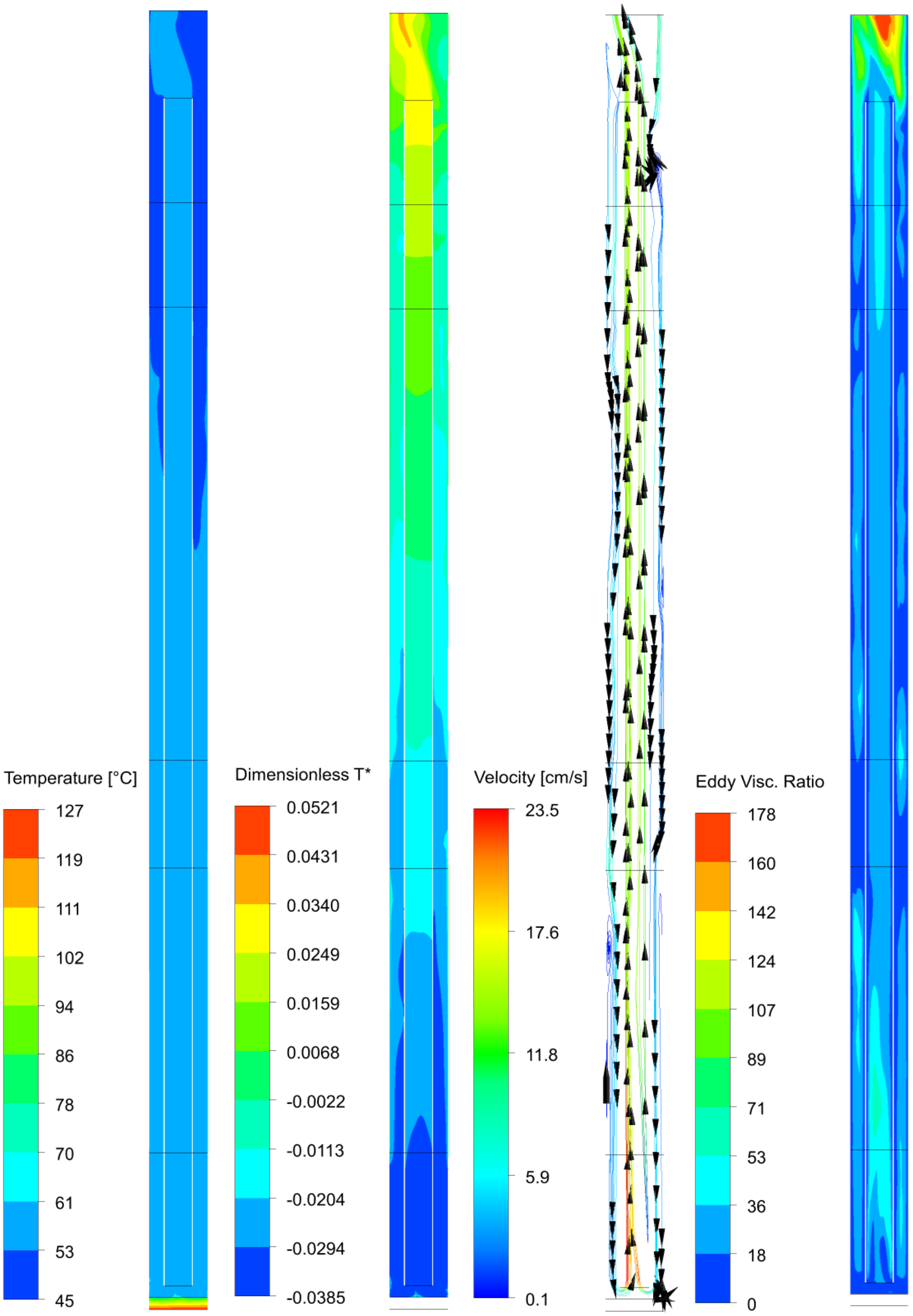

Figure 4.17: (Starting left to right, transient averaged values over 30 s, displaying the entire tall test rig) temperature in the baseplate and liquid column; dimensionless T^* in the water indicating boiling regions; streamlines in the water with superimposed arrow heads indicating flow direction; and eddy viscosity ratio indicating turbulence intensity.

4.6 Comparison: Thermal Resistance and CFD Investigations

Table 4.13 lists the values of the area average temperatures and heat transfer coefficients for all three cases, 2D axisymmetric short test rig, the 3D short test rig, and the 3D tall test rig. The areas were taken as the lower plate surface, the upper plate surface, a user defined surface in the midpoint of the water column, and at the opening, which treats the free surface. The bulk temperature for the condensation heat transfer coefficient underneath the base plate is 126.9°C. Likewise the bulk temperature for the remaining heat transfer coefficients on all other surfaces is the ullage temperature, which is 45.8°C.

Test Rig	T_{stm} [°C]	T_{pl} [°C]	T_{pu} [°C]	T_{mid} [°C]	T_{fs} [°C]	T_{ulg} [°C]	h_{csn} [W/m^{2}K]	h_{pu} [W/m^{2}K]	h_{mid} [W/m^{2}K]	h_{fs} [W/m^{2}K]
2D Axisym.	126.9	125.8	83.9	47.4	46.8	45.8	28909	837	0.1	6.4
3D Short	126.9	125.7	79.1	47.0	46.8	45.8	28596	1035	25	37
3D Tall	126.9	125.7	82.5	55.9	50.1	45.8	28697	921	4.2	1268

Table 4.13: Area average values of temperature and heat transfer coefficient at the lower plate surface, upper plate surface, mid surface in the water column and free surface. The bulk temperatures for the heat transfer coefficients for the surface underneath the base plate is the steam temperature 126.9 °C, and all other surfaces is the ullage temperature 45.8 °C.

The CFD values in Table 4.13 do not correspond well with the pure conduction results in the thermal resistance investigation presented in Table 4.3. The natural reason is because Table 4.3 is a completely different heat transfer system compared to the CFD case (pure conduction versus free convection). The CFD temperature distributions in Table 4.13 do not agree with the temperature distributions calculated for the free convection thermal resistance cases. However, despite this, the same orders of magnitude of the heat transfer coefficients reported for both investigations are obtained. This suggests fixing the heat flux in one direction in the thermal resistance case may not be prudent as the heat flux is implied to vary in the CFD cases, and hence in reality.

The temperatures and heat transfer coefficients reported in the CFD simulations agree to the same order of magnitude with the nucleate boiling thermal resistance investigation presented in Table 4.5. This is despite using boiling correlations for the thermal resistance case, and the CFD cases being single phase convective flow. The likely explanation is due to the velocities at the upper plate forcing larger heat transfer rates on that surface, which yields larger heat transfer coefficients. The CFD simulations did indicate boiling may occur on the upper plate surface.

4.7 Summary

In this chapter one dimensional thermal resistance investigations were performed on the short test rig and the tall test rig. In addition to this, CFD simulations of the two test rigs were also performed. A structured hexahedral meshing approach was taken to reduce discretization error in the meshes, and a mesh sensitivity study was performed, with the final meshes used indicating that the discretisation error was no more than 2%, but the extrapolated errors were high. In order to challenge the assumption that symmetry may be used as a modelling technique, two cases for the short test rig were performed, which were 2D axisymmetric and full 3D. For the tall test rig only a full 3D simulation was performed.

Thermal resistance networks were proved to be a computationally inexpensive tool to predict temperatures, heat transfer coefficients, and heat fluxes in a heat transfer system when compared to complex and expensive CFD simulations. They provided useful information such as temperature distributions and values of heat fluxes, without needing to resort to expensive methods such as CFD

However, there is poor agreement between pure conduction and free convection thermal resistance cases and the CFD investigation. There is, however, reasonable agreement between the nucleate boiling case and CFD investigations. In the nucleate boiling thermal resistance case ,there is good agreement between the six different boiling heat transfer coefficients used, and the solutions in all three thermal resistance cases are not sensitive to the type of condensation heat transfer coefficient used.

Poor flow physics is observed in the 2D axisymmetric geometry in the CFD simulations of the short test rig. This is because the symmetry planes enforce an unphysical solution that is broken in the simulations using a full 3D geometry. Hence, the use of 2D axisymmetric conditions to model buoyancy driven flow in the test rigs is not recommended, even if the 3D solution is symmetric.

T^* distributions in the short test rig indicate that nucleate boiling at the upper plate may occur, and in the tall test rig, the T^* distributions indicate that the liquor is heated above its saturation temperature in the upper regions of the test rig. The CFD simulations have shown that phase change in the liquor is highly dependent on the pressure head of the liquid column.

The symmetry will be broken in Evaporator C which has a similar fill height to vessel width. This is because Evaporator C has blockages such as the internal structure including the coils, which were not represented inside the short test rig. Furthermore the draught tube in the tall test rig forces the behaviour of the water to behave in a way counter to its natural tendency.

Chapter 5

Computational Analysis on the Scaled Test Rigs

5.1 Introduction

The thermal resistance and CFD investigations on the two unscaled test rigs provided insight into the potential for boiling in systems similar to Evaporator C. The thermal resistance investigation was one dimensional and limited in the information it could output. The CFD simulations provided greater insights into possible locations of boiling, but did not actually simulate it. Furthermore, in the absence of experimental verification, it would have been difficult to ascertain if boiling simulations on the unscaled test rigs may or may not have been correct. Lastly, all indications of evaporation suggested that it may occur principally in two locations, at heated surfaces, and at the free surface.

The purpose of this chapter is to describe how the CFD models were developed and validated to perform boiling water simulations in a one quarter scaled test rig slice of Evaporator C. The simulations were multiphase phase flows, performed within the Eulerian-Eulerian modelling framework.

5.2 The Scaled Test Rig

The test rig (D. McNeil et al., 2015) represents a one-quarter scale thin slice of the evaporating section of Evaporator C, as shown in Figure 5.1. The test rig comprised a main test section, and two additional sections stacked on top of each other. All sections were manufactured from stainless steel, but accommodated a glass-viewing window to observe flow patterns. The lower section was the main test section. It is 0.75 m wide, 1 m high and 98 mm deep. The lower section also contained two tube bundles, a left hand side bundle and a right hand side bundle. The right hand side tube bundle was raised 32 mm higher than the left hand side bundle. This was intended to replicate the sloping effect of the internal helical coils of Evaporator C, as shown by Figure 5.1 (right). The tube bundles were made of brass, had an outside diameter of 28.5 mm, and were 5 mm thick. Finally, the front face of the lower test section was a glass panel.

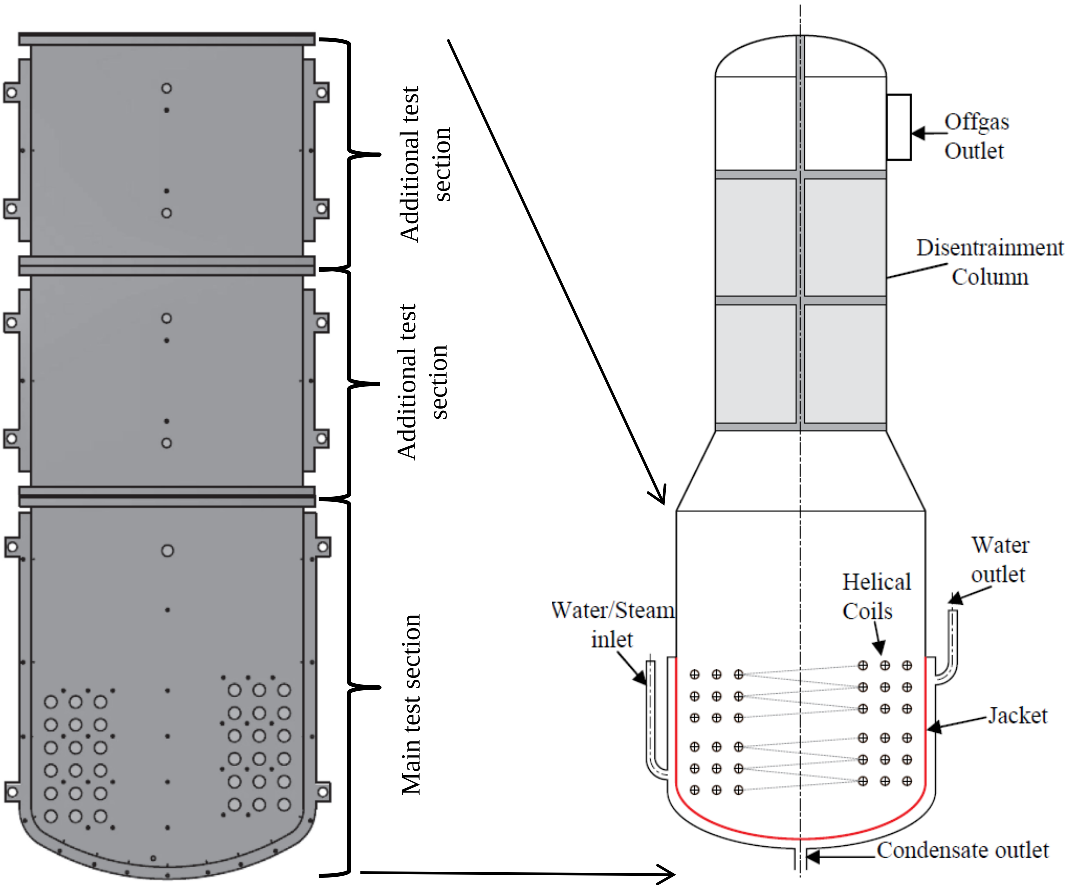

Figure 5.1: One-quarter scale thin slice test rig (left) of the evaporating section of Evaporator C (right). Test rig image courtesy of McNeil et al. (2015), and Evaporator C image courtesy of Perry & Geddes (2011).

An issue with the one-quarter scale design is that the head effect of the liquid column would disappear if the Evaporator C liquid depth was also scaled, since the liquid depth in Evaporator C was 2.35 m, and one quarter of this is 0.59 m. Therefore two additional test sections were required, stacked on top of the main test section, to accommodate greater liquid depths as found in Evaporator C. The two test sections had heights of 0.6 m each. This allowed liquid depths up to 2 m to be tested.

The vessel had two methods of heating. These were via the coils, and/or via heating pads, which were attached to the sides of the vessel. Heating from the coils was achieved via Joule heated rod heaters inserted into the cavities of the brass tubes. The heating pads on the sides of the vessel were also Joule heated.

The test facility, shown in Figure 5.2, is located at the Heriot-Watt University. The scaled test rig operates in a closed system, devoid of air, and the operating liquid is deionised water. McNeil et al. (2015) described how the scaled test rig achieved operating conditions:

1. The vacuum pump was activated until the pressure inside the system read 500 mbar.

2. The drain valve was opened, allowing deionised water to flow from the storage tanks to the test section, and the valve shut when the desired liquid depth was achieved.
3. The hot well drain valve was opened, allowing water to flow to the hot well from the storage tank, and the valve closed when the desired water height was achieved in the hot well sight glass.
4. Remaining air from the system was purged by activating the circulating pump, and opening the water control valves and the evaporator entry shut-off valves. When steady state flow was obtained inside the evaporator, the shut-off valve was closed.
5. The required head space ullage pressure was achieved by activating the vacuum pump under the correct settings corresponding to the required pressure.
6. The heat supply was activated at 90% of full power which, after some time, caused the water to boil. This allowed any remaining air to accumulate inside the hot well, which allowed the final opportunity to remove the remaining air from the system.
7. Any vapour that was generated at 90% full power was condensed in the overhead condenser and pumped back to the test section. McNeil et al. (2015) reported that steady state conditions were achieved in around 3 hours of operation.
8. Finally, the required heating conditions were applied, which allowed experimental readings to take place.

The experimental readings were comprised of temperatures which were outputted from a number of k-type thermocouples embedded in strategic locations inside the test section. There were three groups of thermocouples. The first group were termed stream thermocouples, and were placed inside the bulk liquid. The second group were termed tube thermocouples, and were embedded inside the brass tube walls. The final group of thermocouples were termed the fluid thermocouples, and placed between the heated coils.

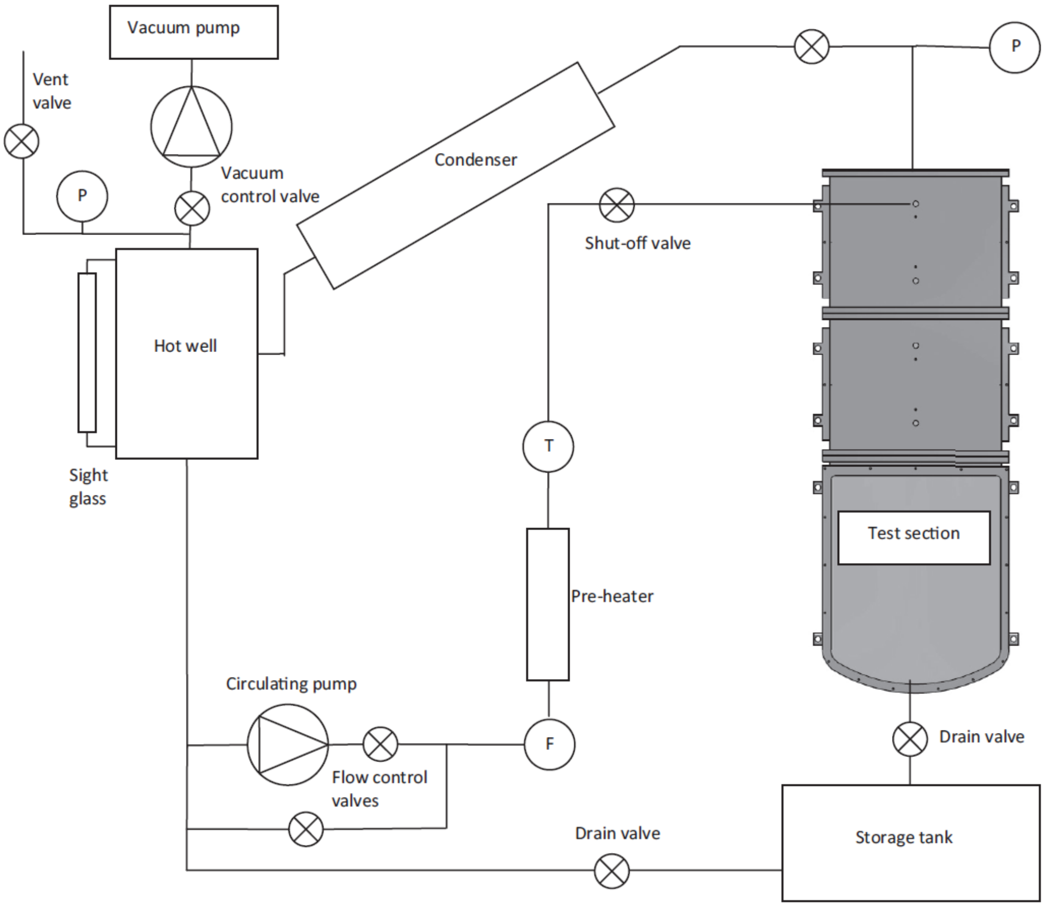

Figure 5.2: The Heriot-Watt facility which houses the scaled test rig (D. McNeil et al., 2015)**.**

5.3 Past Work

McNeil et al. (2015) performed an experimental investigation of boiling water at low pressure 50 mbar, and comparatively high pressure 850 mbar, in the one quarter scale test rig. Two water depths were tested for the low pressure series: 0.8 m and 2 m. The high pressure series tested water depths at only 0.8 m. Heating to the water was supplied by the tubes only, and the side heating pads were not activated. The tube heat flux range for the low and high pressure series was varied from 10 to 70 kW/m^2.

At 50 mbar pressure, for both high and low water levels, vapour generation on the tube walls was not observed until heat fluxes of 40 kW/m^2 or greater were achieved. Below this heat flux value, the tubes were in the single phase convective regime with very little nucleation. This suggests that the wall temperatures were less than the temperature onset of nucleate boiling for that given condition.

Above 40 kW/m^2, and at 50 mbar pressure for both water depths, the tubes were in the sub-cooled nucleate boiling regime. Vapour bubbles were generated, but did not detach from the tube walls, and collapsed back into the sub-cooled liquid. During the 50 mbar tests, the bulk liquid temperature was largely uniform during boiling, and was similar to the saturation temperature at the free surface. Due to the input of heat into the system, vapour generation at the free surface did occur. A constant water level was maintained by condensing the off gas vapour and returning it back to the main test section. In the low pressure tests, the local saturation pressure changed significantly with pool depth since the hydrostatic pressure head of the pool was a large fraction of the total pressure.

For the tests at 850 mbar, the local saturation pressure does not change significantly with pool depth (0.8 m), since the pressure head was a smaller fraction of the total pressure. For the high pressure tests, boiling occurred on all tube surfaces at all tube heat fluxes tested. This indicated that large superheats were required for boiling at 50 mbar, compared to boiling at 850 mbar.

5.4 Computational Approach and Boundary Conditions

Since boiling inside Evaporator C occurs at low pressures, the 50 mbar, 0.8 m depth dataset of McNeil et al., (2015) was used to help develop and validate the CFD models. The 0.8 m depth was chosen, and not the 2 m depth, to save on computational resources, since a 0.8 m depth required a smaller computational physical flow domain, and hence fewer mesh cells compared to the 2 m depth case. The high heat flux data set of 65 kW/m^2 was chosen. This is because, at these heat fluxes, sub-cooled nucleate boiling was observed. Hence the CFD simulations modelled evaporative flows under these conditions in the scaled test rig.

The CFD domain had the same dimensions as the test rig described by McNeil et al. An annotated schematic of the CFD domain with the indicated 0.8 m water level is shown in Figure 5.3 (Left). The coils were not modelled as a conjugate heat transfer problem. Instead only the outside profile of the coils were included in the physical flow domain, and appropriate heat fluxes were applied to those surfaces. Inside the CFD domain, monitor points of temperature, velocity, dimensionless T^*, volume fraction, and absolute pressure were recorded at the positions which corresponded to the stream and fluid thermocouple positions in the actual test rig, as shown in Figure 5.3 (Right). The stream thermocouples begin at TS5 and end at TS15, because thermocouples TS1 to TS4, and TS16 to TS18 were above the free surface position, and therefore superfluous for the CFD investigation (they would be used if CFD simulations of the 2 m water depth were performed).

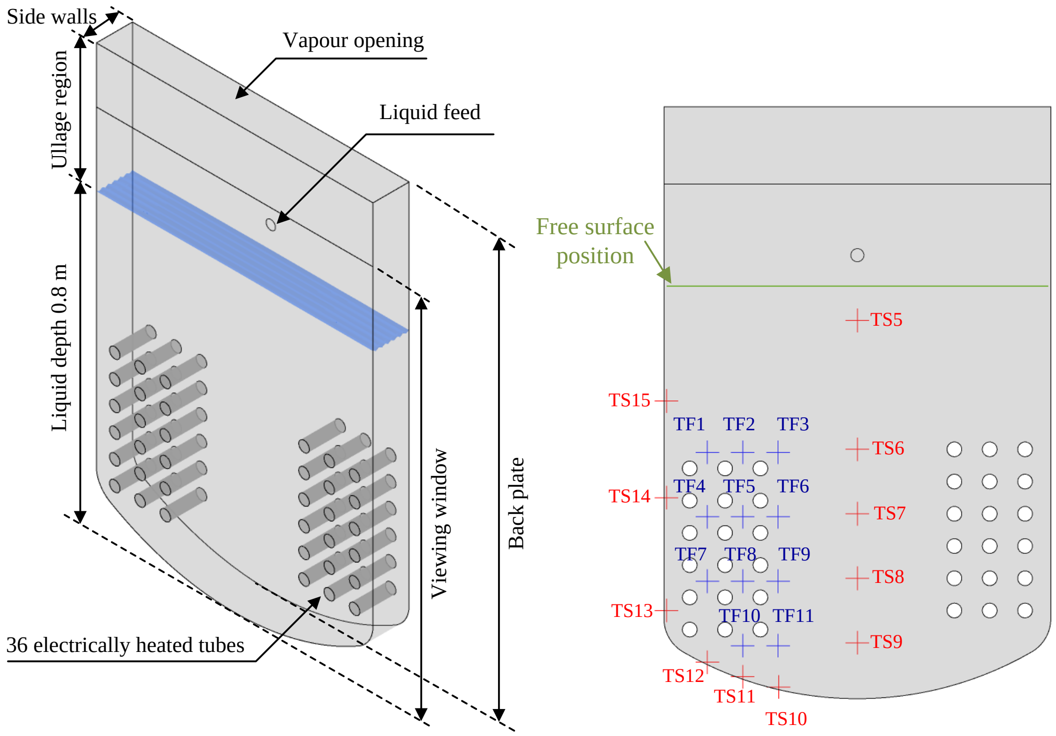

Figure 5.3: (Left) general arrangement of the experimental test rig, (right) thermocouple positions in the experimental test rig.

The CFD boundary conditions were identical to the experimental boundary conditions of McNeil et al. The ullage pressure was set to 50 mbar. All 36 tube surfaces had a heat flux of 65 kW/m^2 applied to them. The liquid depth was set to 0.8 m. The entire geometry of the scaled test rig was not modelled. Instead the headspace above the free surface was cut off at an arbitrary height above the free surface such that the position of the vapour opening in Figure 5.3 (Left) had no influence on the flow physics at the free surface. Hence, the vapour opening was modelled as an opening boundary condition, with an opening temperature of 32.9 °C (corresponding to saturation pressure of 50 mbar). This allowed generated vapour above the free surface to escape, as is possible in the scaled test rig. To maintain a constant water level the liquid feed inlet above the free surface was included in the physical flow domain, at the same position as found in the experimental test rig. The liquid feed rate was set equal to the rate of evaporation to guarantee continuity, and the incoming feed had a temperature of 11 °C.

In the CFD investigation the non-heated walls were assumed to be heat loss walls. The boundary walls were not modelled as a conjugate heat transfer problem, but rather as a thin wall problem. Hence heat loss from the walls of the unscaled test rig were assumed to be via conduction heat transfer through the wall thicknesses, and a combination of convection and radiation heat transfer to the environment. This was modelled by inputting an overall heat transfer coefficient and a specified temperature at the boundaries of the physical flow domain. The outside temperature was assumed to be 15 °C. A similar method of heat loss was taken in modelling the flows inside the unscaled test rigs in CHAPTER 4. Figure 5.4 illustrates the modes of heat loss from the scaled test rig.

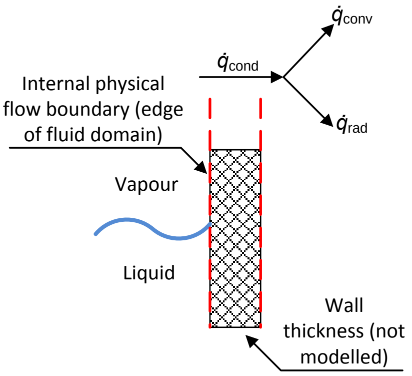

Figure 5.4: Heat from the physical flow domain and lost from the walls of the flow boundaries via conduction, and a combination of convection and radiation to the surroundings.

The heat loss heat transfer coefficient, h_{loss} for each wall was determined using the expression as shown in Eq. 5.1. The expression is a function of the wall normal thickness δn_{wall} and the thermal conductivity λ_{wall}, and contains contributions due to convection h_{cvn} and radiation h_{rad}.

$$h_{loss} = \left[\frac{\delta n_{wall}}{\lambda_{wall}} + \frac{1}{(h_{cvn}+h_{rad})}\right]^{-1} \tag{5.1}$$

In Figure 5.3 (Left) the viewing window is a 19 mm thick borosilicate glass, with thermal conductivity 1.13 W/m K (Wilson, 2004) and thermal emissivity of 0.9. The sidewalls and back plate are 5 mm thick stainless steel walls, of thermal conductivity 15.1 W/m K (taken to be AISI 302), and thermal emissivity of 0.33 (corresponding to lightly oxidised stainless steel). Values of the thermal emissivity of glass and steel and the thermal conductivity of steel were taken from Bergman et al., (2011). The Churchill and Chu (1975) free convection heat transfer coefficient in Eq. 5.2 was used for the convective heat transfer component in Eq. 5.1, which was also reported in Bergman et al., (2011). This correlation was used as it is valid under all ranges of Rayleigh number.

$$\mathrm{Nu} = \frac{h_{cvn}L}{\lambda} = \left\{0.825 + \frac{0.387\mathrm{Ra}^{1/6}}{\left[1+(0.492/\mathrm{Pr})^{9/16}\right]^{8/27}}\right\}^2 \tag{5.2}$$

The radiation heat transfer coefficient in Eq. 5.1 was computed by using the linearized relation as shown in Eq. 5.3.

$$h_{rad} = \varepsilon\sigma(T_{wall} + T_{air})\left(T_{wall}^2 + T_{air}^2\right) \tag{5.3}$$

This simplification for the radiation heat transfer coefficient is only valid where the surroundings are much larger than the heated surface. Since the scaled test rig is in a large laboratory room at the Heriot-Watt facility this assumption holds true.

5.5 Statement on Nucleate Boiling and Evaporation

Within the framework of the CFD, thermal phase change at the free surface due to evaporation was modelled. However thermal phase change at the heated walls due to nucleation was not modelled. The rationale behind this was that, in the experimental study, any vapour bubbles which nucleated at the coil surfaces quickly collapsed back inside the bulk sub-cooled water, therefore it was assumed that modelling such complex physics in CFD was unnecessary. In addition to this, modelling wall boiling is computationally restrictive due to the small time scales involved (bubble detachment, growth, collapse, coalescence and breakup), and due to the limited information in the literature on wall boiling at sub-atmospheric pressures.

The most popular and widely used wall nucleate boiling model in CFD is the so-called RPI boiling model, developed by Kurul & Podowski (1991). This model has been implemented into most commercial and open source CFD solvers and has been validated and used extensively in high pressure boiling applications. The RPI boiling model is a mechanistic phase change model, applied at heated walls where bubble nucleation is expected to occur, and complements a bulk boiling phase change model, but does not replace it. The bulk boiling phase change model is described later.

This model was originally developed for flow applications above atmospheric pressures, such as in pressurised water nuclear reactors, and high pressure steam generators, and this model has been used with success in those and other applications. See for example the work of Milnes et al. (2012) who used the RPI wall boiling model to model boiling flows in the hypervapotron high heat flux cooling device employed in fusion reactors.

The wall boiling model comprises a number of sub models for nucleate boiling at the wall. The original model of Kurul & Podowski (1991) employed empirical correlations for these sub-process, many of which were only valid for boiling at high pressure, hence require modification for boiling at atmospherics and sub-atmospheric pressures (Tu and Yeoh, 2002). These are listed below. For brevity, references are given, but detailed equations are omitted.

- Bubble departure diameter, d_{Bw}: the original model of Kurul & Podowski (1991)) employed the correlation of Tolubinsky and Kostanchuk (1970), which was developed for pressurised water data, and expresses the bubble departure diameter as a function of local liquid sub-cooling.
- Wall nucleation site density, n'': the current models implemented, and those that are widely used assume a formulation proposed by Lemmert and Chawla (1977) whereby the number of nucleation sites per unit area is modelled as a function of wall superheat.

- Bubble detachment frequency, f: The correlation by Von Ceumern-Lindenstjerna (1977) is employed. This depends on the acceleration due to gravity, so it is based on pool boiling., which is somewhat at odds with the application of the model to high pressure forced convective boiling
- Bubble waiting time, t_w: is modelled according to Tolubinsky and Kostanchuk (1970). It is assumed that the waiting time between each bubble departure is 80% of the bubble detachment period.
- Area influence factors: Kurul and Podowski (1991) assumed that the diameter of influence of a nucleating bubble is twice the bubble departure diameter. In addition to this, the maximum area fraction for bubble influence is also required to be known

In addition to these mechanistic sub-models, the heat flux to the wall is split into three separate contributions, due to evaporative, convective, and quenching heat transfer.

- Evaporative heat transfer, Q_e: The evaporative heat transfer rate at the wall is given in terms of the above quantities, as follows:

$$Q_e = \frac{\pi}{6} d_{bW}^3 \rho_g f n'' \Delta H_{lg} \tag{5.4}$$

- Convective heat transfer, Q_c: is assumed to occur in the near wall region away from the influence of departing bubbles. Kurul and Podowski (1991) modelled this using a convective heat transfer coefficient h_c based on the Stanton number correlation for convective heat transfer in a pipe

$$Q_c = h_c(T_{wall} - T_l) \tag{5.5}$$

- Quenching heat transfer, Q_q: refers to the heating of sub-cooled liquid as it displaces the space occupied by rising bubbles between the bubble and the superheated wall. This is assumed to occur in the area of influence of the rising bubbles. The quenching heat transfer coefficient is modelled according to Del Valle & Kenning (1985) based on the solution of the transient heat conduction equation in a semi-infinite slab. In this model

$$Q_q = h_q(T_{wall} - T_l) \tag{5.6}$$

  Where the quenching heat transfer coefficient h_q is a function of the bubble departure frequency f and the waiting time t_w.

The partitioning of the wall heat flux into evaporative, convective and quenching parts yields an equation relating the total wall heat flux to the wall temperature:

$$Q = Q_e + Q_c + Q_q \tag{5.7}$$

This relationship is non-linear, so it has to be solved iteratively to determine the wall temperature for a specified wall heat flux. Once determined, the wall temperature gives the three individual components of the wall heat flux, including the evaporation rate.

The original model of Kurul and Podowski (1991) was found to be strongly mesh dependent. This was mainly due to the use of the Stanton number correlation for convective heat transfer, which employed the liquid velocity at the centre of the near-wall cell, and the use of the Tolubinsky and Kostanchuk (1970) correlation for bubble departure diameter, which depended on the near wall liquid sub-cooling. These problems were solved by Krepper et al., (2007) who modelled the convective heat transfer using turbulent wall functions, and computed near-wall liquid sub-cooling at a fixed vale of $Y^{+} = 250$ for use in the bubble departure diameter and quenching heat transfer correlations.

Based on the large number of sub models which would be required to be adapted to sub-cooled nucleate boiling, a separate independent investigation would have be undertaken to critically evaluate each sub model and provide bespoke formulations for boiling at pressures close to vacuum. In addition to this, formulations would also have to be developed which describe complex interface structures, such as a vapour bubbles escaping at the free surface if it occurs. However in the first instance, a bulk phase change model, that is boiling and condensation at liquid-vapour interfaces, would need to be validated first, which this work attempted to do. Lastly, the work by McNeil et al. (2015) suggests that, at very low pressures, such as those found in Evaporator C, vapour bubbles nucleated at walls tend to collapse back into the sub-cooled bulk liquid. Therefore bypassing wall boiling in the first instance was an adequate first step into attempting to solve this complex problem.

5.6 The Eulerian - Eulerian Approach

There are two methods to solve the conservation equations in the Eulerian - Eulerian framework, the homogeneous and inhomogeneous approaches. For a given transport process, the inhomogeneous approach assigns individual transport equations to each phase. For example, for the case of momentum transport, each phase is governed by its own momentum transport equation which determines its own velocity field. The phasic momentum equations are coupled together by the inclusion of terms which take into account interphase transfer processes such as interfacial drag, and momentum transfer due to interphase mass transfer (Drew and Passman, 2006). Throughout this chapter, variables assigned to the liquid phase will be given the subscript α, and variables assigned to the vapour phase will be given the subscript β.

The homogenous approach to momentum transfer assumes that the individual phase velocities may be described by a shared velocity field. This is a reasonable assumption in separated flow with a free surface. The governing conservation equations are derived by summing the individual phasic momentum transport equations over all of the phases denoted by subscripts α and β. Thus, the homogeneous momentum equation is described by Eq. 5.8.

$$\frac{\partial}{\partial t}\left(\rho_{\alpha\beta}\boldsymbol{U}\right) + \nabla\cdot\left(\rho_{\alpha\beta}\boldsymbol{U}\otimes\boldsymbol{U} - \mu_{\alpha\beta}\left(\nabla\boldsymbol{U} + (\nabla\boldsymbol{U})^T\right)\right) = -\nabla P \tag{5.8}$$

The mixture density $\rho_{\alpha\beta}$ and viscosity $\mu_{\alpha\beta}$ are given by Eq. 5.9 and Eq. 5.10 respectively, and are a function of the phasic volume fraction, r_α or r_β.

$$\rho_{\alpha\beta} = \rho_\alpha r_a + \rho_\beta r_\beta \tag{5.9}$$

$$\mu_{\alpha\beta} = \mu_\alpha r_a + \mu_\beta r_\beta \tag{5.10}$$

Eq. 5.8 is essentially a single phase momentum equation with variable density and viscosity to account for the difference in phase properties. All interfacial transfer terms in the inhomogeneous momentum equations cancel out in the summation procedure, as they are equal and opposite.

For the simulations computed in this chapter, a homogeneous approach for momentum was taken. A homogeneous approach to momentum is less computationally intensive since there are fewer equations to solve compared to an inhomogeneous approach. The inhomogeneous approach also requires knowledge of the interfacial drag coefficient, which was difficult to determine for complex transient flows such as boiling under vacuum. Researchers at the Helmholtz Zentrum Dresden Rossendorf (HZDR) in Germany have investigated modelling approaches to simulate inhomogeneous interphase transfer such as drag, turbulence and momentum in complex flow phenomena (Thomas Höhne and Lucas, 2011), however these are for restricted cases and require further generalisation.

In a similar manner to momentum, a homogeneous approach to turbulence was employed, using the two equation $k - \omega$ shear stress transport model (Menter, 1994), which was also used in the single phase simulations of the scaled test rig in CHAPTER 4. The difference in this case is common fields of turbulence kinetic energy and specific dissipation rates are shared amongst both phases in the homogeneous turbulence approach.

The mass conservation equations are the same for both homogeneous and inhomogeneous approaches, as shown in Eq. 5.11. If an inhomogeneous approach to momentum were to be employed, the velocity term in Eq. 5.11 would be phase specific. A simple volume conservation law used, which states that volume fractions must sum to unity within the control volume.

$$\frac{\partial}{\partial t}(r_\alpha \rho_\alpha) + \nabla \cdot (r_\alpha \rho_\alpha \boldsymbol{U}) = \Gamma_{\alpha\beta} \tag{5.11}$$

The source term $\Gamma_{\alpha\beta}$ is very important to the continuity equation. It describes the interphase mass flow rate per unit volume from one phase to another. The source term is direction specific. For example, phase change due to boiling would yield a positive value for the source term in the vapour phase continuity equation, and a negative value for the liquid phase continuity equation, with the opposite occurring for phase change due to condensation. However the source term is not exclusive to boiling and condensation, and may be used to model a diverse range of applications such as melting, solidification and isothermal cavitation. The interphase mass flow rate per unit volume due to thermal phase change is expressed in Eq. 5.12. This is the bulk phase change model that was mentioned earlier. It can accommodate both boiling and condensation and is the product of the interfacial area density (IAD), $A_{\alpha\beta}$ and interphase mass transfer rate, $\dot{m}_{\alpha\beta}$, which itself is described by the liquid side interfacial heat flux $\dot{q}_\alpha = h_\alpha(T_\alpha - T_{sat})$, divided by the enthalpy of vaporisation ΔH_{lg}. The IAD is fundamental to this investigation, and is discussed in the following subsection.

$$\Gamma_{\alpha\beta} = A_{\alpha\beta}\dot{m}_{\alpha\beta} = A_{\alpha\beta}\frac{h_{\alpha\beta}(T_\alpha - T_{sat})}{\Delta H_{lg}} \tag{5.12}$$

Heat transfer is the main driving mechanism for the flow phenomena studied in this work. It is responsible for driving the entire system and is tightly coupled with momentum and continuity. Heat transfer across the boundaries and into the liquid causes the density variations and allows the liquid to recirculate. This was modelled by the momentum equation. At the same time heat transfer in the liquid caused it to reach saturation conditions, leading to evaporative mass transfer, which were modelled by adding source terms to the continuity equations. It is prudent then to model heat transfer as accurately as possible.

A homogeneous approach for energy transport is appropriate in situations where thermodynamic equilibrium can be assumed between both phases, due to very fast interphase heat transfer from one phase to the other, assumed to be almost instantaneous. This can be modelled by solving for a common temperature field, or by solving for individual phasic internal energy or static enthalpy fields, with thermodynamic equilibrium enforced by setting an extremely large interphase heat transfer coefficient between the two phases. Neither was appropriate for this application, as Eq. 5.12 indicates that interphase mass transfer takes place at a finite rate, governed by a finite interfacial heat transfer coefficient and interfacial area density. Therefore, the homogeneous approach to energy transport would not have allowed saturated vapour to be modelled at a different temperature that is in contact with the liquid. Hence an inhomogeneous approach to the energy conservation equation was required which allowed each phase to possess individual temperature fields, and did not assume instantaneous interphase heat transfer. The inhomogeneous energy conservation equation for the liquid phase which was used is described by Eq. 5.13.

$$\frac{\partial}{\partial t}(r_\alpha \rho_\alpha H_\alpha) + \nabla \cdot (r_\alpha \rho_\alpha \boldsymbol{U_\alpha} H_\alpha - r_\alpha \lambda_\alpha \nabla T_\alpha)$$

$$= r_\alpha S_\alpha + \sum_{\beta=1}^{N_p} Q_{\alpha\beta} \tag{5.13}$$

The term S_α denotes the total external heat source per unit volume to phase α, and $Q_{\alpha\beta}$ denotes the interphase heat transfer to the phase α from phase β. This includes contributions from both sensible heating and interphase mass transfer.

Since an inhomogeneous approach to energy was employed for the liquid phase, there is an expectation that an equivalent energy conservation equation for the vapour phase should also be used. However it was assumed that the vapour phase was at saturation conditions at all times, which requires only the saturated pressure and temperature to be known. This was determined using Antoine’s thermodynamic relation which was described in CHAPTER 4.

Constant properties were used for the water phase, and the Boussinesq approximation was use to predict the density variations in the liquid. An ideal gas approximation was used for the vapour phase.

In summary, a homogeneous approach to momentum and turbulence was taken. An inhomogeneous approach to energy was adopted, allowing each phase to possess its own temperature field. It is interesting to note that simulating phase change using a homogeneous energy approach is termed the equilibrium phase change model, and the opposite of this is the non-equilibrium phase change model.

5.7 Interphase Heat Transfer

The interphase heat transfer term in Eq. 5.13, denoted by $Q_{\alpha\beta}$, describes the interphase heat transfer to the liquid phase α from the vapour phase β. It takes the formulation shown in Eq. 5.14.

$$Q_{\alpha\beta} = A_{\alpha\beta}\dot{q}_{\alpha\beta} \tag{5.14}$$

The interfacial heat flux $\dot{q}_{\alpha\beta}$ is determined by applying an overall heat balance across the interphase contact area, including contributions from both sensible heat flux, and heat flux due to interphase mass transfer. The sensible heat fluxes from the interface into both phases are denoted by Eq. 5.15.

$$\dot{q}_{\alpha s} = h_\alpha(T_s - T_\alpha), \qquad \dot{q}_{\beta s} = h_b\left(T_s - T_\beta\right) \tag{5.15}$$

In Eq. 5.15 T_s denotes the interfacial temperature. Assuming thermodynamic equilibrium at the interface, $T_s = T_{sat}$. Since the vapour is assumed to be saturated at all times, there is negligible sensible heat transfer to the vapour phase, but significant heat transfer to the subcooled liquid phase. A zero resistance approach was adopted for the vapour phase, using a large vapour-side heat transfer coefficient $h_b \to \infty$. This had the effect of forcing the vapour temperature to be the same as the interfacial temperature, which was assumed to be the saturation temperature at all times (determined by Antoine's thermodynamic relation, which was described in CHAPTER 4).

The interfacial heat transfer coefficient h_α was prescribed in terms of the dimensionless Nusselt number, Nu which was defined as shown in Eq. 5.16 in terms of the interfacial length scale, $L_{\alpha\beta}$ and mixture conductivity $\lambda_{\alpha\beta}$.

$$\mathrm{Nu} = \frac{h_\alpha L_{\alpha\beta}}{\lambda_{\alpha\beta}} \tag{5.16}$$

The interfacial length scale was related to the interfacial area density, and is discussed in the next sub section. Pure conduction was assumed to occur across the interphase contact area as shown in Eq. 5.17.

$$\dot{q}_{\alpha s} = \left(\lambda_\alpha \frac{T_\alpha - T_{sat}}{L_{\alpha\beta}}\right)\vec{n} \tag{5.17}$$

The relation in Eq. 5.17 assumed pure conduction occurred normal to the interface, $\vec{n}$. From Eq. 5.17 the equivalent "conductive heat transfer coefficient" was described by Eq. 5.18.

$$h_\alpha \equiv \lambda_{\alpha\beta} \frac{1}{L_{\alpha\beta}} \tag{5.18}$$

This expression was substituted into Eq. 5.16 to yield a value of 1 for the interfacial Nusselt number, which controlled the interfacial heat transfer depending on the value of the length scale $L_{\alpha\beta}$. Sun et al., (2012) used the assumption of pure conduction across the water - vapour interface with success to develop a volume-of-fluid phase change model. The assumption performed well when it was benchmarked against a one dimensional Stefan problem and a two dimensional film boiling problem which yielded excellent agreement between the analytical solutions and the simulated results.

Finally, the total interfacial heat fluxes to phases α and β, including both sensible heat fluxes, and contributions due to phase change, are given by Eq. 5.19.

$$\dot{q}_{\alpha\beta} = \dot{q}_{\alpha s} + \dot{m}_{\alpha\beta} H_{\alpha s}, \qquad \dot{q}_{\beta\alpha} = \dot{q}_{\beta s} - \dot{m}_{\alpha\beta} H_{\beta s} \tag{5.19}$$

In Eq. 5.19, $\dot{q}_{\alpha\beta}$ denotes the total interfacial heat flux to phase α from phase β, $\dot{m}_{\alpha\beta}$ denotes the interfacial mass flux to phase α from phase β, and $H_{\alpha s}$, $H_{\beta s}$ denote interfacial values of liquid and vapour phase enthalpies.

From an overall heat balance $\dot{q}_{\alpha\beta} + \dot{q}_{\beta\alpha} = 0$, and Eq. 5.19 determines the interfacial mass flux:

$$\dot{m}_{\alpha\beta} = \frac{\dot{q}_{\alpha s}+\dot{q}_{\beta s}}{H_{\beta s}-H_{\alpha s}} \tag{5.20}$$

Under the additional assumption of zero resistance to heat transfer on the vapour side, and assuming that interfacial enthalpies are equal to the liquid and vapour saturation enthalpies, $H_{\alpha s} = H_{\alpha,sat}$, $H_{\beta s} = H_{\beta,sat}$, Eq. 5.20 determines Eq. 5.12, repeated here for convenience,

$$\Gamma_{\alpha\beta} = A_{\alpha\beta}\dot{m}_{\alpha\beta} = A_{\alpha\beta}\frac{h_{\alpha}(T_{\alpha}-T_{sat})}{\Delta H_{lg}} \tag{5.12 repeated}$$

where $\Delta H_{lg} = H_{\beta,sat} - H_{\alpha,sat}$ is the latent heat of vaporisation.

5.8 The Interfacial Area Density

The governing conservation equations for mass, momentum and energy are time-averaged. The two phases in this study, water and vapour are treated as interpenetrating continua. Due to the averaging process, all of the information regarding the contact area between the phases per unit volume is lost, and therefore needs to be prescribed to the CFD solver. This is called the interfacial area density. It is also sometimes called the interfacial area concentration. Hence within the framework of Eulerian – Eulerian flow, interface structures and their positions can be tracked, however the contact area per unit volume of the phases, that is the interfacial area density, IAD, is a fundamental variable which also needs to be modelled.

Good predictions of the IAD are imperative, since the interfacial transfer of momentum, heat and mass is directly dependent on the contact surface area between the two phases. There are a number of correlations which attempt to describe the IAD. Unfortunately, a universal correlation does not yet exist for the IAD to describe all types of flow, since many flows are chaotic and contain a combination of complex morphologies such as free surface, bubbly and droplet flows. Researchers at the Helmholtz Zentrum Dresden Rossendorf (HZDR) in Dresden, Germany have developed an algebraic interfacial area density (AIAD) model which attempts to describe the interfacial contact area general gas-liquid and liquid-liquid flow (Thomas Höhne and Lucas, 2011). However, this has only been validated using non-phase change applications, and requires further development and validation before it may be used for problems with phase change.

ANSYS CFX contains a simpler algebraic model for the IAD, known as the mixture model, which treats both fluids symmetrically, as indicated by Eq. 5.21. In the ANSYS Fluent software, it is called the symmetric model (Ansys, 2011).

$$A_{\alpha\beta} = \frac{r_\alpha r_\beta}{L_{\alpha\beta}} \tag{5.21}$$

The quantity $L_{\alpha\beta}$ is known as the interfacial length scale. It must be prescribed by the user as a constant value, or as a function of the flow field. Thus, the mixture model is not a uniquely defined model in its own right. Rather, it is a tool to enable researchers to investigate specific models which conform to this structure, as was done here. The formulation can be used to attempt to model all kinds of flow, such as dispersed gas in a continuous liquid, dispersed liquid in a continuous gas, or the interactions between two continuous fluids (Thomas Höhne and Lucas, 2011).

5.9 The Interfacial Length Scale

The interfacial length scale brings closure to all of the models that have been discussed here. In this work, an expression for $L_{\alpha\beta}$ was derived for boiling and condensing flows which was applied to the expression for the IAD in Eq. 5.21, and was an extension of the work of Lee (1980) , who developed a bulk phase change model. Before the proposed formulation is discussed for the interface length scale, $L_{\alpha\beta}$ that was used, the model of Lee (1980) is first introduced.

5.9.1 The Lee (1980) Bulk Phase Change Model

Lee (1980) developed a generalised bulk phase change model, which was used to simulate liquid - vapour phase change, as shown in Eq. 5.22. The model provided the volumetric mass transfer rate for boiling or condensation, which had units of kg/m^{3}s. Detailed derivations of this model can be found in the texts by Lee (1980).

$$\begin{aligned} \Gamma_{\alpha\beta}^{+} &= \beta r_\alpha \rho_\alpha \frac{T_\alpha - T_{sat}}{T_{sat}}, \quad T_\alpha > T_{sat}, \quad \text{Liquid phase (boiling)} \\ \Gamma_{\alpha\beta}^{-} &= \beta r_\beta \rho_\beta \frac{T_{sat} - T_\beta}{T_{sat}}, \quad T_\beta < T_{sat}, \quad \text{Vapour phase (condensation)} \end{aligned} \tag{5.22}$$

The model is a function of a phase change rate constant, β, which has units of frequency and takes a value depending on the flow regime. In the work of Lee (1980) it was taken to be 0.1 Hz.

Yang et al., (2008) implemented Lee's model (1980) as a source term in the continuity equations using the CFD code ANSYS Fluent to predict boiling flows of refrigerant R141B in a coiled tube. An experimental investigation was first undertaken to achieve a benchmark to test the CFD results against. The CFD methods used the specialised Eulerian – Eulerian volume of fluid (VOF) method to track the liquid – gas interface during phase change. The reported interface structures were consistent with those observed in the experiments, as shown in Figure 5.5, and the numerically reported heat fluxes and temperatures corresponded with the experimental readings.

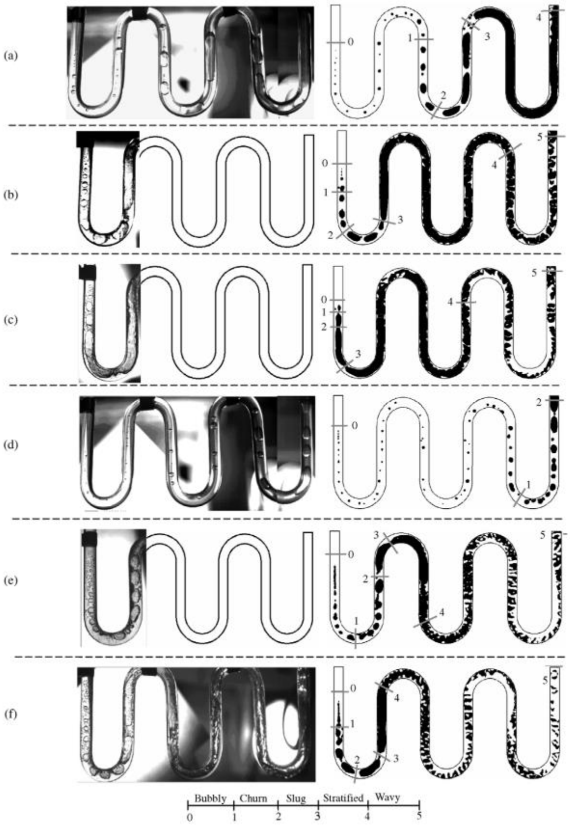

Figure 5.5: Works by Yang et al., (2008) using the bulk boiling model proposed by Lee (1980) implemented into the commercial CFD package Ansys Fluent. Left hand side indicates flow patterns from experiment, right hand side indicates flow patterns from the numerical study.

Yang et al., used a phase change rate constant of 100 Hz in their investigations. Larger values of β caused their simulations to diverge, whereas smaller values caused significant deviation between the interfacial temperature and the saturation temperature.

DeSchepper et al., (2009) also implemented the model of Lee (1980) into the CFD code ANSYS Fluent, to simulate the evaporation of hydrocarbon feedstock in a steam cracker. The same modelling approach as Yang et al. (2008) was used. In addition to this, DeSchepper et al., also attempted to include heat transfer contributions to the energy fields due to phase change. This was modelled using additional source terms in the energy equations, by appending the latent heat of vaporisation or condensation to the original expressions as shown in Eq. 5.23. The energy conservation equations were not treated by Yang et al. (2008).

$$\begin{aligned} &\Gamma_{\alpha\beta}^{+} = \beta r_\alpha \rho_\alpha \frac{T_\alpha - T_{sat}}{T_{sat}} \Delta H_{lg}, \quad T_\alpha > T_{sat}, \qquad \text{Liquid phase (boiling)} \\ &\Gamma_{\alpha\beta}^{-} = \beta r_\beta \rho_\beta \frac{T_{sat} - T_\beta}{T_{sat}} \Delta H_{lg}, \quad T_\beta < T_{sat}, \quad \text{Vapour phase (condensation)} \end{aligned} \tag{5.23}$$

In their work DeSchepper et al., benchmarked their CFD simulations against industrial data for the mass weighted volume fraction of the liquid phase at the outlet. For their given conditions, industrial plant data suggested that the mass weighted volume fraction of the liquid at the outlet of the hydrocarbon steam cracker was equal to 0.3. The CFD simulations predicted a value of 0.49. It was suggested that the discrepancy occurred due to the simplifications made in the boundary conditions in the CFD model. Interestingly DeSchepper et al. used a value of 0.1 Hz for the phase change rate constant, which was orders of magnitude smaller than that of Yang et al., (2008).

Alizadehdakhel et al., (2010) also used the model to predict phase change in a closed loop thermosyphon system, and compared the CFD results to experimental data. The numerical implementation was the same as DeSchepper et al., (2009), including the specification of 0.1 Hz for the phase change rate constant. In the experimental work, surface temperatures as a function of heat transfer rate inside the thermosyphon were measured, and this was used as the basis for comparison in the equivalent CFD work. There was good agreement between the experimental data and the CFD investigation for the temperature profiles inside the thermosyphon.

Finally, Goodson *et al.*, (2010) used the model to simulate boiling flows in a vapour venting micro channel, and compared simulation results to experimental data performed by other authors. The CFD results compared well against the flow patterns and interface structures produced in the equivalent experimental study. The study by Goodson *et al.*, (2010) was the only one shown to have been used with success at small scales (micro channels), whereas the other studies concentrated on larger scales. In their work, Goodson *et al.*, (2010) used a phase change rate constant of 100 Hz to compute their simulations.

Many other authors have used the model of Lee (1980) in CFD solvers, for a range of engineering applications. In the works discussed above, it is interesting to note that the large range of values taken for the value of the phase change rate. Lee (1980), DeSchepper et al. (2009) and Alizadehdakhel et al., (2010) all used a value of 0.1 Hz, whereas the works by Yang et al., (2008) and Goodson *et al.*, (2010) used a value of 100 Hz. Clearly, a universal value of the rate constant does not exist, and must be determined for each application.

The model by Lee (1980) was used in this work to form the basis of prescribing an expression for the interface length scale $L_{\alpha\beta}$, which was required for the interfacial area density in Eq. 5.21 which closed the Eulerian – Eulerian approach.

5.10 Proposed Interfacial Length Scale

In this work, the Lee (1980) phase change model in Eq. 5.22 is generalised by introducing a complementary volume fraction term, as shown in Eq. 5.24. This ensures that, when either one of the volume fractions r_α or r_β approaches zero, the interphase mass transfer rate also approaches zero.

$$\Gamma_{\alpha\beta} = \beta r_\alpha r_\beta \rho_\alpha \frac{T_\alpha - T_{sat}}{T_{sat}} \tag{5.24}$$

Only the liquid phase is taken into consideration. This is because, in this work, the vapour phase is assumed to be at the saturation temperature at all times, and therefore $\frac{T_{sat}-T_\beta}{T_{sat}} = 0$. This does not mean in the formulation for the length scale $L_{\alpha\beta}$, condensation was disregarded since in Eq. 5.24 when $T_\alpha < T_{sat}$ would occur. Hence, a more generalised form of Eq. 5.24 replaces the phase specific density with the mixture density as described by Eq. 5.9, resulting in the generalised form in Eq. 5.25.

$$\Gamma_{\alpha\beta} = \beta r_\alpha r_\beta \rho_{\alpha\beta} \frac{T_\alpha - T_{sat}}{T_{sat}} \tag{5.25}$$

The bulk thermal phase change model that was used was described in Eq. 5.12. Replacing the IAD term $A_{\alpha\beta}$ in Eq. 5.12 for its definition in Eq. 5.21 yielded Eq. 5.26.

$$\Gamma_{\alpha\beta} = \frac{r_\alpha r_\beta}{L_{\alpha\beta}} \frac{h_\alpha (T_\alpha - T_{sat})}{\Delta H_{lg}} \tag{5.26}$$

The bulk thermal phase change model defined in Eq. 5.26 is analogous to the generalised model by Lee (1980) , defined by Eq. 5.25. Equating these provides a relationship between the interface length scale $L_{\alpha\beta}$ and the phase change rate constant β as shown in Eq. 5.27.

$$\frac{r_\alpha r_\beta}{L_{\alpha\beta}} \frac{h_\alpha (T_\alpha - T_{sat})}{\Delta H_{lg}} = \beta r_\alpha r_\beta \rho_{\alpha\beta} \frac{T_\alpha - T_{sat}}{T_{sat}} \tag{5.27}$$

The volume fraction terms and temperature difference terms cancelled out. This yielded the expression as shown in Eq. 5.28.

$$L_{\alpha\beta} = \frac{h_\alpha}{\beta} \frac{T_{sat}}{\Delta H_{lg}} \frac{1}{\rho_{\alpha\beta}} \tag{5.28}$$

The heat transfer coefficient in Eq. 5.28 is replaced with the Nusselt number correlation described by Eq. 5.16. This allows the final expression for the interfacial length scale to be determined as shown in Eq. 5.29.

$$L_{\alpha\beta} = \left(\frac{\mathrm{Nu}}{\beta}\frac{T_{sat}}{\Delta H_{lg}}\frac{\lambda_{\alpha\beta}}{\rho_{\alpha\beta}}\right)^{1/2} \tag{5.29}$$

Therefore substituting the proposed interfacial length scale into the expression for the IAD in Eq. 5.21 completes the Eulerian – Eulerian model. The IAD with the proposed length scale model is shown in Eq. 5.30.

$$A_{\alpha\beta} = \frac{r_\alpha r_\beta}{L_{\alpha\beta}} = r_\alpha r_\beta \left(\frac{\mathrm{Nu}}{\beta}\frac{T_{sat}}{\Delta H_{lg}}\frac{\lambda_{\alpha\beta}}{\rho_{\alpha\beta}}\right)^{-1/2} \tag{5.30}$$

The proposed length scale is a function of the flow dynamics, which therefore allows the IAD to be a function of the flow dynamics. It is applicable at a saturated interface which has thermal conductivity and density mixture properties, $\lambda_{\alpha\beta}$ and $\rho_{\alpha\beta}$, which depended on the phase volume fraction. The interfacial Nusselt number can take any value the user requires. The model must be fine-tuned for individual applications by determining the value of the rate constant β for each application.

In this work an interfacial Nusselt number of unity is taken, as derived in section 5.7. A range of values was tested for the rate constant, and their results were compared to experimental data reported by McNeil et al., (2015). The values tested range from 0.1 Hz to 100 Hz, and correspond to the range reported in the literature discussed in section 5.9.1. The effect the rate constant has on the interfacial length scale and on the IAD is displayed in Figure 5.6. For the graph, the thermophysical properties of water were evaluated at 50 mbar saturated pressure (ullage pressure used in the work by McNeil et al., (2015)) and assuming the volume fractions are at 0.5.

In Figure 5.6 the effect on the length scale and interfacial area density can be observed when increasing the rate constant. Beginning with rate constant of 0.1 Hz, as used by Lee (1980), DeSchepper et al., (2009) and Alizadehdakhel et al., (2010) yields an interface length scale of 0.9 mm, which corresponds to an interfacial area density less than 1000 m^{-1}. Increasing rate constant decreases the interfacial length scale, yet increases the interfacial area density. At a rate constant of 100 Hz, which was used by Yang et al., (2008) and Goodson et al., (2010), the interfacial length scale becomes very small, less than 0.1 mm, but the interfacial area density increases to approximately 9000 m^{-1}.

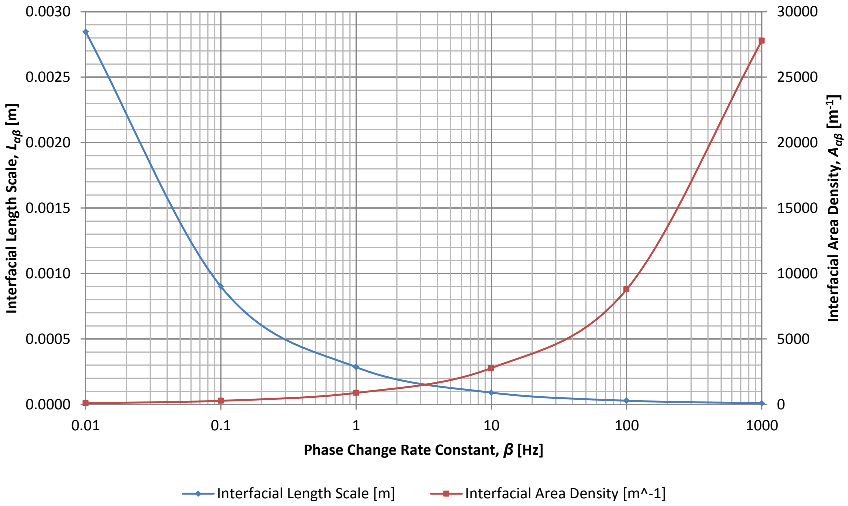

Figure 5.6: Interfacial length scale and area density as a function of the phase change rate constant assuming interfacial volume fractions for both phases are 0.5. Note the horizontal axis is logarithmic.

5.11 Energy and Material Balance

In the simulations, bulk evaporation was modelled. The bulk rate of evaporation was not reported in the works of McNeil et al., (2015). Therefore, this was evaluated by performing an energy and material balance, so that the experimental evaporation rates could be compared to the evaporation rates produced by the CFD simulations. The energy balance is shown in Eq. 5.31.

$$\dot{E}_{coils} + \dot{E}_{feed} - \dot{E}_{environment} - \dot{E}_{evap} = 0 \tag{5.31}$$

In the experimental test rig, there were 36 electrically heated tubes, and for the experimental configuration which the CFD simulations were benchmarked against, each tube operated at a heat flux of 65 kW/m^2. The outside surface area of each tube is 0.316 m^2, therefore the total energy input from 36 coils was calculated at 20532 W. The feed was assumed to enter the test rig at a temperature of 11 °C, and at the same rate as the vapour leaving the free surface, which maintained a constant level. McNeil et al., (2015) reported that the cooling power of the condenser was found to be 96% of the heating power. This suggests 4% of the heating power was attributed to heat loss, which is 821 W. Lastly, heat was lost at the free surface due to evaporation at 50 mbar. The completed energy balance is shown in Eq. 5.32.

$$20532\ [\mathrm{W}] + \dot{M}_{feed}\Delta H_{l,feed}[W] - 821[W] - \dot{M}_{evap}\Delta H_{lg,evap}[W] = 0 \tag{5.32}$$

The single phase enthalpy of feed $\Delta H_{l,feed}$ at 11 °C was known, and the enthalpy of vaporisation at the free surface $\Delta H_{lg,evap}$ was also known. In addition to this, the rate of evaporation was assumed to be the same as the rate of feed, therefore the overall evaporation and feed rates were determined to be 0.0078 kg/s.

5.12 Initial Conditions

The initial conditions of the simulations were set to the same conditions that were used in the low pressure low level experimental test. Thus, the initial liquid depth was 0.8 m, and the ullage pressure was 50 mbar. In the tests, the ullage region was devoid of air, and consisted of pure saturated vapour, with pressure and temperature of 50 mbar and 32.8 ºC. The initial temperature of the water was set to 31.8 °C. This was justified as a means of accelerating the thermal flow fields of the water. The initial velocity was set to 0 mm/s, with a mean global turbulence intensity set to 5%. The heat flux on the coils were set to 65 kW/m^2, and all other surfaces had the heat loss heat transfer coefficients applied to them, as described by Eq. 5.1. The ambient outside temperature was assumed to be 15 ºC. Initially the value of the rate constant was set to 0.1 Hz.

5.13 Solution Strategy

The solution strategy used for the simulations on the scaled test rig was not the same as that for the unscaled test rigs. The strategy used is as follows:

1. Three significantly different meshes were generated, where each successive mesh increased in element density according to the Grid Convergence Index (GCI) procedure (Celik et al., 2008), described in CHAPTER 3.
2. A steady free convection simulation was performed on mesh 1 (the boiling model was not activated), beginning from the initial conditions. The purpose of this step was to establish and stabilise the flow fields for the next step.
3. In this step, the mesh sensitivity study was performed. Transient free convection simulations were performed on meshes 1 to 4, using the results of the steady free convection simulation as the initial condition. This step was also used to generate the the initial conditions for subsequent bulk boiling simulations. The dimensionless T^* scale, described in CHAPTER 4, was monitored at three points equidistant on a horizontal line, and 2 cm below the free surface, as shown in Figure 5.7. Since the simulations were multiphase, the dimensionless T^* scale became phase specific. Hence T^* in the water phase is denoted by T_α^*. The transient free convection simulations were set to stop when $T_\alpha^* = 0$ at any one of these three points, as this indicated that phase change was imminent.

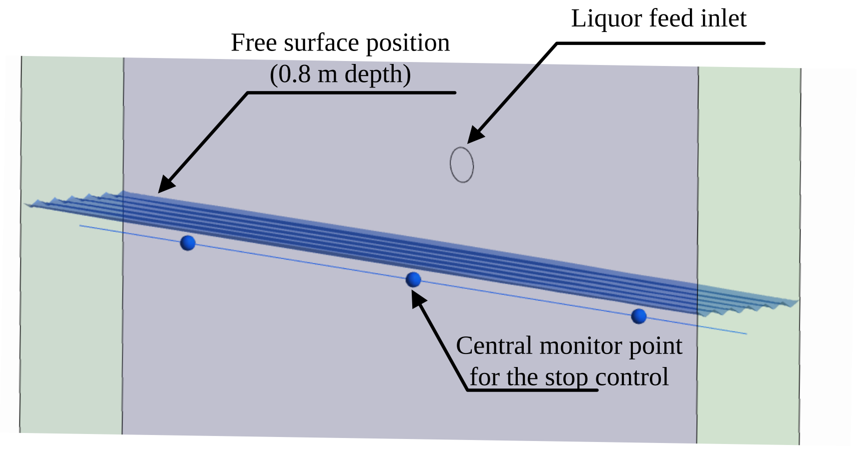

Figure 5.7: Three equidistant points 2 cm below the free surface were monitored to enable a stop control to stop the transient free convection simulations when $T_\alpha^* = 0$ at any of these points.

When $T_\alpha^* > 0$ boiling may occur, and when $T_\alpha^* < 0$ the liquid is subcooled. The reason for this procedure is that, if a boiling simulation is started from an initial guess with significantly superheated liquid, the CFD code tends to diverge very quickly, due to the large amount of vapour that is generated very quickly in the superheated regions (Milnes at al. 2012). At the end of the simulations, the results were analysed as part of the mesh sensitivity study, and a suitable mesh was selected for onward simulations in the phase change cases.

4. Using the chosen mesh from the sensitivity study, the bulk thermal phase change model was activated using a rate constant of 0.1 Hz. The purpose of this was to evolve the flow fields as much as possible to achieve a pseudo-steady state condition, which was subsequently used as the initial condition in the final transient simulations described in the next step. At the end of one steady state boiling simulation, the value of the rate constant was increased by a factor of 10 using the previous steady state boiling result as the initial state. This procedure was performad for four values of the rate constant, 0.1, 1, 10 and 100 Hz.
5. Finally, to home into a final converged boiling solution, transient boiling simulations were performed for 60 simulation seconds, for all four values of the rate constant. The steady state boiling results corresponding to each rate constant were employed as the initial conditions for the final transient cases.

5.14 Numerical Accuracy

The time step for the simulations was determined using the expression in Eq. 5.33 (Ansys Inc, 2010b) as a base line, and then halving it as a conservative measure to ensure the time step was within the bounds of simulation stability.

$$\Delta t = \sqrt{gL} \tag{5.33}$$

The term L is denoted to be a suitable length scale, so $L_{\alpha\beta}$ was chosen, which depended on the value of the rate constant. Using the time step selection strategy for the unscaled test rigs in this investigation caused the simulations to diverge, as that strategy produced time steps that were too large.

The residual target for all conservation equations in all simulations was 1E-5. This could not be achieved for the steady state simulations since the physical problem was transient in nature. Furthermore this level of tight convergence was not required for the steady state simulations as their purpose was to be used as a tool to accelerate the flow fields. Pseudo-steady state was ensured by monitoring key variables such as evaporation rate, temperature and velocity, and ensuring they did not fluctuate significantly with iteration. The steady state analysis used high resolution schemes for the advection and turbulence numerics.

In all transient simulations time step convergence was obtained between 1 and 11 iterations per time step, or coefficient loops. The transient cases maintained high resolution for the advection and turbulence numerics, and a second order backward Euler scheme for the transient numerics. For the transient simulations global equation imbalances of less than 1% was achieved to ensure conservation of all solved equations. This was not achieved for the steady state simulations as they were not fully converged.

Monitor points of interest, such as bulk stream temperature, bulk stream velocity, evaporation and liquor feed rates were monitored to ensure that the simulation produced physically realistic results during the solution process.

In all simulations, the implicit volume fraction coupling approach was adopted, where the volume fractions were coupled to and solved in the same matrix as pressure and velocity. This had the advantage of allowing for larger than usual time steps in otherwise time step sensitive multiphase simulations. The disadvantage was increased memory demand during the solving process. This was due to the solver performing large matrix inversions containing the variables pressure, velocity and volume fractions. This is in contrast to performing matrix inversions containing pressure and velocity variables in a segregated solver.

5.15 Computational Resources

The simulations were performed on the high performance computing facilities at the University of Leeds facility ARC2 (Advanced Research Computing 2). The simulations were performed on 3 nodes of 16 CPUs (48 CPUs) with 32GB of error correcting code memory per node available to the CFD solver. The highest solve time for the transient free convection simulations was 10 wall clock hours, and the highest solve time for the transient boiling simulations was around 340 wall clock hours. These time exclude simulation queue wait times.

5.16 Mesh Sensitivity Results

Three meshes were generated as part of the sensitivity study. The generated meshes were structured, containing hexahedral cells only. Although structured meshes are not a requirement in modern CFD applications, they are desirable since they reduce numerical diffusion, as the cells are more likely to be aligned with the direction of the flow. This was discussed in CHAPTER 3, and structured meshes were used for the work in CHAPTER 4.

The blocking strategy that was used for all three meshes is shown in Figure 5.8. Since the computational domain had the same depth everywhere, the blocking strategy used a swept approach, where the blocks were swept uniformly across the thickness of the domain. The strategy harnessed numerous block splits, which was required to perform the O-grid blocking at the coils, knuckle, and liquid feed. This approach is commonly referred to as a top-down approach. Due to the many O-grids that were required around the coils, and feed, the blocking strategy was far more complex than that of the unscaled test rigs, and required more thought in order to achieve a successful mesh.

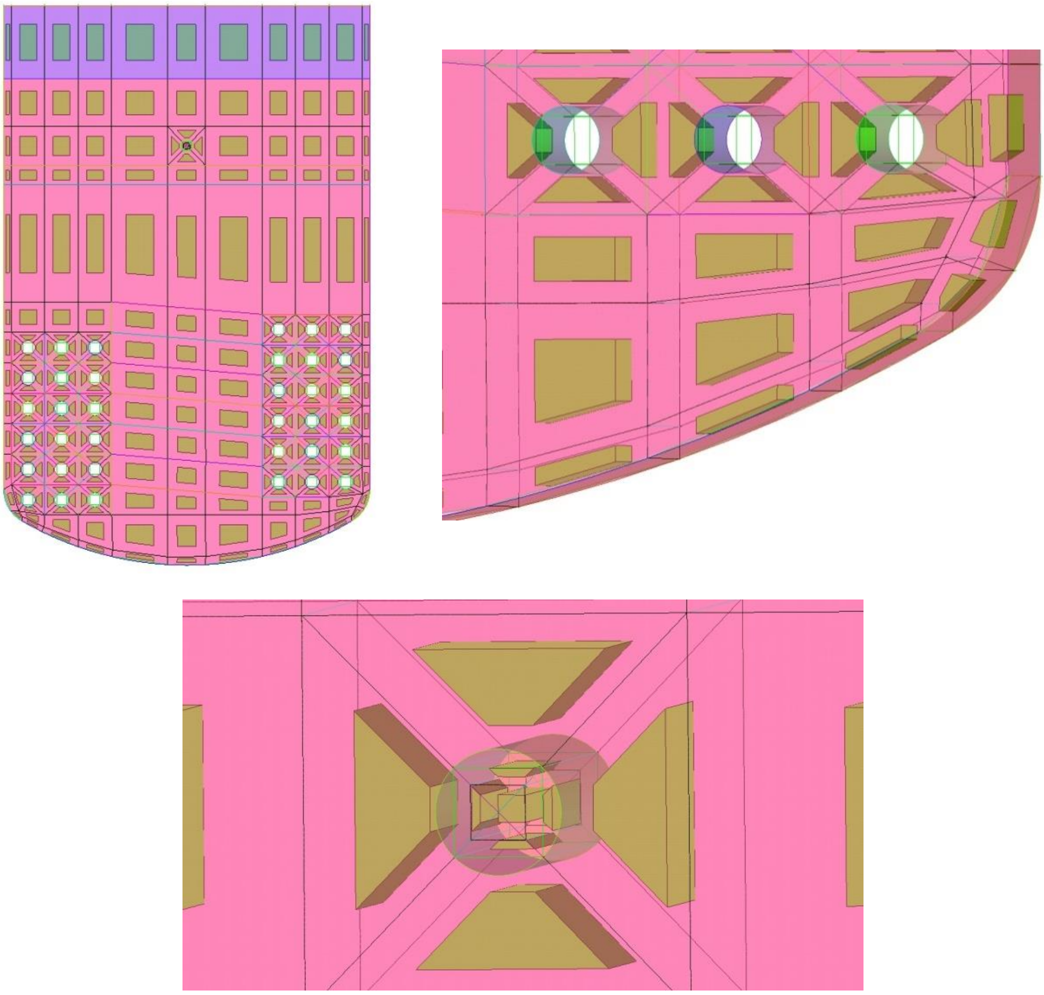

Figure 5.8: (Beginning top left, clockwise) Blocking strategy for the overall computational domain; O-Grid blocking at the coils and knuckle; double O-Grid blocking at the inlet feed.

The final mesh that was selected as the solution independent mesh is shown in Figure 5.9, which was mesh 2. There were some sudden jumps in mesh sizing, primarily at the region just below the liquid feed. Although the mesh statistics for each mesh did not violate the criteria set out in CHAPTER 4, such sudden jumps should be avoided where possible. Unfortunately, this could not be avoided, without a significantly increase in the number of cells. However since the sudden jump occurs is in the ullage head space, its effect is expected to be insignificant, since the ullage head space is not a significant area of interest to the CFD results.

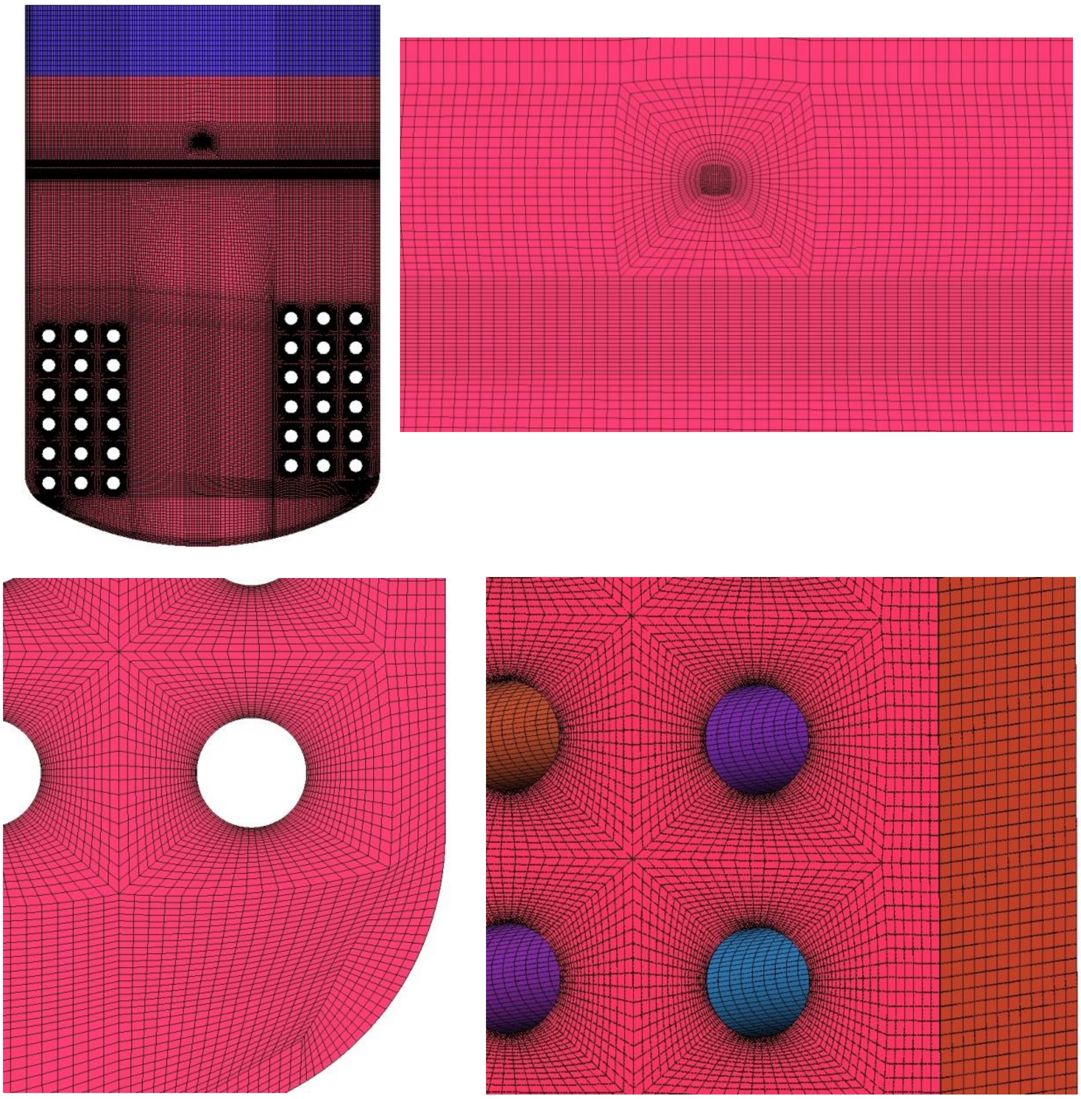

Figure 5.9: (Beginning top left, clockwise) Overall mesh in the computational domain; o-grid mesh at water inlet; uniform mesh thickness; and o-grid mesh at the coils and knuckle.

The meshes were designed to be solution independent around the coils and at the free surface. The values of Y^+ and IAD were targets as the independent variables at the coils and free surface respectively. This meant there was local mesh refinement around the coils and the free surface area.

The statistics for the three meshes which were generated are tabulated in Table 5.1. Each mesh ran a transient free convection simulation, using a rate constant of 0.1 Hz, and using the steady state free convection results as the initial state. The simulations were stopped at the onset of boiling. This was described in section 5.13 Solution Strategy. The simulation times taken to reach $T^* = 0$ at the free surface is tabulated in Table 5.1. All three meshes reached $T^* = 0$ at the free surface to within 2 s of each other. This was despite each successive mesh refining the free surface area significantly.

	Mesh Statistics				**Mesh Information**		
Mesh	**Max. Face Angle [°]**	**Min. Face Angle [°]**	**Max. Edge Length Ratio**	**Max. Element Volume Ratio**	**No. of Nodes**	**No. of Elements**	**Sim. time for $T^{*}=0$ [s]**
1	154.7	26.8	11.6	5.2	283888	249480	18.15
2	154.8	26.0	38.6	5.6	1067261	965928	18.95
3	154.9	26.0	89.0	5.6	1549436	1414530	19.95

Table 5.1: Mesh statistics for the three meshes used in the sensitivity study.

The generated values from the GCI mesh sensitivity study are tabulated in Table 5.2. The largest IAD that was produced was 1071 m^{-1} for mesh 1, and the smallest was 1012 m^{-1} for mesh 3. The percentage difference between these is 5.7%. However the discretisation error due to the meshes are far smaller. The grid convergence index between meshes 2 and 1 is 0.02%, and between 3 and 2 is 1.9%. This means the errors on the IAD values due to the meshes fall to within acceptable limits for all three meshes. In fact mesh refinement at the free surface seems to have little effect on the values of the IAD.

	ϕ = Area and transient average interfacial area density [m^{-1}]	**ϕ = Area and transient average Y^{+} on all coil surfaces**
$\boldsymbol{\phi_1}$	1071 [m^{-1}]	1.37
$\boldsymbol{\phi_2}$	1055 [m^{-1}]	0.18
$\boldsymbol{\phi_3}$	1012 [m^{-1}]	0.11
$\boldsymbol{r_{21}}$	1.570	1.570
$\boldsymbol{r_{32}}$	1.136	1.136
$\boldsymbol{P}$	10.41	2.52
$\boldsymbol{\phi_{ext,21}}$	16 [m^{-1}]	1.75
$\boldsymbol{\phi_{ext,32}}$	59 [m^{-1}]	0.25
$\boldsymbol{e_{apx,21}}$	1.5%	87.0%
$\boldsymbol{e_{apx,32}}$	4.1%	38.2%
$\boldsymbol{e_{ext,21}}$	6719.4%	21.9%
$\boldsymbol{e_{ext,32}}$	1688.5%	28.2%
$\boldsymbol{GCI_{21}}$	0.02%	51.3%
$\boldsymbol{GCI_{32}}$	1.9%	126.4%

Table 5.2: Results from the mesh sensitivity study using the GCI method (Celik et al., 2008).

Relying solely on the GCI values for the IAD was superficial. Figure 5.10 (Top) shows the instantaneous values of volume fractions at the last time step at the free surface for all three meshes. With each successive mesh, smearing of the volume fractions at the free surface reduced. A sharp interface was required, since it reduced numerical diffusion across the interface, which was important since the transfer of continuity, momentum and energy occurred across this interface, which was a fundamental part of this study. Figure 5.10 (Bottom) shows how smearing was reduced for each successive mesh.

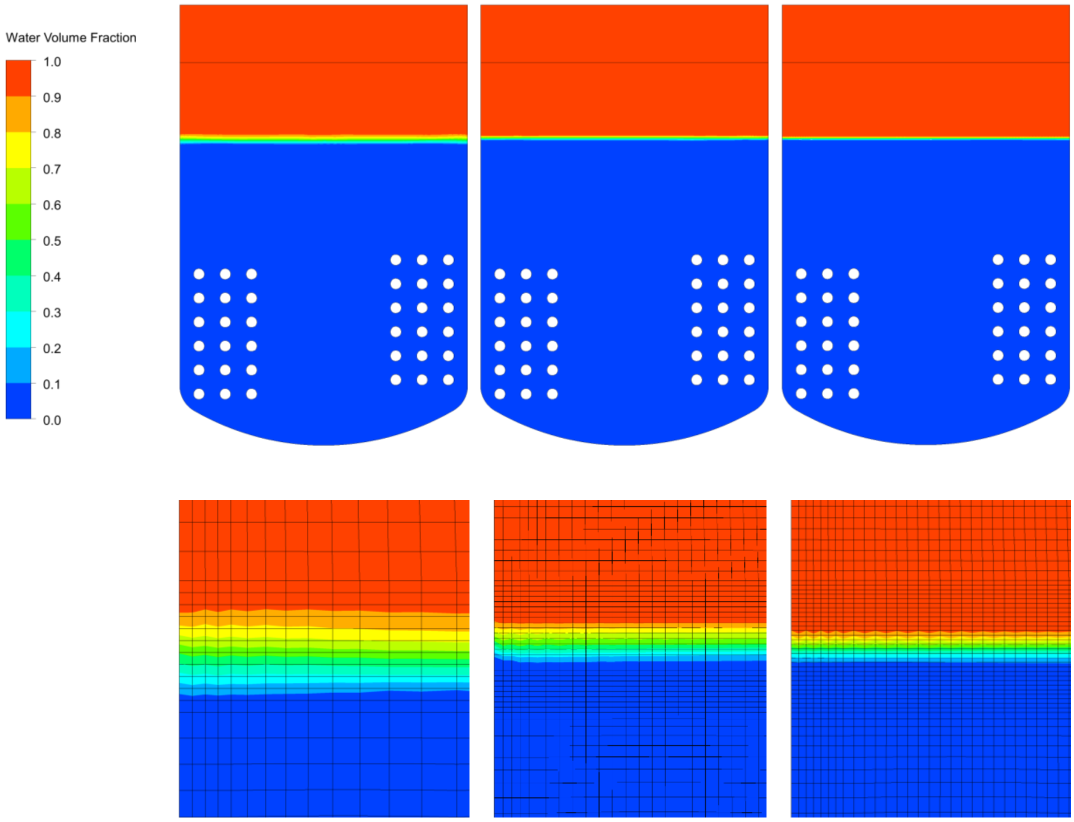

Figure 5.10: (Top) Instantaneous values of volume fractions of water at the last time step for mesh1 (left), mesh 2 (centre) and mesh 3 (right). (Bottom) Volume fractions zoomed in at the free surface, for mesh 1, mesh 2 and mesh 3 respectively. Volume fraction smearing at the free surface is reduced with each successive mesh, and hence numerical diffusion across the interface is reduced with each successive mesh.

One of the goals for the mesh sensitivity study was to refine the mesh such that a value $Y^+ < 1$ at the heated coils could be achieved. This was very difficult since Y^+ by its very definition is a function of the wall shear stress. This changes as a function of the flow regime, which over time undergoes sudden changes as is the nature of buoyancy driven flow, such as sudden reversed flow, vortex shedding and impingement at the coils. Therefore guaranteeing $Y^+ < 1$ at for all time steps was very difficult. Observing transient averaged values of Y^+ was useful as it provided mean values of Y^+ for the entire transient simulation without having to critically analyse each transient time step.

In Table 5.2 the transient averaged Y^+ values for all three meshes are listed. Mesh 1, 2 and 3 produced values of 1.37, 0.18 and 0.11 respectively. Mesh 2 and 3 demonstrated Y^+ values were less than 1, which was required for the turbulence wall treatment.

From the mesh sensitivity study mesh 2 was chosen to be the mesh independent of the solution. For the IAD Figure 5.10 (Bottom) showed further mesh refinement after mesh 2 did not significantly reduce smearing of the volume fractions at the free surface. With regards to Y^+, since the values reported were less than 1 on mesh 2, it satisfied the criteria that $Y^+ < 1$. The large errors were attributed to the large relative difference between the Y^+ values reported.

5.17 Presentation of the Results

It is very difficult to display 3D flow phenomenon in a 2D perspective. The visual results such as contours and velocity vectors are presented on the mid-plane unless explicitly stated, as shown in Figure 5.11. In order to provide a meaningful CFD analysis, the CFD results were compared to the experimental results of McNeil et al., (2015). One of the methods used was to compare experimental thermocouple data with CFD temperature data at the same locations where the thermocouples existed in the test rig. The thermocouple positions are shown in Figure 5.3 (Right). The contours of volume fraction in Figure 5.10 were plotted on the mid-plane shown in Figure 5.11.

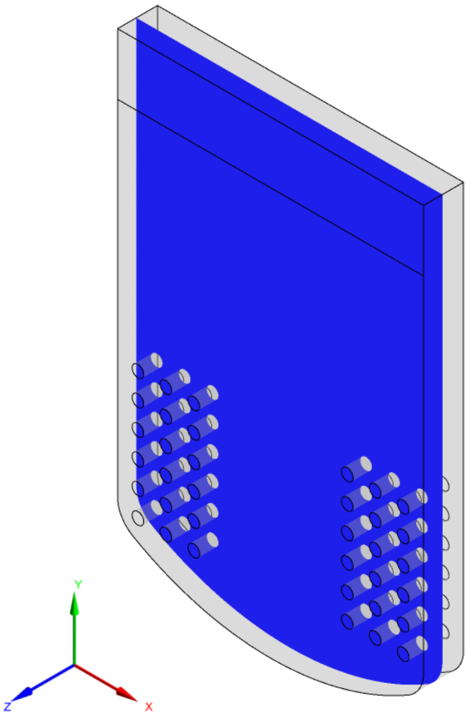

Figure 5.11: Mid plane (blue) in the computational domain where the results are plotted on.

5.18 Results: Free Convection, $\beta = 0.1$ Hz

Since the transient free convection simulations were also used for the simulations in the mesh sensitivity study, only the results from mesh 2 are shown, which was the mesh selected in the study for further work. Figure 5.12 displays the root mean square residuals of the transient free convection simulation on mesh 2, and a rate constant rate constant, $\beta = 0.1$ Hz. Convergence of all equations per time step was achieved to a maximum root mean square residual of 1x10^{-5}. Coefficient loop convergence per time step is not shown on the graph. The simulation took 18.95 simulation seconds to reach $T^* = 0$ on the stop control on the right hand side of the domain (see Figure 5.7). The residual graph is a representative example and subsequent residual graphs for the other simulations discussed will not be shown as they were identical.

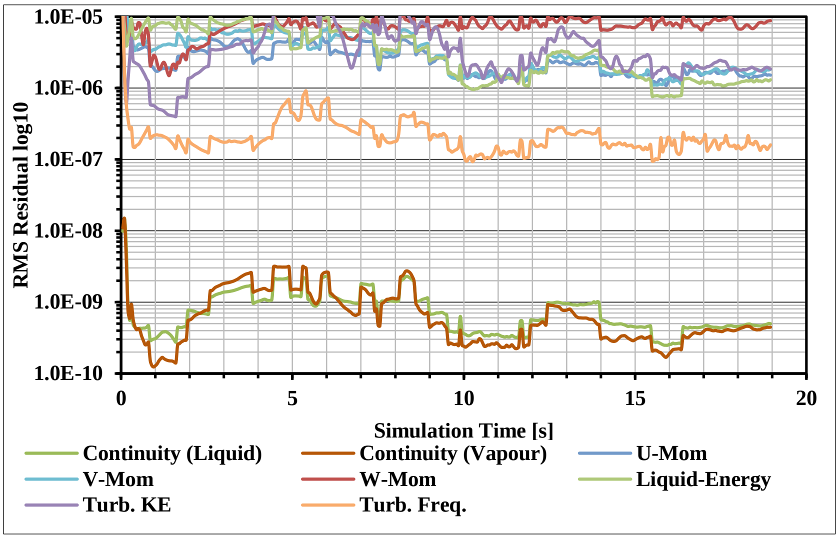

Figure 5.12: Root mean square residuals for the free convection simulation using mesh 2 and a rate constant of 0.1 Hz.

Figure 5.13 (Top) displays the stream temperatures corresponding to each respective thermocouple location. The readings begin between 32°C and 33°C for all thermocouple locations. This provided the initial conditions in step 2, outlined in the subsection 5.13 Solution Strategy. During the course of the simulation the stream temperatures do not fluctuate more than 38°C, and on observation, all temperatures fluctuate around the 34°C mark. The saturation temperature at the free surface corresponding to 50 mbar is 33°C. During the simulation, the bulk liquid temperature throughout the domain remains close to the saturation temperature at the free surface. McNeil et al., (2015) also witness a similar pheonomena in their boiling studies, where the stream temperatures were very close to the free surface saturation temperature.

Figure 5.13 (bottom) represents the fluid temperatures between the coils of the right hand side tube bank in the geometry (see Figure 5.7 for clarification). In a similar fashion to the stream temperatures, the fluid temperatures are in close agreement to the free surface saturation temperature, despite a heat flux of 65 kW/m^2 being driven through each heating coil. The information in Figure 5.13 suggests that heat is quickly dissipated, due to advection rather than diffusion. If the dissipation was dominated by diffusion then the stream and fluid temperatures would be much higher, corresponding to pure conduction in the liquid.

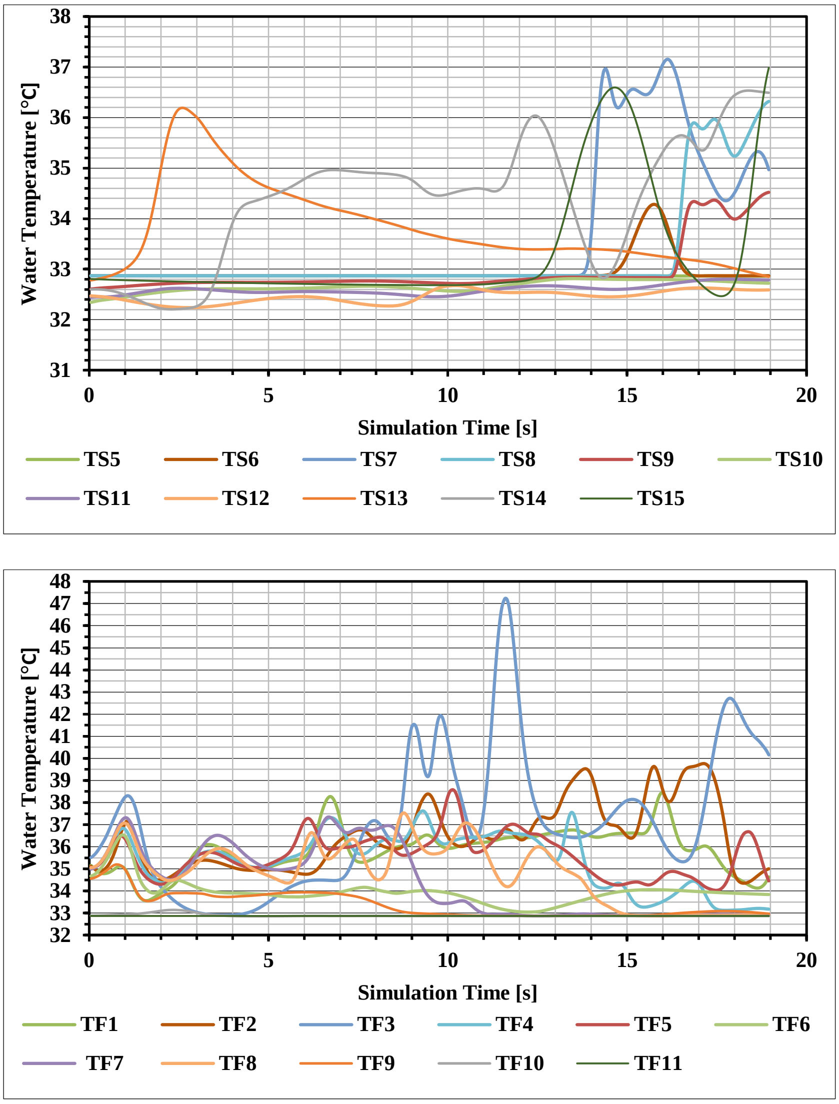

Figure 5.13: Temperature plots from the transient free convection simulation, on mesh 2, and β = 0.1 Hz. (Top) stream temperatures, (bottom) fluid temperatures.

One of the advantages of the CFD analysis is its ability to output information in a more complete way than the capabilities of experimental analysis. Figure 5.14 (Top) represents T^* variations in the water corresponding to the stop control positions (see Figure 5.7 for clarification) and respective stream thermocouple positions. The values are all negative, which indicates that the water is sub cooled below its local saturation temperature. The only value which is not negative is the one corresponding to Stop Right at the end of the simulation, which was one of three monitors which were used to control when the transient free convection simulation would stop just prior to boiling at the free surface.

Figure 5.14 (Bottom) is a plot of velocity variation at each thermocouple position. Although velocities were not produced as an output in the experimental works of McNeil et al., (2015), they are outputted here as they complement the data set. The highest velocities are 80 mm/s and the lowest around 10 mm/s by the end of the simulation. The simulations of the tall unscaled test rig in CHAPTER 5 produced velocities of up to 230 mm/s in the centre of the draught tube, which is almost three times the velocities produced in the scaled test rig. This suggests the momentum behaviour induced due to the draught tube in the tall unscaled test rig is not indicative of the momentum behaviour found in the scaled test rig.

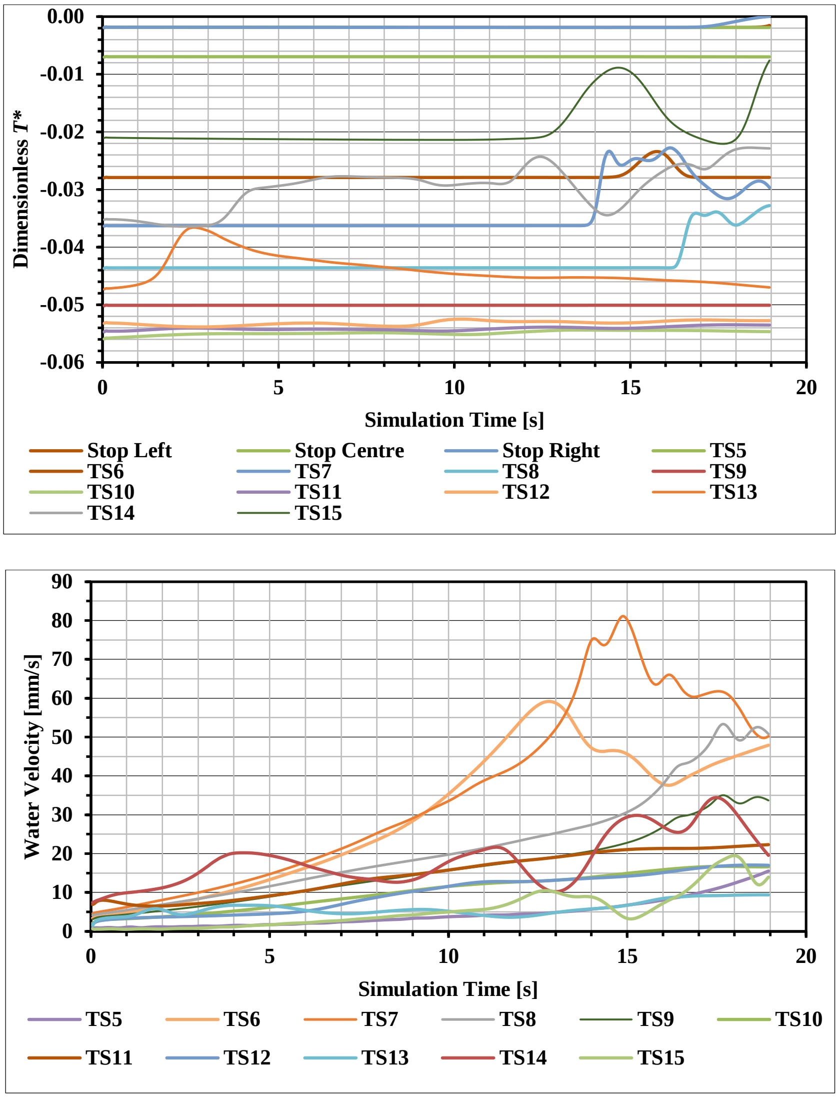

Figure 5.14: (Top) T^* variations at the three stop positions, and at the stream thermocouple positions. (Bottom) water velocity variations inside the test rig at the stream thermocouple locations.

Figure 5.15 (top) displays transient averaged contours of temperature in the liquid and on the coil surfaces. The contours of temperature in the water were clipped to a maximum of 40 °C, because the temperature contours in the liquid were dominated by a very narrow band of high temperature water next to the coils, which skewed the scale and made the analysis of the temperature distributions very difficult. For reference, in the unclipped range, the maximum transient averaged temperature in the liquid was 115 °C, directly adjacent to the coils, and the remaining bulk liquid was at 32°C. The temperature distribution in the liquid shows plumes of high temperature water rising above the coils. These plumes were localised to the upper surfaces of the coils. The contours of wall temperature show non-uniform distributions on the coil surfaces. The upper hemispheres of each coil surface were hotter than all other locations. This corresponded to the temperature distributions in the water, where plumes were seen rising above the coil surfaces.

Figure 5.15 (middle) shows the contours of time averaged T^* in the liquid and free surface, which showed values greater than 0 in the liquid directly above the coil surfaces, and having a value of 0 at the free surface. The T^* contours indicate that the water is superheated above the coils. If a wall boiling model had been activated at the coils, then nucleation may have occurred. However this is a crude approximation to the problem, since other factors which affect wall boiling such as the onset temperature of nucleate boiling, nucleation site density, and other parameters (as detailed in Section 5.4) would also need to be determined. The T^* parameter is a better bulk boiling indicator, where an interface already exists between the liquid and vapour, such as the free surface. This is because the complex parameters which are required to be satisfied for wall boiling are not required for boiling at the free surface, and is simply controlled by the transfer of latent heat across the interface. Therefore the contours of T^* at the free surface, where the values were 0 suggested boiling at the free surface, were imminent in that area.

Figure 5.15 (bottom) illustrates the transient averaged heat transfer coefficient distributions on the coil surfaces, and the streamlines on the mid plane (as shown in Figure 5.11). The bulk temperature for the heat transfer coefficient was set to 32.87 °C, which was the saturation temperature corresponding to the ullage pressure 50 mbar. The greatest heat transfer coefficients occur on the lower hemisphere of the bottom three coils of the left tube bank. These had a value of 1594 W/m^{2}K, and the lowest value was 226 W/m^{2}K which occurred on the upper hemisphere of the coils. This could be explained by observing the transient averaged streamlines and direction of flow in Figure 5.15 (bottom). The water travels down the centre of the vessel, and upward between the coils and vessel walls. Two distinct convection cells were generated. The impingement of the water on the lower surfaces of the coils induces large heat transfer coefficients. Kreith et al., (2010) suggested water which undergoes convection has heat transfer coefficients corresponding to 300–18,000 W/m^{2}K. Using this guideline, the tubes in the scaled test rig are in the convection regime.

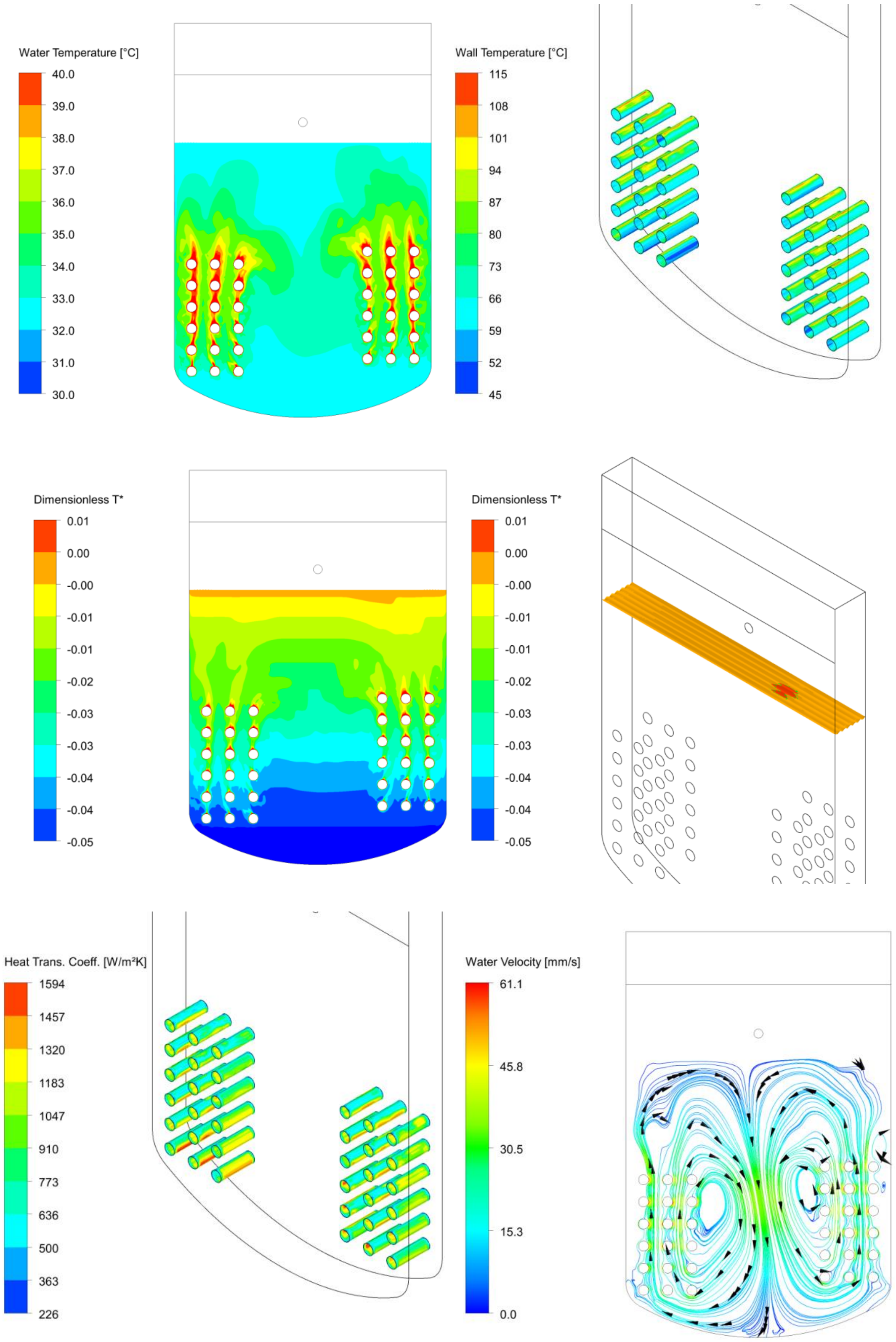

Figure 5.15: (Top) transient averaged contours of temperature distributions in the liquid and on the coil surfaces; (middle) transient averaged T^* distributions in the liquid and at the free surface; (bottom) heat transfer coefficient distributions on the coil surfaces, and velocity variations streamlines inside with superimposed velocity vectors.

The boiling simulations were compared to the experimental boiling data of McNeil et al., (2015), which is discussed in the next section.

5.19 Steady State Boiling Results

In the boiling cases, the bulk thermal phase change model was activated using the transient free convection simulation as the initial state. This was step 4 of the solution strategy, outlined in section 5.13. The boiling simulations did converge to a steady state solution. Monotonic convergence was not achieved for the solution residuals. Before the simulation ended, measures were taken to ensure a pseudo steady condition had been achieved. This was done by observing the monitor points of certain key variables, such as the rate of evaporation, temperature, velocity, and volume fractions. Those variables fluctuated around a mean value suggesting the problem was pseudo steady, but could only be modelled accurately using a transient solver. The results from these simulations are not presented, since they are not complete solutions to the problem. Figure 5.16 demonstrates the mass flow of evaporation and feed as a function of iteration for the rate constant 0.1 Hz. The evaporation rates are negative as mass physically leaves the system, whereas the feed rates are positive since mass renters the system. The two rates are equal and opposite because the feed rate was set to the same rate of evaporation.

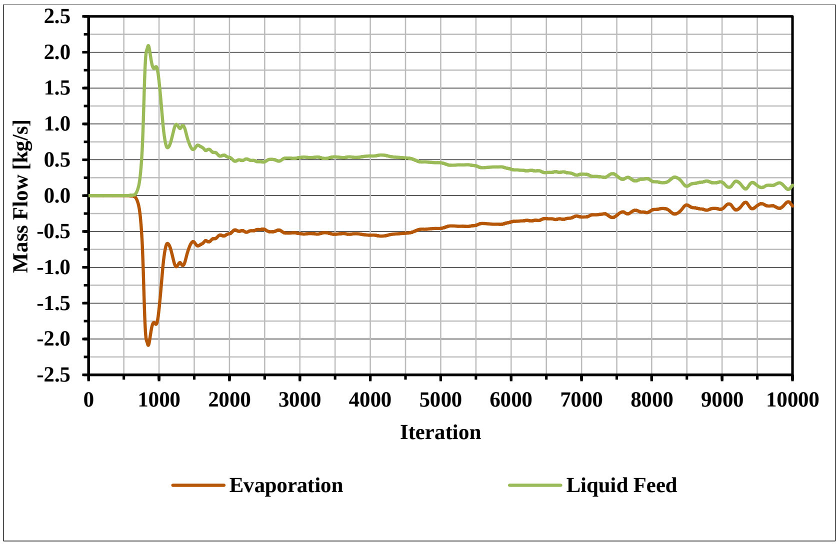

Figure 5.16: Evaporation rate and liquid feed rate of the steady state boiling simulation, using the transient free convection results as the initial state, and with a rate constant $\beta = 0.1$ Hz.

Figure 5.17 represents the water velocity during the steady state solve process at the 12 thermocouple positions. Velocity at position TS5 showed erratic behaviour after 7500 iterations, whilst the velocities at the remaining thermocouples were steady.

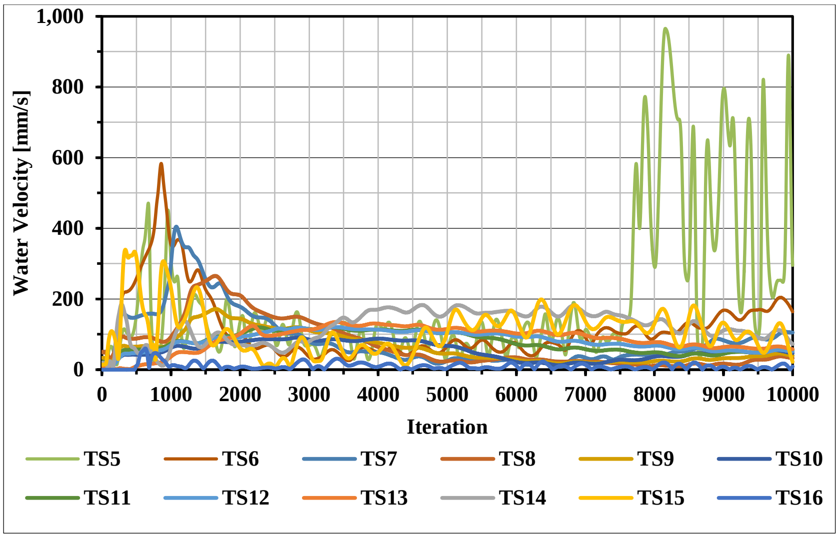

Figure 5.17: Water velocity at the thermocouple positions.

Figure 5.18 is a plot of volume fractions at six equidistant positions in the ullage head space. All values remained close to 0.9, which suggested some water in its liquid phase remained in the head space.

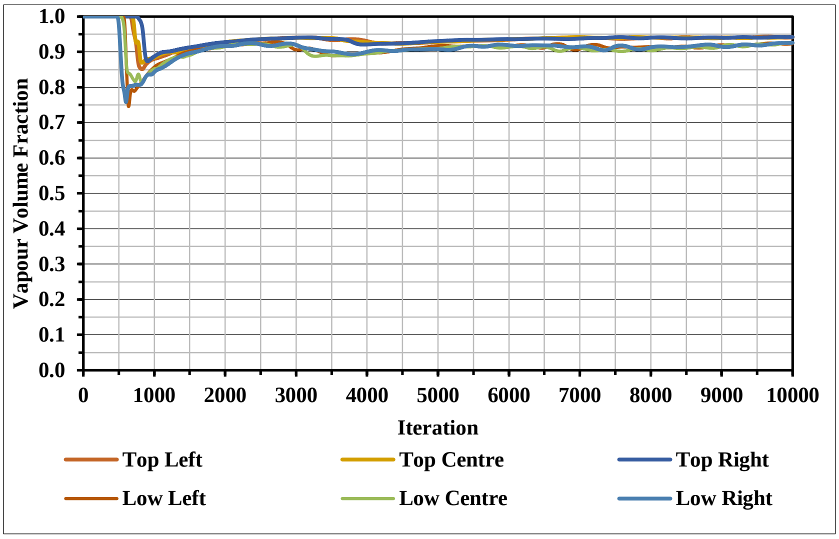

Figure 5.18: Vapour volume fraction at six points in the ullage space above the free surface.

An interesting observation was that, when the rate constant was set to greater than 1 Hz, (that is 10 and 100 Hz) in the steady state simulations, calculation of the simulations was very difficult using the time step described by Eq. 5.33. The simulations often diverged after 1000 iterations, and the monitor points yielded physically unrealistic values for the evaporation and feed mass flow, which reported values of at least 10 kg/s. In addition to this, the monitor points of water velocities reported values in the region of 50 m/s. This was clearly a numerical error, which required investigating. In response to the erroneous simulations, a number of parameters were changed for the 1 and 10 Hz cases.

1. For the 10 and 100 Hz cases, the time step was halved twice, from the calculated value reported by Eq. 5.33. Unfortunately, this did not improve the simulation behaviour and divergence of the solution was achieved.
2. The steady state boiling simulations began with the initial condition of the transient free convection simulation, using the rate constant at the free surface equal to 0.1 Hz. Hence, better initial states were provided to the 10 and 100 Hz cases. These were the steady state boiling case when $\beta = 1$ Hz. Even when providing a closer initial state to the 10 and 100 Hz cases, the simulations still diverged.
3. To force a solution, the numerics were switched from high resolution for the advection and turbulence schemes, to upwind. This introduces a lot of false diffusion which aids the overall convergence of the solution. It was hoped that this step would be successful, and would act as the initial state for additional high resolution steady state boiling cases for the 10 and 100 Hz cases. However, divergence occurred even when using upwind schemes and small time steps.
4. As a last resort, coarser meshes were used. These meshes corresponded to a resolution less than that reported by the statistics of mesh 1 in Table 5.1. With an extremely coarse mesh the simulations of 10 and 100 Hz were slightly more stable, in that the simulations were computed for a longer number of iterations before eventually diverging.
5. As a further last resort, steps 1 to 4 were repeated, but by using a transient solver. The simulations did not diverge, however the results were physically unrealistic and unreportable. Large mass flow were produced for the evaporation and feed, and the magnitude of the water velocities were comparable to speeds achieved in transonic flow.

Due to the simulation issues faced with the rate constants of 10 and 100 Hz, they were not used for further analysis. Only 0.1 and 1 Hz were used. The omission of the 10 and 100 Hz rate constants was taken prudently, and only when all reasonable doubt was removed as to its possible success.

Recall that, in the works of Lee (1980), DeSchepper et al., (2009) and Alizadehdakhel et al., (2010), a rate constant of 0.1 Hz was used. They suggested values greater than this caused numerical divergence in their simulations and significant deviations between the interfacial temperature and the saturation temperature. However, Yang et al., (2008) and Goodson *et al.*, (2010) used a value of 100 Hz, and also claimed using values less than 100 Hz caused significant deviation of the interfacial temperature from the saturation temperature. Clearly, the two groups of works are contradictory in their advice provided.

A significant differentiator between the two groups of work who used either 0.1 Hz or 100 Hz is the interface structure. The works of Lee (1980), DeSchepper et al., (2009) and

Alizadehdakhel et al., (2010), who used 0.1 Hz, were all largely stratified flows, with small volume fractions of bubbles and droplets. The works of Yang et al., (2008) and Goodson et al., (2010) were largely bubbly and droplet flows, with little stratification. This helps to explain why the steady state boiling simulations using 10 and 100 Hz diverged significantly, since the free surface in the scaled test rig is stratified at the free surface. Therefore, in order to gauge the value of the rate constant β, information on the flow structure must be known.

This explanation also agrees with the mathematical modelling. In the proposed length scale in Eq. 5.29 for the mixture model IAD in Eq. 5.21, small values of β yield large length scales, providing small values of the IAD. Conversely large values of β yields small length scales, providing large values of the IAD. Since bubbles and droplets have large IADs compared to planar surfaces, a small value of β would be required at the free surface. In addition to this, small values of IAD limit the transfer of continuity, momentum and energy across the interface, yielding lower evaporative mass flow compared to that which would be provided if a high rate constant were used. This gives additional credence to the theory that the rate constant is dependent on the interface structure, which is required to be known in order to prescribe the IAD.

5.20 Transient Boiling Results ($\boldsymbol{\beta = 0.1}$ Hz and 1 Hz)

The transient boiling simulations represented the last step in the solution strategy which was described in section 5.13. They also represent the stage where two values of the rate constant were tested (0.1 Hz and 1 Hz; support for 10 Hz and 100 Hz was discontinued at this stage due to the numerical instabilities), and benchmarked against experimental data.

Unlike the steady state boiling cases, the transient cases did converge satisfactorily for each time step, to within 1 and 11 iterations per time step. Furthermore the domain imbalances throughout the simulations were between ±1 % of the global fluxes in the domain.

Figure 5.19 represents the evaporation rates corresponding to $\beta = 0.1$ and 1 Hz. The graph also includes the theoretical evaporation rate calculated in the energy and material balance, in section 5.11. The theoretical evaporation rate had a value of 0.0078 kg/s. In addition to this, the transient averaged evaporation rates are also plotted for both rate constants. The average evaporation rate for $\beta = 0.1$ Hz was 0.071 kg/s, and for $\beta = 1$ Hz was 0.016 kg/s.

In Figure 5.19 sporadic peaks were found in the evaporation rates for both $\beta = 0.1$ and 1 Hz. For $\beta = 0.1$ Hz a cyclic evaporation rate occurred which had a negative trend, with the greatest evaporation rate reading 0.20 kg/s. The evaporation rate for $\beta = 0.1$ Hz plateaued at

6 s and fluctuated around 0.05 kg/s. For $\beta = 1$ Hz, cyclic evaporation rates were also achieved, having a minimum of 0 kg/s and a maximum of 0.05 kg/s for the first 8.5 s. After this time, the evaporation rate quickly rose to a value of approximately 0.25 kg/s.

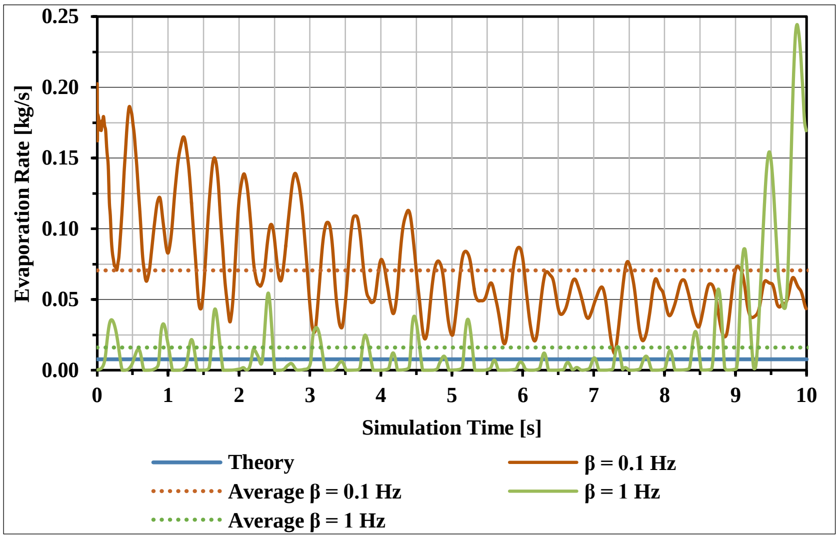

Figure 5.19: Evaporation rates for β = 0.1 and 1 Hz for 10 s simulation time.

It is far more reasonable to compare the average values of the evaporation rates to the theoretical one. The theoretical evaporation rate was calculated from the energy and material balance, which assumed steady state conditions. During operation when the scaled test rig is analysed over a long time frame, it is also steady state, as is Evaporator C. The theoretical evaporation rate was determined to be 0.0078 kg/s and the average evaporation rates for $\beta =$ 0.1 Hz and for $\beta = 1$ Hz were 0.071 kg/s and 0.016 kg/s respectively. These corresponded to relative errors of 810% and 105% respectively.

For both rate constants, the average evaporation rates were over predicted compared to the expected evaporation rate. For $\beta = 0.1$ Hz the average evaporation rate was skewed by the initial state at $t = 0$ s, which had a relatively high evaporation rate of 0.20 kg/s. This initial state was supplied by the steady state boiling simulations which were performed prior to the transient simulations. The large values of the evaporation rates for $\beta = 0.1$ Hz were due to the values taken by the IAD. At $\beta = 0.1$ Hz, the length scale was 0.9 mm, which provided an IAD value of approximately 278 m^{-1}. The average evaporation rate reduced significantly by 126% from 0.071 kg/s for $\beta = 0.1$ Hz to 0.016 kg/s for $\beta = 1$ Hz. The length scale for $\beta = 1$ Hz was 0.3 mm, which was three times less than that for $\beta = 0.1$ Hz. This corresponded to an IAD value of 878 m^{-1}. Therefore more realistic evaporation rates were achieved with $\beta = 1$ Hz, which had a greater IAD than $\beta = 0.1$ Hz.

The average evaporation rate for $\beta = 1$ Hz was skewed by the rising trend in the last 1.5 s of the simulation. This had a very high rate of evaporation due to the absence of a wall boiling model. The free surface contained a superheated layer of water which originated from the coils. This layer continually flashed to steam, and the thickness of this layer varied with time. In the last 1.5 s of the simulations for the $\beta = 1$ Hz case, the thickness of the layer was considerably greater than the previous 8.5 s. In the last 1.5 s the flash evaporation due to the combined effects of the latent heat and superheat generated evaporation rates greater than expected. If a wall boiling model were activated, the latent heat contained within the liquid may have nucleated into vapour bubbles. The average rate of evaporation for $\beta = 1$ Hz for the first 8.5 s is 0.006 kg/s, and is plotted in Figure 5.20.

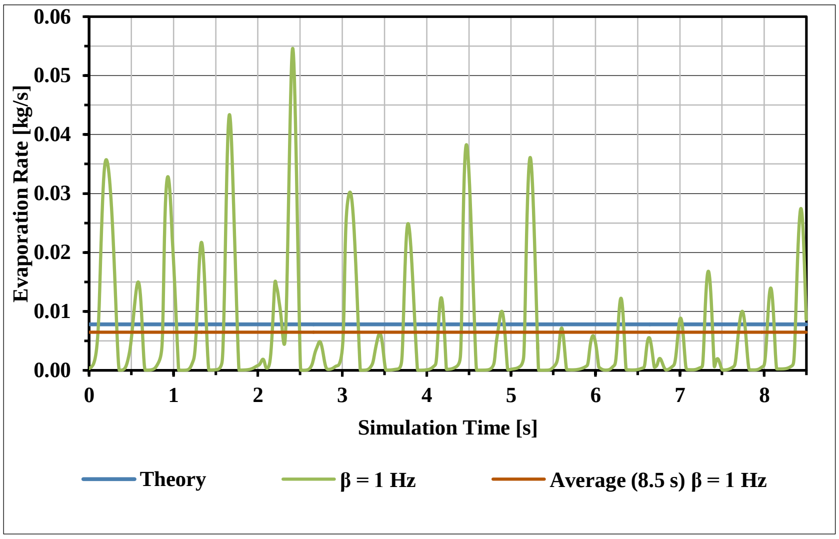

Figure 5.20: Evaporation rates for β = 1 Hz for the first 8.5 s simulation time.

The relative errors between the theoretical evaporation rate of 0.0078 kg/s and the 8.5 s averaged rate of 0.006 kg/s for $\beta = 1$ Hz is 26%. This excludes the unphysical behaviour exhibited after 8.5 s, which yielded the unrealistic rates of evaporation.

The results suggest that a rate constant between the values 1 Hz and 10 Hz would yield an evaporation rate close to the expected value of 0.0078 kg/s. However, the simulations for the case $\beta = 10$ Hz were numerically unstable. Furthermore increasing the rate constant has the effect of reducing the simulation time step, as described by Eq. 5.33. The simulations were performed on the high performance computing facilities at the University of Leeds ARC2 (Advanced Research Computing 2) facility. The simulations were performed on 3 nodes of 16 CPUs (48 CPUs) with 32GB of error correcting code memory per node available to the CFD solver. The solve time for $\beta = 0.1$ Hz was 144 hours, and for $\beta = 1$ Hz was 292 hours. These were solved on mesh 2, which had 965928 cells, and the domain represented a one quarter scale slice of Evaporator C. It is clear that Evaporator C would require a greater number of computational cells, due to its large size compared to the scaled test rig. Therefore a rate constant greater than 1 Hz, would decrease the solver time step, which would increase simulation run times which, and this would be a very limiting factor when simulating

Evaporator C. Therefore significant time investment would be required in order to home into a rate constant which yields an evaporation rate close to 0.0078 kg/s. In addition to this, $\beta = 1$ Hz yielded a 26% error for the rate of evaporation, outputting an average value of 0.006 kg/s compared to the expected value of 0.0078 kg/s. Greater accuracy would require disproportionately greater computational resources. Based on these arguments $\beta = 1$ Hz was selected as the rate constant for future simulations of Evaporator C.

The proceeding illustrations demonstrate the simulated behaviour of the scaled test rig for $\beta = 1$ Hz. The results for $\beta = 0.1$ Hz showed similar behaviour to $\beta = 1$ Hz, and since $\beta = 1$ Hz was selected as the chosen rate constant. Visual results for $\beta = 0.1$ Hz are not shown. Figure 5.21 are the instantaneous values of volume fractions at 0 s, 5 s, and 10 s for $\beta = 1$ Hz. The volume fractions show significant smearing at the free surface. This was due to transition from liquid to vapour due to evaporation. Bubbly and misty structures occur at evaporating free surfaces. However, those length scales were not captured by the simulations, due to the mesh resolution, which was too low to capture the micro scale phenomena associated with bubbly and misty flow.

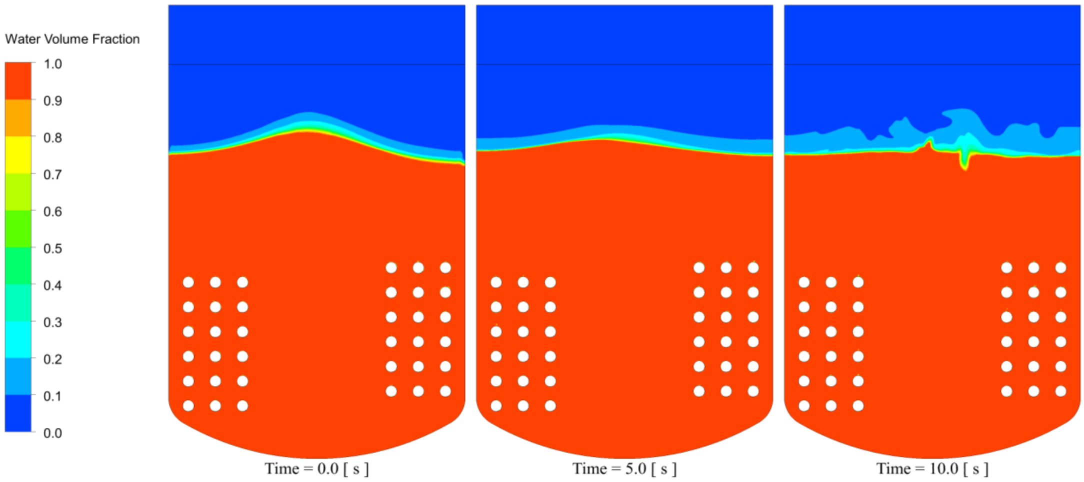

Figure 5.21: Volume fractions at 0 s, 5 s and 10 s for $\beta = 1$ Hz.

Figure 5.22 are the instantaneous isosurfaces when the volume fraction of water r_α was 0.5. The isosurfaces are coloured by the interfacial area density. The free surface has an IAD of 813 m^{-1}, and the incoming water has an IAD of 361 m^{-1}. The IAD reduces when the free surface is close to the side walls of the physical flow domain. This suggests that the greatest rate of heat transfer through the water-vapour interface occurs at the centre. The isosurfaces also show that the free surface is chaotic, having no discernible pattern.

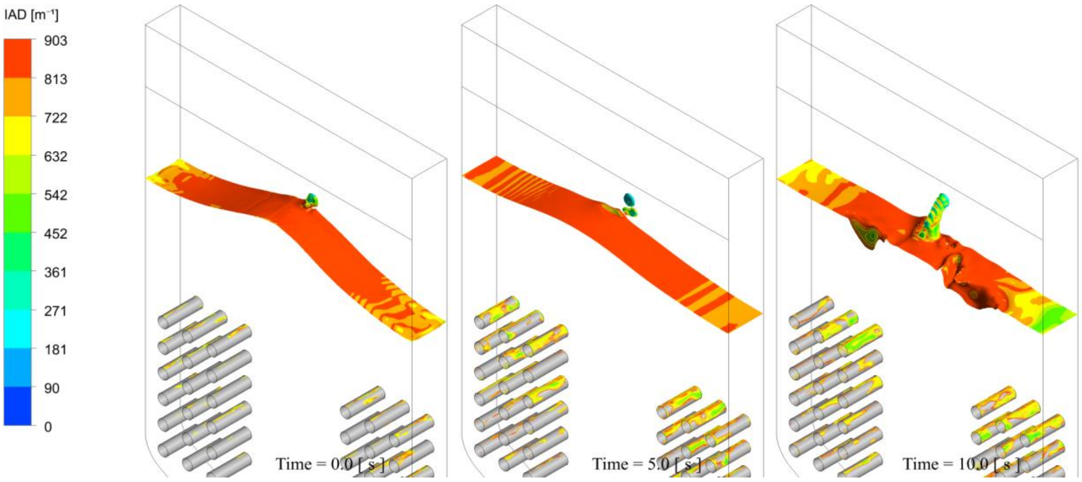

Figure 5.22: Isosurface at $r_\alpha = 0.5$, coloured by interfacial area density, at 0 s, 5 s and 10 s for $\beta = 1$ Hz.

Figure 5.23 shows the temperature distributions in the water. The distributions did not vary significantly, having values close to 32.9 °C, which is the saturation temperature corresponding to the 50 mbar ullage pressure. Since the temperature in the pool was at least 34 °C at the free surface, then the temperature distributions indicate the free surface was superheated by 1.1 °C. The stagnant temperatures inside the pool are supported by the experimental data of McNeil *et al*., (2015), who also reported the same finding. At 0 s two plumes develop and begin to coalesce and by the end of the simulations.

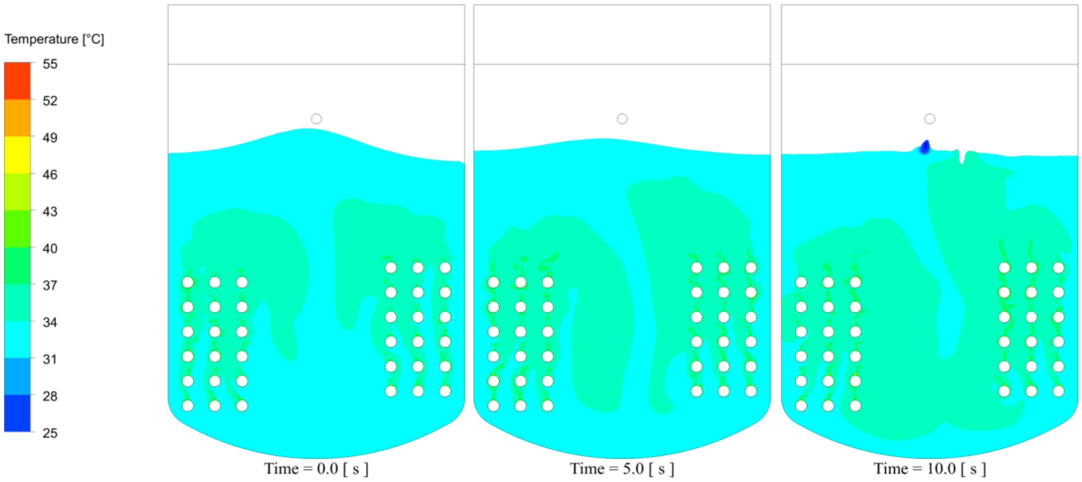

Figure 5.23: Temperature distributions in the water at 0 s, 5 s and 10 s for $\beta = 1$ Hz.

In Figure 5.24 the T^* distributions show a band of superheated water at the free surface, coloured in orange. In this band $T^* > 0$ which suggested the temperature of this band was greater than the local saturation temperature. This is in support of the temperature distributions in Figure 5.23. As the superheated layer flashed to steam, it was continually supplied with heat from the coils, and hence the superheated layer did not disappear as the simulation time progressed.

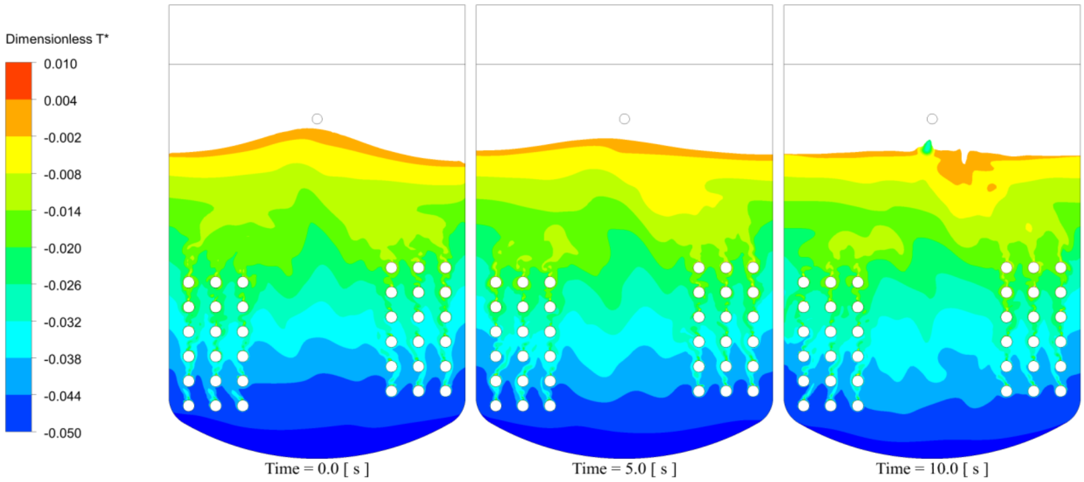

Figure 5.24: T^* distributions in the water at 0 s, 5 s and 10 s for $\beta = 1$ Hz.

The stagnant temperatures inside the water during boiling suggest that circulations occurred which were able to dissipate heat effectively through the liquid. This is supported by the streamline distributions shown in Figure 5.25. The distributions generally show that water travels down the centre of the vessel, and vertically upward through the heated coils. A distinct vortex develops at 0 s, at the left hand side tube bank, which over time increases intensity. The vortex above the right hand side tube bank is broken during the evaporation process. The greatest velocities reported in the simulations were 20 cm/s in the centre of the domain, and strong vortex region at the left hand side tube bank contains the lowest velocities. Consequently, the behaviour of the scaled test rig can be interpreted as that of an unconstrained thermosyphon.

It is interesting to relate these patterns to those produced for the unscaled test rigs. The patterns in Figure 5.25 are in agreement with the patterns produced for the three-dimensional simulations of the short test rig, which produced a similar behaviour. In the short test rig, water flowed down the centre, and rose up adjacent to the vessel walls. In contrast to this, the velocity behaviour of the tall test rig which contained a draught tube produced flow patterns where the water flowed down the sides of the vessel walls, and up the centre.

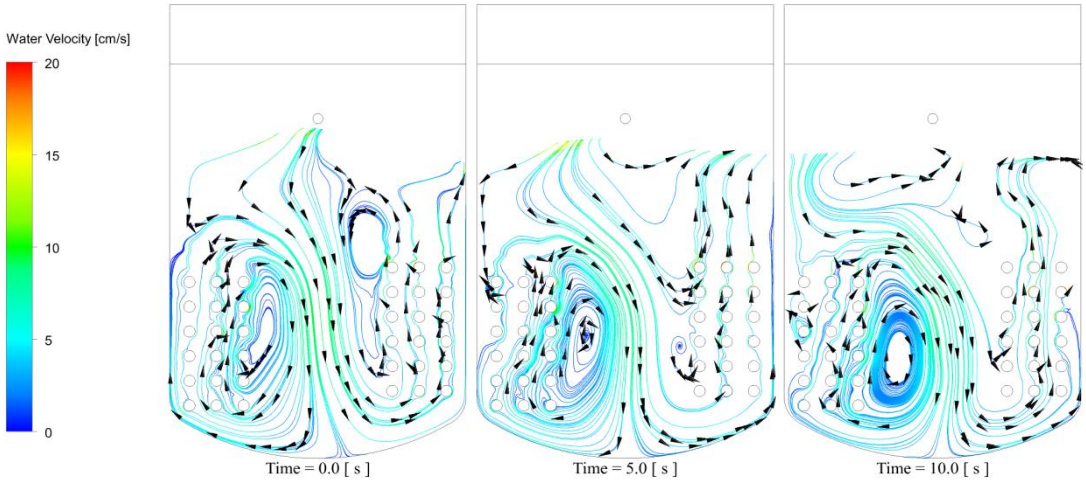

Figure 5.25: Steamline distributions with superimposed velocity vectors in the water at 0 s, 5 s and 10 s for $\boldsymbol{\beta = 1}$ Hz.

5.21 Comparison to Experimental Data

The information in Table 5.3 and Table 5.4 contains the values of the tube wall surface temperatures and tube wall heat transfer coefficients for the two rate constants tested, which were 0.1 Hz and 1 Hz. The tables also contain the experimental tube wall temperatures reported by McNeil *et al.*, (2015), and the computed relative percentage errors between the temperatures for $\beta = 0.1$ Hz and 1 Hz and the experimental temperatures. In Table 5.3 and Table 5.4, the rows shaded in green indicate values from the CFD investigations. The rows shaded in blue refer to experimental temperatures, and finally shaded in purple refer to the percentage errors between CFD and experiment.

The surface heat fluxes were 65 kW/m^2, and the heat transfer coefficient was defined in terms of the ullage temperature, which was 32.9 °C corresponding to the ullage pressure of 50 mbar. The data is presented for the coils in the left hand side tube bank only in the test rig. The row numbers begin from bottom closest to the base of the test rig, to top closest to the free surface. The column numbers begin from the left closest to the test rig walls, to right, closest to the centre of the test rig.

The CFD values for the temperatures and heat transfer coefficients on the right hand side coil of the test rig were similar to those on presented in Table 5.3 and Table 5.4. Only data from the left hand side tube bank were extracted as McNeil et al., (2015) presented their experimental data for the left hand side tube bank.

	Row 1			**Row 2**			**Row 3**		
Column	**1**	**2**	**3**	**1**	**2**	**3**	**1**	**2**	**3**
$T_{tube,\beta=0.1}$ **[°C]**	75.4	77.8	77.0	78.1	77.8	76.1	79.6	77.5	75.0
$T_{tube,\beta=1}$ **[°C]**	75.8	78.9	78.2	78.8	78.3	76.4	77.7	77.6	78.7
T_{exp} **[°C]**	64.1	63.2	60.2	56.4	59.9	60.5	55.2	60.5	60.9
$Err_{\beta=0.1}$ **[%]**	17.6	23.1	27.8	38.4	29.9	25.8	44.3	28.1	23.2
$Err_{\beta=1}$ **[%]**	18.3	24.9	29.8	39.7	30.7	26.3	40.8	28.2	29.2
T_{sat} **[°C]**		48.6			47.5			46.3	
T_{ONB} **[°C]**		7.4			7.3			7.2	
$h_{\beta=0.1}$ **[W/m²K]**	1399	1327	1364	1310	1305	1375	1202	1287	1408
$h_{\beta=1}$ **[W/m²K]**	1184	1236	1256	1206	1201	1327	1202	1159	1099

Table 5.3: Transient averaged and area weighted wall temperatures and wall heat transfer coefficients for $\beta = 0.1$ Hz and $\beta = 1$ Hz. The data are for the left hand side tube bank of the test rig for rows 1 to 3.

	Row 4			**Row 5**			**Row 6**		
Column	**1**	**2**	**3**	**1**	**2**	**3**	**1**	**2**	**3**
$T_{tube,\beta=0.1}$ **[°C]**	80.8	79.4	75.4	80.2	79.3	78.5	79.6	78.6	77.7
$T_{tube,\beta=1}$ **[°C]**	76.4	76.3	77.3	76.0	75.2	76.0	75.1	74.1	73.8
T_{exp} **[°C]**	56.7	59.3	58.6	53.8	56.4	56.1	51.8	52.0	52.6
$Err_{\beta=0.1}$ **[%]**	42.6	33.8	28.7	49.0	40.7	40.0	53.6	51.2	47.6
$Err_{\beta=1}$ **[%]**	34.8	28.6	32.0	41.2	33.5	35.5	44.9	42.5	40.2
T_{sat} **[°C]**		45.1			43.9			41.7	
T_{ONB} **[°C]**		7.0			7.0			6.8	
$h_{\beta=0.1}$ **[W/m²K]**	1142	1193	1376	1111	1125	1206	1151	1149	1177
$h_{\beta=1}$ **[W/m²K]**	1204	1172	1094	1185	1055	1045	1078	1041	1064

Table 5.4: Transient averaged and area weighted wall temperatures and wall heat transfer coefficients for $\beta = 0.1$ Hz and $\beta = 1$ Hz. The data are for the left hand side tube bank of the test rig for rows 4 to 6.

Comparatively there is little difference between the temperatures and heat transfer coefficients reported for $\beta = 0.1$ Hz and $\beta = 1$ Hz. Therefore, data on the tube walls were almost independent of the rate constant, and consequently the interfacial length scale and the interfacial area density. These CFD models were used to simulate boiling flows in the same way for Evaporator C. If the selected rate constant is incorrect, there would be reasonable confidence to suggest the surface data of the CFD results of Evaporator C simulations would be reasonably unaffected.

The smallest and largest errors between experimental temperatures and the CFD temperatures were 17.6% for row 1, column 1, and 53.6% for row 3, column 1, for 0.1 Hz. Likewise for 1 Hz the smallest and largest errors were 18.3% for row 1, column 1, and 44.9% for row 3, column 1. In both cases row 1, column 1 and row 3, column 1 provide the smallest and largest errors. This is due to the momentum behaviour of the water over those coils.

Referring to Figure 5.25, row 1, column 1 exhibits high velocities which have the potential to advect heat and provide a quenching effect. On the other hand, row 3, column 1 has relatively moderate to low velocities, which reduces heat transfer rates from that coil.

Wall boiling was not modelled in the CFD simulations. Therefore, excess superheat accumulated at the coil surfaces, and left the system via boiling at the free surface. The consequence of not modelling wall boiling is that the reported wall temperatures in the CFD were 10 – 20 °C greater than the experimental values, due to the accumulated superheat.

One of the aims of this investigation was to provide accurate predictions of the wall temperatures at the heated surfaces in Evaporator C. By not modelling wall boiling, caution should be advised since excess temperatures reported by the CFD can have the effect of over predicting corrosion rates. Perry and Geddes (2011) report that the corrosion rates double with every 8 °C rise in surface temperature. However, vapour nucleation from wall boiling would have condensed back into the liquid pool because it was sub cooled at all times, as shown by the temperature and T^* distributions in Figure 5.23 and Figure 5.24 respectively. However this behaviour is not guaranteed in Evaporator C.

In Table 5.3 and Table 5.4, the saturation temperature for each row was determined at the centroid of each coil. The saturation temperature decreases with increasing row number, as expected. As the row numbers increased, the hydrostatic head had a lesser effect on the saturation pressure.

The temperature for onset of nucleate boiling was determined by evaluating the correlation by Sato and Matsumura (1964), Eq. 5.34 at each coil.

$$\Delta T_{ONB} = T_{wall} - T_{sat} = \left(\frac{8\sigma_{\alpha\beta} T_{sat} \dot{q}_{wall}}{\lambda_{\alpha} \Delta H_{lg} \rho_{\beta}}\right)^{0.5} \tag{5.34}$$

The onset values had a range between 6.8 °C and 7.4 °C. The values were calculated directly by inputting Eq. 5.34 into the CFD solver. The thermophyiscal properties of water were assumed constant, and T_{ONB} extracted at the post processing stage of the simulations. McNeil *et al*., (2015) also determined the onset temperatures using Eq. 5.34, but did so by evaluating variable thermophysical properties as a function of pressure and temperature from steam tables. The reported onset wall superheat temperatures were typically between 4 °C and 6 °C. Therefore, the computational simulations overshot the evaluation of Eq. 5.34 by at least 1 °C for the expected minimum and maximum range.

The magnitude of the heat transfer coefficients on each coil corresponded to the single phase convection heat transfer. There were no significant deviations in the heat transfer coefficients for the coils and for the different values of the rate constants. The heat transfer coefficients could not be compared to those reported by McNeil *et al.*, (2015) because they were based on nucleate boiling flow, and therefore not suitable for a comparative study.

5.22 Summary

The model of Lee (1990) has been generalised, and implemented in ANSYS CFX, and the predictions of the generalised model have been compared with the experimental investigations of McNeil et al. 2015 on a scaled test rig designed to replicate some of the features of flow in Evaporator C. The original model of Lee (1990) included source terms in the liquid and vapour continuity equations, based on an empirically determined rate constant β. In order to translate the model into the thermal phase change model framework in ANSYS CFX, it was necessary to modify it slightly, and re-express it in terms of a model for the interfacial area density (IAD). The ANSYS CFX mixture model framework was selected for this, in which the IAD is expressed in terms of a modelled interfacial length scale, which depends in turn on the rate constant β. The value of this constant was not known a priori, and four values were tested, which were 0.1 Hz, 1 Hz, 10 Hz and 100 Hz.

Using rate constants of 10 and 100 Hz caused excessive numerical instabilities within the solution and a fully converged solution was not accomplished. Fully converged solutions were accomplished using rate constants of 0.1 Hz and 1 Hz. The results using a rate constant of 0.1 Hz yielded excessive evaporation rates at the free surface which were unrepresentative of the true rates of evaporation. The rate constant 1 Hz yielded a solution closer to the physically realistic expected value.

The results using the rate constants 0.1 Hz and 1 Hz have little effect on the heat and momentum distributions inside the water, but do have significant implications on the evaporative mass transfer across the interface. There was good agreement between the stream temperatures reported in the experimental data and the numerical results outputted from the CFD investigations. This was despite the CFD investigations not allowing for wall boiling to occur on the heated coils.

The flow patterns during boiling appear to confirm the motivating hypothesis that the flow behaves like an unconstrained thermosyphon reboiler, with internal temperatures similar to the temperature adjacent to the ullage region. The results also indicate that most phase change occurs as flash evaporation on the top, not as boiling from the coils, as originally thought.

Chapter 6

The Industrial Evaporator Design

6.1 Introduction

Geometrically the industrial evaporator, Sellafield Evaporator C is unlike the unscaled and scaled test rigs. The evaporator is far greater in size compared to the test rigs which were simulated in CHAPTER 4 and 5. However the unscaled and scaled test rigs do provide insightful knowledge on the potential flow regimes inside Evaporator C. For example the investigation on the short and tall test rigs proved that in steam heated systems, conduction through the metal would be the limiting resistance to heat transfer. There is no reason to believe this would not be true for Evaporator C. The scaled test rig was able to show under evaporative conditions the liquid pool remains close to the free surface saturation temperature with little temperature variation in the water. Therefore nucleated vapour from heated walls would condense back into the liquid pool, whilst the free surface undergoes evaporation. On this premise it is expected Evaporator C would follow similar behaviour.

Prior to full operation, during the period of 13 March to 31 March 1990, Evaporator C was tested on a continuous run as part of the system commissioning studies. During the commissioning tests, water was evaporated, and the system was tested for control, durability, performance, induced stresses associated with the external heating jacket and internal helical coils, and operator instructions. The conditions which these tests were performed under were recorded. The CFD simulations of Evaporator C were performed based on the conditions in the commissioning tests. Condensation inside the steam heated jackets and coils were not simulated directly. They were accommodated by applying an overall heat transfer coefficient at the surfaces in contact with the water which accommodated condensation inside the jacket and coils, and conduction through the walls.

In order to perform simulations on Evaporator C, a CAD geometry had to be produced from old engineering drawings. The engineering drawings for Evaporator C were supplied by National Nuclear Laboratory. These described the general arrangement and detailed dimensions of Evaporator C. The drawings were produced in 1978, stored on microfilm media and unfortunately were of poor quality when reprinted. This meant some dimensions which were not printed clearly had to be estimated based on the dimensions of adjacent pipework and fittings. The reproduction of the CAD geometry from the engineering drawings was arduous. Despite their shortcomings, the drawings were sufficient enough for a CAD geometry to be recreated. The CAD geometry was produced beyond a high degree of confidence that it represented that which was described in the engineering drawings for Evaporator C.

Once the geometry was produced, it was meshed so that a CFD analysis could be performed. Meshing the CAD geometry was challenging due to the complex structure of the vessel. This required careful attention in order to avoid degenerate cells within the mesh. Hence an ordered structured mesh which was used for the analysis of the test rigs in CHAPTER 4 and 5 could not be produced for Evaporator C. Instead an unstructured approach was taken. Details of the mesh are outlined in CHAPTER 7.

6.2 The Design of Evaporator C

The design of Evaporator C can be thought of as two component systems: the outer shell, and the inner apparatus. The shell of Evaporator C comprises two sections, a lower evaporating section, and an upper distrainment section. The external heating jacket is an attachment to the lower evaporating section. The shell of Evaporator C houses the inner apparatus which also contributes to its operation. These are:

1. Upper inner coil and condensate outlet
2. Upper middle coil and condensate outlet
3. Upper outer coil and condensate outlet
4. Lower inner coil and condensate outlet
5. Lower middle coil and condensate outlet
6. Lower outer coil and condensate outlet
7. Liquor feed pipe which is positioned above the free surface
8. Three liquor outlet pipes submerged inside the liquor
9. Steam sparger which is used to agitate and dislodge settled particulate solids
10. Three thermometer probes
11. Density probe
12. Pneumercator probe used to measure local pressure
13. Packing frame which fixes and supports the positions of the internal apparatus

The evaporator is constructed from corrosion resistant austenitic stainless steel of grade 18/13/1 (Dobson and Phillips, 2006). This material is a specific variant of the generalised stainless steel AISI 304 (Richardson, 2009 chap. 2), which has a thermal conductivity of 14.9 W/mK.

6.3 Evaporator C Design: Outer Shell

Figure 6.1 represents the reproduced CAD geometry of the outer shell of Evaporator C. The steam heated evaporating section is coloured in purple, and the ullage section above it is coloured in green. The geometry represents the inner walls of the evaporator in contact with the water. Hence the wall thicknesses and external heating jacket are not shown, and were not directly modelled in the CFD simulations. Figure 6.1 is annotated with dimensions which provides a sense of scale, especially when compared to the unscaled test rigs in CHAPTER 4 which were 0.1 m in diameter, and the scaled test rig in CHAPTER 5 which was 0.75 m wide.

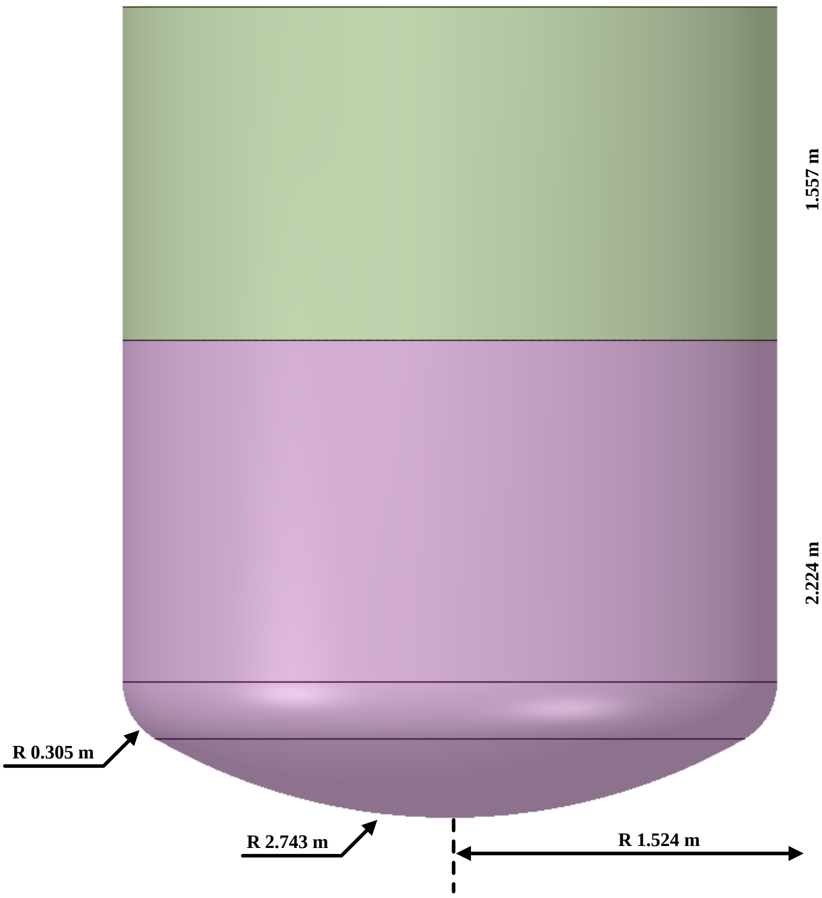

Figure 6.1: Outer shell details of Evaporator C.

The evaporating section can be thought of as being made of three component parts: an upper cylindrical section, a lower dished section, and a toroidal knuckle section. The toroidal knuckle section is at a tangent to the cylindrical and dished sections. This allows a smooth transition between the vertical cylinder walls and the curved lower dish.

In Figure 6.1 the external heating jacket surrounds the purple evaporating section. Hence steam heating is supplied to the evaporating section only, and not to the green ullage section above it. Figure 6.2 is a half slice of Evaporator C which shows the jacketed arrangement. In Figure 6.2 the ullage section is not shown. Steam enters the external heating jacket via one inlet only and leaves as condensate via one outlet, hence Figure 6.2 does not represent a symmetrical situation. Furthermore the internal apparatus such as the heating coils and instrumentation are not shown in Figure 6.2.

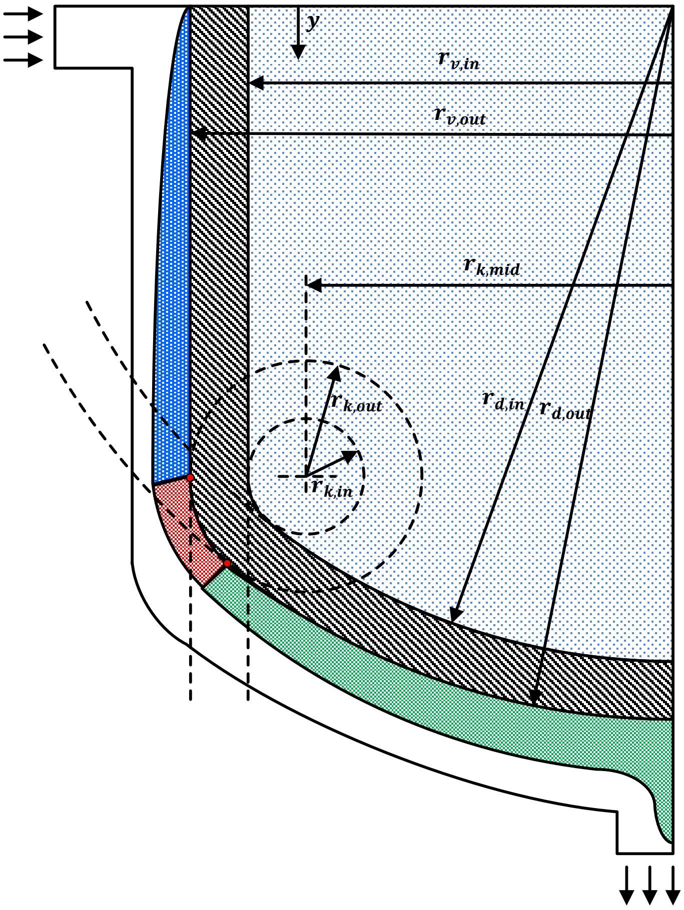

Figure 6.2: Outer shell details of Evaporator C.

At this stage it is pertinent to reveal that the free surface depth is 2.35 m. From the information in In Figure 6.1 the heated portion of the outer shell, coloured in purple, is 2.224 m. Therefore a band of liquid 0.126 m thick at the free surface that is in contact with the outer shell is not directly heated by the jacket. During normal operation, thermal conduction inside the shell walls would cause this band to be heated. However since Evaporator C is not being modelled as a conjugate problem, heat transfer at the free surface may be slightly under predicted.

The overall dimensions of the outer shell are summarised in Table 6.1. The values should be cross referenced with the information in In Figure 6.1 and Figure 6.2 to provide some context.

Description	Symbol	Value
Inner diameter of upper cylindrical section	$r_{v,in}$	1.524 m
Outer diameter of upper cylindrical section	$r_{v,out}$	1.556 m
Inner diameter of toroidal knuckle	$r_{k,in}$	0.305 m
Outer diameter of toroidal knuckle	$r_{k,out}$	0.337 m
Inner diameter of lower dish	$r_{d,in}$	2.743 m
Outer diameter of lower dish	$r_{d,out}$	2.775 m
Total height of the jacketed section	-	2.224 m
Total height of the ullage walls	-	1.557 m
Depth of the liquid	-	2.35 m
Thermal conductivity of vessel (stainless steel grade 18/13/1)	λ	14.9 W/mK

Table 6.1: Dimensions of the outer shell of Evaporator C. Data to be read in conjunction with Figure 6.1 and Figure 6.2.

In Figure 6.2 steam enters the jacket close to the free surface, and condenses on the outer wall surfaces of the evaporator shell. The enthalpy from the steam condensation is transferred to the water inside the evaporator via conduction through the evaporator walls. This process is most efficient at $y = 0$ m on the cylindrical part of the shell, when the condensate thickness is at its lowest point. The condensate adheres to the outer surfaces of the evaporator walls due to surface tension effects, which is commonly referred to as condensate retention (Briggs and Rose, 1994). Natural gravity drainage and the continuous addition of steam causes the condensate layer to grow with vertical position. The increasing thickness of the condensate limits the amount of heat transfer into the vessel due to the thermal resistance of the condensate. At the end of the vertical cylinder the condensate transitions onto the toroidal knuckle region and eventually onto the lower dished sections, where it is drained. Steam condensation would also occur on the jacket surfaces not in contact with the evaporator. Therefore a proportion of the enthalpy released by condensation will be lost to the ambient surroundings and will not be transferred into the vessel.

Condensing heat transfer coefficients would be greatest at the top of the heating jacket where condensation begins to occur, and less at the bottom of the jacket where it is fully flooded. In fact at the bottom of the jacket, if it is fully flooded, the heat transfer regime would be single phase convection in the condensate, which yields far lower heat transfer coefficients compared to condensation.

6.4 Evaporator C Design: Internal Apparatus

The internal apparatus of Evaporator C was difficult to reproduce compared to the relatively simple shell geometry as shown by Figure 6.1. Due to the unique geometrical variations, each part had to be drawn individually. For example, the lower inner coil could not be replicated and made larger to represent the lower middle coil due to geometrical non-similarity. Figure 6.3 is the reproduced CAD drawings of the internal apparatus of Evaporator C and illustrates the complex nature of the internal structure of Evaporator C. The illustration represents the outer surfaces of the internal apparatus in contact with the liquid.

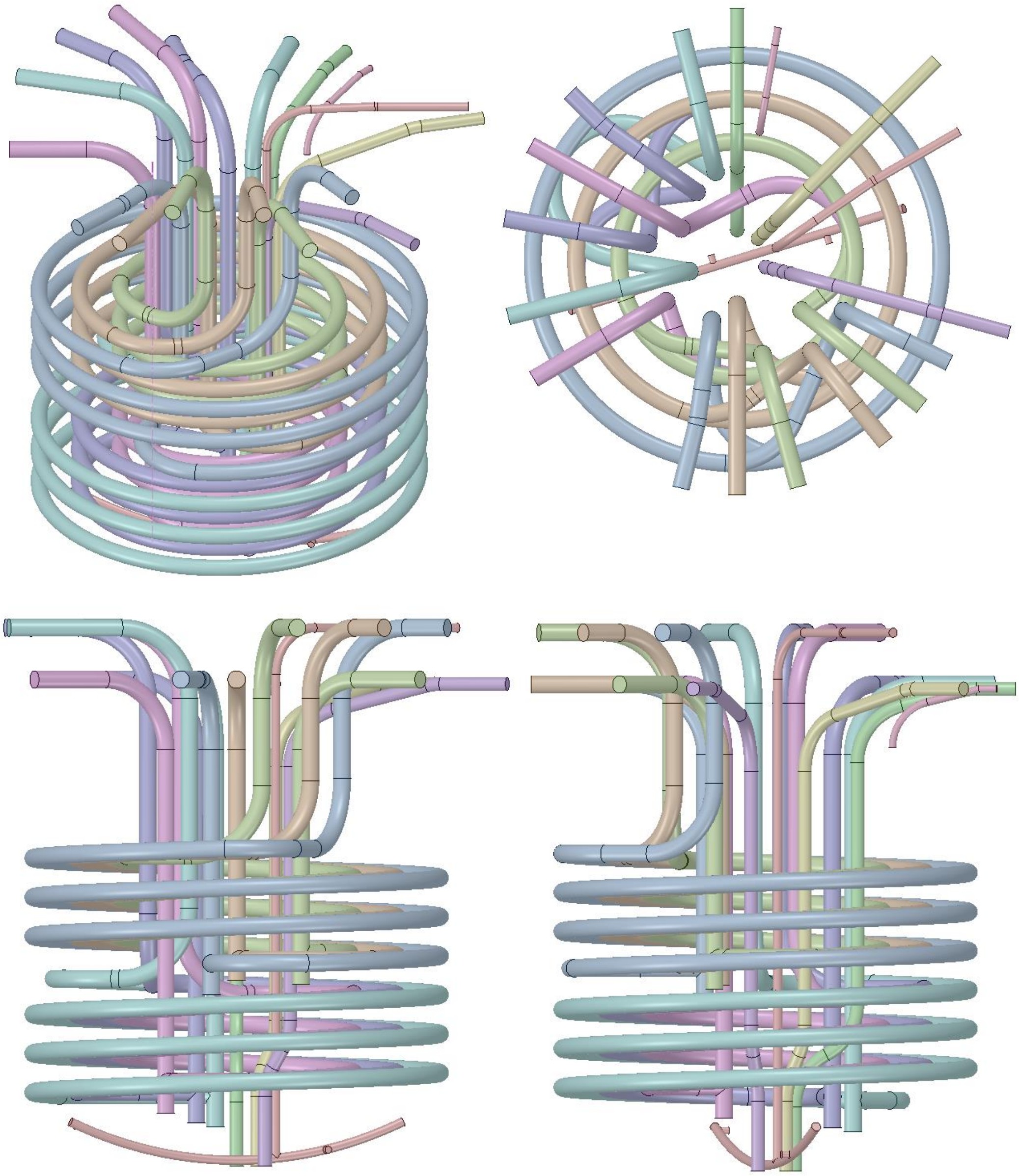

Figure 6.3: Internal apparatus of Evaporator C in four different projections.

An annotated top projection of the internal apparatus of Evaporator C is shown in Figure 6.4. The direction of the arrows indicates the direction of flow inside the apparatus. For the case of the six heating coils, flow enters as gaseous steam, and leaves as liquid condensate.

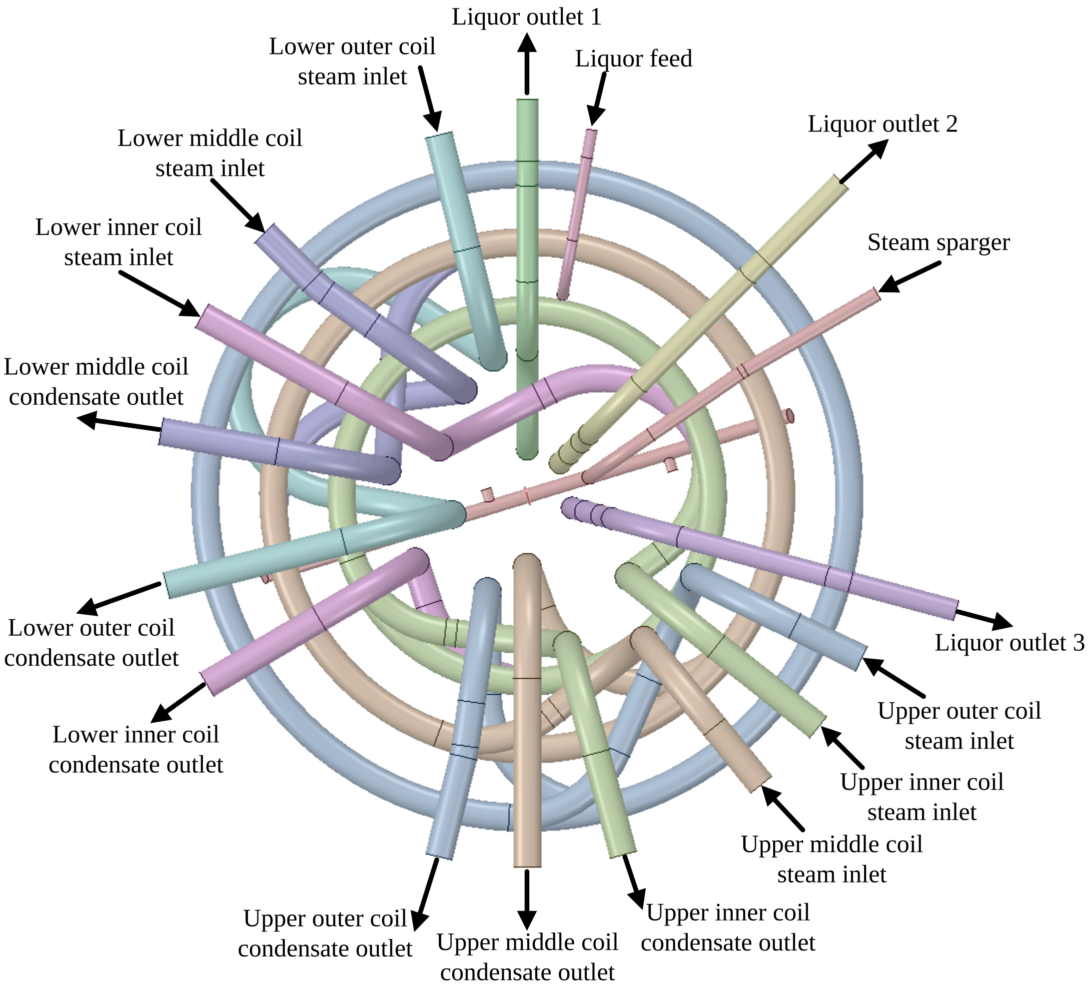

Figure 6.4: Annotated top projection of the internal apparatus of Evaporator C. Arrow direction indicates the direction of flow inside the apparatus.

Figure 6.5 displays the annotated isometric projection of the internal apparatus of Evaporator C. Once again the direction of the arrows indicates the direction of flow inside the apparatus. In the CAD geometry the instrumentation equipment and the supporting packing frame were not included. Recall the instrumentation comprised three thermometer probes, one density probe and one pneumercator probe. The instrumentation was deliberately excluded in anticipation of ensuring a small mesh size as possible. The instrumentation probes have a small diameter 1.27 cm and a long length of 2 m. Meshing around the small features of the instrumentation equipment would yield a significantly large mesh size due to the requirement of needing small cell sizes to capture the circumference. The supporting frame was not included in the CAD geometry due to its geometrical complexity. In addition to this, it was felt that the coils provided suitable blockage to the flow negating the need to include the packing frame, which is designed to be as least obtrusive to flow as possible.

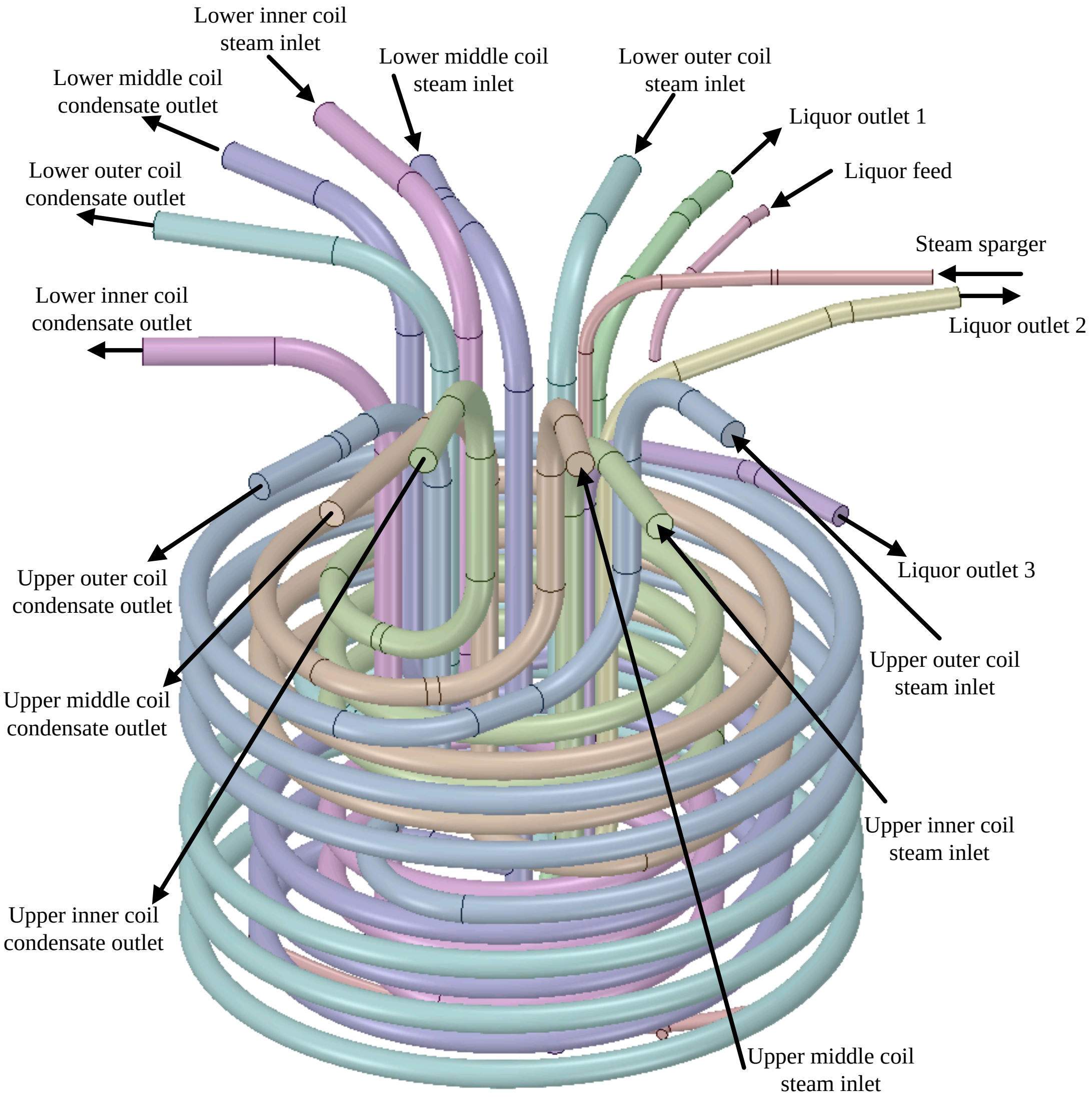

Figure 6.5: Annotated isometric projection of the internal apparatus of Evaporator C. Arrow direction indicates the direction of flow inside the apparatus.

Evaporator C was designed to have no penetrations in the vessel below the liquid surface (Perry and Geddes, 2011). This is a safety feature designed into the evaporator to remove potential points of leakage at weld points. This better visualised when the internal apparatus is coupled together within the shell of the evaporator, as shown by Figure 6.6.

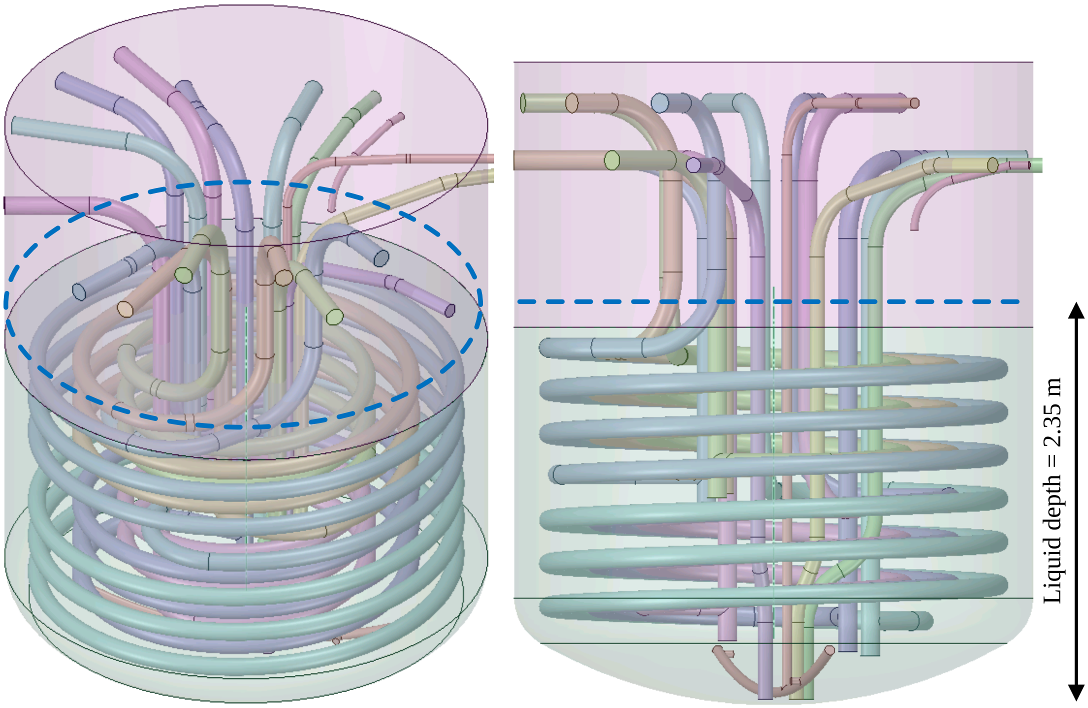

Figure 6.6: Complete Evaporator C CAD assembly showing the external shell, and the internal apparatus. The dashed blue line indicates the liquid depth.

The internal apparatus is also constructed from the same material as the outer shell, which is grade 18/13/1 stainless steel. It is not prudent to list every dimension of each part of the internal apparatus, since they are geometrically complex. However a brief overview of the dimensions of each part is supplied.

6.4.1 Helical Coils

The internal helical coils comprise two sections: a steam section and a condensate section. This is clearly displayed in Figure 6.7, which details the lower inner coil, and is true for the remaining five coils. The section coloured in orange is the steam section, and the condensate section is coloured in red. Steam enters the steam section coloured in orange, and begins to condense with respect to position travelled on contact with the inside walls of the coils. This means the physics inside the condensing steam section is two phase heat transfer flow, containing gaseous steam and condensed liquid. The condensate section coloured in red is single phase convective flow, which contains liquid condensate. Each coil contains a steam trap housed inside the stub at the interface of the steam and condensate sections, which is circled in Figure 6.7. The steam trap collapses all steam by the time it has reached the condensate section. Hence the conditions inside the coils will always be changing, and it is very unlikely that steady conditions are ever reached.

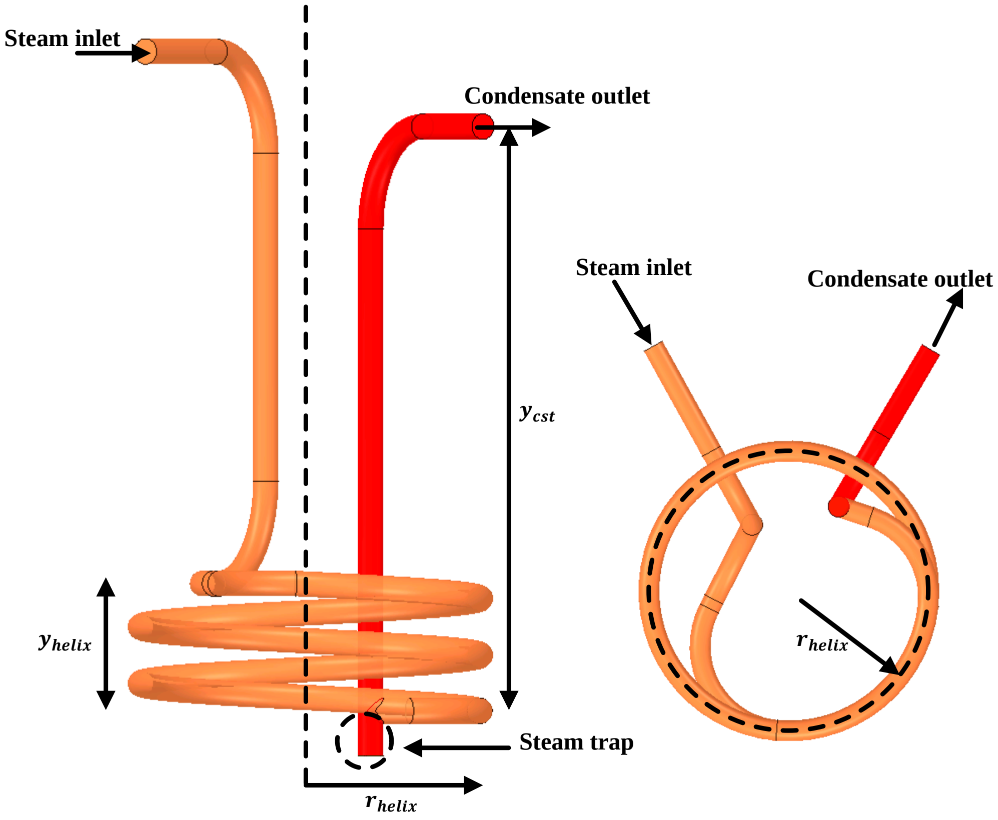

Figure 6.7: Lower inner coil with the main details annotated.

The coils also have the ability to replace incoming steam with cooling water. This is also true for the external heating jacket. The primary use of this is to cool the concentrated batch of liquor after the desired reduction rate has been achieved. The condensate section houses another parallel pipe within it (not displayed in Figure 6.7) which effectively makes the condensate line a double concentric pipe. When cooling water is used instead of steam, it leaves via the inner pipe. Consequently condensate leaves via the outer annulus. In this study, the condensate section of each coil was treated as a single non double concentric pipe. The key dimensions of the coils are listed in Table 6.2. In the interests of brevity these are not the complete dimensions which would enable complete replication of the coils by the reader. However they do relay sufficient bulk information of the coils.

The coils took a significant amount of time to draw in this investigation. In service to the time invested in recreating the complex coils in the CAD geometry, they are shown in Figure 6.8, in isometric projection.

Description	Symbol	Value [m]
Coil tube inner radius	$r_{coiltube,inner}$	0.044
Coil tube outer radius	$r_{coiltube,outer}$	0.057
Radius of the helical section for inner coils	$r_{helix,inner}$	0.762
Radius of the helical section for middle coils	$r_{helix,middle}$	1.04
Radius of the helical section for outer coils	$r_{helix,outer}$	1.32
Approximate helix height for inner coils	$y_{helix,inner}$	0.601
Approximate helix height for middle coils	$y_{helix,middle}$	0.703
Approximate helix height for outer coils	$y_{helix,outer}$	0.753
Approximate condensate pipe height for upper coils	$y_{cst,upper}$	1.85
Approximate condensate pipe height for lower coils	$y_{cst,lower}$	2.71
Approximate number of full helix turns for the inner coils	-	2.37
Approximate number of full helix turns for the middle coils	-	2.77
Approximate number of full helix turns for the outer coils	-	2.96

Table 6.2: Key geometrical values of the six helical coils.

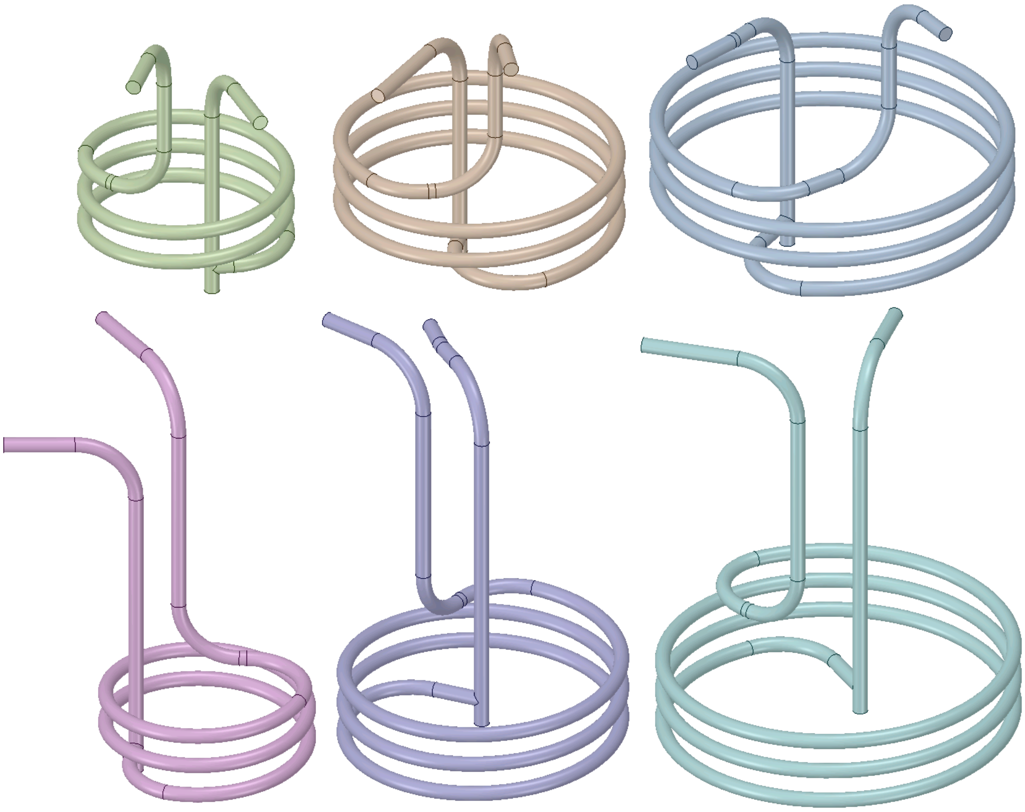

Figure 6.8: (Top row, left to right) upper inner coil, upper middle coil, upper outer coil. (Bottom row, left to right) lower inner coil, lower middle coil, lower outer coil.

6.4.2 Liquor Feed, Liquor Outlets and Steam Sparger

The liquor feed pipe does not physically come into contact with the liquid. The feed pipe is fixed in a position above the free surface, such that replenished liquid drops onto the free surface as the liquor is evaporated. To maintain the same liquor level the rate of replenishment must be the rate of evaporation.

The liquor feed pipe has an internal diameter of 0.048 m, and an outside diameter of 0.10 m. The feed pipe was reproduced according to the internal diameter dimensions as only the feed rate through the internal diameter need be modelled, therefore the walls of the feed pipe were treated as thin walls. An annotated diagram of the liquor feed pipe is shown in Figure 6.9. The feed pipe is 0.838 m from the centreline of the evaporator and the outlet is 0.44 m above the free surface.

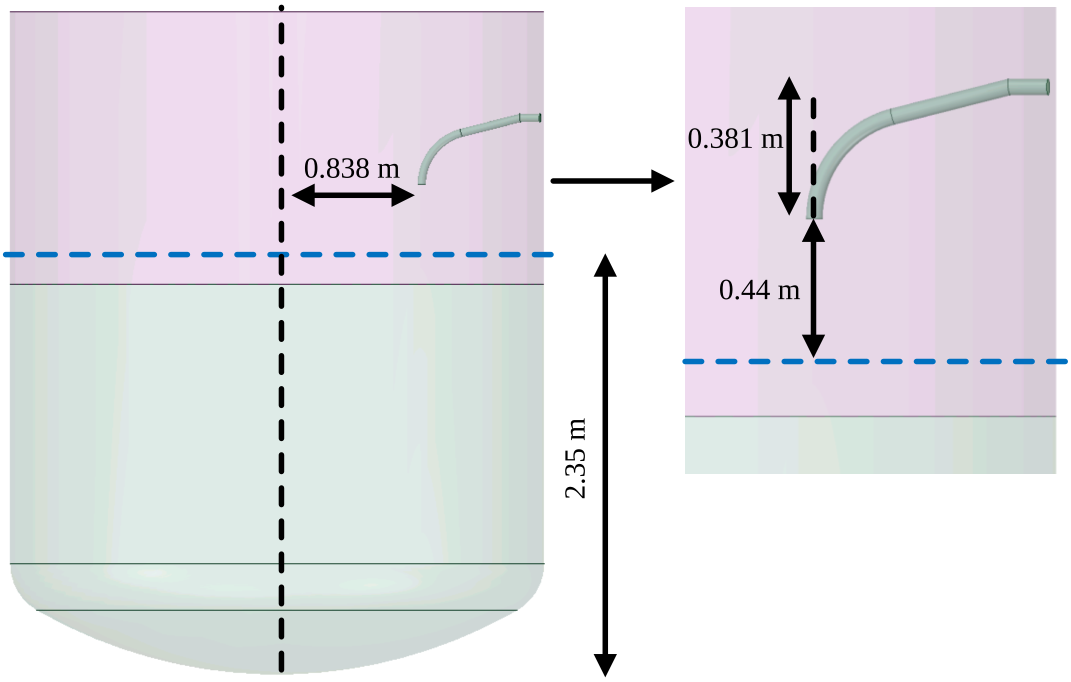

Figure 6.9: Annotated diagram of the liquor feed pipe above the liquid free surface.

The three liquor outlets are identical to each other. The liquor outlets have an outer diameter of 0.089 m, and 1 cm thick walls. In the CAD geometry the outer surface in contact with the liquid was drawn. The liquor outlets were included in the simulations of Evaporator C only to reproduce the blockage effects against the flow of the liquid. Their configuration inside Evaporator C is shown in Figure 6.10.

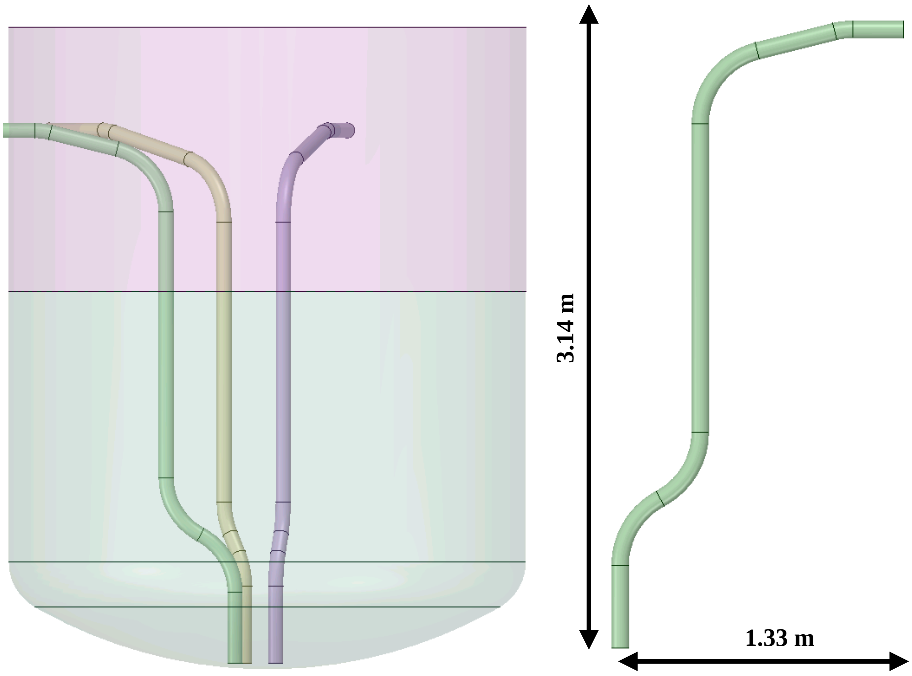

Figure 6.10: Annotated diagram of the liquor outlet pipes.

The liquor outlets operate via vacuum ejection. The suction points of the liquor outlets are positioned as close to the bottom most dip of the dished base as possible. This is to ensure as much concentrated liquor is collected as possible at the end of a processed batch. The clearance between the three liquor outlets and the bottom of the base is 0.64 cm, as shown in Figure 6.11.

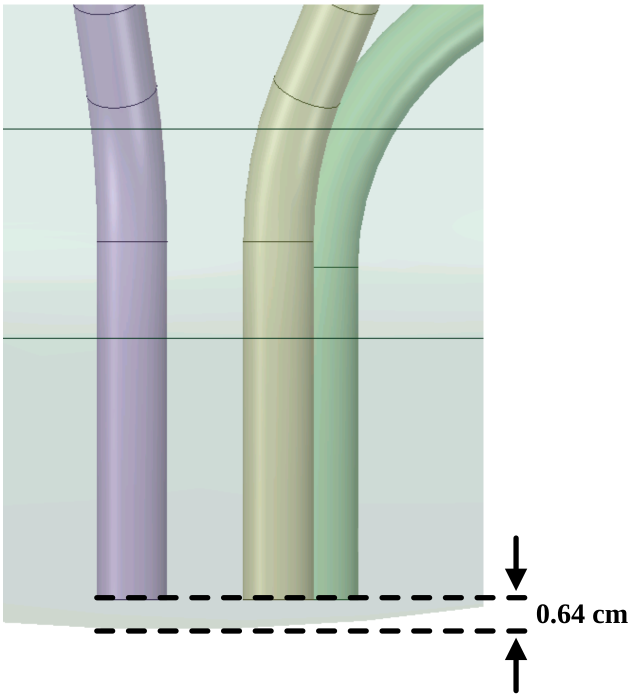

Figure 6.11: Clearance between the liquor outlets and the base of the evaporator shell.

The final apparatus is the steam sparger which is used to dislodge settled particles at the base of the evaporator. The steam sparger has an outside diameter of 0.06 m. The general arrangement of the steam sparger and its dimensions are shown in Figure 6.12. The steam enters the sparger via the inlet at the top, and exits via three outlets submerged inside the liquid near the base of the evaporator, as shown in Figure 6.13. The image also displays the close proximity of the steam sparger to the base of the evaporator, running parallel with it.

The dimensions provided on the original microfilm drawings were drawn to good mechanical engineering standards. The least amount of information was provided as to not overwhelm the reader by displaying many dimensions. In spite of adhering to good standards, drawing the CAD geometry was a difficult and arduous process. It involved performing forensic analysis of the presented dimensions, and back calculating to determine more fundamental dimensional information. This was performed by utilising trigonometric functions and general shape theory. Not all dimensions could be calculated to complete the CAD assembly. Where this was the case good engineering judgement was exercised and some dimensions approximated.

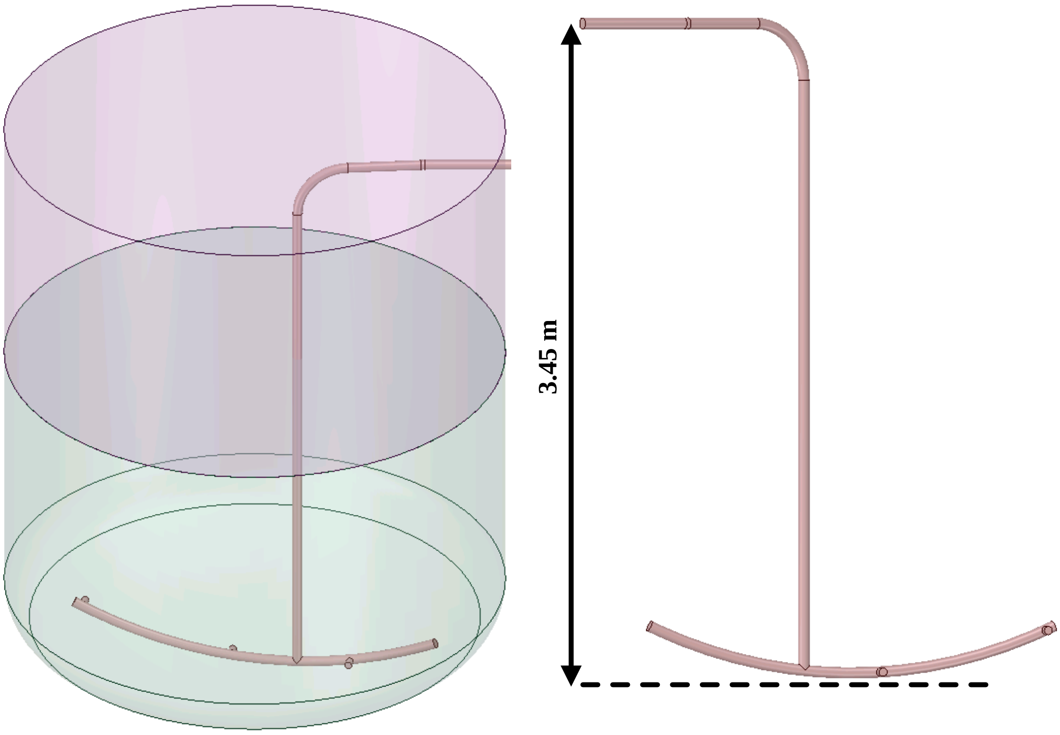

Figure 6.12: Steam sparger general arrangement and dimensions.

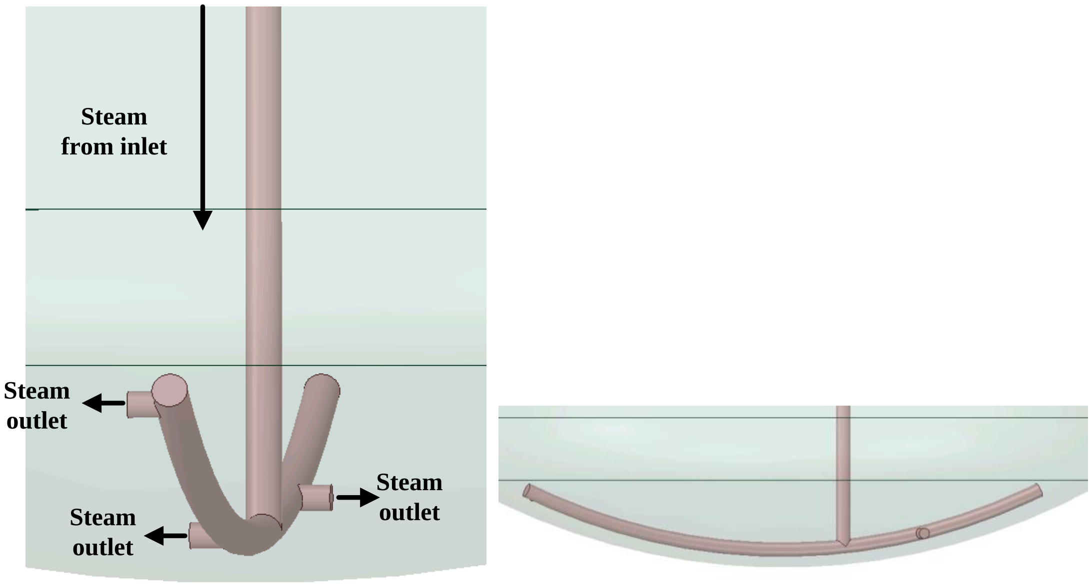

Figure 6.13: (Left) Steam sparger flow direction, (right) steam sparger seated parallel to the base.

6.5 The Physical Flow Domain of Evaporator C

In order to reduce the mesh size of Evaporator C, and consequently reduce the simulation run times, the redundant volume in the ullage space was removed from the overall Evaporator C geometry. This is better visualised in Figure 6.14. A volume in the ullage section was sliced on a plane coincident with the liquor feed outlet. Simulation details of the feed entering the system and boiling at the free surface could still be captured. Hence the physical flow domain in Figure 6.14 (right) was used for the simulations of Evaporator C.

This method provided good simulation stability when it was used in the simulations of the scaled test rig in CHAPTER 5. In the case of the scaled test rig and the Evaporator C physical flow domain, just enough volume was included in the ullage space such that:

1. Details of the liquor feed was not obstructed
2. Evaporation at the free surface could still be modelled
3. The position of the top most face, which acts as an opening boundary condition did not influence the simulation results in any way

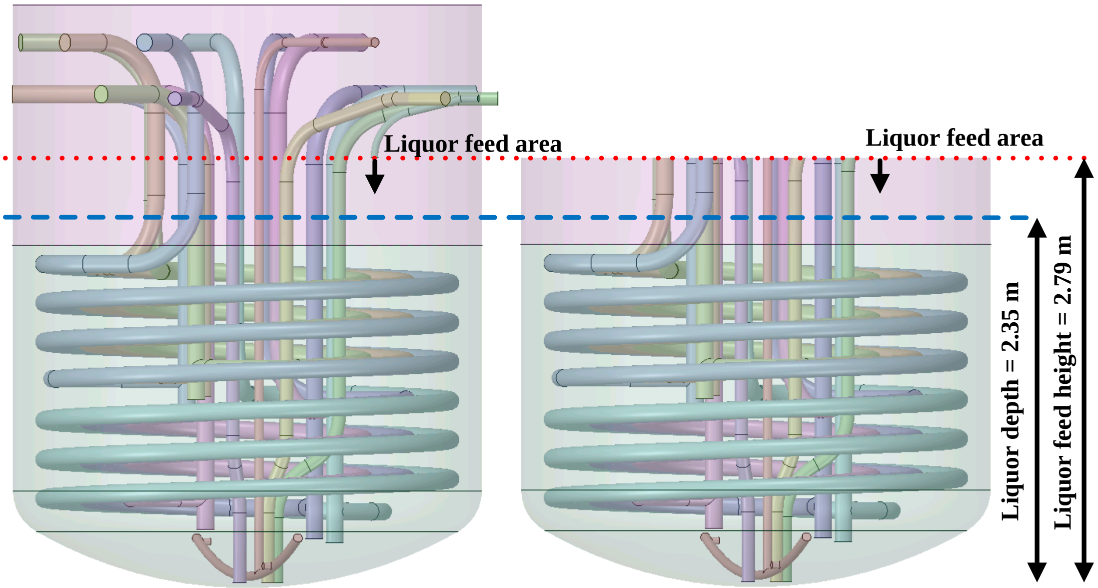

Figure 6.14: (Left) Evaporator C physical flow domain with large ullage area, (right) smaller physical flow domain which is used in the simulations of Evaporator C.

6.6 Evaporator C Operating Conditions

In the simulations water is used as the liquor that is being evaporated. The liquor has a depth of 2.35 m, and steam heated by the external heating jacket in contact with the evaporator shell, and the internal helical coils submerged inside the liquor. The steam pressure and temperature inside the jacket is 2.3 bar and 124.7 ºC, and for the coils is 2.5 bar and 127.4 ºC respectively. The remaining unheated areas of the evaporator shell are treated as heat loss walls, with an ambient outside temperature of 15 °C. The remaining apparatus inside the liquor such as the liquor outlets and steam sparger are treated ad adiabatic walls. The ullage pressure above free surface is assumed to be 0.1 bar based on the data from the commissioning tests, and information provided in the open literature (Upson, 1984; Robson and Candy, 2009; Geddes et al., 2009). The evaporation rate and the feed rate are assumed to be equal and opposite. The inlet feed temperature is 20°C.

6.7 Energy and Material Balance on Evaporator C

The prescription of the boundary conditions inside the coils requires the knowledge of the steam mass flow rate. Therefore a reverse energy and material balance must be performed on Evaporator C. The steam mass flow rates are not required for the prescription of the boundary conditions in the external heating jacket as they are not a function of the steam mass flow rate. The precise correlations used for the boundary conditions are discussed later. The energy balance is described by Eq. 6.1.

$$\dot{E}_{In} - \dot{E}_{Out} + \dot{E}_{Generation} - \dot{E}_{Consumption} = \dot{E}_{Accumulation} \tag{6.1}$$

The energy balance assumes steady state conditions which is a realistic assumption for Evaporator C, since under operation the evaporation rates are steady. That is the rate of evaporation is equal to the feed rate which maintains a constant liquor level. To maintain this steady evaporation rate, the steam supply is also likely to be steady when analysed over a long time period. This is not unrealistic since the evaporator operates for several weeks evaporating one batch of liquor at a time.

In Eq. 6.1 it is assumed that no generation, consumption or accumulation of energy occurs in the system. The problem then reduces to

$$\dot{E}_{In} - \dot{E}_{Out} = 0 \tag{6.2}$$

During operation crystalline salt solids are precipitated as the liquor is evaporated. These solids are heat emitting, and the liquor itself may also be heat emitting due to radioactive decay heat. Therefore a complete analysis of Evaporator C would take heat generation into consideration, however it is not considered for this work. The energy inputs and outputs into and out of Evaporator C are listed in Table 6.3.

Heating Types	**Denoted by**	**Heat Input or Output?**
Evaporation at free surface	$\dot{E}_{Evap,Out}$	Output
Liquor replenishment from the liquor feed	$\dot{E}_{Feed,In}$	Input
Steam heating to the liquor via the external jacket	$\dot{E}_{Jacket,In}$	Input
Heat loss from the non-heated walls in contact with the liquid	$\dot{E}_{Loss,Out}$	Output
Steam heating to the liquor via the internal helical coils	$\dot{E}_{Coils,In}$	Input

Table 6.3: Summary of heat inputs and outputs in Sellafield evaporator C.

Table 6.3 summarises five heating types. At the free surface evaporation occurs, which is considered a type of heat output from the liquid and is denoted by $Q_{Evap,Out}$. Conversely, liquor is replenished at the same rate of evaporation. This occurs via the feed pipe which is positioned above the free surface. The liquor replenishment into the system is considered a heat input and is denoted by $Q_{Feed,In}$. Steam heating via the external jacket is denoted by $Q_{Jacket,In}$ and is a heat input. There are two sides to the external steam jacket. One side is directly in contact with and faces inward toward the evaporator. The other side is not in contact with the evaporator, and is directed outward away from the evaporator to the surroundings. In this case $Q_{Jacket,In}$ refers to the former case and not the latter. There is some area of the walls of the ullage headspace in contact with the liquid which is not being heated, and is denoted by $Q_{Loss,Out}$ in Table 6.3 as it will behave as a heat loss wall. Lastly steam heating to the liquor via the internal helical coils is denoted by $Q_{Coils,In}$. There are six coils in total, and $Q_{Coils,In}$ is the sum of the heating contribution from each coil. Figure 6.6

The information in Table 6.3 is summarised as shown by Eq. 6.3.

$$\underbrace{\dot{E}_{Jacket,In} + \dot{E}_{Coils,In} + \dot{E}_{Feed,In}}_{\text{Heat Inputs}} \underbrace{-\dot{E}_{Evap,Out} - \dot{E}_{Loss,Out}}_{\text{Heat Outputs}} = 0 \tag{6.3}$$

In the commissioning tests the rate of evaporation was recorded and known, which implied the feed rate is also known since it is equal and opposite to the evaporation rate. Therefore rearranging Eq. 6.3 into known quantities on the left hand side, and unknown to the right yields Eq. 6.4, and consequently Eq. 6.5.

$$\dot{E}_{Evap,Out} - \dot{E}_{Feed,In} = \dot{E}_{Jacket,In} + \dot{E}_{Coils,In} - \dot{E}_{Loss,Out} \tag{6.4}$$

$$\left(\dot{M}\Delta H_{lg}\right)_{Evap,Out} - \left(\dot{M}\Delta H_{l}\right)_{Feed,In} = \dot{E}_{Jacket,In} + \dot{E}_{Coils,In} - \dot{E}_{Loss,Out} \tag{6.5}$$

During evaporator operation a constant liquor level is maintained. This implies the rate of evaporation is equal to the feed rate $\dot{M}_{Feed,In} = \dot{M}_{Evap,Out}$. Upson (1984) and Robson and Candy (2009) state 60 m^3/day of nitric acid based liquor is evaporated in Evaporators A, B, and C. Data from the commissioning tests reveal evaporation rates of 90 m^3/day of water. However it is not clear if both evaporation rates were obtained under identical conditions.

In this investigation the data from the commissioning tests are used to provide the operating conditions for the simulations. Therefore the evaporation rate of water is used. Coupled with the knowledge that the thermophysical properties of water are known, where as highly active liquor is not. Given the density of water at 0.1 bar is 990 kg/m^3, then 90 m^3/day of evaporating water is equivalent to 1.03 kg/s. Therefore $\dot{M}_{Evap,Out} = \dot{M}_{Feed,In} = 1.03\ \mathrm{kg/s}$.

The mass flow rates on the left hand side of Eq. 6.5 are known. Evaporation at the free surface occurs at 0.1 bar and at saturated conditions, therefore the enthalpy of vaporisation is known. The single phase enthalpy due to the feed entering the system at 20ºC is known. Substituting the known quantities into Eq. 6.5 yields $\dot{E}_{Evap,Out} - \dot{E}_{Feed,In} = \left(\dot{M}\Delta H_{lg}\right)_{Evap,Out} - (\dot{m}\Delta H_{l})_{Feed,In} = 2380388$ W. The calculated values are summarised in Table 6.4.

Description	Denoted By	Value
Evaporation rate / feed rate	$\dot{M}_{Evap,Out}$ / $\dot{M}_{Feed,In}$	90 m^3/day
Evaporation rate / feed rate	$\dot{M}_{Evap,Out}$ / $\dot{M}_{Feed,In}$	1.03 kg/s
Heat transfer due to liquor replenishment from the liquor feed	$\dot{E}_{Feed,In}$	86490 W
Heat transfer due to evaporation at free surface	$\dot{E}_{Evap,Out}$	2466878 W
Heating requirement	$\dot{E}_{Evap,Out} - \dot{E}_{Feed,In}$	2380388 W

Table 6.4: Summary of the evaporation and feed flow rates, and their respective energy inputs and outputs.

From all of the information presented so far the energy balance is summarized by Eq. 6.6.

$$\dot{E}_{Jacket,In} + \dot{E}_{Coils,In} - \dot{E}_{Loss,Out} = 2380.4\ \text{kW} \tag{6.6}$$

The proportional contribution to 2380.4 kW can be determined by analyzing the heat transfer surface areas since,

$$\dot{E} = Q = hA\Delta T \tag{6.7}$$

the surface areas A in contact with the liquid can be compared for $\dot{E}_{Jacket,In}$, $\dot{E}_{Coils,In}$ and $\dot{E}_{Loss,Out}$.

The information in Table 6.5 describes the inside and outside surface areas for the steam section for each heating coil. The information is divided into total and partial areas. Total area refers to the entire area of a section irrespective of if it is in contact with the liquor. Partial areas refer only to the area of a section that is in contact with the liquor. The total unwound length corresponding to the total and partial areas for the inside and outside areas of the tubes are also listed. Table 6.6 describes the inside and outside surface areas and lengths of the condensate section of each helical coil. Table 6.7 contains information on the helical coils for the combined (steam and condensate sections) total and partial outside surface areas, and the combined total and partial inside surface areas. These surface areas are required to determine the contribution of the energy balance in Eq. 6.6.

Coil	Steam Section Total Area [m^2]	Steam Section Partial Area [m^2]	Steam Section Total Length [m]	Steam Section Partial Length [m]	Steam Section Total Area [m^2]	Steam Section Partial Area [m^2]
	Outside surface area				Inside surface area	
TIC	5.62	4.94	15.65	13.77	4.37	3.85
TMC	7.97	7.34	22.19	20.43	6.20	5.71
TOC	10.35	9.71	28.81	27.05	8.05	7.56
BIC	5.76	5.01	16.04	13.94	4.48	3.89
BMC	8.29	7.60	23.08	21.16	6.45	5.91
BOC	10.95	10.16	30.50	28.30	8.52	7.90

Table 6.5: Surface areas and lengths of each helical coil in the steam section.

Location	Condensate Total Area [m^2]	Condensate Partial Area [m^2]	Condensate Total Length [m]	Condensate Partial Length [m]	Condensate Total Area [m^2]	Condensate Partial Area [m^2]
TIC	0.98	0.39	2.74	1.10	0.76	0.31
TMC	1.06	0.39	2.96	1.07	0.83	0.30
TOC	1.05	0.42	2.92	1.17	0.82	0.33
BIC	1.29	0.70	3.58	1.94	1.00	0.54
BMC	1.33	0.72	3.69	2.00	1.03	0.56
BOC	1.30	0.73	3.62	2.03	1.01	0.57

Table 6.6: Surface areas and lengths of each helical coil in the steam section.

Location	Combined Outside Total Area [m^2]	Combined Outside Partial Area [m^2]	Combined Inside Total Area [m^2]	Combined Inside Partial Area [m^2]
TIC	6.60	5.34	5.14	4.15
TMC	9.03	7.72	7.02	6.01
TOC	11.40	10.13	8.86	7.88
BIC	7.05	5.70	5.48	4.44
BMC	9.61	8.31	7.48	6.47
BOC	12.25	10.89	9.53	8.47

Table 6.7: Combined outside and inside surface areas of the coils.

There is a hydrostatic head effect in the condensate line due to the height of the condensate line between the condensate inlet and the condensate outlet. This is better represented in Figure 6.15.

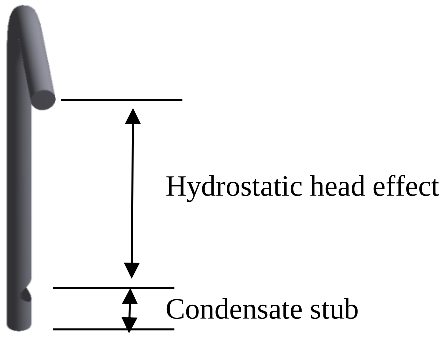

Figure 6.15: Example of the hydrostatic head effect in the top inner coil.

In Figure 6.15 the hydrostatic head effect ignores the stub, which is below the condensate inlet. The top three coils have a head of 1.85 m, and the bottom three coils has a head of 2.71 m which was described in Table 6.2. This corresponds to absolute pressures of 1.17 and 1.25 bar, assuming the reference pressure is 1 bar. Table 6.8 summarises this information, along with some selected thermophysical properties of the condensate at the respective pressure heads. This information is required at a later stage.

Coil Group	Pressure Head [m]	Hydrostatic Pressure [bar]	Saturation Temperature [°C]	Saturated Liquid Enthalpy [J/kg]	Saturated Vapour Enthalpy [J/kg]
Top Coils	1.85	1.17	104	436688	2682275
Lower Coils	2.71	1.25	106	444825	2685262

Table 6.8: Hydrostatic pressure and selected thermophysical properties of condensate in the condensate line.

Table 6.9 lists the areas of the outer shell walls that are in contact with the liquid. The mass flow of steam entering the jacket and each coil is required. The steam pressure for the jacket and coils are 2.3 and 2.5 bar respectively, however this is not enough information to determine the mass flow.

Location	Surface Area [m^2]
Jacket vertical wall	15.25
Jacket knuckle wall	2.95
Jacket dish wall	6.33
Total jacketed area	24.54
Area of the walls in the ulllage region that are in contact with the liquid	1.26

Table 6.9: Parts of the outer walls that are in contact with the liquid.

The mass flow inside the jacket and coils can be determined by first calculating the proportional heat duty on each surface, and then dividing by the vaporisation enthalpy as shown by Eq. 6.8.

$$\dot{m} = \frac{Q}{\Delta H_{lg}} \tag{6.8}$$

In order to accomplish this, the proportional heat duty on each surface was first determined. There is a proportionality of heat transfer rates between the different surfaces, where the proportionality is given by Eq. 6.9.

$$\underbrace{\text{Jacket}}_{Q_{Jacket,In}} : \underbrace{\text{TIC}: \text{TMC} : \text{TOC} : \text{BIC} : \text{BMC} : \text{BOC}}_{Q_{Coils,In}} : \underbrace{\text{Loss}}_{Q_{Loss,Out}} \tag{6.9}$$

In Eq. 6.9 heat transfer due to the coils have been subdivided into its six parts (for example TIC refers to “top inner coil” et cetera). Only the heat transfer surfaces in contact with the liquid are considered. This is because the surfaces in contact with the liquid yields a heat transfer rate into the liquid of 2380.4 kW and evaporation rate of 1.03 kg/s of water (recall not all of the coil surfaces are in contact with liquid).

The contribution by each surface toward the calculated heat transfer rate was determined by examining the total heat flux.

$$\dot{q} = \frac{Q_{Jacket,In} + Q_{Coils,In} - Q_{Loss,Out}}{\sum_{i=1}^{n}(\text{Area in contact with the liquid})} \tag{6.10}$$

Since the total heat transfer rate is $Q_{Jacket,In} + Q_{Coils,In} - Q_{Loss,Out} = 2380.4$ kW, and since the total area in contact with the liquid (termed <u>partial</u> area) is 73.90 m^2 then the overall combined <u>partial</u> heat flux into the system is 32211 W/m^2. This information is summarised in Table 6.10.

Description	Value
Heat input based on partial areas [W]	2380388
Combined partial area in contact with the liquid [m^2]	71.38
Heat flux input based on partial areas [W/m^2]	33350

Table 6.10: Summary of heat transfer and heat fluxes into Evaporator C during steady evaporation.

The area relating to the unheated walls of the ullage section in contact with the liquor was assigned a negative prefix to account for that fact that the ullage walls behave as heat loss walls (that is $Q_{Loss,Out}$ is negative).

The partial heat flux 33350 W/m^2 was multiplied by each area in contact with liquor to determine its contribution to 2380.4 kW. A tabulation of the results are listed in Table 6.11.

Heat Transfer Area	**Partial Heat Transfer Rate [W]**
Top inner coil partial steam area	164912
Top inner coil partial condensate area	13137
Combined top inner coil[1]	178048
Top middle coil partial steam area	244701
Top middle coil partial condensate area	12853
Combined top middle coil[1]	257555
Top outer coil partial steam area	323987
Top outer coil partial condensate area	13957
Combined top outer coil[1]	337944
Bottom inner coil partial steam area	166993
Bottom inner coil partial condensate area	23198
Combined bottom inner coil[1]	190191
Bottom middle coil partial steam area	253356
Bottom middle coil partial condensate area	23942
Combined bottom middle coil[1]	277298
Bottom outer coil partial steam area	338925
Bottom outer coil partial condensate area	24259
Combined bottom outer coil[1]	363184
Jacket vertical wall	508586
Jacket knuckle wall	98402
Jacket dish wall	211258
Combined coil areas[1]* $\boldsymbol{Q_{Coils,In}}$	1604220
Combined external heating jacket* $\boldsymbol{Q_{Jacket,In}}$	818246
Ullage walls in contact with the liquid* $\boldsymbol{Q_{Loss,Out}}$	-42078
Total*	2380388

Table 6.11: The contribution to the total heat transfer rate, 2380388 W by each surface in contact with the liquid.

In Table 6.11 the total partial heat transfer rate is 2380388 W, which agrees with the value in Eq. 6.6. The total value was calculated by summating the values in Table 6.11 tagged with the superscript *. The contribution due to the combined partial coil areas was calculated by summating the values tagged with the superscript ^{1}. In Table 6.11 the total heat transfer to the liquid is greater for the coils than for the heating jacket. In fact the coils contribute almost twice the amount of heat than the external heating jacket does.

6.8 Mass Flow of Steam Calculations

The surface area of the external heating jacket not facing Evaporator C is 27.55 m^2. This is 1.12 times more than the area of the external heating jacket facing the evaporator, which is 24.54 m^2 as read from Table 6.9. When the steam enters the jacket it condenses on both sides of the jacket: (1) the side directly in contact with the evaporator, (2) and side which is not in contact with the evaporator and which faces outward. Therefore when determining the steam mass flow through the jacket, the entire condensing area must be taken into consideration. Therefore the heat transferred to this surface via steam heating must be 1.12 times more than steam heating to the walls of the heating jacket in contact with the evaporator which was calculated as 818246 W.

$$\dot{m} = \frac{Q_{Jacket,In} + 1.12 Q_{Jacket,In}}{\Delta H_{lg}\big|_{2.3\text{ bar}}} \tag{6.11}$$

Hence the steam mass flow through the jacket is 0.79 kg /s, calculated using the relation in Eq. 6.11.

The steam enters the coils from above the free surface as shown in Figure 6.7. The steam will condense inside the coils before it has reached the free surface due to pressure losses in the steam, and due to the relative ambient ullage temperature being at a relatively low temperature. Therefore this was taken into consideration when the steam mass flow through the coils was determined.

As an example we take the top inner coil partial steam area, which transmits heat into the system at 164912 W (see Table 6.11). The partial heat transfer area is 4.94 m^2 (as described in in Table 6.5). This yields a heat flux of 33350 W/m^2. In fact when any surface is chosen Table 6.11, and its heat transfer rate converted to a heat flux by dividing by the area, the value will yield 33350 W/m^2. Therefore using this value and multiplying it by the total coil areas (as tabulated in Table 6.5, Table 6.6 and Table 6.7) produces the heat transfer rates in Table 6.12.

Location	Partial Heat Transfer Rate [W]	Total Heat Transfer Rate [W]	Percentage Change [%]
Top inner coil partial steam area	164912	187426	14
Top inner coil partial condensate area	13137	32796	150
Combined top inner coil[1]	**178048**	**220223**	**24**
Top middle coil partial steam area	244701	265729	9
Top middle coil partial condensate area	12853	35401	175
Combined top middle coil[1]	**257555**	**301129**	**17**
Top outer coil partial steam area	323987	345031	6
Top outer coil partial condensate area	13957	35004	151
Combined top outer coil[1]	**337944**	**380035**	**12**
Bottom inner coil partial steam area	166993	192125	15
Bottom inner coil partial condensate area	23198	42855	85
Combined bottom inner coil[1]	**190191**	**234980**	**24**
Bottom middle coil partial steam area	253356	276437	9
Bottom middle coil partial condensate area	23942	44209	85
Combined bottom middle coil[1]	**277298**	**320646**	**16**
Bottom outer coil partial steam area	338925	276437	18
Bottom outer coil partial condensate area	24259	43308	79
Combined bottom outer coil[1]	**363184**	**408506**	**12**

Table 6.12: Total heat transfer rates in the coils.

In Table 6.12 it is evident condensation heat transfer occurring in the coils above the free surface cannot be ignored. This is because the percentage change between the heat transfer rates associated with the partial and total areas are not negligible. The condensate lines are more sensitive to this, with the smallest heat transfer change being 79%.

A simplified schematic depicting the internal helical coils at the steam/condensate interface is shown in Figure 6.16. The stub in the condensate line is not depicted.

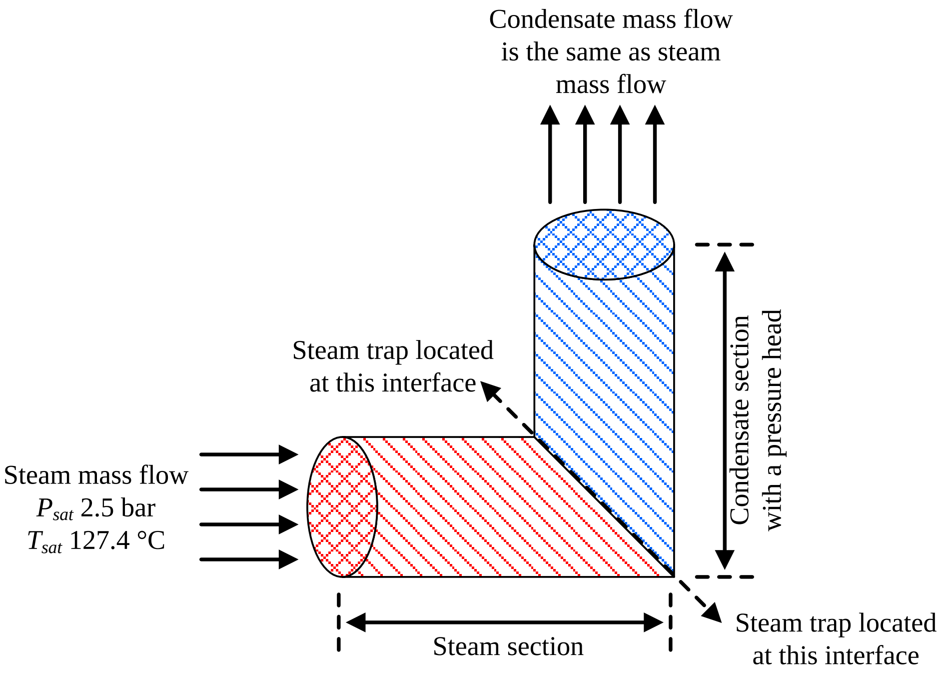

Figure 6.16: A simplified depiction of the steam coils showing the steam and condensate mass flow.

The mass flow of steam entering each helical coil is equal to the mass flow of condensate leaving at the condensate outlet. They are governed by Eq. 6.12 and Eq. 6.13.

$$Q_{TI,Steam} = \dot{M}\Delta H_{lg} \tag{6.12}$$

$$Q_{TI,Condensate} = \dot{M}\Delta H_{l} \tag{6.13}$$

For Eq. 6.13 the change in enthalpy is related to the change in temperature assuming isobaric heat capacity as shown in Eq. 6.14.

$$\Delta H_l = C_{P,l}\Delta T \tag{6.14}$$

Hence substituting this into Eq. 6.13 yields Eq. 6.15.

$$Q_{TI,Condensate} = \dot{M}C_{P,l}\Delta T \tag{6.15}$$

Therefore by taking the overall heat of the coils into consideration the mass flow in each coil can be determined by the expression in Eq. 6.16.

$$\dot{M} = \frac{Q_{TI,Steam}+Q_{TI,Condensate}}{\Delta H_{lg}+C_P\left(T_{stm,l}-T_{cst,out}\right)} \tag{6.16}$$

In Eq. 6.16 all values are known except from the mass flow of steam $\dot{M}$ and the condensate outlet temperature $T_{cst,out}$. The condensate outlet temperature is likely to take values between 10 °C to 100 °C as the reference ambient temperature for the absolute pressure is 1 bar. These values are tabulated in Table 6.13. These values are an extreme. This is because the liquid enthalpy at the condensate section is determined at saturated conditions (that is at the onset of phase change) and not at subcooled conditions.

Cond. Temp. [°C]	**Temp. Diff. $\Delta T = T_{stm} - T_{cst}$ [°C]**	**UIC Mass Flow, $\dot{M}_{UIC}$ [kg/s]**	**UMC Mass Flow, $\dot{M}_{UMC}$ [kg/s]**	**UOC Mass Flow, $\dot{M}_{UOC}$ [kg/s]**	**LIC Mass Flow, $\dot{M}_{LIC}$ [kg/s]**	**LMC Mass Flow, $\dot{M}_{LMC}$ [kg/s]**	**LOC Mass Flow, $\dot{M}_{LOC}$ [kg/s]**
10	117.4	0.082	0.112	0.142	0.088	0.120	0.153
15	112.4	0.083	0.113	0.143	0.088	0.121	0.154
20	107.4	0.084	0.114	0.144	0.089	0.122	0.155
25	102.4	0.084	0.115	0.145	0.090	0.123	0.156
30	97.4	0.085	0.116	0.147	0.091	0.124	0.158
35	92.4	0.086	0.117	0.148	0.091	0.125	0.159
40	87.4	0.086	0.118	0.149	0.092	0.126	0.160
45	82.4	0.087	0.119	0.150	0.093	0.127	0.161
50	77.4	0.088	0.120	0.151	0.094	0.128	0.163
55	72.4	0.089	0.121	0.153	0.094	0.129	0.164
60	67.4	0.089	0.122	0.154	0.095	0.130	0.166
65	62.4	0.090	0.123	0.155	0.096	0.131	0.167
70	57.4	0.091	0.124	0.157	0.097	0.132	0.169
75	52.4	0.092	0.125	0.158	0.098	0.133	0.170
80	47.4	0.092	0.126	0.160	0.099	0.135	0.171
85	42.4	0.093	0.128	0.161	0.100	0.136	0.173
90	37.4	0.094	0.129	0.162	0.100	0.137	0.175
95	32.4	0.095	0.130	0.164	0.101	0.138	0.176
100	27.4	0.096	0.131	0.165	0.102	0.140	0.178

Table 6.13: Steam and condensate mass flow rates for the six internal helical coils as a function of condensate temperature.

The values of temperature difference against mass flow in Table 6.13 have been plotted in Figure 6.17. There is no information as to the true temperature of the condensate, and where this temperature reading is taken. As a conservative estimate the mean value of the maximum and minimum temperature was taken (100 °C and 10 °C) which yields a value of 45 °C. The resultant mass flow of steam is tabulated in Table 6.14.

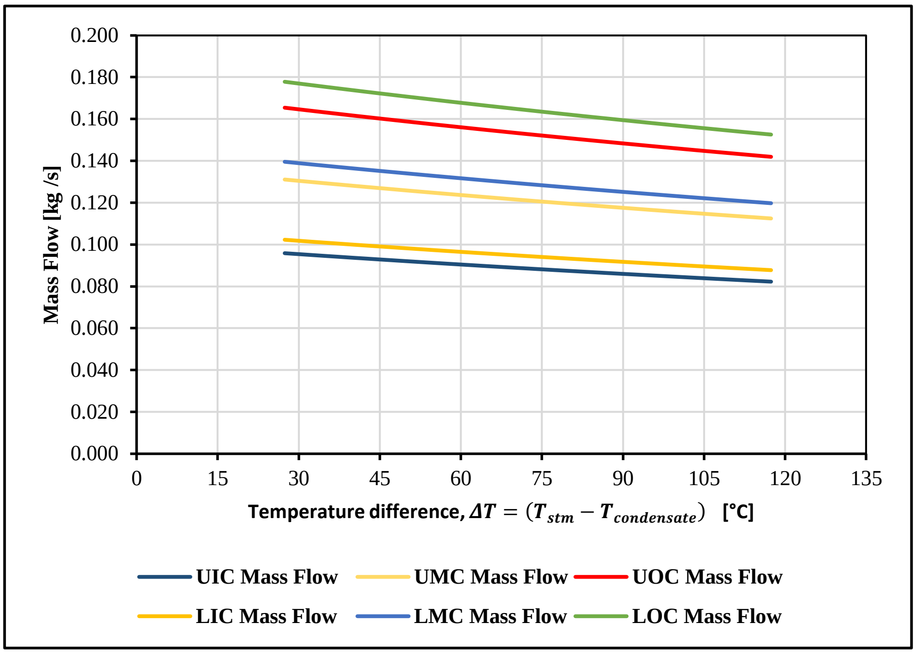

Figure 6.17: Steam and condensate mass flow as a function of temperature difference between the inlet steam (fixed at 127.4 °C) and the condensate temperature (variable).

Mean Condensate Temperature [°C]	Temperature difference $T_{stm,l} - T_{cst,out}$ [°C]	UIC Mass Flow [kg/s]	UMC Mass Flow [kg/s]	UOC Mass Flow [kg/s]	LIC Mass Flow [kg/s]	LMC Mass Flow [kg/s]	LOC Mass Flow [kg/s]
45.0	82.4	0.091	0.124	0.156	0.097	0.132	0.168

Table 6.14: Mass flow of steam in the internal helical coils.

From an engineering design point of view, it is likely that the steam feed to the coils originate from a common steam feed. Therefore the overall steam feed to the coils would be 0.768 kg/s.

6.8.1 Comparison with Evaporator C Commissioning Data

When Evaporator C was commissioned, the plant underwent a number of operational tests before being allowed to evaporate highly active liquor. During the commissioning period, tests were conducted for control, durability and performance under different configurations. The commissioning tests used water as the process fluid inside Evaporator C.

A selection of some of the relevant results from the commissioning data is displayed in Table 6.15. The steam pressures used in the tests were reported at 2.3 kg/cm^2. This is around 2.26 bar. However in the commissioning report it is not clear where this reading was taken inside the steam line. Furthermore, the condensate temperatures reported are mean temperatures, and once again it is not clear at which position downstream of the condensate line these readings were taken, and over how many days the average was taken. So this data is used as a gauge for general accuracy when compared to the calculated values in Table 6.14.

	Test Date 20/08/1990	**Test Date 22/08/1990**	**Average**
Evaporation rate, $\dot{m}_{evap}$ (m^3/day)	90.0	91.7	90.9
Evaporation rate, $\dot{m}_{evap}$ (kg/s)	1.04	1.06	1.05
Jacket condensate temperature, $T_{jkt,cst}$ [°C]	82	80	81
UIC condensate temperature, $T_{UIC,cst}$ [°C]	82	82	82
UMC condensate temperature, $T_{UMC,cst}$ [°C]	84	84	84
UOC condensate temperature, $T_{UOC,cst}$ [°C]	72	78	75
LIC condensate temperature, $T_{LIC,cst}$ [°C]	83	83	83
LMC condensate temperature, $T_{LMC,cst}$ [°C]	86	87	86.5
LOC condensate temperature, $T_{LOC,cst}$ [°C]	83	84	83.5

Table 6.15: Condensate data from the commissioning tests.

The general condensate temperatures reported in Table 6.15 from the commissioning tests are higher than the mean temperature approach reported in Table 6.14. Unfortunately the condensate temperatures from the commissioning reports cannot be used as the conditions under which they were generated had not be specified.

6.9 Boundary Conditions: The Outer Shell

The external heating jacket comprise of three sections, a vertical section, a knuckled section and a dished section. Since each section is geometrically unique they were treated independently with regards to the boundary conditions on those surfaces. A depiction of the external heating jacket with its three sections is pictured in Figure 6.18. This is a more detailed version of the same picture presented in Figure 6.2.

There are two common resistances to heat transfer into the vessel. These are steam condensation on the outside surface of the shell, and conduction heat transfer through the shell. This is analogous to the work performed in CHAPTER 4 for the unscaled test rigs. Those were heated in a similar manner: dry saturated steam condensed on the lower surface of the horizontal stainless steel baseplate, and conduction heat transfer transmitted the heat into the water column above it. The underlying governing equations which describe the conditions shown in Figure 6.18 are shown in Eq. 6.17 and Eq. 6.186.18.

$$\dot{q} = h_{csn}\left(T_{stm} - T_{w,out}\right) \tag{6.17}$$

$$\dot{q} = h_{cdn}\left(T_{w,out} - T_{w,in}\right) \tag{6.18}$$

It is not strictly accurate to call h_{cdn} a heat transfer coefficient, as it is simply a resistance to conduction heat transfer through the vessel walls due to the wall thickness and thermal conductivity. However for simplicity and consistency in the nomenclature h_{cdn} is used to refer to conduction through the walls.

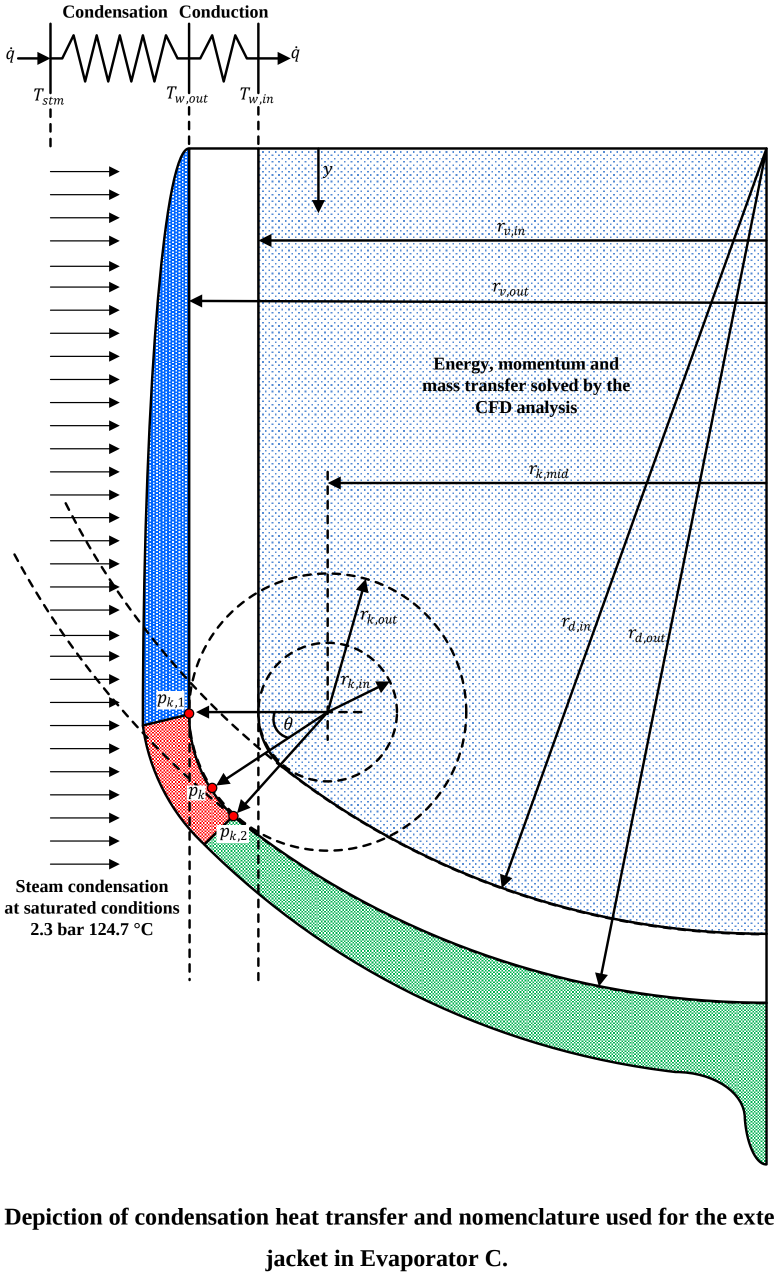

Figure 6.18: Depiction of condensation heat transfer and nomenclature used for the external heating jacket in Evaporator C.

The relations shown in Eq. 6.17 and Eq. 6.186.18 combine to form an overall relation shown in Eq. 6.19, where the overall heat transfer coefficient is described by Eq. 6.20.

$$\dot{q} = h\left(T_{stm} - T_{w,in}\right) \tag{6.19}$$

$$h = \left(\frac{1}{h_{csn}} + \frac{1}{h_{cdn}}\right)^{-1} \tag{6.20}$$

In the CFD analysis the heat flux $\dot{q}$ and inside wall temperature $T_{w,in}$ are solved for implicitly in the usual iterative approach. At the boundaries the heat transfer coefficient h is prescribed along with the “outside temperature” which is the steam saturation temperature. This approach is not novel here, as this type of approach was used in CHAPTER 4 and CHAPTER 5.

Three different condensation heat transfer coefficients in Eq. 6.20 were used depending on the location on the heated portion of the outer shell (vertical wall, toroidal knuckle and dished bottom). In Eq. 6.20 conduction through the vertical section of the external heating jacket is treated as a hollow cylinder, which is described by Eq. 6.21.

$$h_{cdn} = \frac{\lambda_w}{r \ln\left(\frac{r_{v,out}}{r_{v,in}}\right)} \tag{6.21}$$

Conduction through the walls of the knuckle is treated as conduction through a hollow sphere, and is described by Eq. 6.22.

$$h_{cdn} = \frac{\lambda_w}{r^2\left[\left(\frac{1}{r_{k,in}}\right)-\left(\frac{1}{r_{k,out}}\right)\right]} \tag{6.22}$$

Finally conduction through the walls of the lower dish is also treated as conduction through a hollow sphere, and is described by Eq. 6.23.

$$h_{cdn} = \frac{\lambda_w}{r^2\left[\left(\frac{1}{r_{d,in}}\right)-\left(\frac{1}{r_{d,out}}\right)\right]} \tag{6.23}$$

Assuming steady conditions, heat transfer rates in one direction in radial systems are constant. However under the same conditions heat flux rates in one direction are not constant, and are dependent on the position r between the outer and inner radii r_1 and r_2. This means in order to use Eq. 6.21, Eq. 6.22 and Eq. 6.23 the position r needs to be defined. This is taken as the inner radius that is in contact with the liquor. Therefore for Eq. 6.21 $r = r_{v,in}$, for Eq. 6.22 $r = r_{k,in}$ and finally for Eq. 6.23 $r = r_{d,in}$.

6.9.1 The External Heating Jacket: Vertical Walls

For the vertical walls of the external heating jacket the analytical Nusselt heat transfer coefficient is used for the condensation heat transfer coefficient shown by Eq. 6.24.

$$\mathrm{Nu} = \frac{h_{csn}L}{\lambda_l} = \left[\frac{g\rho_l(\rho_l-\rho_g)\lambda_l^3\Delta H'_{lg}}{4\mu_l(T_{stm}-T_{w,out})y}\right]^{\frac{1}{4}} \tag{6.24}$$

In Eq. 6.24 the heat transfer coefficient is a function of the vertical position. This is because the condensate film thickness increases with position, as shown in Figure 6.18. The characteristic length is taken as the height of the vertical section of the external heating jacket, which is 1.59 m. The modified latent heat takes place of the regular latent heat at shown in Eq. 6.25. This allows the condensate sub-cooling effects due to advection to be taken into account, and was originally proposed by Rohsenow (1956).

$$\Delta H'_{lg} = \Delta H_{lg} + 0.68 C_{P,l}\left(T_{stm} - T_{w,out}\right) \tag{6.25}$$

6.9.2 External Heating Jacket: Knuckle Section

The knuckled section allows a smooth transition between the upper vertical and lower dished walls of the evaporator. The correlation described by Perry and Geddes (2011) is used to treat the condensation heat transfer coefficient on the knuckle. This was discussed in CHAPTER 2, and is displayed again in Eq. 6.26, and is best understood when referred to Figure 6.18.

$$h_{csn} = \lambda_l \left[\frac{\delta_l^4 (r_0 + r_k)^{4/3} + 4\tilde{A} r_k \int_0^\theta (r_0 + r_k \cos\theta)^{4/3} (\cos\theta)^{1/3} d\theta}{(\cos\theta (r_0 + r_k \cos\theta))^{4/3}}\right]^{-1/4} \tag{6.26}$$

The correlation requires the user to discretise the path from $p_{k,1}$ to $p_{k,2}$ in Figure 6.18 into elements, where the angle between the elements is denoted by θ, and where the origin is where $r_{k,in}$ and $r_{k,out} = 0$ m. No guidance is provided by Perry and Geddes as to how many elements should be used between $p_{k,1}$ and $p_{k,2}$. Figure 6.19 is an illustration of the knuckle region only. In Figure 6.19, the top left quadrant shows the theoretical condensate layer attached to the knuckle, coloured in salmon pink. The top right quadrant shows the model condensate layer thickness coloured in olive green, when the knuckle has just two nodes, and one element. There is a linear fit in the condensate profile, and the portion of condensate coloured in daffodil yellow is lost. The amount of loss decreases when the number of nodes increases to 3, as shown in the lower left quadrant of Figure 6.19. Finally, in the last quadrant, there is very little loss of condensate. Please note, Figure 6.19 is a representative example purely for illustrative purposes only, and is not to scale.

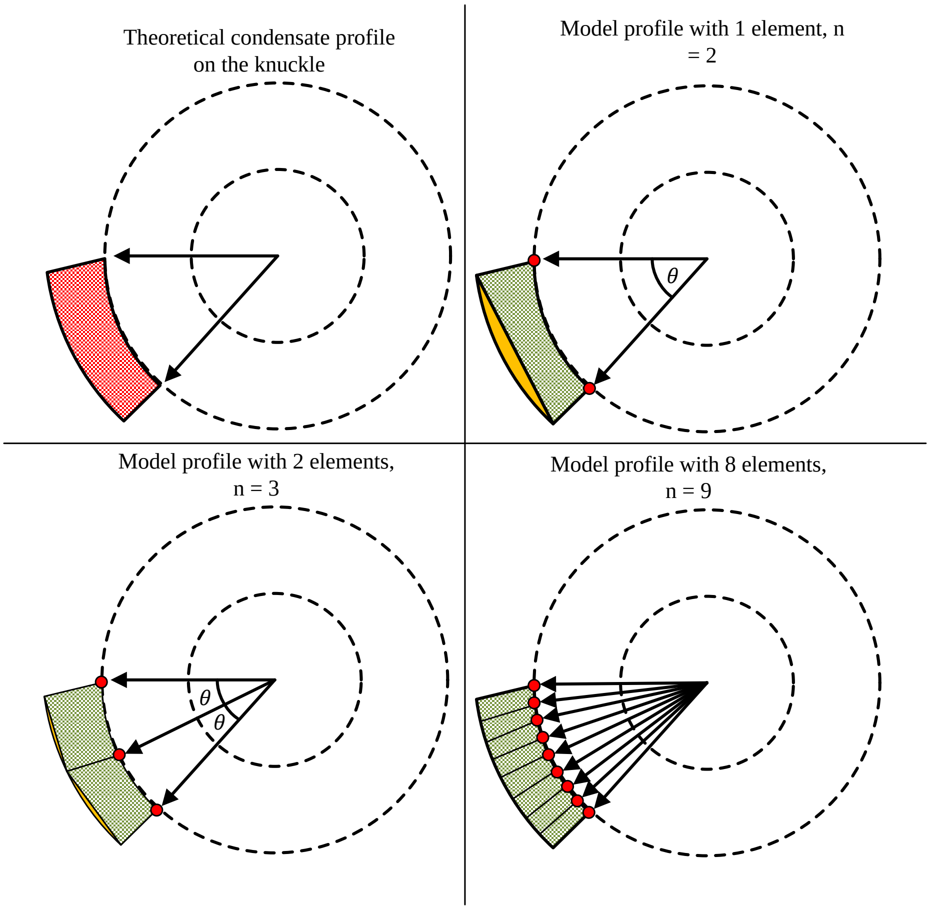

Figure 6.19: Condensation film thickness on the knuckle, showing the effect of increasing the number of elements for the Perry and Geddes (2011) condensation heat transfer model.

The correlation in Eq. 6.26 is a function of the condensate layer thickness at each element in the knuckle, and the thickness must be computed for each element. The thickness is determined using the correlation in Eq. 6.27.

$$\delta_k = \left[\frac{\delta_l^4 (r_0+r_k)^{4/3} + 4\tilde{A} r_k \int_0^{\theta} (r_0 + r_k \cos\theta)^{4/3} (\cos\theta)^{1/3} d\theta}{(\cos\theta (r_0 + r_k \cos\theta))^{4/3}}\right]^{1/4} \tag{6.27}$$

The condensate thickness in Eq. 6.27 is itself a function of the condensate thickness in the previous section. For example, to compute the thickness in the first element the condensate thickness that leaves the vertical walls of the external heating jacket needs to be determined. This is the condensate at the interface of the royal blue and salmon pink area in Figure 6.18. This thickness is determined using the well-known Nusselt formulation as shown in 6.28.

$$\delta_v = \left[\frac{4\lambda_l \mu_l (T_{stm} - T_{w,in}) y}{g \rho_l (\rho_l - \rho_g) h_{lg}}\right]^{\frac{1}{4}} \tag{6.28}$$

Lastly the correlations for the condensing heat transfer coefficient and condensate thickness requires the user to determine the definite integral with respect to the angle in the knuckle. The thermophysical properties in Eq. 6.26 and Eq. 6.27 is grouped into a constant, as shown in Eq. 6.29.

$$\tilde{A} = \frac{\mu_l \lambda_l (T_{sat} - T_w)}{\rho_l (\rho_g - \rho_l) g \Delta H'_{lg}} \tag{6.29}$$

6.9.3 External Heating Jacket: Dished Section

Prescription of the condensation heat transfer coefficient at the dished section brings the external heating jacket to a completion. The bottom of the dish is where the condensate is allowed to drain from, as shown by Figure 6.18. This means in theory, the condensate should be at its thickest here, or fully flooded.

The correlation by Popiel and Boguslawski (1975) was used to estimate the condensation heat transfer coefficient at the dished section, where the thickness of the condensate takes the thickness of the condensate of the last element in knuckle region. The local condensation heat transfer coefficient is described by Eq. 6.30.

$$h_{csn} = \lambda_l \left[\frac{4\tilde{A} r_{d,out} \int_{\alpha_2}^{\alpha_1} (\sin\alpha)^{\frac{5}{3}} d\alpha + \delta^4 (\sin\alpha)^{\frac{8}{3}}}{(\sin\alpha)^{\frac{8}{3}}} \right]^{-\frac{1}{4}} \tag{6.30}$$

Note the thermophsyical properties are grouped into a constant described by Eq. 6.29.

The correlation by Perry and Geddes (2011) for the condensation of vapours on the knuckle region follows the technique used by Popiel and Boguslawski (1975). In fact, in Eq. 6.26, if $r_{k,mid} = 0$ and $r_{k,out} = r_{d,out}$ then the correlation reduces to Eq. 6.30 which is for spheres.

6.9.4 External Heating Jacket: Final Remarks

Condensation on each of these geometries will yield different condensing heat transfer coefficients on those surfaces because the condensate layer profile varies with respect to position. Therefore the analytical Nusselt condensation formulation is used for the vertical walls, as shown in Eq. 6.24, the custom Perry and Geddes formulation for the knuckle is used, as shown in Eq. 6.26, and finally the Popiel and Boguslawski formulation for the dish as shown in Eq. 6.30.

The condensation heat transfer coefficients are a function of the temperature difference between the steam and the outside wall surface. This can be obtained by rearranging Eq. 6.17 to make the outside wall temperature the subject of the formula. However this relies on knowing the wall heat flux and heat transfer coefficient (which itself is a function of the temperature difference) at each iteration in the compute process, which is unknown and is being solved for. Therefore by using the rearranged version of Eq. 6.17 to satisfy the temperature difference would give rise an iterative recursion error, where the solution is a function of the value being solved for. This is very dangerous to implement into a CFD configuration as it leads to numerical instability of the CFD solution. However if the inside wall temperature in Eq. 6.17 was a function of a single field variable (either heat flux or outside wall temperature) then this would not be a problem as the problem is not being constrained and maintains some degree of freedom. Hence as an estimate, the outside wall temperature is treated as a halfway point between the steam temperature and the inside wall temperature as shown in Eq. 6.31.

$$T_{w,out} = \frac{(T_{stm} + T_{w,in})}{2} \tag{6.31}$$

Finally the "outside temperature" used in conjunction with the heat transfer coefficient applied to the surfaces of the external heating jacket was 124.7 ºC corresponding to 2.3 bar saturation pressure.

6.10 Boundary Conditions: Internal Helical Coils

In a similar fashion to the external heating jacket the boundary conditions at the coils took the form of a heat transfer coefficient and "external temperature". In this case the heat transfer coefficient was a combination of the in tube condensation heat transfer coefficient and conduction heat transfer through the tube walls as described by Eq. 6.19 and Eq. 6.20.

Conduction heat transfer through the coil walls takes the expression as shown in Eq. 6.32.

$$h_{cdn} = \frac{\lambda_w}{r_{coil,out} \ln\left(\frac{r_{coil,out}}{r_{coil,in}}\right)} \tag{6.32}$$

The condensing heat transfer coefficient inside the tubes varies according to position and steam quality. Recall from Figure 6.7 the coils have horizontal and vertical components. From Figure 6.7 steam enters the coils at the horizontal position, and then travels downward before reaching the helical spiral, which can be thought of as a horizontal tube. It leaves the coil system via the condensate which is in the vertical position. Therefore two modes of in tube condensation will occur inside the internal helical coils of Evaporator C. These are in tube condensation inside horizontal tubes, and in tube condensation inside vertical tubes.

When in tube condensation occurs in horizontal pipes, the flow of the condensate film adheres to the upper hemisphere of the tube, and floods the lower hemisphere as shown in Figure 6.20.

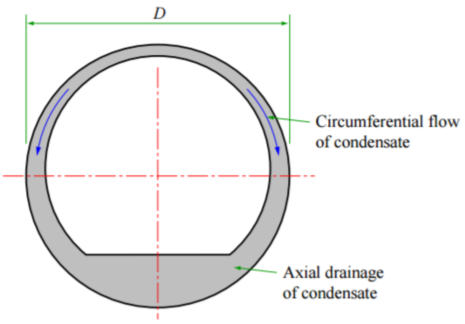

Figure 6.20: Cross section of in tube condensation for a horizontal pipe. Image courtesy of ESDU-94041 (1994).

The typical vapour condensate profile for low liquid loadings in horizontal pipes is shown by Figure 6.21. This behaviour may occur at the beginning of the internal helical coils where the condensate effects are at their lowest.

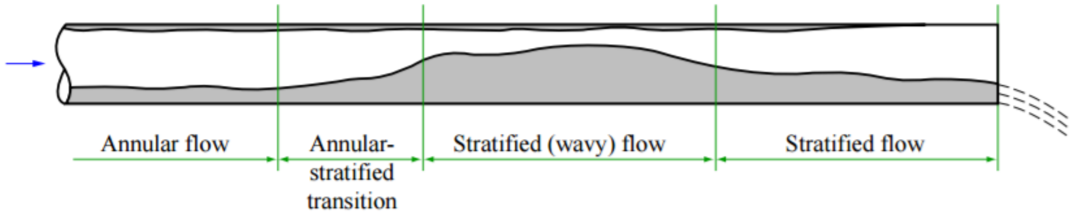

Figure 6.21: Vapour condensate profile for low liquid loadings in a horizontal pipe. Image courtesy of ESDU-94041 (1994).

The typical vapour condensate profile for high liquid loadings in horizontal pipes where the condensate fully floods the coils is shown by Figure 6.22. This could occur toward the end of the steam section of the helical coils just prior to reaching the condensate line.

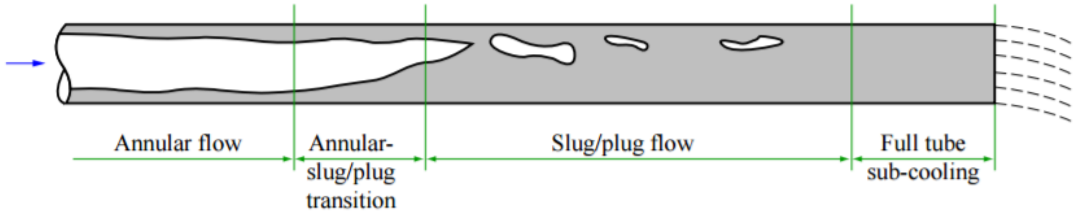

Figure 6.22: Vapour condensate profile for high liquid loadings in a horizontal pipe. Image courtesy of ESDU-94041 (1994).

In tube condensation behaves differently when the position of the tube is in the vertical position. The idealised behaviour of the vapour condensate profile for high liquid loadings in vertical pipes is shown in Figure 6.23.

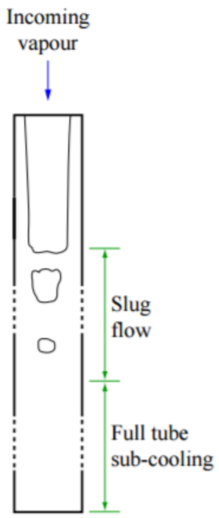

Figure 6.23: Vapour condensate profile for high liquid loadings in a vertical pipe. Image courtesy of ESDU-91024 (2001).

Based on this information, condensation heat transfer coefficients describing in tube condensation in either the horizontal position or vertical position was applied to satisfy the condensation heat transfer coefficient requirements in Eq. 6.20.

6.10.1 Internal Helical Coils Geometrical Division

To facilitate a varied condensation heat transfer coefficient as a function of position inside the helical coils, the steam section of the coils were divided into component parts at the geometry production stage. This is shown in Figure 6.24 for the lower inner coil. The remaining five coils followed the same format. The condensate line was not divided.

Dividing the steam section by individual areas was done strategically in order to apply unique thermal boundary conditions to those areas. Correlations for in tube condensation heat transfer coefficients are a function of steam quality, and mass flow which was calculated via the energy balance. The steam quality was assumed to be 1 at the inlet and 0 by the time it had reached the condensate line. A proportion of the steam quality was applied to each steam area in Figure 6.24 weighted by their surface area. Steam areas 2 and 4 were treated as horizontal pipes.

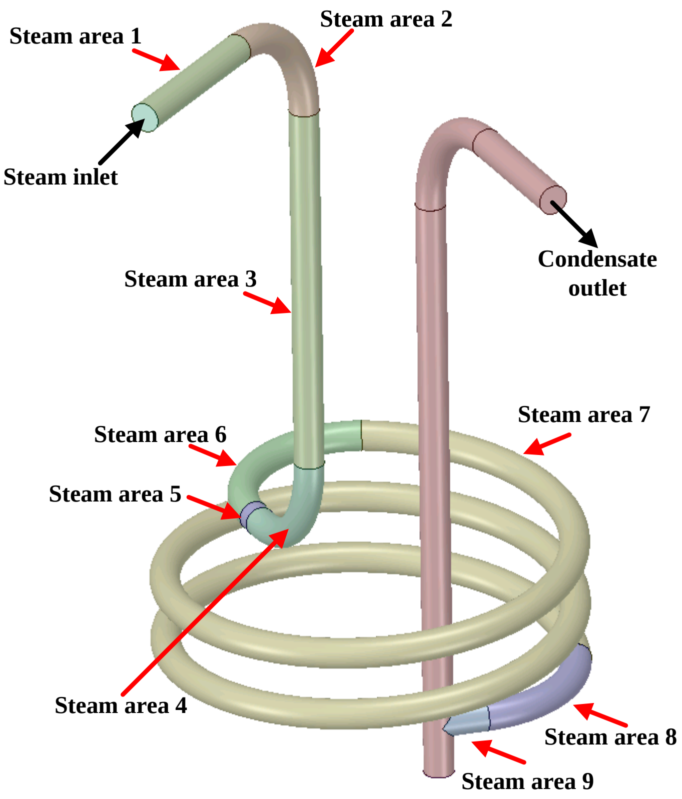

Figure 6.24: Partitioned steam areas of the lower inner coil. The remaining five coils followed the same format.

6.10.2 Internal Helical Coils: Condensation Heat Transfer Coefficient

The in tube condensation heat transfer coefficients described in guide ESDU-94041 (1994) for the horizontal portion of the tubes, and ESDU-91024 (2001) for the vertical portion of the tubes was used respectively. The procedure was based on the work of Nusselt (1916) who studied laminar film condensation on vertical surfaces and inside tubes; and the work of Taitel and Dukler (1976) who provided models predict two phase flow regime transitions inside tubes; and finally and Breber *et al.*, (1980) who provided a model to predict in tube steam condensation inside horizontal tubes.

The guides outline the procedure process to determine the condensing heat transfer coefficients inside the internal helical coils. The procedure process for the horizontal sections of the internal helical coils was as follows.

1. Calculate the dimensionless superficial gas phase velocity inside the tubes.

$$j_g^* = \frac{\dot{M}_g}{\frac{\pi}{4} D_{coil}^2 \left[D_{coil} \rho_g (\rho_l - \rho_g) g\right]^{\frac{1}{2}}} \qquad (6.33)$$

2. Calculate the Martinelli parameter.

$$X_{tt} = \left(\frac{1-x_g}{x_g}\right)^{0.9} \left(\frac{\rho_g}{\rho_l}\right)^{0.5} \left(\frac{\mu_l}{\mu_g}\right)^{0.1} \tag{6.34}$$

3. Calculate the product of the dimensionless superficial velocity and the cube root of the Martinelli paramter. Based on flow maps by Taitel and Dukler (1976) and Breber *et al.*, (1980) then if:
    - $j_g^* X_{tt}^{1/3} > 1$ and $X_{tt} \leq 1.5$ then the flow may be assumed annular
    - $j_g^* X_{tt}^{1/3} \leq 1$ and $X_{tt} \leq 1.5$ then the flow may be assumed stratified
    - $X_{tt} > 1.5$ then the flow may be considered slug/plug

If the flow is annular inside the horizontal tube section then the heat transfer coefficient took the form as shown in Eq. 6.35. The dimensionless Nusselt number in Eq. 6.35 took the definition as described by Eq. 6.36.

$$h_{csn} = \mathrm{Nu}\lambda_l \left[\frac{\rho_l(\rho_l-\rho_g)g}{\eta_l^2}\right]^{1/3} \tag{6.35}$$

$$\mathrm{Nu} = \left[0.31\mathrm{Re}_{cst}^{-1.32} \left(\frac{\mathrm{Re}_{cst}^{2.4}\mathrm{Pr}_{cst}^{3.9}}{2.37\times10^{14}}\right)^{1/3} + \frac{\mathrm{Pr}_{cst}^{1.5}\tau_i^*}{771.6}\right]^{1/2} \tag{6.36}$$

The Nusselt number in Eq. 6.36 is a function of condensate film Reynolds number as shown by Eq. 6.37 and Eq. 6.38 respectively.

$$\mathrm{Re}_{cst} = \frac{4(1-x_g)\dot{M}}{\pi D_{inner}\eta_l} \tag{6.37}$$

$$\mathrm{Pr}_{cst} = \frac{\mu_l C_{P,l}}{\lambda_l} \tag{6.38}$$

The dimensionless interfacial shear stress also features in the definition of the Nusselt number in Eq. 6.36 which is shown in Eq. 6.39.

$$\begin{aligned} x_g < 0.81 \quad \tau_i^* &= \Omega\left(\frac{x_g}{1-x_g}\right)^{1.4} \mathrm{Re}_{cst}^{1.8} \\ x_g > 0.81 \quad \tau_i^* &= 0.383\Omega\left(\frac{\mathrm{Re}_{cst}}{1-x_g}\right)^{1.8} \end{aligned} \tag{6.39}$$

Finally the thermophysical properties are absorbed inside the operator Ω which has the definition as shown in Eq. 6.40.

$$\Omega = \frac{0.252\mu_l^{1.177}\mu_g^{0.156}}{D_{inner}^2 g^{2/3}\rho_l^{0.553}\rho_g^{0.78}} \tag{6.40}$$

If the condensing heat transfer coefficient was determined to be in the stratified flow regime in the horizontal pipes then the relation in Eq. 6.41 was used.

$$\begin{aligned} &\mathrm{Re}_{stm} > 7780 \quad h_{csn} = 0.09\mathrm{Re}_{stm}^{0.2}\frac{\Omega}{(D_{inner}\Delta T)^{0.25}} \\ &\mathrm{Re}_{stm} \leq 7780 \qquad h_{csn} = \frac{0.54\Omega}{(D_{inner}\Delta T)^{0.25}} \end{aligned} \tag{6.41}$$

The steam Reynolds number is defined as shown in Eq. 6.42. The thermphysical properties was absorbed by the operator Ω which did not have the same definition defined by Eq. 6.40, but took the definition in Eq. 6.43.

$$\mathrm{Re}_{stm} = \frac{4x_g\dot{M}}{\pi D_{inner}\eta_g} \tag{6.42}$$

$$\Omega = \left[\frac{g\rho_l(\rho_l-\rho_g)\lambda_l^3\Delta H_{lg}}{\mu_l}\right]^{1/4} \tag{6.43}$$

Finally if the flow regime in the horizontal sections of the internal helical coils was in the slug/plug regime then the heat transfer coefficient took the form as shown in Eq. 6.44. The definition of the condensate Prandtl number were the same as that defined for annular flow. The condensate Reynolds number was defined as shown in Eq. 6.45 which was a function of the void fraction as shown in Eq. 6.46.

$$h_{csn} = 0.023\frac{\lambda_l}{D_{inner}}\mathrm{Re}_{cst}^{0.8}\mathrm{Pr}_{cst}^{0.4} \tag{6.44}$$

$$\mathrm{Re}_{cst} = \frac{4\dot{M}(1-x_g)}{\pi\eta_l D_{inner}(1-\varepsilon_g)} \tag{6.45}$$

$$\varepsilon_g = \frac{1}{1+\left(\frac{1-x_g}{x_g}\right)\left(\frac{\rho_g}{\rho_l}\right)^{2/3}} \tag{6.46}$$

Finally the mean condensing heat transfer coefficient for the vertical portion of the steam section of the internal helical coils was provided by the relation in Eq. 6.47. The modified Nusselt number is provided by Eq. 6.48.

$$h_{csn} = \mathrm{Nu}\lambda_l\left[\frac{g\rho_l(\rho_l-\rho_g)}{\mu_l^2}\right]^{1/3} \tag{6.47}$$

$$\mathrm{Nu} = \left(\mathrm{Re}_{cst}^{-0.44} + \frac{\mathrm{Re}_{cst}^{0.8}\mathrm{Pr}_{cst}^{1.3}}{1.718\times10^5} + \frac{\mathrm{Pr}_{cst}^{1.5}\tau_i^*}{771.6}\right)^{1/2} \tag{6.48}$$

The condensate Prandtl number took the same form as that shown in Eq. 6.38. The dimensionless mean interfacial shear stress is defined in Eq. 6.49.

$$\tau_i^* = \Omega\mathrm{Re}_{cst}^{1.8}\left(\frac{\mathrm{Re}_{cst}}{\mathrm{Re}_{stm}}\right)^{0.4}\left(1.25 + 0.39\frac{\mathrm{Re}_{cst}}{\mathrm{Re}_{stm}}\right)^{-2} \tag{6.49}$$

The operator for the thermophysical properties took the form described by Eq. 6.40. The condensate Reynolds number was defined by Eq. 6.37, and the steam Reynolds number by Eq. 6.42.

The driving temperature in the condensation heat transfer coefficients was the steam temperature for the coils, which was 127.4 ºC corresponding to 2.5 bar. The calculated parameters, including the local heat transfer coefficients at each area on the steam section of the internal helical coils are tabulated in Table 6.16, Table 6.17, Table 6.18, Table 6.19, Table 6.20 and Table 6.21.

Condensate leaving the internal helical coils would be sub cooled single phase liquid. ESDU-91024 (2001) reports that for sub cooled condensate leaving a vertical pipe the single phase heat transfer coefficient can be predicted by the relation in Eq. 6.50. This correlation has the benefit of accounting for buoyancy body forces in its prescription, which is absent in heat transfer correlations of the form $\mathrm{Nu} = x\mathrm{Re}^{n}\mathrm{Pr}^{n}$. The correlation in Eq. 6.50 is based on recommendations by Mueller (1983).

$$h = 0.0057\mathrm{Re}^{0.4}\mathrm{Pr}^{0.34}\left(\frac{\mu_l^2}{\left(\rho_l - \rho_g\right)^2}\right)^{-1/3}\lambda_l^{-1} \qquad (6.50)$$

The heat transfer coefficient for the condensate section of the internal helical coils was coupled with an outside temperature. This was the mean condensate temperature 45.0 °C which is tabulated in Table 6.14 along with other key information relating to the coils.

Upper Inner Coil	**Area 1 Horizontal**	**Area 2 Horizontal**	**Area 3 Vertical**	**Area 4 Horizontal**	**Area 5 Horizontal**	**Area 6 Horizontal**	**Area 7 Horizontal**	**Area 8 Horizontal**	**Area 9 Horizontal**
Steam Quality, x	0.97	0.93	0.89	0.84	0.84	0.81	0.05	0.01	0.00
Mass Flow Rate of Steam, $\dot{M}_{stm}$ [kg/s]	0.088	0.084	0.081	0.076	0.076	0.073	0.004	0.001	0.000
Mass Flow Rate of Condensate, $\dot{M}_{cst}$ [kg/s]	0.003	0.007	0.010	0.014	0.014	0.017	0.086	0.090	0.091
Dimensionless Superficial Velocity, j_g^*	0.421	0.402	0.386	0.366	0.365	0.351	0.021	0.003	0.000
Martinelli Parameter, X_{tt}	0.002	0.005	0.008	0.011	0.011	0.014	0.746	3.926	-
Product, $j_g^* X_{tt}^{1/3}$	0.054	0.070	0.076	0.082	0.082	0.084	0.019	0.005	-
Flow Regime	Stratified	Stratified	Stratified	Stratified	Stratified	Stratified	Stratified	Slug Plug	Almost single phase condensate
Vapour Phase Reynolds Number	95516	91007	87434	82927	82637	79443	4741	781	0
Liquid Phase Reynolds Number	164	438	654	927	945	1138	5665	5905	5952
Condensing Heat Transfer Coefficient [W/m^{2}K]	18070	17839	2751	17402	17385	17204	9257	305	209
Overall Heat Transfer Coefficient (Condensation and Wall Conduction) [W/m^{2}K]	981	980	753	979	979	978	933	236	174

Table 6.16: Upper inner coil calculated parameters for in tube condensation heat transfer coefficients.

Upper Middle Coil	**Area 1 Horizontal**	**Area 2 Horizontal**	**Area 3 Vertical**	**Area 4 Horizontal**	**Area 5 Horizontal**	**Area 6 Horizontal**	**Area 7 Horizontal**	**Area 8 Horizontal**	**Area 9 Horizontal**
Steam Quality, x	0.99	0.95	0.93	0.90	0.89	0.87	0.05	0.01	0.00
Mass Flow Rate of Steam, $\dot{M}_{stm}$ [kg/s]	0.122	0.118	0.115	0.111	0.111	0.108	0.007	0.001	0.000
Mass Flow Rate of Condensate, $\dot{M}_{cst}$ [kg/s]	0.002	0.006	0.009	0.013	0.013	0.016	0.117	0.123	0.124
Dimensionless Superficial Velocity, j_g^*	0.584	0.565	0.551	0.532	0.530	0.518	0.031	0.004	0.000
Martinelli Parameter, X_{tt}	0.001	0.003	0.005	0.007	0.007	0.009	0.686	4.586	-
Product, $j_g^* X_{tt}^{1/3}$	0.060	0.084	0.094	0.103	0.103	0.107	0.028	0.007	-
Flow Regime	Stratified	Stratified	Stratified	Stratified	Stratified	Stratified	Stratified	Slug Plug	Almost single phase condensate
Vapour Phase Reynolds Number	132468	128118	124871	120523	120198	117369	7084	900	0
Liquid Phase Reynolds Number	112	375	572	836	855	1027	7710	8084	8139
Condensing Heat Transfer Coefficient [W/m^{2}K]	19717	19542	3646	19226	19212	19091	9257	373	269
Overall Heat Transfer Coefficient (Condensation and Wall Conduction) [W/m^{2}K]	986	985	808	984	984	984	933	274	213

Table 6.17: Upper middle coil calculated parameters for in tube condensation heat transfer coefficients.

Upper Outer Coil	**Area 1 Horizontal**	**Area 2 Horizontal**	**Area 3 Vertical**	**Area 4 Horizontal**	**Area 5 Horizontal**	**Area 6 Horizontal**	**Area 7 Horizontal**	**Area 8 Horizontal**	**Area 9 Horizontal**
Steam Quality, x	0.99	0.96	0.95	0.92	0.91	0.89	0.04	0.01	0.00
Mass Flow Rate of Steam, $\dot{M}_{stm}$ [kg/s]	0.155	0.151	0.148	0.144	0.142	0.139	0.007	0.002	0.000
Mass Flow Rate of Condensate, $\dot{M}_{cst}$ [kg/s]	0.002	0.006	0.008	0.012	0.014	0.017	0.149	0.154	0.156
Dimensionless Superficial Velocity, j_g^*	0.740	0.721	0.708	0.689	0.681	0.666	0.033	0.010	0.000
Martinelli Parameter, X_{tt}	0.001	0.003	0.004	0.006	0.006	0.008	0.817	2.454	-
Product, $j_g^* X_{tt}^{1/3}$	0.070	0.099	0.111	0.122	0.126	0.132	0.031	0.013	-
Flow Regime	Stratified	Stratified	Stratified	Stratified	Stratified	Stratified	Stratified	Slug Plug	Almost single phase condensate
Vapour Phase Reynolds Number	167712	163478	160396	156162	154259	150995	7427	2259	0
Liquid Phase Reynolds Number	109	365	552	809	924	1122	9822	10135	10272
Condensing Heat Transfer Coefficient [W/m^{2}K]	20997	20854	4495	20601	20534	20417	9257	566	324
Overall Heat Transfer Coefficient (Condensation and Wall Conduction) [W/m^{2}K]	989	988	843	988	988	987	933	366	247

Table 6.18: Upper outer coil calculated parameters for in tube condensation heat transfer coefficients.

Lower Inner Coil	**Area 1 Horizontal**	**Area 2 Horizontal**	**Area 3 Vertical**	**Area 4 Horizontal**	**Area 5 Horizontal**	**Area 6 Horizontal**	**Area 7 Horizontal**	**Area 8 Horizontal**	**Area 9 Horizontal**
Steam Quality, x	0.96	0.91	0.82	0.78	0.77	0.72	0.05	0.01	0.00
Mass Flow Rate of Steam, $\dot{M}_{stm}$ [kg/s]	0.093	0.088	0.080	0.075	0.075	0.069	0.005	0.001	0.000
Mass Flow Rate of Condensate, $\dot{M}_{cst}$ [kg/s]	0.004	0.008	0.017	0.021	0.022	0.027	0.092	0.096	0.097
Dimensionless Superficial Velocity, j_g^*	0.444	0.423	0.381	0.360	0.358	0.332	0.022	0.004	0.000
Martinelli Parameter, X_{tt}	0.003	0.006	0.013	0.016	0.017	0.022	0.751	3.455	-
Product, $j_g^* X_{tt}^{1/3}$	0.064	0.077	0.089	0.092	0.092	0.093	0.020	0.006	-
Flow Regime	Stratified	Stratified	Stratified	Stratified	Stratified	Stratified	Stratified	Slug Plug	Almost single phase condensate
Vapour Phase Reynolds Number	100535	95841	86240	81549	81186	75345	5023	959	0
Liquid Phase Reynolds Number	259	543	1125	1409	1431	1785	6047	6293	6351
Condensing Heat Transfer Coefficient [W/m^{2}K]	18319	18086	2916	17324	17304	16962	9257	336	220
Overall Heat Transfer Coefficient (Condensation and Wall Conduction) [W/m^{2}K]	982	981	765	979	979	978	933	254	182

Table 6.19: Lower inner coil calculated parameters for in tube condensation heat transfer coefficients.

Lower Middle Coil	**Area 1 Horizontal**	**Area 2 Horizontal**	**Area 3 Vertical**	**Area 4 Horizontal**	**Area 5 Horizontal**	**Area 6 Horizontal**	**Area 7 Horizontal**	**Area 8 Horizontal**	**Area 9 Horizontal**
Steam Quality, x	0.98	0.95	0.89	0.86	0.85	0.83	0.05	0.01	0.00
Mass Flow Rate of Steam, $\dot{M}_{stm}$ [kg/s]	0.129	0.125	0.117	0.113	0.113	0.109	0.006	0.002	0.000
Mass Flow Rate of Condensate, $\dot{M}_{cst}$ [kg/s]	0.003	0.007	0.015	0.019	0.019	0.023	0.126	0.130	0.132
Dimensionless Superficial Velocity, j_g^*	0.618	0.598	0.560	0.540	0.539	0.522	0.029	0.009	0.000
Martinelli Parameter, X_{tt}	0.002	0.004	0.008	0.010	0.010	0.012	0.785	2.219	-
Product, $j_g^* X_{tt}^{1/3}$	0.072	0.093	0.112	0.117	0.118	0.121	0.027	0.012	-
Flow Regime	Stratified	Stratified	Stratified	Stratified	Stratified	Stratified	Stratified	Slug Plug	Almost single phase condensate
Vapour Phase Reynolds Number	140028	135576	126877	122428	122120	118273	6541	2128	0
Liquid Phase Reynolds Number	181	451	978	1248	1266	1499	8270	8537	8666
Condensing Heat Transfer Coefficient [W/m^{2}K]	20011	19839	3858	19307	19294	19130	9257	517	282
Overall Heat Transfer Coefficient (Condensation and Wall Conduction) [W/m^{2}K]	986	986	818	985	984	984	933	345	222

Table 6.20: Lower middle coil calculated parameters for in tube condensation heat transfer coefficients.

Lower Outer Coil	**Area 1 Horizontal**	**Area 2 Horizontal**	**Area 3 Vertical**	**Area 4 Horizontal**	**Area 5 Horizontal**	**Area 6 Horizontal**	**Area 7 Horizontal**	**Area 8 Horizontal**	**Area 9 Horizontal**
Steam Quality, x	0.98	0.95	0.91	0.88	0.88	0.85	0.04	0.01	0.00
Mass Flow Rate of Steam, $\dot{M}_{stm}$ [kg/s]	0.164	0.160	0.152	0.148	0.148	0.143	0.006	0.002	0.000
Mass Flow Rate of Condensate, $\dot{M}_{cst}$ [kg/s]	0.004	0.008	0.016	0.020	0.020	0.025	0.162	0.166	0.168
Dimensionless Superficial Velocity, j_g^*	0.784	0.765	0.729	0.710	0.709	0.685	0.030	0.010	0.000
Martinelli Parameter, X_{tt}	0.002	0.003	0.007	0.008	0.008	0.011	0.943	2.513	
Product, $j_g^* X_{tt}^{1/3}$	0.096	0.116	0.137	0.143	0.144	0.150	0.030	0.014	
Flow Regime	Stratified	Stratified	Stratified	Stratified	Stratified	Stratified	Stratified	Slug Plug	
Vapour Phase Reynolds Number	177728	173434	165252	160960	160665	155301	6852	2366	0
Liquid Phase Reynolds Number	271	532	1027	1288	1305	1630	10626	10898	11041
Condensing Heat Transfer Coefficient [W/m^{2}K]	21324	21186	4797	20768	20758	20571	9257	593	343
Overall Heat Transfer Coefficient (Condensation and Wall Conduction) [W/m^{2}K]	989	989	853	988	988	988	933	377	258

Table 6.21: Lower outer coil calculated parameters for in tube condensation heat transfer coefficients.

6.11 Boundary Conditions: Ullage Walls

The unheated ullage walls in contact with the liquid was treated as heat loss walls, in the same way they were treated for the investigation on the scaled test rig in CHAPTER 5. Hence heat loss from the unheated walls was a combination of conduction through the unheated portions of the external shell, and a combination of convection and radiation. These correlations were described by Eq. 5.1, Eq. 5.2 and Eq. 5.3 in CHAPTER 5. The ambient outside temperature was taken as 15°C.

6.12 Boundary Conditions: Liquor Feed and Internal Apparatus

The mass flow of the liquor feed was set equal and opposite to the rate of evaporation, and had an inlet liquor temperature of 20 °C. The unheated internal apparatus in contact with the liquid (steam sparger and liquor outlets) were treated as adiabatic walls.

6.13 Operating Conditions

The CFD models which were developed to simulate boiling flows inside the scaled test rig in CHAPTER 5 were used to model the flows inside Evaporator C. Hence two phase Eulerian – Eulerian boiling simulations were performed. The custom formulation for the interfacial length scale was used in the prescription for the interfacial area density. Based on the validation studies on the scaled test rig in CHAPTER 5, the phase change rate constant took a value of 1 Hz. In the simulations water was taken as the process fluid, which was the same fluid that was used in the commissioning tests of Evaporator C. The water depth was 2.35 m. The top surface of the physical flow domain was set to an opening boundary condition.

6.14 Summary

The design of Evaporator C was explored, which shows the vessel to have a complex geometrical setup. Based on engineering drawings, a CAD model of Evaporator C was prepared to facilitate a CFD boiling analysis. Analysis of Evaporator C has shown there to be large areas inside the vessel which will act as blockages against the natural flow of liquor. These blockages are caused by the presence of six internal helical coils which provide heating to the liquor, three liquor outlets which extract liquor concentrate at the end of a batch, and a steam sparger which helps to dislodge settled solids at the base of the evaporator.

Instrumentation is also present, such as thermocouples, a pneumercator and a density probe. However these were not included in the evaporator CAD geometry as they would make meshing the vessel extremely difficult, and would give rise to an extremely high number of mesh cells.

Each of the evaporator coils houses steam traps at the interface of the steam and condensate piping sections. The steam traps ensure no steam is allowed to continue on into the condensate piping sections. The incoming steam temperature in the coils is 127.4 ºC corresponding to 2.5 bar, however the steam mass flow was not known, which had to be determined in order to apply the appropriate thermal boundary conditions. Another heat transfer mode into the evaporator vessel occurs via an external heating jacket attached to the evaporator outer shell. The external heating jacket surrounds the liquor, except from a small area at the free surface. The incoming steam inside the jacket is 124.7 ºC corresponding to 2.3 bar saturation pressure.

The total heat flux input into Evaporator C to evaporate 90 m^3/day of water (1.03 kg/s) in steady state mode is 33350 W/m^2. By performing a reverse energy and material balance based on the available information, the conditions required for the CFD analysis was determined, and the results presented in CHAPTER 7.

Chapter 7

Simulation Results of the Industrial Evaporator

7.1 Introduction

The results of the simulations of the industrial evaporator, Sellafield Evaporator C are presented here. The computational methods which were used for the scaled test rigs were used to simulate Evaporator C, using a phase change rate constant of 1 Hz. The boundary conditions were described in CHAPTER 6.

First a steady state free convection simulation was performed to establish the flow fields. This was used as the initial state for the second step, which was to perform transient free convection simulations on three meshes which increased in cell density. The transient free convection simulations were the basis of the mesh sensitivity study, and were used to ensure that boiling conditions had been reached at the free surface prior to activating the boiling model. Once a suitable mesh was determined from the sensitivity study, a steady state boiling simulation was performed on the chosen mesh, using the transient free convection result as the initial state. The purpose of this was to advance the boiling flow fields sufficiently in time to overcome the initial transient effects. Lastly, transient boiling simulations were performed for a total time of 10 s.

7.2 Mesh Generation

Unstructured patch dependent meshes were used for the simulations of Evaporator C. These were different to the structured meshes used for the unscaled and scaled test rigs in CHAPTER 4 and CHAPTER 5 respectively.

The method described in CHAPTER 3 was used to generate the unstructured patch dependent meshes. In summary the method used was to first generate an octree volume and surface mesh. The volume elements were then deleted and the surface mesh was retained. The surface mesh was then refined using smoothing algorithms, and then a Delaunay volume mesh was created, using the smoothed surface mesh as seed points. Lastly inflation layers were inserted to relevant boundaries of interest.

Three meshes were generated for the mesh sensitivity study for Evaporator C. Mesh 2 was selected as the independent mesh in the mesh sensitivity study. The mesh generation steps that were used to generate the meshes are described here. Unstructured meshing method was used because of the difficulty of designing blocking topologies associated with structured meshes. Since the Evaporator C geometry is very complicated, generating a block topology and hence structured meshes would have been extremely difficult.

7.2.1 Geometry Diagnostics

Geometry diagnostics were required prior to meshing. In the structured approach used in CHAPTER 4 and 5, these were simple tests of the geometry to check for undesired sharp edges and slivers in the physical domain. More detailed tests were required for the unstructured meshes since an unstructured patch dependent mesh was used which is very sensitive to badly formed features on the surfaces of the geometry (described in CHAPTER 3).

The tests required checking for and removing hard and soft edges and points. These were unnecessary construction edges and points which were superfluous, and once removed did not alter the proportions of the geometry. The geometry was checked for completeness by scanning for holes. Closely sealed “watertight” geometries are required for unstructured patch dependent meshes. During the checking process, no holes were detected. In addition to this, sharp angles, slivers and spikes which were unrepresentative of the physical geometry were scanned for and removed. All surfaces and bodies were also tested to ensure they met the requirements for the meshing algorithm.

7.2.2 Octree Mesh

In the first step of the mesh generation process an octree mesh was computed. The octree method is a robust mesh method which guarantees a successful mesh generation at the expense of mesh quality. This is achieved by using a “top-down” algorithm where the mesh is seeded within the volume of the physical flow domain, and grows in an orderly fashion from the inside out. When the mesh is expanded to surface boundaries from the inside out, the ordering stops, and the remaining gaps are flood filled with random tetrahedron cells based on cell quality. Further details on octree meshes and their applications to CFD can be found in the works of Owen (1998).

Table 7.1 summarises the octree settings that were selected for all three meshes tested in the mesh sensitivity study. The mesh size for the octree meshes increased substantially with refinement. It is important to note these are not the final meshes that were generated for the CFD simulations. They were the final meshes generated for the octree step of the mesh generation.

Mesh	Maximum element size [m]	Minimum Cell Quality	Maximum Number of Iterations	No. of Nodes in Octree Mesh	No. of Elements in Octree Mesh
1	0.03	0.5	5	5,377,287	31,899,600
2	0.02	0.4	5	7,342,848	43,557,588
3	0.01	0.4	10	12,720,135	75,457,187

Table 7.1: Octree statistics for the three meshes used in the mesh sensitivity study.

Using the octree meshes generated in Table 7.1 would yield erroneous results in the CFD simulations. This is because surface meshes associated with the octree methods require refinement, and inflation layers need to be inserted. Figure 7.1,

Figure 7.2 and Figure 7.3 illustrate the octree mesh for mesh 2 on an *x-y* plane at the position of the free surface; the outer and middle coils and knuckle; and lower dished area respectively. The ordered nature of the octree mesh can be seen for the bulk volume, flanked by the disordered flood filled tetrahedron cells at the surface boundaries.

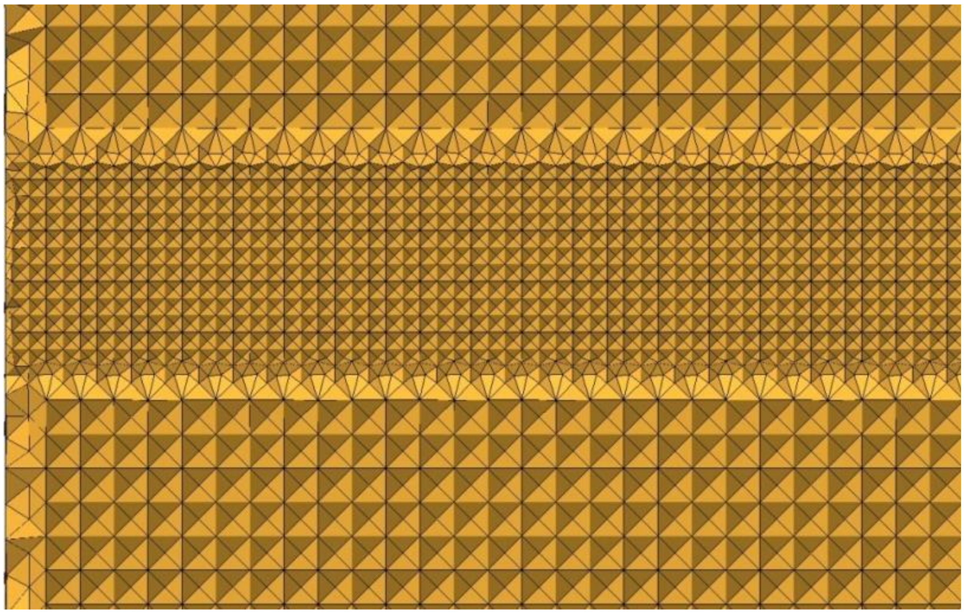

Figure 7.1: Octree refinement for mesh 2 where the liquid-vapour free surface would appear. Plotted on an *x-y* plane intersecting the geometry.

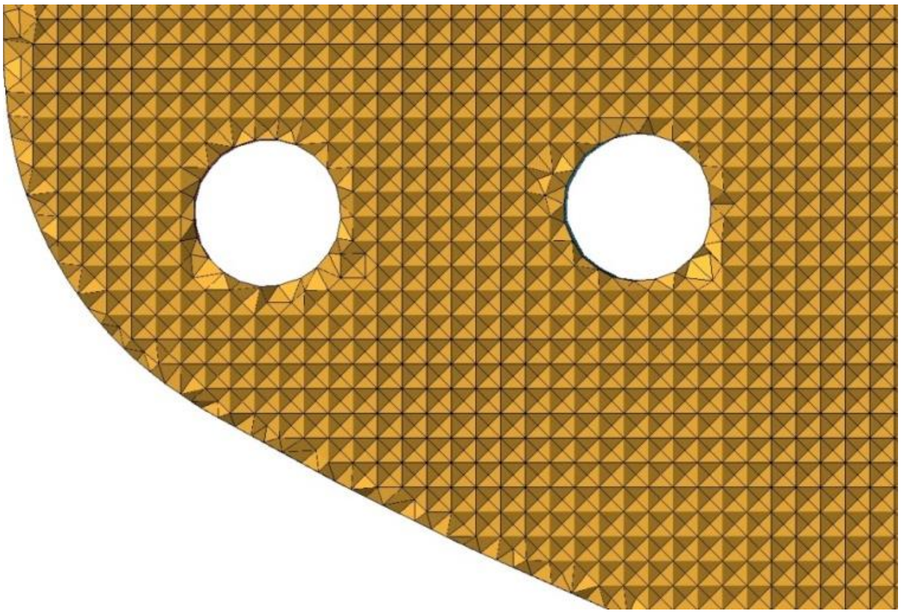

Figure 7.2: Octree mesh for mesh 2 at the position of the outer and middle coils, and knuckle. Plotted on an *x*-*y* plane intersecting the geometry.

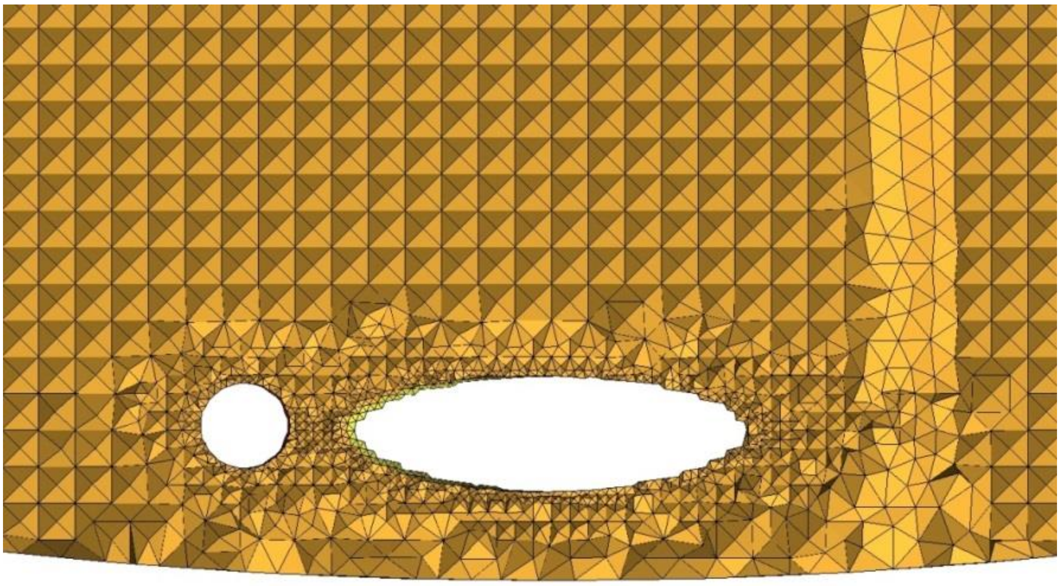

Figure 7.3: Octree mesh for mesh 2 at the lower dished area and the steam sparger. Plotted on an *x*-*y* plane intersecting the geometry.

The purpose of the octree mesh generation step was to guarantee a mesh was generated since the octree method is a guaranteed mesh method. The additional purpose was to achieve a patch dependent surface mesh. The volume mesh was of little use and was deleted as described in the next sub section.

7.2.3 Laplace Surface Mesh

Once the top-down octree mesh was generated, the volume mesh was deleted, but the surface mesh was retained. This meant the surfaces had a mesh associated with them, and the bulk volume did not. The three surface meshes were of fair quality but required refining in order to meet good mesh standards. Furthermore a good surface mesh was required for the next step in the mesh generation which was creating a Delaunay volume mesh, which required good surface mesh statistics.

The Laplace mesh smoother was used as the refining algorithm for the surface mesh smoothing due to its ability to capture boundary surface details in patch conforming methods. Furthermore the Laplace algorithm generally produces good surface mesh qualities with relatively low number of cells compared to other methods such as orthogonal smoothers (Freitag, 1997).

The surface mesh was refined according to the mesh quality criteria set out in CHAPTER 3. Laplace surface mesh smoothing was accomplished for all three meshes to within 30 smoothing iterations. Table 7.2 summarises the surface mesh characteristics for all three meshes used in the sensitivity study.

Mesh	No. of Nodes in the Smoothed Surface Mesh	No. of Elements in the Smoothed Surface Mesh
1	395,434	795,095
2	416,332	836,941
3	438,334	880,989

Table 7.2: Surface mesh statistics after applying the Laplace mesh smoother.

The smoothed surface mesh is displayed in Figure 7.4, Figure 7.5 and Figure 7.6, which illustrated the meshes on the lower outer coil; the central core; and an isometric view above the evaporator.

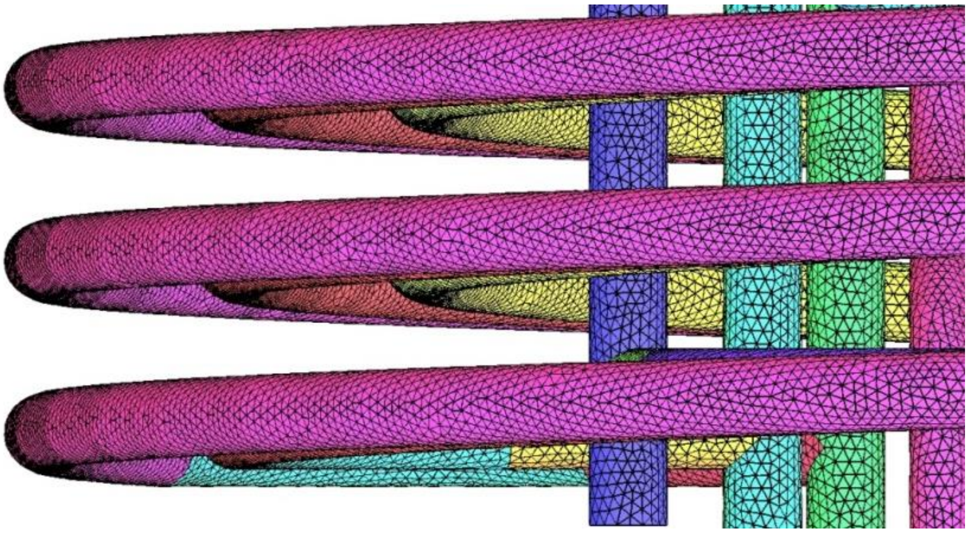

Figure 7.4: Surface mesh for mesh 2 after smoothing using the Laplace method. Image is of the lower outer coil, with some of the intermediate and inner coils shown.

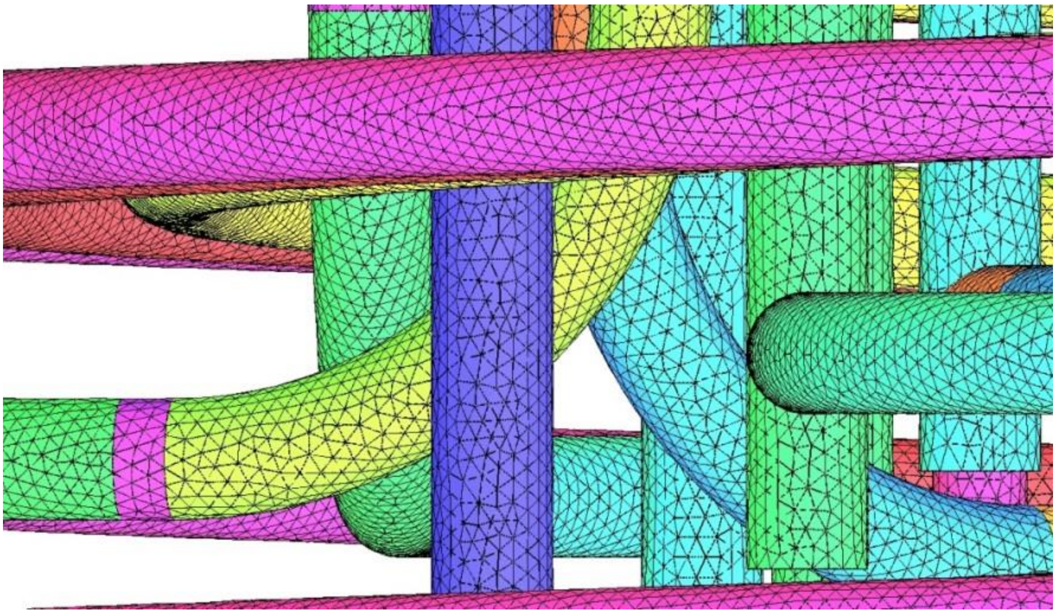

Figure 7.5: Surface mesh for mesh 2 after smoothing using the Laplace method. Image is of the central core of Evaporator C.

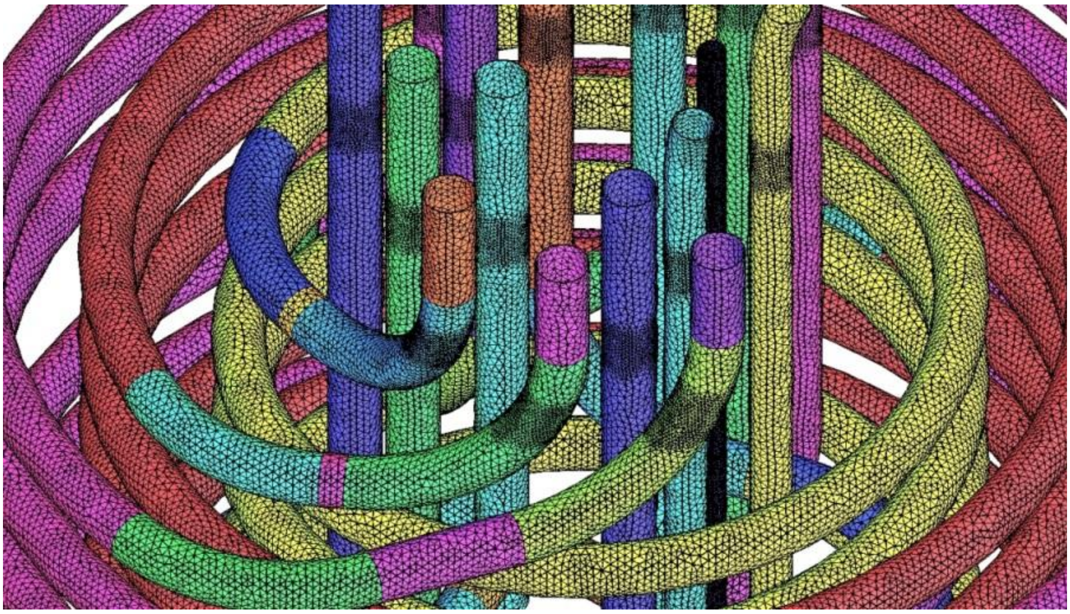

Figure 7.6: Surface mesh for mesh 2 after smoothing using the Laplace method. Image is an isometric view looking above into the core of Evaporator C.

7.2.4 Delaunay Volume Mesh

Once the high quality surface mesh was refined by using the Laplace smoother, a volume mesh was generated by using the Delaunay algorithm, using the surface mesh as the initial seed points. The algorithm may generate a mesh without existing seed points, however this usually does not guarantee a successful volume mesh, and the end product is usually a poor volume mesh. Therefore the Delaunay algorithm was used to obtain a high quality volume mesh, seeded from the high quality surface mesh.

The Delaunay mesh comprised pure tetrahedral cells. The mesh is shown in Figure 7.7 on a surface in the *x*-*y* plane intersecting the geometry. Figure 7.8 illustrates the Delaunay mesh in a *y*-*z* plane intersecting the geometry, and Figure 7.9 is the mesh in the *x*-*z* plane. The Delaunay mesh method produced a smooth transition from the boundaries, and gradually increased in size in the bulk volume. This is in contrast to the Octree volume mesh shown in Figure 7.1 which features a uniform volume mesh, and no smooth transition from the surfaces of the domain. The transition volume ratio from cell to cell was set to 1.18. This was important to implement since sudden transitions as featured in the Octree volume meshes generate spurious results in those areas.

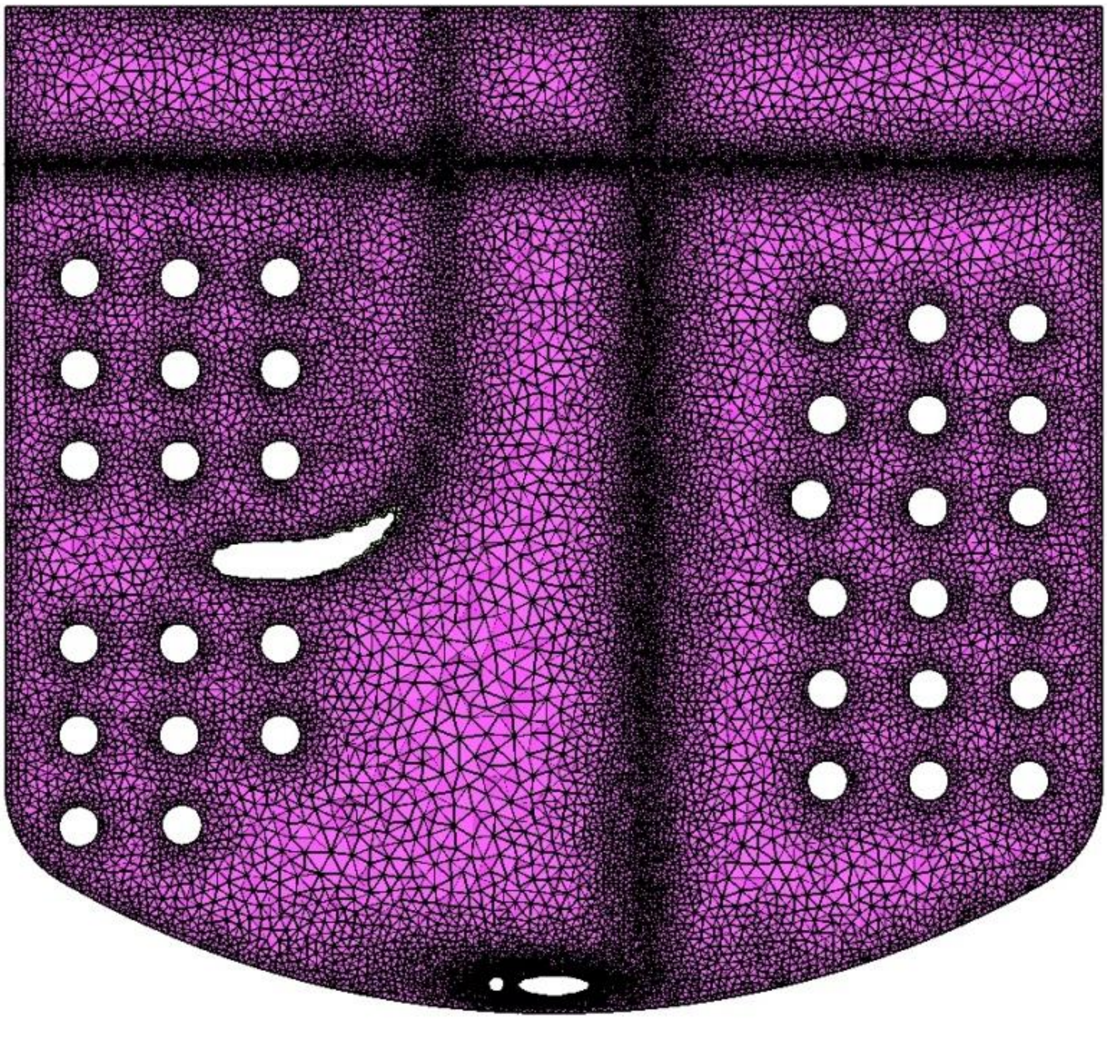

Figure 7.7: Delaunay mesh for mesh 2 plotted on an *x*-*y* plane intersecting the geometry.

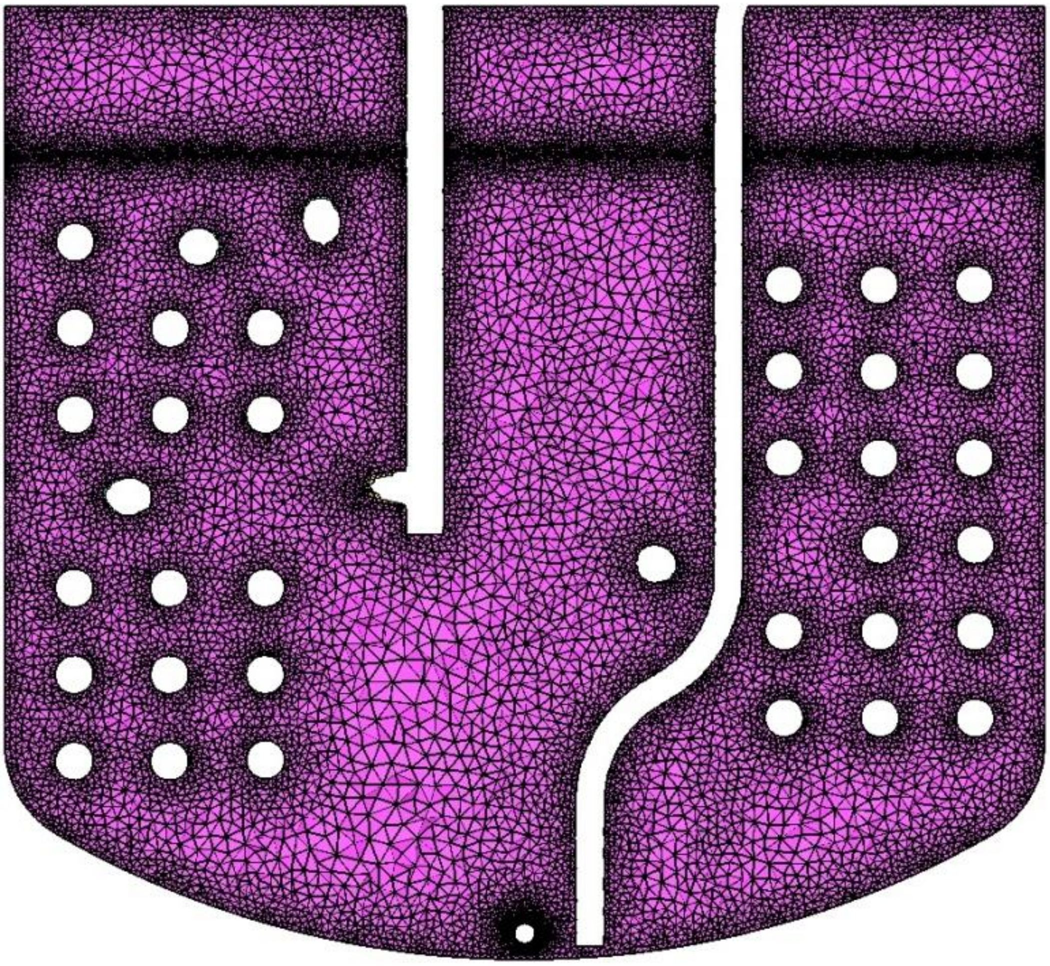

Figure 7.8: Delaunay mesh for mesh 2 plotted on a *y-z* plane intersecting the geometry.

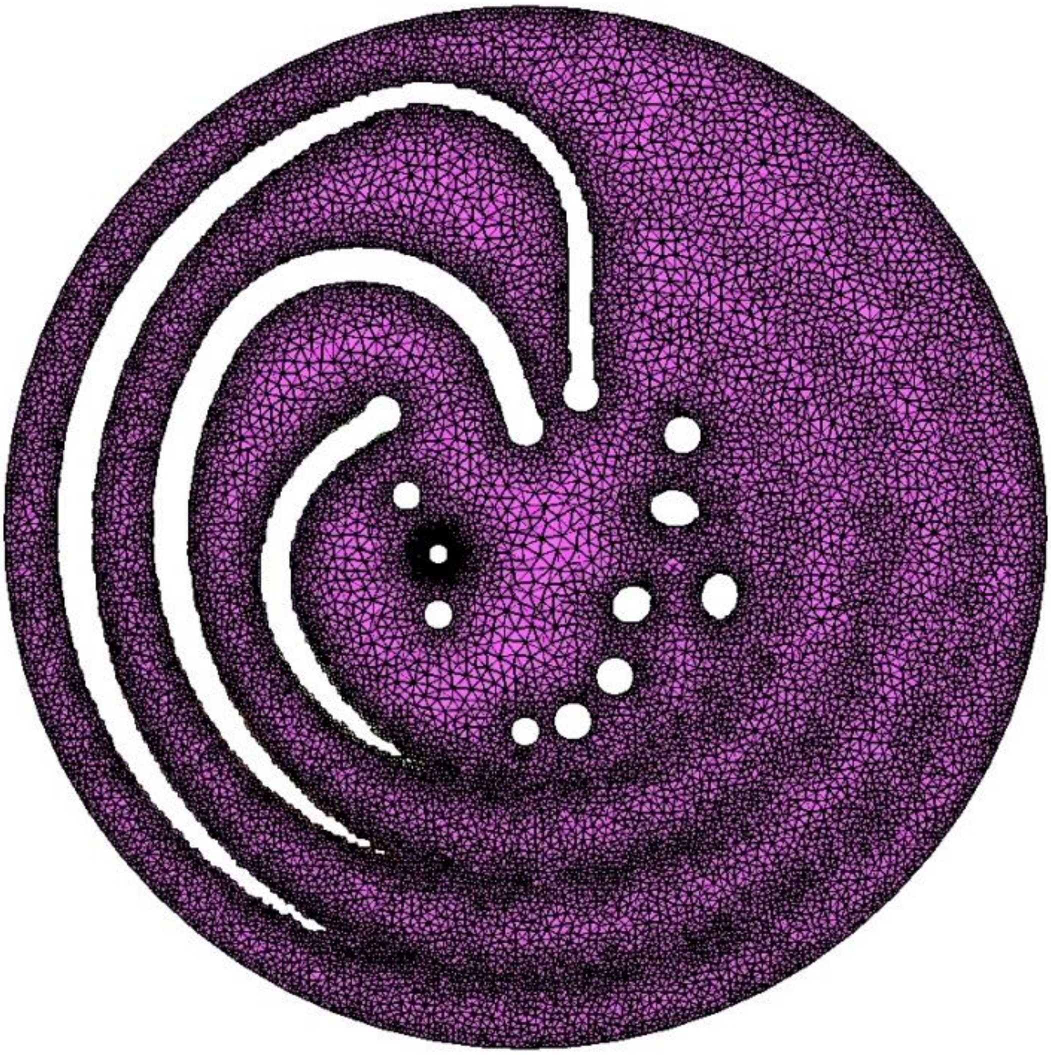

Figure 7.9: Delaunay mesh for mesh 2 plotted on an *x-z* plane intersecting the geometry.

7.2.5 Inflation Layers and Final Mesh

To complete the mesh generation process, inflation layers were inserted at the boundaries of the external heating jacket, the ullage walls, and at the walls of the helical coils and associated condensate pipes. They were not inserted at the adiabatic boundaries of liquor outlets and the steam sparger. This was because capturing boundary layer flows on those surfaces was not important to the investigation, and applying inflation layers to those surfaces would have significantly increased the mesh density and solution run times.

The post-mesh inflation algorithm was selected as the chosen inflation law. This was one of two available laws, the other being pre-mesh inflation. As the name suggests, pre-mesh inflation occurs before the volume mesh is generated. If it was used, it would occur before generating a volume mesh using the Delaunay algorithm. The advantage of using pre-mesh inflation is that it generates good quality prism cells for the inflation layers if the geometries do not contain small gaps. In pre-mesh inflation, since a volume mesh has not been created prior to implementation, the pre-mesh algorithm is not aware of potential collision locations. This makes pre-mesh inflation difficult to implement in complex geometries containing small gaps and small features as found in Evaporator C.

If the geometries do contain small gaps, the post-mesh inflation law should be used, which inserts inflation layers after the volume mesh has been created. This is advantageous as, since the volume mesh already exists, collisions and other common problems for inflation are known beforehand. The post-mesh law does not guarantee collision free inflation layers, but it does make them far less likely compared to pre-mesh. The trade-off occurs in inflation quality. Post-mesh laws require good quality surface and volume meshes, which were achieved using the Octree surface mesher coupled with the Laplace smoother; and the Delaunay volume mesher using mesh expansions no greater than 1.18.

The final mesh that was used had the same complexion as that described in the Delaunay step, with the exception of inflation layers inserted to the pertinent locations previously described. Mesh 2, which contained five inflation layers in pertinent wall regions, was the mesh which was selected from the sensitivity study is shown in Figure 7.10, Figure 7.11 and Figure 7.12.

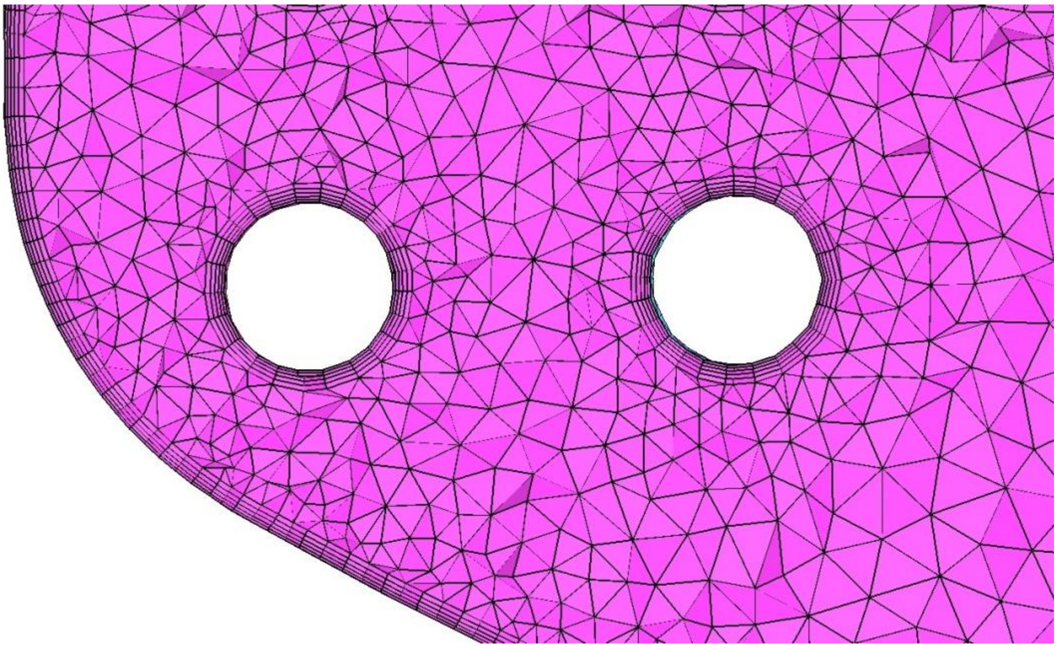

Figure 7.10: Details of the final mesh (mesh 2) showing inflation layers at the lower outer and middle coils and the knuckle. Mesh displayed on the *x-y* plane intersecting the geometry.

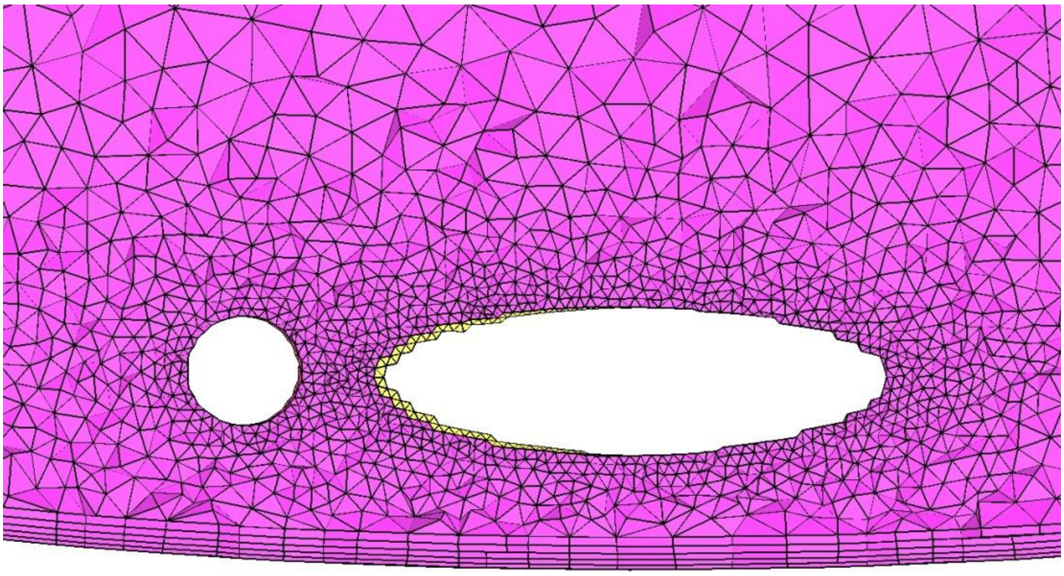

Figure 7.11: Details of the final mesh (mesh 2) showing inflation layers between the bottom dish and the steam sparger. Mesh displayed on the *x-y* plane intersecting the geometry.

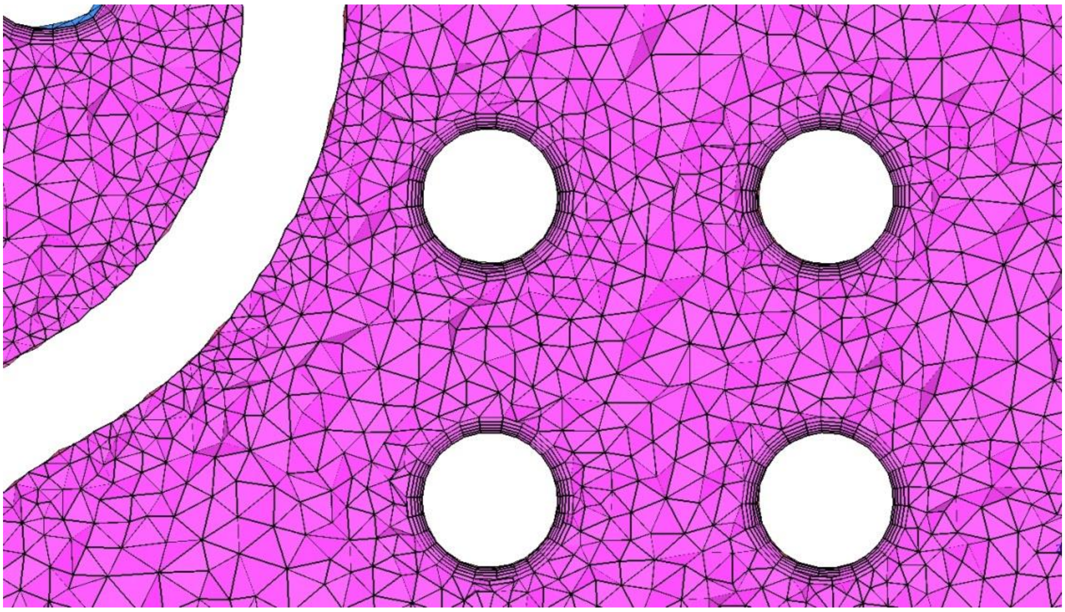

Figure 7.12: Details of the final mesh (mesh 2) showing inflation layers on the coils, but not on the liquor outlet pipe. Mesh displayed on the *x-y* plane intersecting the geometry.

The meshes were designed to be solution independent at the free surface. This was obtained by ensuring that the IAD at the free surface was independent of the mesh. Each subsequent mesh increased the density of inflation layers to ensure the values of Y^+ were less than 1, which ensured a low Reynolds number formulation at the walls could be harnessed, which in turn ensured accurate wall temperature predictions. These were the same methods employed for the mesh sensitivity study for scaled test rig in CHAPTER 5.

The statistics for the three meshes which were generated are tabulated in Table 5.1. Each mesh ran a transient free convection simulation, using a rate constant of 1 Hz, which was validated in CHAPTER 5. The simulations were stopped at the onset of boiling at the free surface where $T^* = 0$. The simulation times taken to reach $T^* = 0$ at the free surface is tabulated in Table 5.1. From the sensitivity study, mesh 2 was chosen as the mesh to proceed with boiling simulations.

	Mesh Statistics				**Mesh Information**		
Mesh	**Max. Face Angle [°]**	**Min. Face Angle [°]**	**Max. Edge Length Ratio**	**Max. Element Volume Ratio**	**No. of Nodes**	**No. of Elements**	**Sim. time for $T^* = 0$ [s]**
1	164.0	0.73	78.1	197.6	3,172,219	11,727,360	7.3 s
2	136.6	11.1	20.0	38.0	3,842,709	15,316,294	12.6 s
3	152.3	19.4	17.6	59.9	4,353,425	19,235,423	12.7 s

Table 7.3: Mesh statistics for the three meshes used in the sensitivity study.

The generated values from the GCI mesh sensitivity study are tabulated in Table 7.4. The table shows the sensitivity results for the area and transient average interfacial area density. The area and transient average Y^+ is absent. This is because the combined area average Y^+ on a large combined surface area (surfaces in contact with the the external heating jacket and six coils) would skew Y^+ unfavourably and would be misleading. Therefore through the mesh independence study the Y^+, was monitored on each independent surface to ensure on average during the simulation time it had fallen to less than 1.

	ϕ = Area and transient average interfacial area density [m^{-1}]
$\boldsymbol{\phi_1}$	1014 [m^{-1}]
$\boldsymbol{\phi_2}$	852 [m^{-1}]
$\boldsymbol{\phi_3}$	840 [m^{-1}]
$\boldsymbol{r_{21}}$	1.20
$\boldsymbol{r_{32}}$	1.562
$\boldsymbol{P}$	8.85
$\boldsymbol{\phi_{ext,21}}$	16 [m^{-1}]
$\boldsymbol{\phi_{ext,32}}$	43 [m^{-1}]
$\boldsymbol{e_{apx,21}}$	1.5%
$\boldsymbol{e_{apx,32}}$	4.1%
$\boldsymbol{e_{ext,21}}$	4573%
$\boldsymbol{e_{ext,32}}$	400.5%
$\boldsymbol{GCI_{21}}$	5.6%
$\boldsymbol{GCI_{32}}$	1.1%

Table 7.4: Results from the mesh sensitivity study using the GCI method (Celik et al., 2008).

The largest IAD that was produced was 1014 m^{-1} for mesh 1, and the smallest was 840 m^{-1} for mesh 3. Mesh 1 produced a very high IAD at the free surface because it was extremely coarse. On further refinement the IAD did not deviate significantly from that produced in mesh 2, which had a value of 852 m^{-1}. The grid convergence index between mesh 2 and 3 for the IAD is 1.1 %. Coupled with low values for the Y^+ mesh 2 was chosen as the mesh that was independent of the solution. Despite using only five inflation layers in mesh 2 (at least ten layers are recommended in the viscous sublayer for) the Y^+ values still remain acceptable.

7.3 Presentation of the Results

The results for the unscaled test rigs, and the scaled test rig were simple to present in comparison to Evaporator C due to their symmetrical nature. The unscaled test rigs were symmetrical cylindrical vessels with no complex internal structures, and the scaled test rig was a planar slice. However the presentation of the results for Evaporator C required more attention due to the asymmetric nature of the vessel, and the asymmetric flow physics.

In an effort to present the Evaporator C results in a meaningful way the following conventions were adopted. The flow distributions inside the water were presented on two intersecting planes in the *x*-*y* and *y*-*z* coordinate frames as shown by Figure 7.13. The planes correspond to an orientation map ranging from 0° to 360°. Hence plane *x*-*y* has extents equivalent to 0/360° and 180°, and *y*-*z* has extents equivalent to 90° and 270° respectively. The flow distributions on the outer surfaces (jacket and ullage wall) were plotted on a projection from 0° to 360° as shown in Figure 7.14. Finally, the distributions on the internal surfaces, such as the coils were plotted on all surfaces displayed in isometric view as shown in Figure 7.15 for the lower coils.

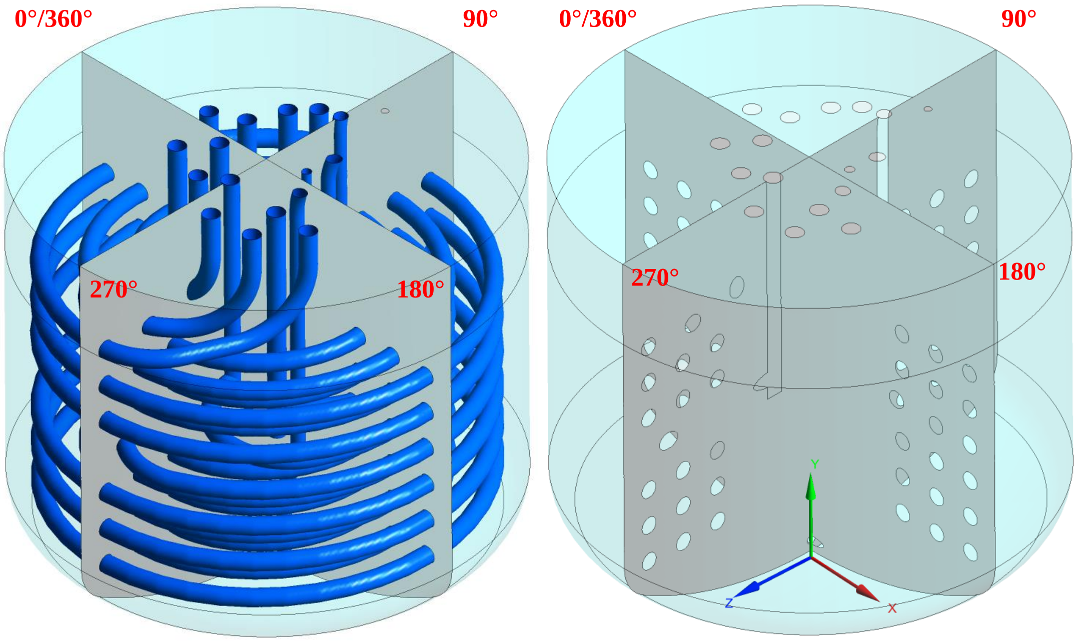

Figure 7.13: Intersecting planes in the *x*-*y* and *y*-*z* coordinate frames showing their relation to the internal structure (left) and without the internal structure (right).

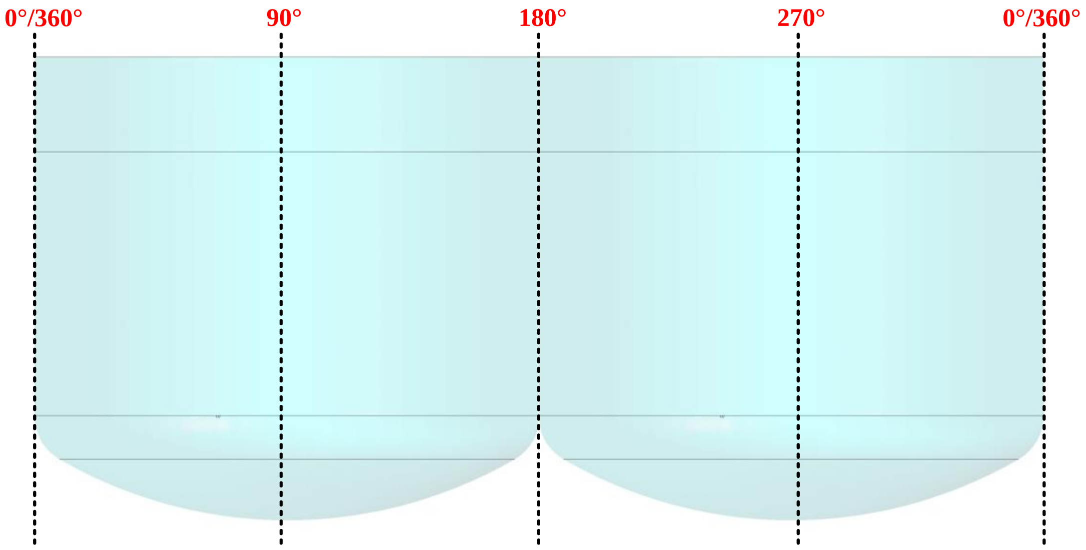

Figure 7.14: Projection map from 0° to 360° for the outer surface of the evaporator.

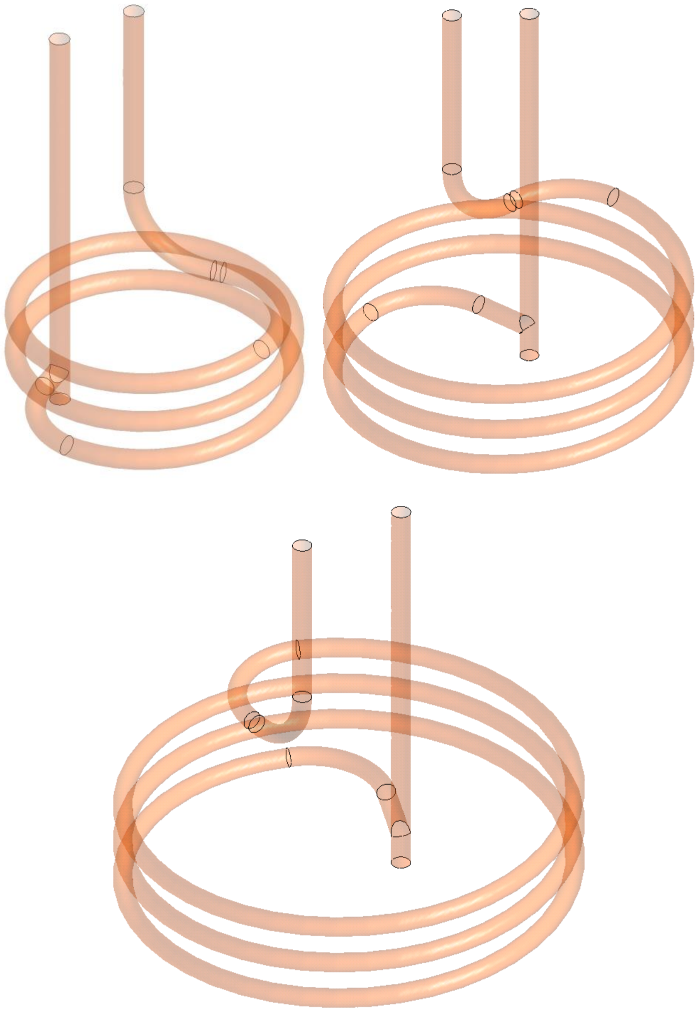

Figure 7.15: Isometric views of the lower inner coil (top left); lower middle coil (top right); and the lower outer coil (bottom).

The procedure that was taken to achieve successful evaporation results was described in CHAPTER 6. This was the same procedure as taken to simulate evaporative flows for the scaled test rig in CHAPTER 5. The results for the initial steady state free convection simulations are not shown here. They were performed to establish the flow fields and supply an initial condition for the transient free convection simulations, which were in turn used as the basis for the mesh sensitivity study. The steady state boiling simulations were performed using the transient free convection result as the initial state in order to advance the boiling flow fields in time, in preparation for the final transient boiling simulations of Evaporator C.

The convergence behaviours of the simulations were similar to those presented for the unscaled and scaled test rigs. Significant errors during the solving procedure were not encountered and the general guidelines outlined in CHAPTER 3 for numerical accuracy were adhered to. Lastly, due to the sheer size of Evaporator C, which has many surfaces of interest, the area and transient averaged results are displayed.

7.4 Monitor Points

Monitor points were enabled during the simulation process to monitor key values such as rates of evaporation, water velocities, temperature, and volume fractions to ensure that physically realistic values were being calculated. Five monitor points as shown by the yellow crosshairs in Figure 7.16 (Top) were inserted onto fictitious planes intersecting the evaporator at five horizontal positions. The first four planes were positioned such that they were 25%, 50%, 75% and 100% from the base of the evaporator, and inside of the liquid. This meant that the plane at 100% height corresponded to the free surface, and 50% height corresponded to the half way fill level. A fifth plane was inserted into the ullage area to monitor variables pertaining to the ullage region. Figure 7.16 (bottom) shows the vertical positions of the monitor points, fitted onto fictitious planes which are not visible. The total number of monitor points was therefore 25 (20 monitor points inside the liquid, and 5 monitor points inside the ullage area).

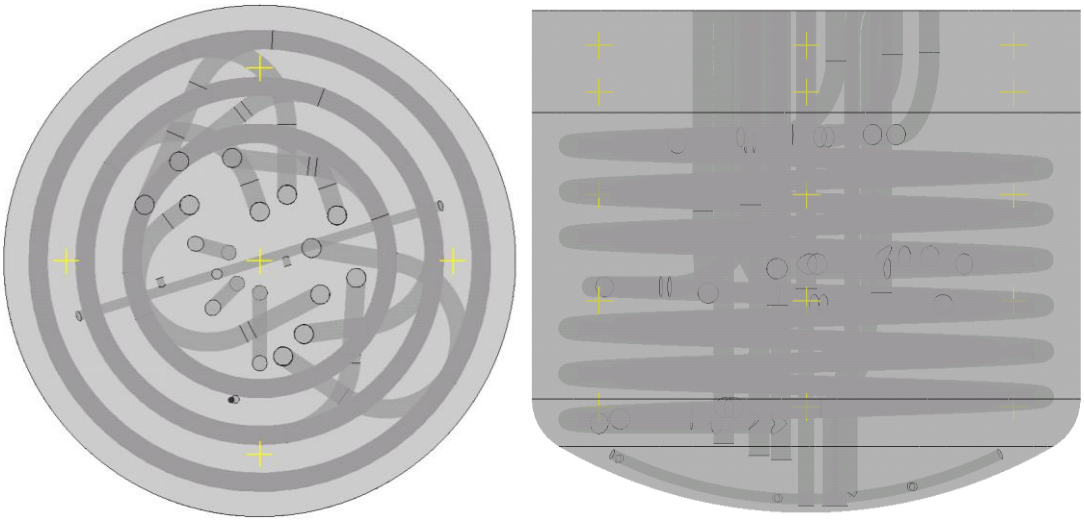

Figure 7.16: (Left) Plan view of the evaporator showing five monitor points on a plane; (right) profile view of the evaporator showing the monitor points at five vertical positions, four of which are inside the liquid.

7.5 Transient Free Convection Results

A steady state free convection simulation was performed using 100 iterations in order to establish the flow fields for the transient simulations. The transient free convection simulations took to 12.6 s to reach evaporative boiling conditions at the free surface for mesh 2, beginning with the steady state free convection simulations as the initial state. Figure 7.17 displays contours of the transient averaged volume fractions of the water. The volume fractions show that the water level is positioned just above the upper coils.

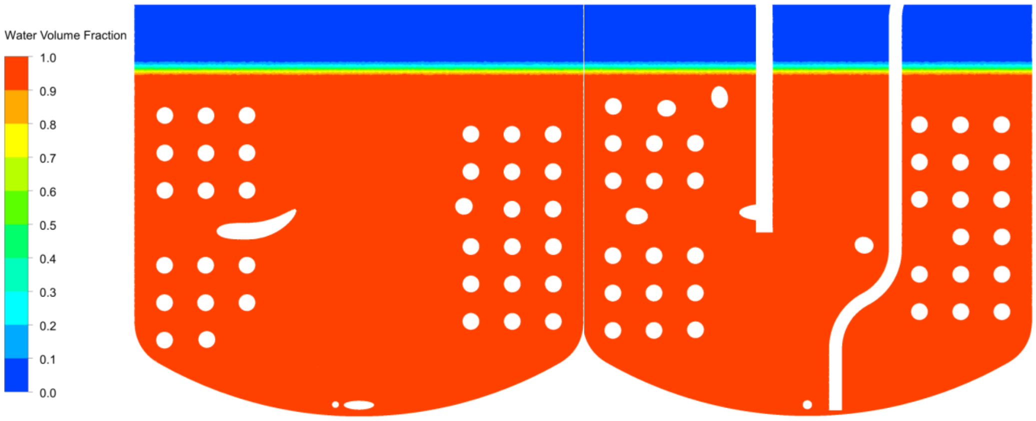

Figure 7.17: Transient average volume fractions in the *x*-*y* and *y*-*z* coordinate frames.

Figure 7.18 displays transient averaged contours of temperature inside the water. The water temperatures in the bulk liquid remain close to 45 °C and increase in temperature in the vicinity of the heated surfaces. The temperatures were close to the ullage temperature which had a value of 45.8 °C corresponding to ullage pressure of 0.1 bar. This behaviour was also exhibited in the unscaled and scaled test rigs, where the bulk liquid was close to the saturation temperature corresponding to the ullage temperature. The uniform temperature distributions inside the bulk liquid imply strong liquid recirculation which is able to transmit heat effectively within the water. The illustration also shows plumes of heat emanating from the heated surfaces and rising to the free surface. This was also exhibited in the simulations of the scaled test rig.

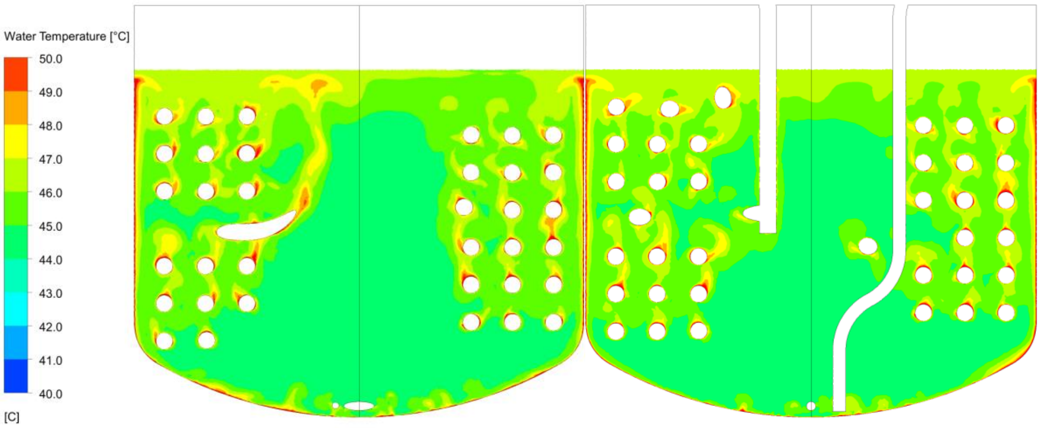

Figure 7.18: Transient average water temperature in the *x*-*y* and *y*-*z* coordinate frames.

Figure 7.19 illustrates the transient average T^* contours in the water. The contours show the water is slightly superheated at the free surface, and sub-cooled everywhere else. The definition of T^* was described in CHAPTER 4, which was a function of the local saturation temperature. The local saturation temperature in Evaporator C at the free surface is 45.8 °C, and at the base of the evaporator is 71.4 °C. The temperature distributions in Figure 7.18

remained relatively constant at approximately 45 °C. Since this did not exceed the local saturation temperature corresponding to the liquid head, it explains the sub-cooled nature of the contours in Figure 7.19.

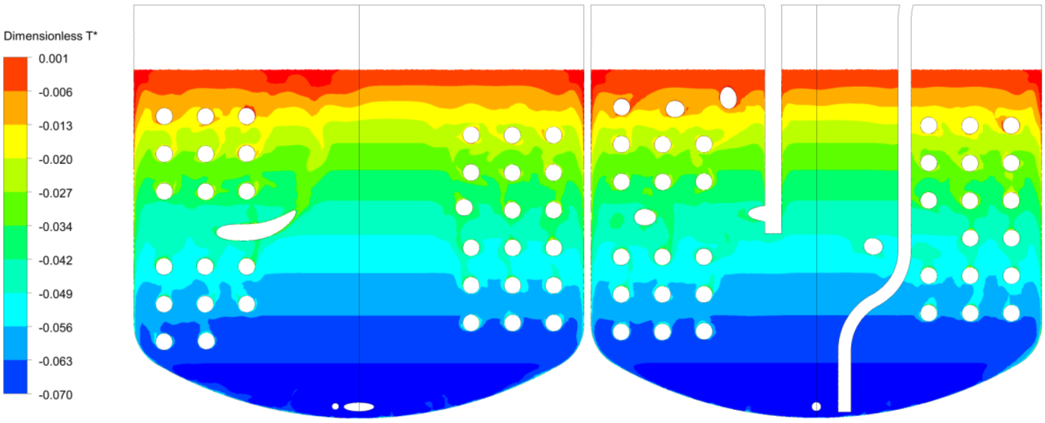

Figure 7.19: Transient average *T in the *x-y* and *y-z* coordinate frames.**

Figure 7.20 displays transient average velocity distributions of the water inside Evaporator C. These visualisations were obtained by plotting streamlines of the transient averaged velocity field, and then by using the streamlines as graphical objects on which to display velocity vectors. The distributions show the greatest velocity was 10 cm/s in a very small region, close to the free surface and the jacketed wall. The distributions indicate two large counter rotating convection cells. Liquid travels down the centre of the vessel, and up between the coils returning to the free surface. There are striking similarities between the distributions in Evaporator C and those simulated for the scaled test rig. Both cases show the same velocity distribution patterns indicating the scaled test rig has the required qualities in order to predict the flow distributions inside Evaporator C.

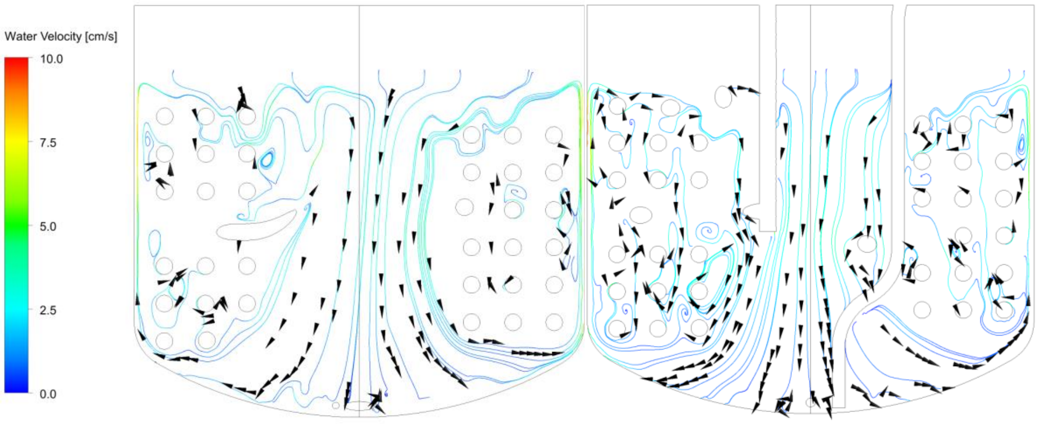

Figure 7.20: Transient average velocity distributions in the *x-y* and *y-z* coordinate frames.

In the free convection simulations, detailed analysis of variables such as heat distributions on walls in contact with the liquid are not shown. This is in the interest of brevity. However these will be shown for the results from the transient boiling simulations.

The most striking observation of the free convection simulations is the similarity between the behaviour found in Evaporator C compared to the behaviour found in the scaled test rig. The results from Evaporator C show that the temperature inside the liquid remains close to the free surface saturation temperature, which was also reported for the simulations in the scaled test rig which was benchmarked against experimental data. This has the consequence of boiling at the free surface as the T^* contours suggest in Figure 7.19. In Figure 7.20 the patterns for the velocity vectors show an ordered pattern. This is despite the blockages present inside the evaporator vessel, such as the internal coils and the steam sparger. The patterns dictate that the liquid travels down the centre of the evaporator core region, and upwards past the coils close to the vessel walls. This pattern was predicted by the scaled test rig in CHAPTER 5, and even in the short unscaled test rig in CHAPTER 4. This pattern was not predicted by the tall unscaled test rig in CHAPTER 4 because the draught affected the natural tendency of the liquid column.

7.6 Steady State Evaporation

The transient free convection simulations were used to provide the initial conditions for the evaporative boiling simulations. Hence at the end of the transient simulations the thermal phase change model was activated. In order to overcome the initial transient behaviour when the thermal phase change model was activated the simulations were first performed in steady state. This was the same approach taken to simulate boiling in the scaled test rig in CHAPTER 5. The steady state simulations were performed for 10,000 iterations to ensure the initial transient behaviour had been overcome when the thermal phase change model was activated. The overall evaporation rate was monitored during the simulation, and values of absolute pressure, temperature, velocity and volume fraction were monitored at the monitor points previously described.

A pseudo steady condition was achieved in the steady state boiling case. Values of the monitored variables fluctuated around mean values. The RMS solution residuals were extremely erratic and did not reduce less than 1×10^{-3}, therefore the simulation was not strictly converged despite achieving pseudo steady behaviour for the monitored variables. However this was considered acceptable as the main purpose of the steady state boiling simulations were to advance the simulation beyond the initial transient effects. The steady state boiling simulations were used as the initial state for final transient boiling simulations. The final results of the transient boiling simulations will be presented in detail in the coming section.

7.7 Transient Boiling Results

Transient boiling simulations were performed with a total simulation time of 10 s, using the steady state boiling simulation as the initial state. From the analysis the transient averaged results are presented, rather than instantaneous results, unless otherwise stated.

7.7.1 Volume Fractions

The volume fractions of water are plotted on the outer evaporator shell and in the *x*-*y* and *y*-*z* coordinate frames are shown in Figure 7.21 and Figure 7.22 respectively. During boiling there is an absence of a sharp free surface, as witnessed by the free convection simulations. Significant smearing of the free surface due to boiling is prevalent at the walls of the vessel shown in Figure 7.21. The large smeared band is less obvious inside the liquid, as shown in Figure 7.22.

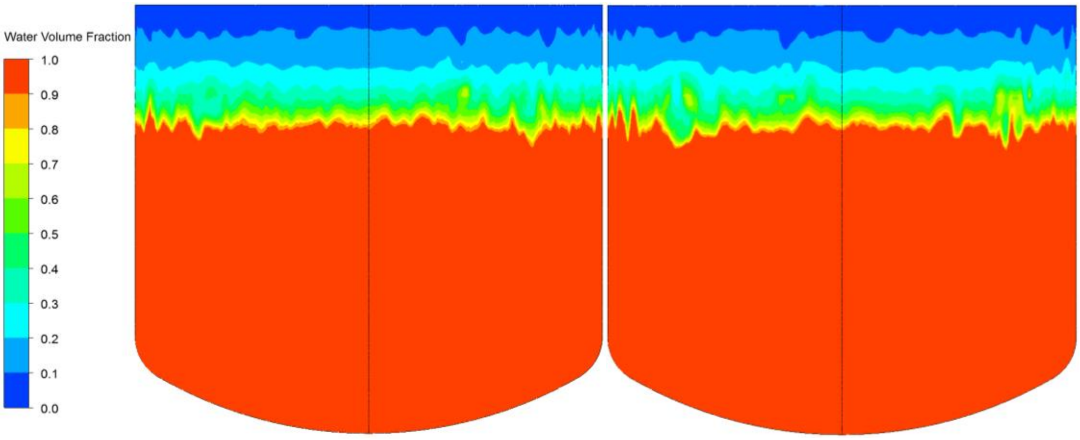

Figure 7.21: Volume fractions of water plotted on the outer evaporator shell.

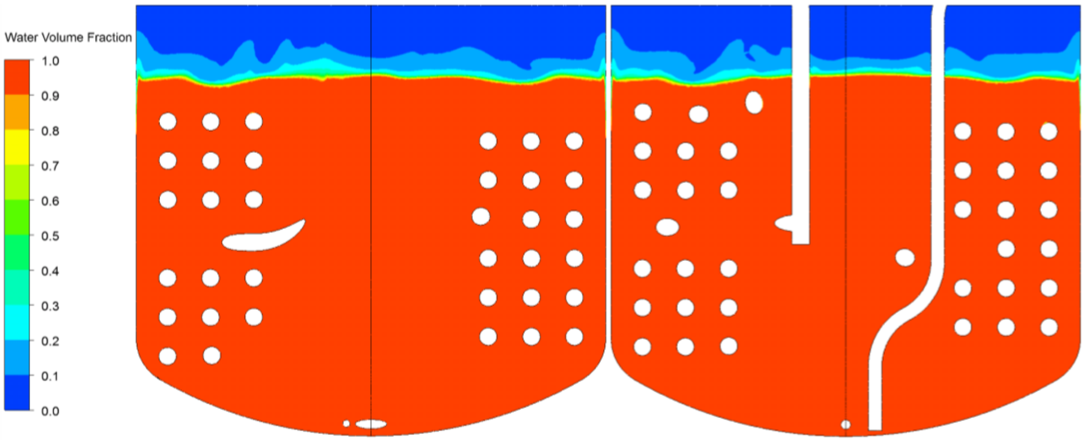

Figure 7.22: Volume fractions of water plotted in the *x-y* and *y-z* coordinate frames.

The isosurface corresponding to water volume fraction values of 0.5 at the free surface is displayed in Figure 7.23. Liquor dropping down from the feed is outlined by the black circle. The isosurface shows that the free surface is not uniform. Distortions and ripples appear at the free surface due to the effect of boiling. As the water is evaporated, liquid from the feed, which has been circled, replenishes the vessel.

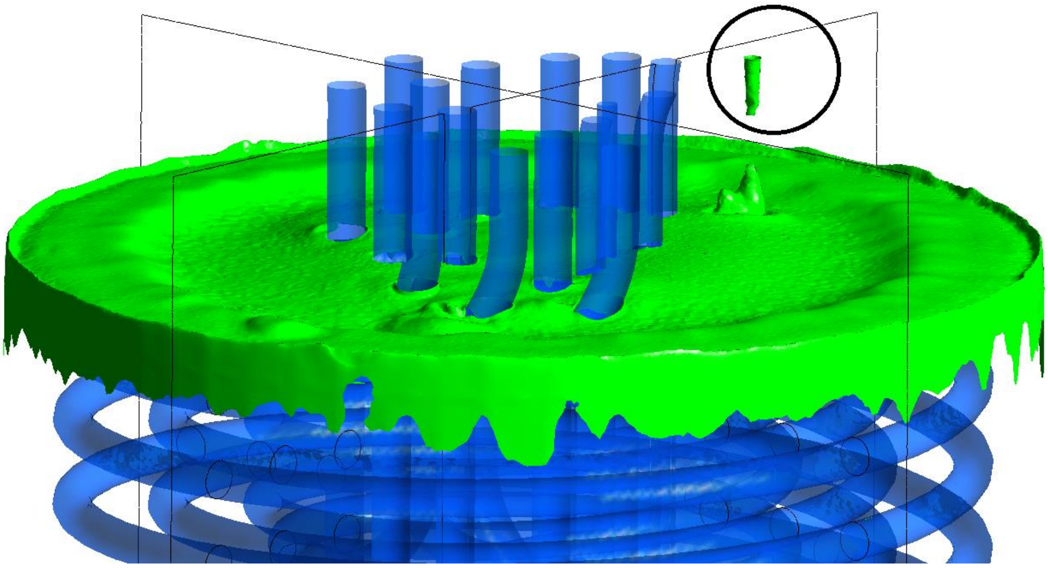

Figure 7.23: Isosurface corresponding to water volume fraction = 0.5.

In Figure 7.23, wavy features are present, due to instabilities caused by boiling at the free surface. These disturbances were not evident inside the free convection simulations. Since the isosurface is weighted according to volume fraction, the free surface structure in Figure 7.23 would vary if it was set to display volume fractions of water anywhere between 0 and 1. Therefore in Figure 7.23 the volume fraction was set to 0.5 because it indicates the half way transition from water to vapour.

7.7.2 Temperature and T^* Distributions

The temperature distributions inside Evaporator C are extremely important to this investigation. From the temperature distributions occurring on the heat transfer surfaces, information on the potential rates of corrosion can be determined (Wakem et al., 2009). The rates of corrosion yields information on the expected lifetime of the evaporator vessel. Corrosion rates as a function of temperature are not discussed here. However the temperature distribution results do provide information for researchers who wish to determine corrosion rates based on the findings in this work.

The temperature distributions inside the liquor are shown in Figure 7.24. The distributions indicate uniform temperature distributions inside the liquid having a temperature of 45°C, which is close to the free surface saturation temperature of 45.8 °C. Larger temperature gradients occur in the liquid at the vicinity of the heated walls where the temperature reaches 50 °C. The temperature distributions are plotted on the *x*-*y* and *y*-*z* coordinate frames and where water is present with at least a volume fraction of 0.5. Therefore temperature distributions inside the ullage space are not shown, and if they were shown they would be limited to the saturation temperature, which is 45.8 °C. Since the water temperature is close to this value, it would be difficult to see the free surface if the temperature of the ullage space was included.

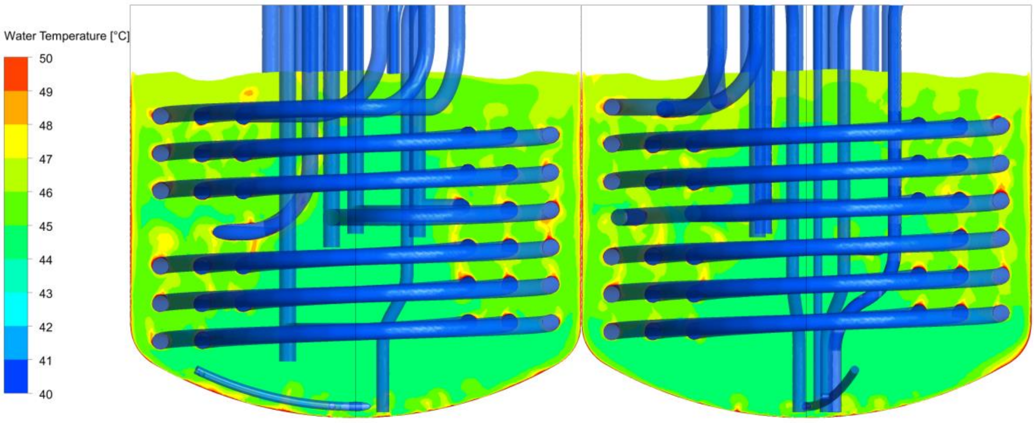

Figure 7.24: Temperature distributions in the water plotted in the *x*-*y* and *y*-*z* coordinate frames.

The temperature distributions plotted in Figure 7.25 are the inside wall surface temperatures of the shell of the evaporator, where the volume fraction of water is at least 0.5. Small localised high temperature regions are present at the knuckle and base of the evaporator, having a value of 60 °C.

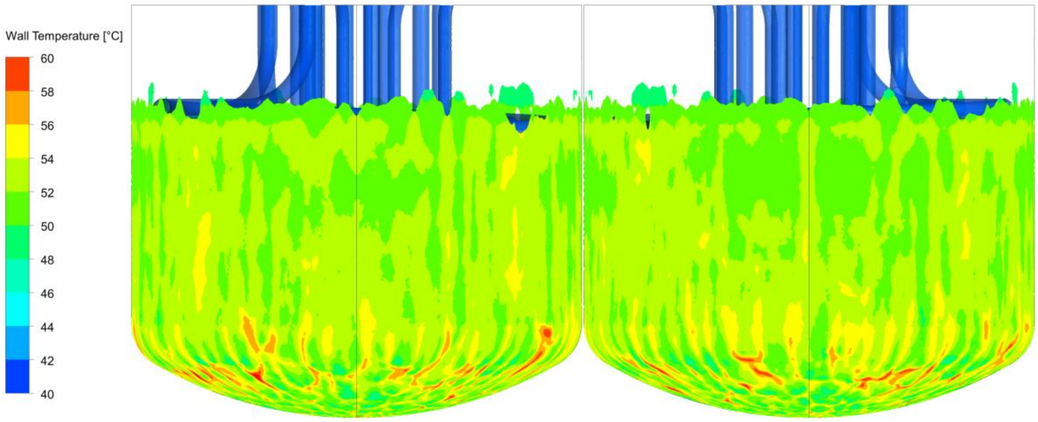

Figure 7.25: Projection map of temperature on the inner surface of the evaporator shell in contact with the water.

At the inside surfaces of the evaporator shell the temperature is largely 50 °C. This corresponds to the plot in Figure 7.24 which suggests the water temperature directly adjacent to the heated shell walls are 50 °C. The driving temperature inside the external heating jacket was set to 124.7 °C corresponding to a steam pressure of 2.3 bar. There is large temperature difference between the steam and the temperature on the inner surface of the shell, corresponding to a driving force of 124.7 – 50 = 74.7 °C. This driving temperature occurs across the resistances in parallel due to condensation resistance inside the jacket, resistance due to conduction and through the shell walls.

Figure 7.26 is the temperature distributions on the outer surfaces of the apparatus housed inside the evaporator. These are the internal helical coils, the liquor outlets and the steam sparger. The immediate observation is that the distributions on the outer surfaces of the apparatus are uniform showing similar behaviour to the temperature distributions of the inner surface of the evaporator shell.

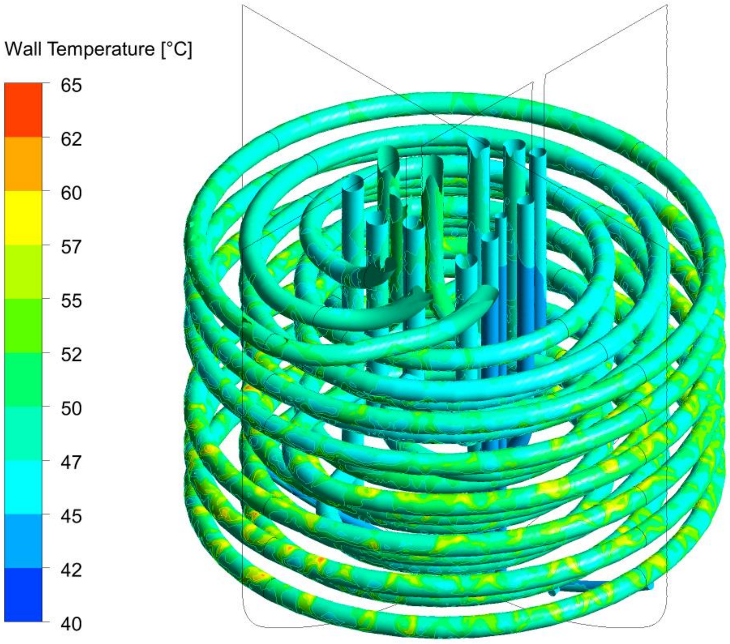

Figure 7.26: Temperature distributions on the outer walls of the evaporator internal apparatus in contact with the water.

The temperature distributions on the coils are shown by Figure 7.27. The distributions on the liquor outlets and the steam sparger are not shown as they were set to adiabatic walls, and hence will have a temperature equal to the liquid in contact with it. The driving temperature inside the coils was set to 127.4 °C corresponding to a steam pressure of 2.5 bar. The condensation heat transfer coefficient inside the coils was set to vary depending on steam quality. Hence at the inlet the quality was set to 1 and varies to 0 at the condensate pipe. Despite this the temperature distributions on the walls remained relatively uniform, with the largest temperature driving force equalling 127.4 – 65 = 62.4 °C. This behaviour was also observed on the internal surfaces of the evaporator shell, where despite the varied condensing heat transfer coefficient as a function of position, the temperature driving force remained steady at 74.7 °C. Since the overall driving force at the coils are larger than that of the external heating jacket, it can be concluded more efficient heat transfer occurs from the coils and into the liquid, compared to from the jacket and into the liquid.

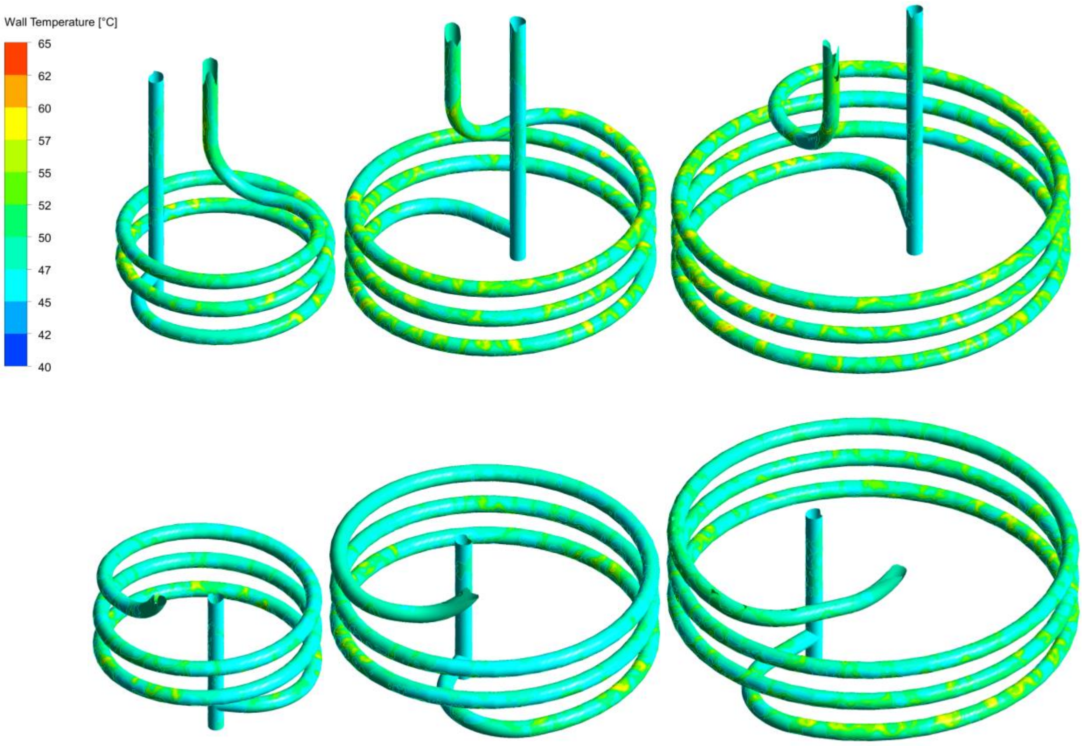

Figure 7.27: (Top) Temperature distributions on the outer walls of the lower coils, and (bottom) the upper coils.

The temperature distributions at the liquid surface are shown in Figure 7.28. The plot shows the incoming water, at a temperature of 20 °C, which replenishes the evaporated liquid. The evaporated liquid is at 45.8 °C which is to be expected as it is the saturation temperature corresponding to the ullage pressure of 0.1 bar.

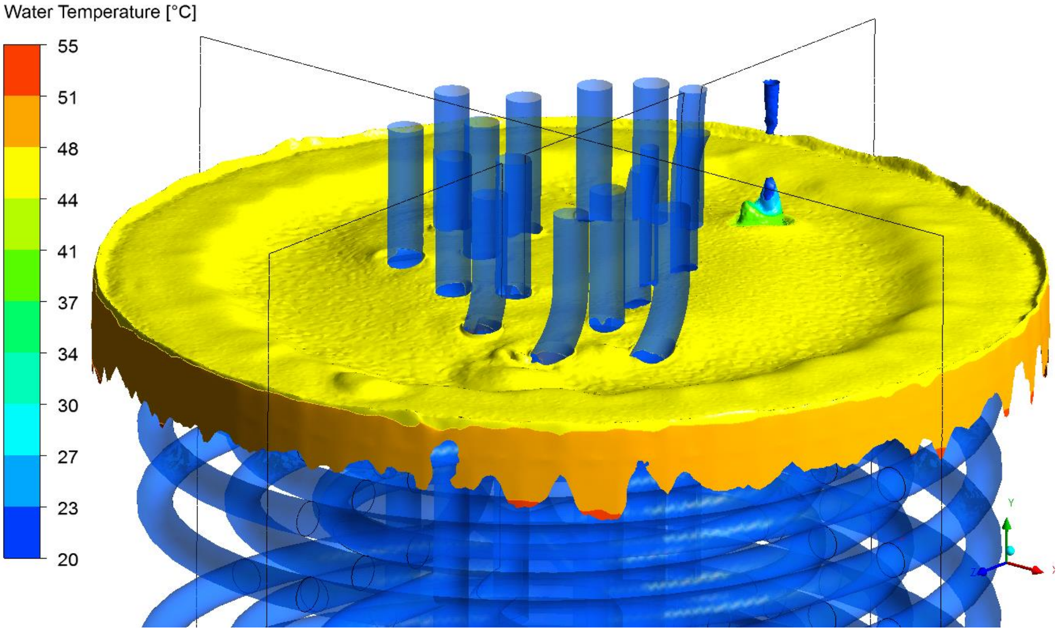

Figure 7.28: Isosurface of water coloured by water temperature when the volume fraction is 0.5.

T^* distributions are an effective way at illustrating where the water is superheated or sub-cooled. They have the potential of showing if phase change will take place and its position within the physical flow domain. The T^* distributions were determined for the simulations of the unscaled test rigs in CHAPTER 4 and the scaled test rig in CHAPTER 5 which showed if boiling may or not occur under the given boundary conditions. The T^* distributions for the inner surface of the evaporator shell in contact with the water is shown in Figure 7.33.

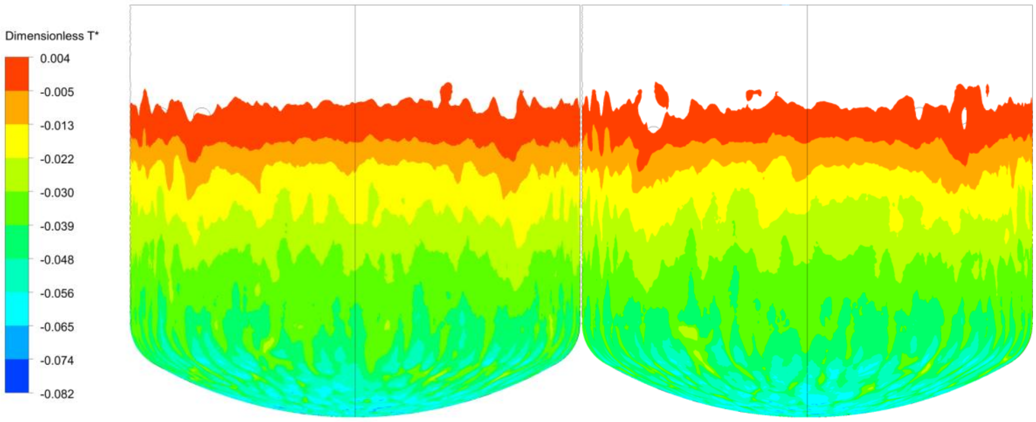

Figure 7.29: Contours of T^* on the inner surface of the evaporator shell in contact with the water.

The contours indicate a band of superheated liquid is present in the vicinity of the liquid free surface. This corresponds with the contours of volume fraction which show boiling occurs at the free surface. An interesting observation is that when Figure 7.33 is compared to the T^* contours inside the liquid as shown by Figure 7.30, the superheated band of liquid is far smaller. This suggests nucleate boiling is likely to occur at the inner surface of the evaporator shell, but only in the vicinity of the free surface. This is a significant finding as wall boiling was not considered in this investigation. This has implications on the predicted surface temperatures in the vicinity of the free surface, as they may be over predicted.

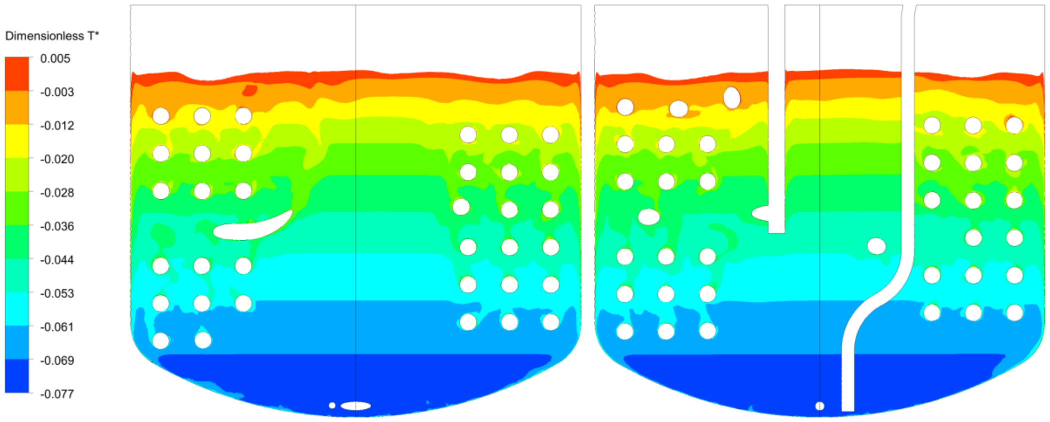

Figure 7.30: Contours of T^* of the water plotted in the *x-y* and *y-z* coordinate frames.

The T^* contours on the outer surfaces of the internal apparatus (internal helical coils, liquor outlets and steam sparger) are shown in Figure 7.31. The immediate observation is that there are small bands of superheated areas on the outer surfaces which are greater than 0. This is shown more clearly in Figure 7.32 which shows the T^* contours on each individual coil.

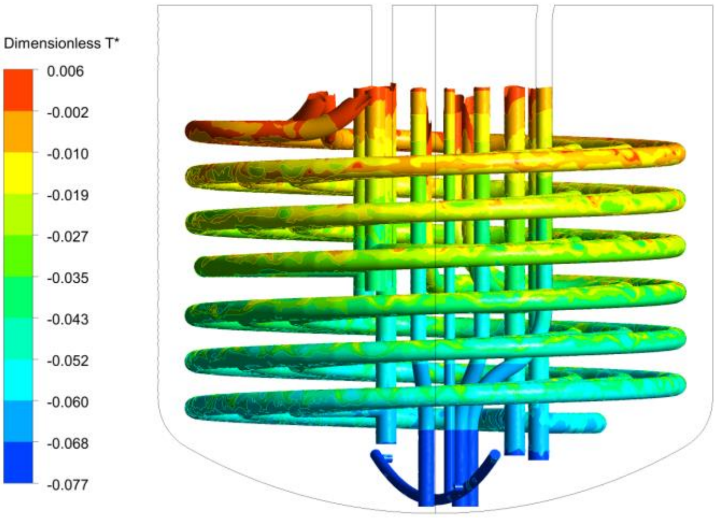

Figure 7.31: Contours of T^* on the outer surfaces of the internal apparatus of the evaporator.

The T^* contours on the coils show large areas of the first pass of the upper coils are superheated. This superheat gradually reduces with vertical position to become sub-cooled. In the of the lower coils the vertical surfaces corresponding to the steam supply and condensate return legs of the pipework show superheated areas. Therefore boiling may even occur on the lower coils, but close to the position of the free surface.

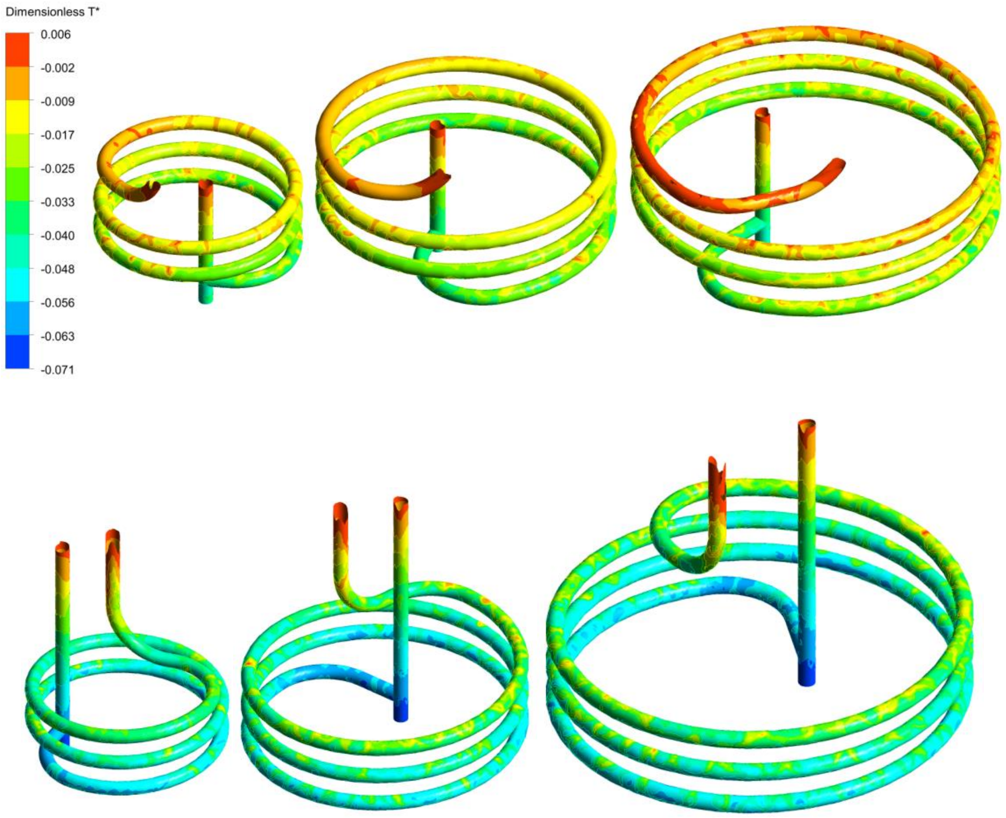

Figure 7.32: Contours of T^* on the outer surfaces of the internal helical coils; top row illustrate the upper coils and the bottom row indicates the lower coils.

The superheated areas depicted in Figure 7.29, Figure 7.30, Figure 7.31, Figure 7.32 correspond to the vicinity of the free surface, where the absolute pressure is at its lowest. This results in a reduced saturation pressure and hence temperature which makes it more likely for nucleate boiling to occur on the heated surface in the area of the free surface.

7.7.3 Heat Transfer Coefficient and Heat Flux Distributions

The heat transfer coefficients for the surfaces in contact with the liquid are based on the ullage temperature behaving as the bulk temperature, taking a value of 45.8 °C. This was chosen because this temperature remains constant inside the heat transfer system, and thus provides a useful for comparison purposes. Hence the heat transfer coefficient takes the form as shown in Eq. 7.1. The heat transfer coefficients are based on the surfaces in contact with the liquid surface only, hence the variables are subscripted with the phase symbol for the liquid α.

$$h_{\alpha} = \frac{\dot{q}_{wall,\alpha}}{T_{wall,\alpha} - T_{ulg}} \tag{7.1}$$

The heat transfer coefficient distribution on the inner surface of the shell in contact with the liquid is shown in Figure 7.33. The distribution is distorted by large values of heat transfer coefficient present at the free surface which has values of 23000 W/m^{2}K. The values are high at the free surface due to evaporation. The contours in Figure 7.33 have clipped to have a water volume fraction of at least 0.5. Therefore the regions where the heat transfer coefficient is very large is limited in size, but occurs at the free surface. This is realistic and expected behaviour since boiling occurs at the free surface, and therefore the heat transfer coefficient at the free surface would be very high. To better visualise the plot in Figure 7.33, the legend is clipped to have a maximum value of 5000 W/m^{2}K, as shown in Figure 7.34.

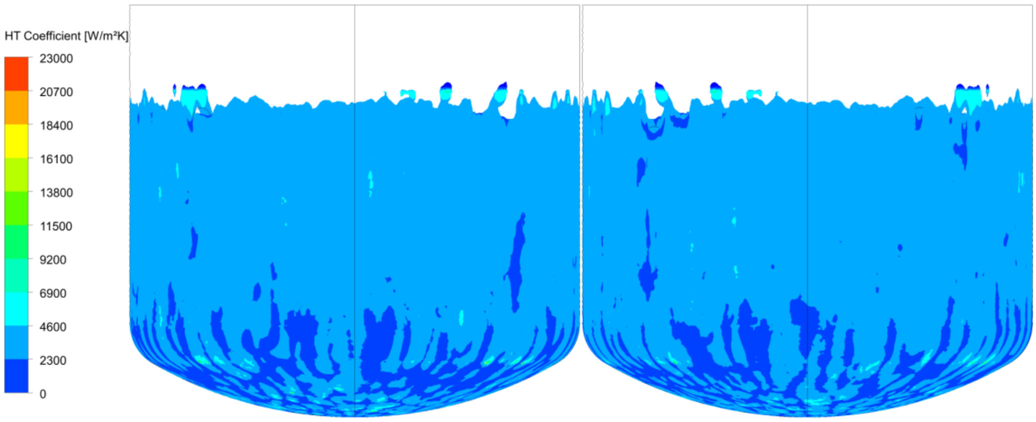

Figure 7.33: Local heat transfer coefficient distribution on the inner wall of the evaporator shell in contact with the liquid.

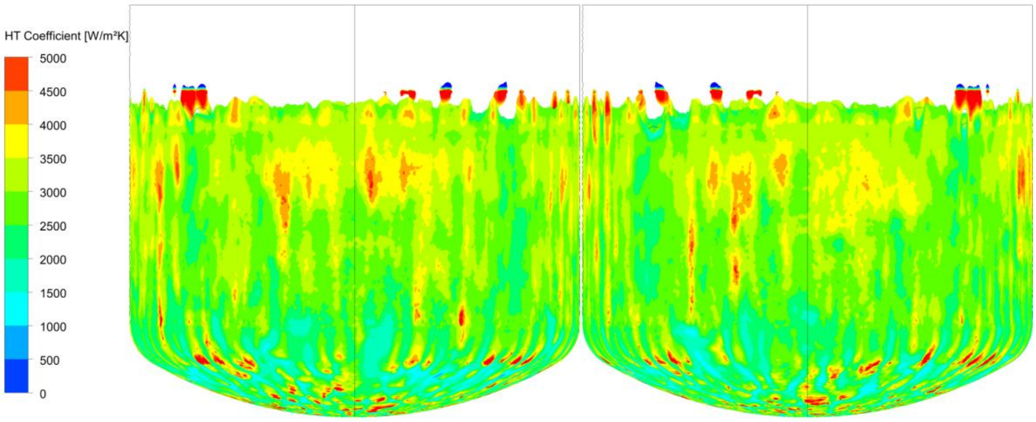

Figure 7.34: Clipped heat transfer coefficient distribution on the inner wall of the evaporator shell in contact with the liquid.

The heat transfer coefficient distribution in Figure 7.34 shows that the inner shell walls in contact with the liquid are in the single phase convection regime. Bergman *et al.*, (2011 chap. 1) suggests surfaces in contact with water are in the forced convection regime if the heat transfer coefficients have values between 100 – 20000 W/m^{2}K.

The heat transfer coefficient distribution on the coil surfaces are shown in Figure 7.35. The heat transfer coefficient distribution has been clipped to a maximum value of 20000 W/m^{2}K. The lower coils which is approximately 1.5 m below the liquid free surface is mainly in the convection regime. There are some localised areas where the heat transfer coefficient reaches a maximum of 20000 W/m^{2}K. These areas are increased for the upper coils which are closer to the free surface. In these areas sub-cooled nucleate boiling may occur.

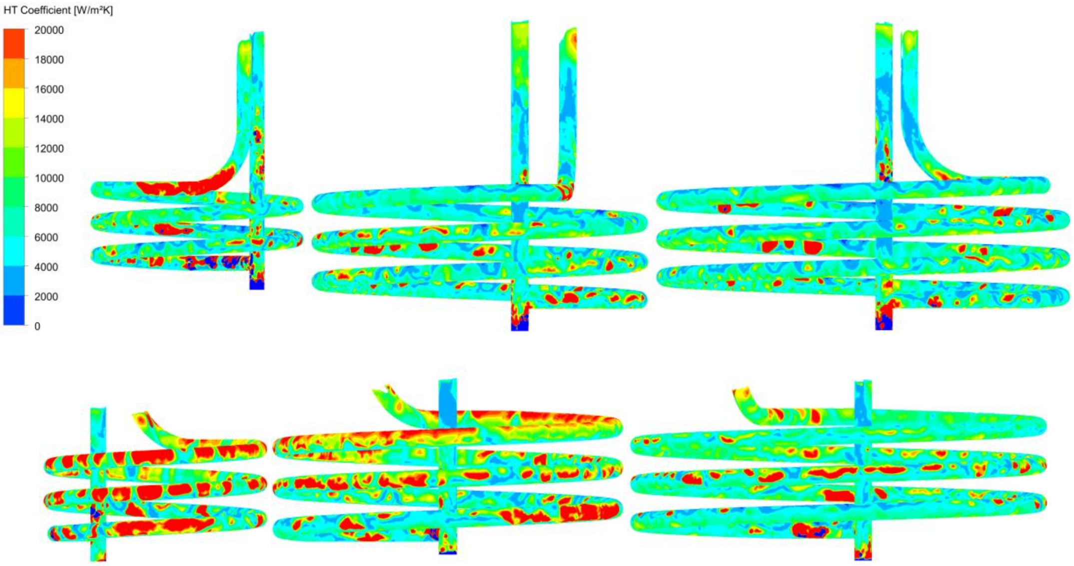

Figure 7.35: (Top) Clipped heat transfer coefficient distributions on the outer walls of the lower coils, and (bottom) the lower coils.

The heat flux distribution on the inside surface of the evaporator shell is shown by Figure 7.36. The distribution shows that the maximum heat flux at that surface is approximately 25 kW/m^2. In Figure 7.36 there are small areas, coloured in blue where the heat flux is negative. This is because in that region the liquid is contact with the walls of the unheated ullage section of inner surface of the evaporator wall. Recall from CHAPTER 6 the free surface position is 2.35 m, which is slightly higher than the height of the jacket, 2.2 m. Since the ullage section acts as heat loss walls with an ambient outside temperature of 15 °C, then any contact of warmer fluid would yield a negative heat flux, indicating heat flow out of the evaporator vessel. This also explains why the heat flux suddenly jumps from negative values to almost 25 kW/m^2 almost instantaneously – it is because a small portion of the wall in contact with the liquid at the free surface is not heated. The heat flux at the inner walls of the evaporator shell is highest where boiling occurs at the free surface.

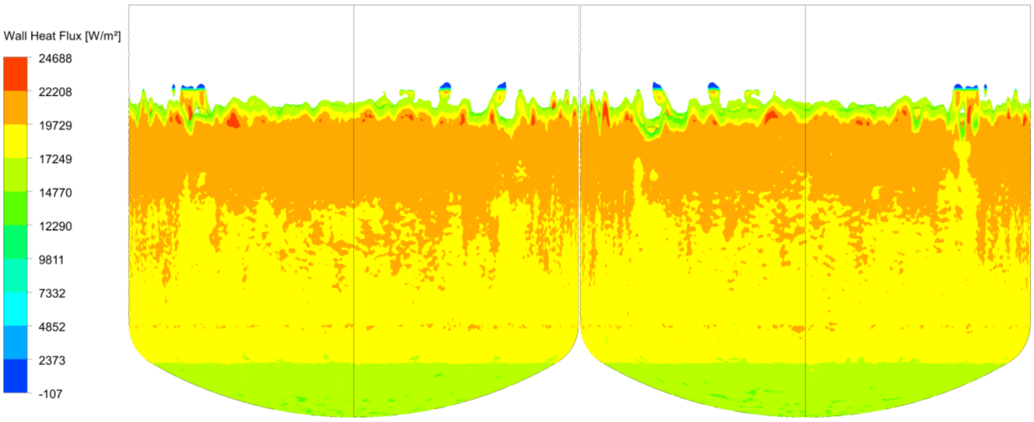

Figure 7.36: Heat flux distribution on the inner surface of the evaporator shell.

The heat flux distribution on the coil surfaces are slightly higher than those presented for the evaporator shell in Figure 7.36. The distribution shows a maximum heat flux of 50 kW/m^2 is achieved where the coils are in the vicinity of the free surface. This is also where boiling occurs.

It is interesting to link these results to the thermal resistance work performed in CHAPTER 4. In the thermal resistance investigation of the unscaled test rigs, when boiling correlations (Forster and Zuber, Mostinskii, Bier et al., Cooper and Rohsenow, and Gorenflo and Kenning) were applied to the heated surface the reported heat flux was around 50 kW/m^2. This suggests that if it is known that boiling does occur, along with its position inside the evaporator, then the heat transmitted at the surface may be predicted by one dimensional heat transfer correlations, despite the evaporator complexity. This gives credence to the thermal resistance methodology in its ability to predict physically representative phenomena.

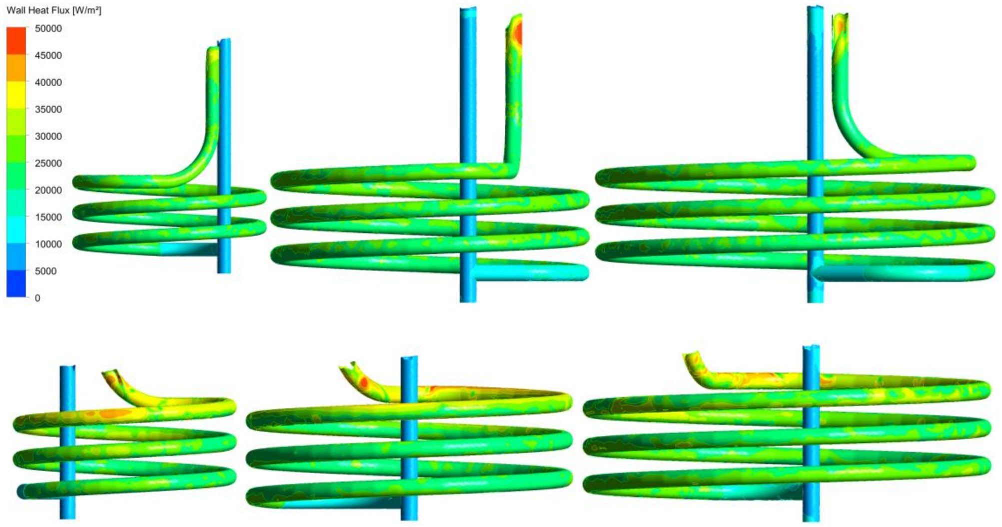

Figure 7.37: (Top) Heat flux coefficient distributions on the outer walls of the lower coils, and (bottom) the lower coils.

7.7.4 Velocity Distributions

The velocity distributions inside the water during boiling are shown Figure 7.38. During boiling conditions the liquid travels down the central core of the evaporator, and up the vertical walls. There are two distinct counter rotating recirculation zones in each plane. The circulation patterns correspond with those predicted in the scaled test rig. Despite the scaled test rig being a one quarter thin slice of Evaporator C, there does appear to be significant agreement with regards to the magnitude and direction of travel.

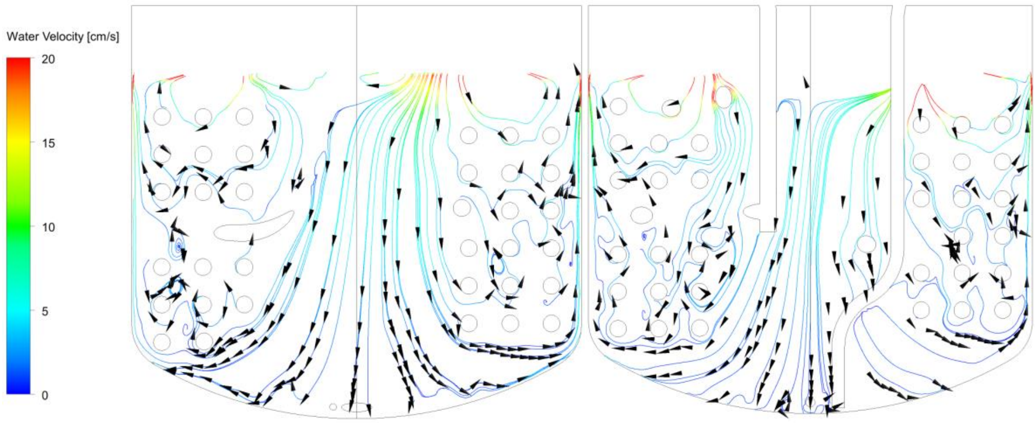

Figure 7.38: Transient average velocity distributions of the water during boiling in the *x-y* and *y-z* coordinate frames.

The velocity patterns do reinforce the concept that the evaporator operates similar to an unconstrained thermosyphon reboiler situation. Thermosyphons represent passive pumpless heat exchange systems. This is an important discovery as it was previously assumed before the works of McNeil et al. (2015) that Evaporator C did not operate in this manner.

7.7.5 Interfacial Area Density

The interfacial area density controls the transfer of mass, momentum and energy through the interphase contact area. In the models used in this work, it is determined by setting a value for the thermal phase change rate constant. From the validation work conducted in CHAPTER 5 when simulations were performed of the scaled test rig, the rate constant was determined to be equal to 1 Hz. This value was also used for the simulations of Evaporator C in this chapter. The interfacial area density corresponding 1 Hz for the Evaporator C simulations are shown in Figure 7.39.

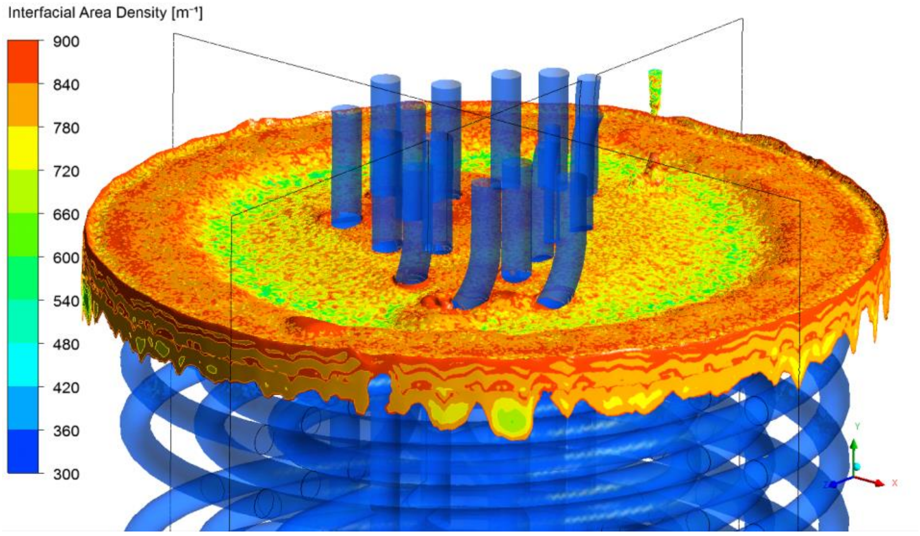

Figure 7.39: Transient average interfacial area density on the isosurface of water when the volume fraction is 0.5.

The interfacial area density contours at the free surface indicates higher values at the shell of the evaporator, and lower values in the core region. This indicates that the model allows for the greatest interfacial transfer of mass, momentum and energy in the areas of Figure 7.39 where the interfacial area density is greatest.

7.8 Summary

Free convection and evaporation simulations were performed of the industrial evaporator, Sellafield Evaporator C. The system was driven by applying fixed heat transfer coefficients at the heated walls. The heated walls comprised the external heating jacket, and the internal helical coils in contact with the liquid. For both the jacket and the coils, the heat transfer coefficient accommodated the thermal resistances due to steam condensation and conduction through walls. The driving steam temperature inside the jacket was 124.7 ºC corresponding to 2.3 bar, and for the coils 127.4 ºC corresponding to 2.5 bar. The remaining surfaces of the shell were set to ambient heat loss conditions, and the non-heated surfaces submerged inside the liquid were treated as adiabatic walls. Finally the liquid was treated as water, had a level of 2.35 m and the ullage pressure above the free surface was 0.1 bar.

The two principle conditions which were tested in Evaporator C were transient free convection, and transient boiling at the free surface. The transient free convection case was also the basis for the mesh sensitivity study, which paralleled the same procedure performed for the mesh sensitivity study for the scaled test rig in CHAPTER 5. The chosen mesh from the mesh sensitivity study was mesh 2. The total number of cells was 15,316,294, which included prism inflation cells, and tetrahedral cells inside the bulk volume. Structured hexahedral meshing, which was used in the meshes of the unscaled and scaled test rigs was not possible for the Evaporator C geometry due to its complexity, and inability to form successful blocking topologies.

A methodological approach to achieving boiling results in the Evaporator C simulations was used. First a steady state free convection simulation was performed, where temperatures inside the liquor was sub cooled. The purpose of this initial step was to initialise the flow fields. This was also the initial state for transient free convection simulations, which were stopped at the onset of boiling at the free surface. The thermal phase change model was then activated, and steady state simulations of boiling at the free surface were allowed to occur. Liquor was continually replenished as vapour left the system to maintain a steady liquor level as found in real plant conditions. Finally, to home into a final converged and reportable solution, transient boiling simulations were then performed.

The final transient free convection simulations took around 2 months to complete; and the boiling simulations took 6 months to complete, which did not account for human and numerical errors which required the need to restart the runs.

The free convection and evaporative boiling simulations of Evaporator C shows that at all times the liquor remains close to the free surface saturation temperature corresponding to 0.1 bar ullage pressure, which was 45.8 °C. This behaviour was also repeated in the unscaled and scaled test rigs. This indicates that the flow inside the evaporator vessel under steady operation represents a well-mixed system. This is further supported by the flow patterns during operation. The flow patterns shows that the liquor is drawn down from the free surface. The liquor impinges onto the lower surface and circulates around the evaporator vessel as it returns to the free surface, over the heated coils. This reinforces the concept that the evaporator vessel behaves like a thermosyphon reboiler system.

The contours of the dimensionless T^* variable shows that boiling is likely to occur on the heated surfaces close to the free surface. Therefore the metal surface temperatures are likely to be highest on the upper coil surfaces where boiling is likely to occur, and on the jacket surfaces close to the free surface. Boiling is likely to occur in those regions since T^* is greater than zero in those areas. This means the rates of corrosion occurring on the boiling surfaces will be higher than the surfaces which do not undergo boiling. Therefore in future work, nucleate wall boiling should be considered as the next step in ensuring greater accuracy in the wall temperatures.

The heat transfer coefficients on the surfaces in contact with the liquor were defined in terms of the ullage temperature acting as the bulk temperature. This was chosen since the ullage temperature is a known value which does not change with flow regime. From the analysis of the heat transfer coefficients, most of the surfaces indicate they are in the single phase convection regime, where free convection occurs. However at the free surface where boiling does occur the heat transfer coefficients increase rapidly and describe coefficients associated with nucleate wall boiling.

The investigations from the simulations of Evaporator C have shown that the heat transfer surfaces at the top of the vessel, close to the free surface, are hotter than the remaining surfaces. At those surfaces, nucleate wall boiling is likely to occur.

Chapter 8

Conclusions and Future Work

8.1 Conclusions

Successful heat transfer and multiphase flow analysis via CFD simulations has been performed on an industrial evaporator, Sellafield Evaporator C. This was achieved by first modelling single phase flow and heat transfer distributions inside two small-scale test rigs. This allowed a baseline understanding to be developed on modelling buoyancy driven flow under sub-atmospheric pressures. This baseline was developed upon and a more complete multiphase boiling simulations of the one-quarter scale thin slice test rig was achieved. Multiphase boiling simulations of the scaled test rig yielded an interfacial length scale as a function of a rate constant, which controlled the value of the interfacial contact area per unit volume of the water and vapour phases. This was achieved by comparing the simulations against experimental data, and thus validating the work. All of the lessons learnt, and models developed were used to model Sellafield Evaporator C.

The small-scale test rigs are two steam heated water columns. The two test rigs differed primarily by size. The short test rig had a vessel width and water depth of 0.1 m. The tall test rig had a width of 0.1 m, and a water depth of 2.235 m. The pressure above the water line in both test rigs was 0.1 bar. Both test rigs were heated by condensing dry saturated steam underneath a stainless steel base plate which the water column sat upon. Heat transfer through the boundaries and into the water caused the water to boil. This system is analogous to the way Sellafield Evaporator C operates.

As a first step one dimensional thermal resistance investigations were performed on the test rigs. These involved generating a series of one dimensional heat transfer transport equations which described the heat flux, temperature and heat transfer coefficient distributions inside the two test rigs. Three idealised cases were tested in the thermal resistance investigation: (i) pure conduction in the water column, (ii) free convection in the water column, (iii) and nucleate boiling on the upper plate surface.

Heat transfer coefficients were selected from the open literature which were used to describe free convection and boiling for the three cases. The governing equations produced an n by n system, where the number of equations equalled the number of unknowns. The investigations showed that the system was insensitive to the condensation heat transfer coefficient that was used. This was because conduction heat transfer through the base plate was the dominating thermal resistance. In the boiling cases, six boiling heat transfer coefficients were benchmarked. Five of the six correlations predicted similar heat transfer coefficient distributions; except from one of the six, which was the Cooper (1984) correlation. The correlation produced boiling heat transfer coefficients orders of magnitude greater than the others that were tested.

Thermal resistance networks were proved to be a computationally inexpensive tool to predict temperatures, heat transfer coefficients, and heat fluxes in the heat transfer system when compared to complex and expensive CFD simulations. They provided useful information such as temperature distributions and values of heat fluxes, without needing to resort to expensive methods such as CFD.

CFD simulations of the two test rigs was also performed. Two geometries for the short test rig were compared. These were a 2D axisymmetric geometry, and a full 3D geometry. Poor flow physics is observed in the 2D axisymmetric geometry. This is because the symmetry planes enforce an unphysical solution that is broken in the simulations using a full 3D geometry. Hence, the use of 2D axisymmetric conditions was not suitable to model buoyancy driven flow. Full 3D simulations of the tall test rig was performed. The tall test rig contained a draught tube which forced the momentum behaviour of the water against its natural tendency.

Indicators for boiling showed that nucleate boiling at the upper plate may occur, and in the tall test rig, the T^* distributions indicate that the liquor is heated above its saturation temperature in the upper regions of the test rig. The CFD simulations have shown that phase change in the liquor is highly dependent on the pressure head of the liquid column.

There was poor agreement between pure conduction and free convection thermal resistance cases and the CFD investigation. There was reasonable agreement between the nucleate boiling case and CFD investigations.

Multiphase boiling simulations of the one-quarter scale slice test rig was performed. The model of Lee (1990) has been generalised, and implemented in ANSYS CFX, and the predictions of the generalised model have been compared with the experimental investigations of McNeil et al. (2015) on a scaled test rig designed to replicate some of the features of flow in Evaporator C. The original model of Lee (1990) included source terms in the liquid and vapour continuity equations, based on an empirically determined rate constant β. In order to translate the model into the thermal phase change model framework in ANSYS CFX, it was necessary to modify it slightly, and re-express it in terms of a model for the interfacial area density (IAD). The ANSYS CFX mixture model framework was selected for this, in which the IAD is expressed in terms of a modelled interfacial length scale, which depends in turn on the rate constant β. The value of this constant was not known a priori, and four values were tested, which were 0.1 Hz, 1 Hz, 10 Hz and 100 Hz.

Using rate constants of 10 and 100 Hz caused excessive numerical instabilities within the solution and a fully converged solution was not accomplished. Fully converged solutions were accomplished using rate constants of 0.1 Hz and 1 Hz. The results with using a rate constant of 0.1 Hz yielded excessive evaporation rates at the free surface which were unrepresentative of the true rates of evaporation. The rate constant 1 Hz yielded a solution closer to the physically realistic expected value.

The results using the rate constants 0.1 Hz and 1 Hz have little effect on the heat and momentum distributions inside the water, but do have significant implications on the evaporative mass transfer across the interface. There was good agreement between the stream temperatures reported in the experimental data and the numerical results outputted from the CFD investigations. This was despite the CFD investigations not allowing for wall boiling to occur on the heated coils.

The flow patterns during evaporation appear to confirm the motivating hypothesis that the flow behaves like an unconstrained thermosyphon reboiler, with internal temperatures similar to the temperature adjacent to the ullage region. The results also indicate that most phase change occurs as flash evaporation on the top, not as boiling from the coils, as originally thought.

Simulations of Evaporator C were performed using the modelling techniques established for the simulations of the scaled test rig in CHAPTER 5. The two phase Euler – Euler framework was used. From the validation work of the scaled test rig the interphase rate constant took a value of 1 Hz for the Evaporator C simulations.

Original estimates of the condition of Evaporator C assumed boiling occurred on all heat transfer surfaces. The simulations have shown this is not true for the lower portion of the evaporator vessel where the hydrostatic pressure, and hence saturation pressure is at its greatest. In fact the lower portions of the evaporator vessel operated in the single phase convective regime, whilst the upper regions close to the free surface underwent boiling.

Under operation the bulk liquor temperatures remained constant, and close to the free surface saturation temperature corresponding to 0.1 bar. The flow patterns during operation were similar to an unconstrained thermosyphon reboiler.

8.2 Future Work

An updated industrial evaporator design, Sellafield Evaporator D is currently being commissioned for use at the Sellafield site. The new evaporator shares many design similarities to Evaporator C and would therefore be an obvious recipient of further work in this field.

The results of Evaporator C show that boiling does have the potential to occur on the coil surfaces close to the free surface. Therefore wall boiling simulations should be performed in conjunction with evaporation at the free surface. This would require detailed investigations into developing sub models applicable to wall boiling at sub-atmospheric pressures. In addition to this, the simulations should be performed for a longer time. In this study, the evaporation simulations only lasted 10 s. There is no guarantee different flow patterns will not emerge after this time. Therefore simulations should be performed for longer in order to truly appreciate repetitive flow patterns.

Performing wall boiling simulations would require a more detailed formulation for the interfacial area density which would take into consideration bubbly flow, droplet flow, free surface flow, and the interactions between the three. Researchers at Helmholtz-Zentrum Dresden-Rossendorf (T Höhne and Lucas, 2011) are currently researching similar systems, but under isothermal conditions without phase change present. Therefore an extension of those models to include heat transfer would be an obvious starting position, which would allow possible wall boiling simulations. Such studies would have to take a fully inhomogeneous approach to the conservation equations which would significantly increase simulation compute times.

The boundary conditions in this study were fixed for Evaporator C. Steam condensation was not modelled directly. Condensation heat transfer coefficients were supplied to the heated surfaces, which had the effect of fixing the heat flux into the system. To allow for a physically realistic simulation, the entire system should be modelled. This will be a coupled simulation of condensation inside the external heating jacket and inside the helical coils, conjugate conduction through the metal walls, and boiling in the liquor. This would provide a near complete analysis of the evaporators.

The Sellafield evaporators boil highly active liquor, which is nitric acid based. The current investigations assumed water inside the test rigs which is not physically representative of highly active liquor. Therefore simulations of HAL should be performed which would provide far greater accuracy for the temperature distributions on the heated surfaces.

It was previously mentioned in CHAPTER 2 that salt solids precipitate during the evaporation process and are transported with the liquid itself. Solids within the system have the potential to completely change the thermal behaviour of the system, and therefore should be modelled in the future.

References

Alane, A. 2007. The Experimental Study of Operating Characteristics, Stability and Performance of a Vertical Thermosyphon Reboiler Under Vacuum. *PhD Thesis, University of Manchester*.

Alane, A. and Heggs, P.J. 2011. Experimental study of complex two-phase instabilities during the start-up of a vertical thermosyphon reboiler operating under vacuum. *Chemical Engineering Research and Design*. **89**(10),pp.2012–2023.

Alizadehdakhel, A., Rahimi, M. and Alsairafi, A.A. 2010. CFD modeling of flow and heat transfer in a thermosyphon. *International Communications in Heat and Mass Transfer*. **37**(3),pp.312–318.

Ansys, A.F. 2011. 14.0 Theory Guide. *ANSYS inc*.,pp.218–221.

Ansys Inc 2010a. *Ansys CFD Solver Theory Guide*. Ansys Inc.

Ansys Inc 2010b. *Ansys CFX solver modelling guide*.

Aydin, M.C. 2012. CFD simulation of free-surface flow over triangular labyrinth side weir. *Advances in Engineering Software*. **45**(1),pp.159–166.

Bejan, A. and Kraus, A.D. 2003. *Heat Transfer Handbook*. John Wiley & Sons.

Bergé, P. and Dubois, M. 1984. Rayleigh-bénard convection. *Contemporary Physics*. **25**(6),pp.535–582.

Bergman, T., Lavine, A., Incropera, F. and DeWitt, D. 2011. *Fundamentals of heat and mass transfer* 7th ed.

Bier, K., Schmadl, J. and Gorenflo, D. 1983. Influence of heat flux and saturation pressure on pool boiling heat transfer to binary mixtures. *Chemical Engineering Fundamentals*. **1**,p.79.

Blazek, J. 2015. *Computational fluid dynamics: principles and applications*. Butterworth-Heinemann.

Breber, G., Palen, J.W. and Taborek, J. 1980. Prediction of horizontal tubeside condensation of pure components using flow regime criteria. *Journal of Heat Transfer*. **102**(3),pp.471–476.

Briggs, A. and Rose, J.W. 1994. Effect of fin efficiency on a model for condensation heat transfer on a horizontal, integral-fin tube. *International journal of heat and mass* *transfer*. **37**,pp.457–463.

Celik, I., Ghia, U. and Roache, P. 2008. Procedure for Estimation and Reporting of Uncertainty Due to Discretization in CFD Applications. *Journal of Fluids Engineering*. **130**(7),p.78001.

Von Ceumern-Lindenstjerna, W.C. 1977. Bubble departure diameter and release frequencies during nucleate pool boiling of water and aqueous sodium chloride solutions. *Heat transfer in boiling. Hrs: E. Hahne, U. Grigull. New York Academic Press*.

Churchill, S. and Chu, H. 1975. Correlating equations for laminar and turbulent free convection from a vertical plate. *International Journal of Heat and Mass Transfer*. **18**,p.1323.

Clift, R., Grace, J. and Weber, M. 1978. *Bubbles, Drops and Particles*. New York: Academic Press.

Cole, R. 1960. A photographic study of pool boiling in the region of the critical heat flux. *AIChE Journal*.

Collier, J. and Thome, J. 1994. *Convective Boiling and Condensation*. Oxford: Oxford University Press.

Collier, J. and Thome, J. 1996. *Convective Boiling and Condensation*. Oxford University Press.

Cooper, M. 1984. Saturation nucleate pool boiling: a simple correlation. *Chemical Engineering Symposium Series*. **86**,p.785.

Davis, E. and Anderson, G. 1966. The incipience of nucleate boiling in forced convection flow. *AIChE Journal*. **12**,p.774.

Dobson, A. and Phillips, C. 2006. High Level Waste Processing in the UK - Hard Won Experience that can Benefit US Nuclear Cleanup Work *In*: *Waste Management Conference*.

Drew, D.A. and Passman, S.L. 2006. *Theory of Multicomponent Fluids*. Springer Science & Business Media.

ESDU-91024 2001. *Condensation inside tubes: condensate film coefficient for vertical downflow*.

ESDU-94041 1994. *Condensation inside tubes: condensate film coefficient for horizontal tubes*.

Forster, H. and Zuber, N. 1955. Dynamics of vapor bubbles and boiling heat transfer. *AIChE*

Journal. **1**,p.531.

Freitag, L.A. 1997. On combining Laplacian and optimization-based mesh smoothing techniques. *ASME Applied Mechanics Division Publications AMD*. **220**,pp.37–44.

Frost, W. and Dzakowic, G.S. 1967. An extension of hte method of predicting incipient boiling on commercially finished surfaces *In*: *Paper presented at ASME AIChE Heat Transfer Conference*., pp. 67-NaN-61.

Geddes, W., Perry, B., Wakem, M. and Wylie, C. 2009. Boiling Heat Transfer in Highly Active Liquors *In*: *The Eleventh UK National Heat Transfer Conference*. Queen Mary, University of London.

Gerstmann, J. and Griffith, P. 1967. Laminar film condensation on the underside of horizontal and inclined surfaces. *International Journal of Heat and Mass Transfer*. **10**(5),pp.567 – 570.

Goodson, K., Rogacs, A., David, M. and Fang, C. 2010. Volume of fluid simulation of boiling two-phase flow in a vapor-venting microchannel. *Frontiers in Heat and Mass Transfer (FHMT)*. **1**(1).

Gorenflo, D. and Kenning, D. 2010. H2 Pool Boiling. *VDI Heat Atlas*.

Harrison, M.E., Batten, W.M.J., Myers, L.E. and Bahaj, A.S. 2010. Comparison between CFD simulations and experiments for predicting the far wake of horizontal axis tidal turbines. *IET Renewable Power Generation*. **4**(6),pp.613–627.

Heggs, P. and Walton, C. 1998. Precedence Ordering Techniques. *Institute of Mathematics and its Applications Conference Series*. **66**,pp.175–180.

Heggs, P.J., Ingham, D.B. and Keen, D.J. 1990. The effects of heat conduction in the wall on the development of recirculating combined convection flows in vertical tubes. *International Journal of Heat and Mass Transfer*. **33**(3),pp.517–528.

Hewitt, G., Shires, G. and Bott, T. 1994. *Process Heat Transfer*. London: CRC Press.

Höhne, T. and Lucas, D. 2011. Numerical simulations of counter-current two-phase flow experiments in a PWR hot leg model using an interfacial area density model. *International Journal of Heat and Fluid Flow*. **32**(5),pp.1047–1056.

Höhne, T. and Lucas, D. 2011. Numerical simulations of counter-current two-phase flow experiments in a PWR hot leg model using an interfacial area density model. *International Journal of Heat and Fluid Flow*.

Incropera, F. and Dewitt, D. 2002. *Fundamentals of Heat and Mass Transfer*.

Kreith, F., Manglik, R. and Bohn, M. 2010. *Principles of Heat Transfer: SI Edition*.

Krepper, E., Končar, B. and Egorov, Y. 2007. CFD modelling of subcooled boiling—concept, validation and application to fuel assembly design. *Nuclear Engineering and Design*. **237**(7),pp.716–731.

Kroll, N., Bieler, H., Deconinck, H., Couaillier, V., van der Ven, H. and Sorensen, K. 2010. *ADIGMA–A European Initiative on the Development of Adaptive Higher-Order Variational Methods for Aerospace Applications: Results of a Collaborative Research Project Funded by the European Union, 2006-2009*. Springer Science & Business Media.

Kurul, N. and Podowski, M. 1991. On the modeling of multidimensional effects in boiling channels. *Proceedings of the 27th National Heat Transfer …*.

Kwong, S. and Graham, S. 2011. Calculations of Flow in Evaporator with Solids Present at the Base *In*: *Waste Management 2011 Conference*. Phoenix, AZ.

Lee, W.H. 1980. A pressure iteration scheme for two-phase flow modeling. *Multiphase transport fundamentals, reactor safety, applications*. **1**,pp.407–431.

Lemmert, M. and Chawla, J.M. 1977. Influence of flow velocity on surface boiling heat transfer coefficient. *Heat Transfer in Boiling*. **237**,p.247.

Linstrom, P. and Mallard, W. 2001. NIST Chemistry webbook; NIST standard reference database No. 69.

Mazumder, S. 2015. *Numerical Methods for Partial Differential Equations: Finite Difference and Finite Volume Methods*. Academic Press.

McAdams, W. 1954. *Heat transmission* 3rd Editio. McGraw-Hill, New York.

McNeil, D. a., Burnside, B.M., Rylatt, D.I., Elsaye, E. a. and Baker, S. 2015. Shell-side boiling of water at sub-atmospheric pressures. *International Journal of Heat and Mass Transfer*. **85**,pp.488–504.

McNeil, D., Burnside, B., Rylatt, D., Elsaye, E. and Baker, S. 2015. Shell-side boiling of water at sub-atmospheric pressures. *International Journal of Heat and Mass Transfer*. **85**,pp.488–504.

Menter, F. 1994. Two-Equation Eddy-Viscosity Turbulence Models for Engineering Applications. *American Institute of Aeronautics and Astronautics Journal*. **32**(8),pp.1598–1605.

Menter, F.R., Kuntz, M. and Langtry, R. 2003. Ten years of industrial experience with the SST turbulence model. *Turbulence, heat and mass transfer*. **4**(1).

Milnes, J., Burns, A. and Drikakis, D. 2012. Computational modelling of the HyperVapotron cooling technique. *Fusion Engineering and Design*.

Mostinski, I. 1963. Application of the rule of corresponding states for calculation of heat transfer and critical heat flux. *Teploenergetika*. **4**,pp.66–71.

Mueller, A. 1983. *Heat Exchanger Design Handbook*. Washington DC: Hemisphere Publishing Corporation.

NNL Private Communication 2013. *NNL Private Communication*.

NNL Private Communication 2011. *NNL Private Communication*.

Nukiyama, S. 1966. The maximum and minimum values of the heat transmitted from metal to boiling water under atmospheric pressure. *International Journal of Heat and Mass Transfer*.

Nusselt, W. 1916. Die Oberflachenkondesation des Wasserdamffes. *Zetrschr. Ver. Deutch. Ing.* **60**,pp.541–546.

Office for Nuclear Regulation 2015a. *Hazard and Risk reduction from Highly Active Liquor*.

Office for Nuclear Regulation 2015b. *Project Assessment Report – HAL Stocks Specification*.

Ogale, V.A. 1968. On the application of the semi-closed thermosyphon system to gas turbine blade cooling.

Owen, S.J. 1998. A Survey of Unstructured Mesh Generation Technology. *In*: *IMR*., pp. 239–267.

Paul, E.L., Atiemo-Obeng, V.A. and Kresta, S.M. 2004. *Handbook of industrial mixing: science and practice*. John Wiley & Sons.

Perry, B. and Geddes, W. 2011. A localised condensation model for the simulation of kettle evaporators *In*: *The Twelfth UK National Heat Transfer Conference*. University of Leeds.

Plumb, G. and Mackay, S. 1988. The application of reduced pressure evaporation for treatment of radioactive liquids *In*: *Waste Management Symposia 1988*., pp. 513–519.

Podowski, M., Alajbegovic, A. and Kurul, N. 1997. Mechanistic modeling of CHF in forced-convection subcooled boiling.

Popiel, C. and Boguslawski, L. 1975. Heat transfer by laminar film condensation on sphere surfaces. *International Journal of Heat and Mass Transfer*. (5),pp.1486–1488.

Promvonge, P., Sripattanapipat, S. and Kwankaomeng, S. 2010. Laminar periodic flow and heat transfer in square channel with 45 inline baffles on two opposite walls.

International Journal of Thermal Sciences. **49**(6),pp.963–975.

Richardson, T.J.A. 2009. *Shreir’s Corrosion*. Elsevier.

Robson, P. and Candy, E. 2009. Designing a New Highly Active Liquid Evaporator *In*: *ASME 2009 12th International Conference on Environmental Remediation and Radioactive Waste Management*. American Society of Mechanical Engineers, pp. 593–600.

Rohsenow, W. 1951. A method of correlating heat transfer data for surface boiling of liquids. *Trans. ASME*. **74**,p.969.

Rohsenow, W. 1956. Heat transfer and temperature distribution in laminar film condensation. *Trans. Asme*. **78**,pp.1645–1648.

Rohsenow, W. and Hartnett, J. 1973. *Handbook of Heat Transfer* 1st Ed. New York: McGraw-Hill Book Company.

Rohsenow, W., Hartnett, J. and Cho, Y. 1998. *Handbook of Heat Transfer* 3rd Ed. New York: McGraw-Hill Book Company.

Rohsenow, W., Hartnett, J. and Ganiac, E. 1985. *Handbook of Heat Transfer Fundamentals* 2nd Ed. New York: McGraw-Hill Book Company.

Rossby, H.T. 1969. A study of Bénard convection with and without rotation. *Journal of Fluid Mechanics*. **36**(2),pp.309–335.

Sato, T. and Matsumura, H. 1964. On the conditions of incipient subcooled-boiling with forced convection. *Bulletin of JSME*. **7**(26),pp.392–398.

De Schepper, S.C.K., Heynderickx, G.J. and Marin, G.B. 2009. Modeling the Evaporation of a Hydrocarbon Feedstock in the Convection Section of a Steam Cracker. *Computers & Chemical Engineering*. **33**(1),pp.122–132.

Schiller, L. and Naumann, A. 1935. A Drag Coefficient Correlation. *Vdi Zeitung*. **77**(318),p.51.

Serth, R. 2007. *Process heat transfer: principles and applications*.

Shewchuk, J.R. 1997. *Delaunay refinement mesh generation*. DTIC Document.

Spindler, K. 1994. Flow Boiling *In*: *Proceedings of the Tenth International Heat Transfer Conference*., pp. 349–368.

Sun, D., Xu, J. and Wang, L. 2012. Development of a vapor–liquid phase change model for volume-of-fluid method in FLUENT. *International Communications in Heat and Mass Transfer*. **39**(8),pp.1101–1106.

Taitel, Y. and Dukler, A.E. 1976. A model for predicting flow regime transitions in horizontal and near horizontal gas-liquid flow. *AIChE Journal*. **22**(1),pp.47–55.

Talebi, S., Abbasi, F. and Davilu, H. 2009. A 2D numerical simulation of sub-cooled flow boiling at low-pressure and low-flow rates. *Nuclear Engineering and Design*.

Tolubinsky, V.I. and Kostanchuk, D.M. 1970. Vapour bubbles growth rate and heat transfer intensity at subcooled water boiling *In*: *International Heat Transfer Conference 4*. Begel House Inc.

Tritton, D. 1988. *Physical Fluid Dynamics* 2nd Ed. Oxford: Oxford University Press.

Trivedi, C., Cervantes, M.J., Gandhi, B.K. and Dahlhaug, O.G. 2013. Experimental and numerical studies for a high head Francis turbine at several operating points. *Journal of Fluids Engineering*. **135**(11),p.111102.

Tu, J.Y. 1999. The Influence of Bubble Size on Void Fraction Distribution in Subcooled Flow Boiling at Low Pressure. *International communications in heat and mass transfer*. **26**(5),pp.607–616.

Tu, J.Y. and Yeoh, G.H. 2002. On Numerical Modelling of Low-Pressure Subcooled Boiling Flows. *International Journal of Heat and Mass Transfer*. **45**(6),pp.1197–1209.

Ünal, H.C. 1976. Maximum bubble diameter, maximum bubble-growth time and bubble-growth rate during the subcooled nucleate flow boiling of water up to 17.7 MN/m2. *International Journal of Heat and Mass Transfer*. **19**(6),pp.643–649.

Upson, P. 1984. Highly active liquid waste management at Sellafield. *Progress in Nuclear Energy*. **13**(1),pp.31–47.

Del Valle, V.H. and Kenning, D.B.R. 1985. Subcooled flow boiling at high heat flux. *International Journal of Heat and Mass Transfer*. **28**(10),pp.1907–1920.

Wakem, M., Wylie, T., Spencer, J., Whillock, G., Ward, T. and Graham, S. 2009. Heat Transfer in a Highly Active Evaporator *In*: *11th UK Heat Transfer Conference*.

Walkley, M. 2011. Newton-Raphson Method.

Westra, R.W., Broersma, L., Van Andel, K. and Kruyt, N.P. 2010. PIV measurements and CFD computations of secondary flow in a centrifugal pump impeller. *Journal of Fluids Engineering*. **132**(6),p.61104.

Wilson, J.S. 2004. *Sensor technology handbook*. Elsevier.

Wilson, P. 1996. *The nuclear fuel cycle from ore to wastes*. Oxford University Press.

Yang, Z., Peng, X.F. and Ye, P. 2008. Numerical and experimental investigation of two phase flow during boiling in a coiled tube. *International Journal of Heat and Mass Transfer*.

51(5),pp.1003–1016.

Yeoh, G., Cheung, S., Tu, J. and Ho, M. 2008. Fundamental consideration of wall heat partition of vertical subcooled boiling flows. *International Journal of Heat and …*.

Zeitoun, O. and Shoukri, M. 1997. Axial void fraction profile in low pressure subcooled flow boiling. *International journal of heat and mass transfer*.

Appendix 1: The Newton Raphson Algorithm

Heat transfer engineers frequently encounter problems where non-linear heat transfer transport equations require solving. Difficulty arises when the solution is a function of one or more of the unknown variables inside the heat transfer system. This peculiarity arises from the use of the heat transfer coefficient, which usually is inconveniently a function of the driving temperature and heat flux, both of which are usually the quantities being solved for. The heat transfer coefficient is the figment of the imagination of the heat transfer engineer.

One method that can be used to overcome this problem is by using the precedence ordering technique (Heggs and Walton, 1998) which involves algebraic manipulation and substitution of heat transfer equations to derive a final equation which describes the heat transfer system in its entirety. The final equation may reduce to a simpler form, and hence an explicit solution may be available. The advantage of the precedence ordering method is that it will indicate if an explicit solution exists, and if it does it will indicate which variables the heat transfer system is dependent on. If an explicit solution to the final equation that was derived does not exist, then an iterative approach must be used to determine the unknown values implicitly. The precedence ordering method has some drawbacks:

1. It requires algebraic manipulation, which is often very complicated which may give rise to errors, and it may be impossible to carry out algebraic manipulation due to the complicated mathematical nature of heat transfer coefficients and how they are expressed.
2. It is impossible to use the precedence ordering technique using curve fitted equations for the thermophysical properties of fluid, as shown in Appendix A for example.
3. If an explicit solution does not exist then one must resort to using implicit methods to determine the solution of the unknowns.

The method used for the works in this document uses the Newton Raphson implicit iterative solver in the first instance, which removes the need for complex algebraic manipulation. Essentially the system of equations that are solved are described by n number of equations with n unknowns. There must be the same number of equations describing the system as there are unknowns.

For the successful use of the Newton Raphson method, a code must be written in MatLab, FORTRAN, C or any other language of choice. The MatLab Newton Raphson code written by Walkley (2011) was used as a basis, and was heavily modified to improve its performance.

To better explain how the Newton Raphson method is employed consider a simple system of equations, with two equations and two unknowns. The unknowns are x_1 and x_2.

$$f_1 = x_1^3 + x_2^2 = 0 \tag{0.1}$$

$$f_2 = x_1^2 - x_2^3 = 0 \tag{0.2}$$

In the MatLab code, the user simply needs to input the above two equations as they are displayed, and supply a sensible initial guess for x_1 and x_2, and a specified convergence precision, where a precision of 1e^{-6} is usually sufficient. Algebraic manipulation is not required of the two equations. Without user intervention the Newton-Raphson method arranges the two equations in the matrix format

$$F(x) = \begin{pmatrix} f_1(x_1, x_2) \\ f_2(x_1, x_2) \end{pmatrix} = \begin{pmatrix} x_1^3 + x_2^2 \\ x_1^2 - x_2^3 \end{pmatrix} = 0 \tag{0.3}$$

A Jacobian matrix which contains the derivatives is computed as

$$J_F(x) = \begin{pmatrix} \frac{\partial f_1}{\partial x_1} & \frac{\partial f_1}{\partial x_2} & \cdots & \frac{\partial f_1}{\partial x_n} \\ \frac{\partial f_2}{\partial x_1} & \frac{\partial f_2}{\partial x_2} & \cdots & \frac{\partial f_2}{\partial x_n} \\ \vdots & \vdots & \ddots & \vdots \\ \frac{\partial f_n}{\partial x_1} & \frac{\partial f_n}{\partial x_2} & \cdots & \frac{\partial f_n}{\partial x_n} \end{pmatrix} \tag{0.4}$$

In the Newton Raphson method the derivatives in the Jacobian matrix is determined using finite differences, where

$$\frac{\partial f_n}{\partial x_n} = \frac{f_n(x+\delta) - f_n(x)}{\delta} \tag{0.5}$$

For the system of equations f_1 and f_2 the Jacobian is computed as

$$J_F(x) = \begin{pmatrix} 3x_1^2 & 2x_2 \\ 2x_1 & -3x_2^2 \end{pmatrix} \tag{0.6}$$

Once the Jacobian is computed the solution is updated using the recursion algorithm

$$x^{(k+1)} = x^{(k)} - J_F\left(x^{(k)}\right)^{-1} F\left(x^{(k)}\right) \tag{0.7}$$

In the first iteration for the solution $x^{(k+1)}$ the initial guess x_0 is used. In the second iteration for the solution $x^{(k+2)}$ the solution from $x^{(k+1)}$ is used in place of x_0. The difference in the solution between $x^{(k+1)}$ and $x^{(k+2)}$ is continually computed to ensure that the residual is no less than the tolerance specified. When sufficient recursions occur, and when the tolerance criteria is met the final solutions are found. For this example the final solutions for x_1 and x_2 are -1 and 1 respectively.

The same algorithm was used in this study to determine the unknown values in the thermal resistance investigation. The following code written in the MatLab language shows the structure of the Newton-Raphson algorithm. Firstly the recursion algorithm “newtonSys” is given as

```
function [ x,f ] = newtonSys( fnon, fjac, x0, tol, maxIt )

% Basic Newton algorithm for systems of nonlinear equations
%  function [ x,f ] = newtonSys( fnon, fjac, x0, tol, maxit )
% Input: fnon - function handle for nonlinear system
%        fjac - function handle for Jacobian matrix
%        x0 - initial state (column vector)
%        tol - convergence tolerance
%        maxIt - maximum allowed number of iterations
% Output: x - final point
%         f - final function value

fprintf(' x     |f(x)|\n')

n = length(x0);

x = x0;             % initial point
f = feval(fnon,x);  % initial function values
it = 0;

while (norm(f)>tol) && (it<maxIt)

  J = feval( fjac, n, x, f, fnon ); % build Jacobian
  delta = -J\f;                           % solve linear system

  x = x + delta;       % update x
  f = feval(fnon,x);   % new function values

  it = it + 1;
  % Print the new estimate and function value.
  fprintf(' %d %12.6f\n',it,norm(f))

end

if( it==maxIt)
    fprintf(' WARNING: Not converged\n')
else
    fprintf(' SUCCESS: Converged\n')
end
```

The Jacobian algorithm takes the following form which the “newtonSys” script above “calls in” (much like a subroutine found in Fortran and other traditional languages).

```
function J =  fdJacobian( n, x0, f0, fnon )

% Finite difference approximation to the Jacobian
%  function J =  fdJacobian( n, x0, f0, fnon )
% Input: n - number of equations
%        x0 - current solution
%        f0 - current function value
%        fnon - nonlinear function handle
% Output: J - Jacobian matrix

J = zeros(n);

h = 10*sqrt(eps); % perturbation

for j = 1:n   % compute column by column

    x = x0;
    x(j) = x(j) + h;         % perturb variable x_j
    f = feval( fnon, x );    % perturbed residual
    J(1:n,j) = ( f - f0 )/h; % add in column j

end
```

The only user input would be to input the system of equations and tolerance, and execute the command to run the Newton Raphson algorithm. For the problem described above the system of equations is written in the following script as

```
function y = example( x )
% function [ y ] = example( x )
% system of 2 nonlinear equations

y = zeros(2,1);
y(1) = x(1)^3 + x(2)^2;
y(2) = x(1)^2 - x(2)^3;

end
```

The script which contains the system of equations is executed in MatLab command window using a single line which obeys the following format

```
>> newtonSys(@example,@fdJacobian,[4;5],1e-6,20)
```

Where “example” is the name of the system of equations, “fdJacobian” is the script which calculates the Jacobian, [4;5] is the initial guess, 1e^{-6} is the tolerance and 20 is the maximum number of iterations. Executing this command reveals the solution for x_1 and x_2 as shown below.

```
>> newtonSys(@example,@fdJacobian,[4;5],1e-6,20)

x      |f(x)|

 1      42.184857

 2      12.821803

 3      3.999149
```

```
 4      1.247068
 5      149.021393
 6      4146.011778
 7      1219.111420
 8      359.552115
 9      105.650117
 10     30.808608
 11     8.840648
 12     2.446174
 13     0.617861
 14     0.120802
 15     0.011125
 16     0.000144
 17     0.000000
 SUCCESS: Converged

ans =
   -1.0000
    1.0000
```